

# Half a Century of Satellite Remote Sensing of Sea-Surface Temperature

P. J. Minnett<sup>1#</sup>, A. Alvera-Azcárate<sup>2</sup>, T. M. Chin<sup>3</sup>, G. K. Corlett<sup>4</sup>, C. L. Gentemann<sup>5</sup>, I. Karagali<sup>6</sup>,  
X. Li<sup>7</sup>, A. Marsouin<sup>8</sup>, S. Marullo<sup>9</sup>, E. Maturi<sup>10</sup>, R. Santoleri<sup>11</sup>, S. Saux Picart<sup>8</sup>, M. Steele<sup>12</sup>,  
& J. Vazquez-Cuervo<sup>3</sup>

<sup>1</sup> Rosenstiel School of Marine and Atmospheric Science, University of Miami, 4600  
Rickenbacker Causeway, Miami, FL 33149, USA

<sup>2</sup> AGO-GHER-MARE, University of Liège, Allée du Six Août 17, Sart Tilman, Liège, 4000,  
Belgium

<sup>3</sup> Jet Propulsion Laboratory, California Institute of Technology, 4800 Oak Grove Drive,  
Pasadena, CA 91109, USA

<sup>4</sup> EUMETSAT, Eumetsat Allee 1, D-64295 Darmstadt, Germany

<sup>5</sup> Earth & Space Research, 2101 4th Ave #1310, Seattle, WA 98121, USA

<sup>6</sup> DTU Wind Energy, Technical University of Denmark, Risø Campus, Frederiksborgvej 399,  
Roskilde, 4000, Denmark

<sup>7</sup> IMSG at Environment Modeling Center, National Center for Environmental Prediction,  
NOAA. 5830 University Research Court, College Park, MD 20740, USA

<sup>8</sup> Météo-France, Centre de Météorologie Spatiale, Avenue de Lorraine, 22307 Lannion, France

<sup>9</sup> Italian National Agency for New Technologies, Energy and Sustainable Economic  
Development - ENEA - Division Models and Technologies for Risk Reduction - Laboratory for  
Climate Modelling - Centro Ricerche Frascati - Frascati Italy

<sup>10</sup> NOAA/NESDIS/STAR, NOAA Center for Weather and Climate Prediction (NCWCP)  
5830 University Research Court, Rm 3711, College Park, MD 20740, USA.

<sup>11</sup> Consiglio Nazionale Ricerche - CNR - Institute of Marine sciences (ISMAR), Venezia, Italy.

<sup>12</sup> Polar Science Center / Applied Physics Laboratory, University of Washington, 1013 NE 40<sup>th</sup>  
Street, Seattle, WA 98105 USA

# Corresponding author:

Peter J Minnett,  
Ocean Sciences,  
Rosenstiel School of Marine and Atmospheric Science,  
University of Miami,  
4600 Rickenbacker Causeway,  
Miami,  
FL 33149,  
USA.  
pminnett@rsmas.miami.edu

38

## Abstract

39 Sea-surface temperature (SST) was one of the first ocean variables to be studied from earth  
40 observation satellites. Pioneering images from infrared scanning radiometers revealed the  
41 complexity of the surface temperature fields, but these were derived from radiance  
42 measurements at orbital heights and included the effects of the intervening atmosphere.  
43 Corrections for the effects of the atmosphere to make quantitative estimates of the SST became  
44 possible when radiometers with multiple infrared channels were deployed in 1979. At the same  
45 time, imaging microwave radiometers with SST capabilities were also flown. Since then, SST  
46 has been derived from infrared and microwave radiometers on polar orbiting satellites and from  
47 infrared radiometers on geostationary spacecraft. As the performances of satellite radiometers  
48 and SST retrieval algorithms improved, accurate, global, high resolution, frequently sampled  
49 SST fields became fundamental to many research and operational activities. Here we provide an  
50 overview of the physics of the derivation of SST and the history of the development of satellite  
51 instruments over half a century. As demonstrated accuracies increased, they stimulated scientific  
52 research into the oceans, the coupled ocean-atmosphere system and the climate. We provide brief  
53 overviews of the development of some applications, including the feasibility of generating  
54 Climate Data Records. We summarize the important role of the Group for High Resolution SST  
55 (GHRSSST) in providing a forum for scientists and operational practitioners to discuss problems  
56 and results, and to help coordinate activities world-wide, including alignment of data formatting  
57 and protocols and research. The challenges of burgeoning data volumes, data distribution and  
58 analysis have benefited from simultaneous progress in computing power, high capacity storage,  
59 and communications over the Internet, so we summarize the development and current

60 capabilities of data archives. We conclude with an outlook of developments anticipated in the

61 next decade or so.

62

## 63 **1 Introduction**

64 Sea-surface temperature (SST) is a very important variable in the earth's climate system. Being  
65 at the interface of the ocean and the atmosphere, SST is critical to both, and to the exchanges of  
66 heat, moisture, momentum, and gases between the two (e.g. Bentamy et al., 2017; Wanninkhof et  
67 al., 2009). The patterns of SST reveal subsurface dynamics, at least those with a surface thermal  
68 expression such as fronts and eddies (e.g. Tandeo et al., 2014), and the modulation of the surface  
69 momentum exchanges across the temperature gradients modify the atmospheric boundary layer  
70 on the mesoscale (e.g. O'Neill et al., 2010; Perlin et al., 2014) and larger (e.g. McPhaden et al.,  
71 2006; Minobe et al., 2008). Temporal changes in patterns of SST on the basin scales can reveal  
72 large-scale perturbations to the global circulation (Dong et al., 2018) and multi-decadal changes  
73 in the climate (e.g. Jha et al., 2014). Since all processes in nature exhibit a temperature  
74 dependence, variations in the SST influence many components of the climate, including the  
75 Ocean Primary Production (OPP; Behrenfeld and Falkowski, 1997; Behrenfeld et al., 2006),  
76 which is important to the flow of carbon through the global environment, and is the base of the  
77 ocean food web. Global sampling of the SST is feasible only from earth-observation satellites,  
78 with sensors on geostationary satellites providing rapid sampling in the tropics and mid-latitudes,  
79 and those on polar orbiting satellites generating global data but less frequently. Satellites in  
80 geostationary orbits rotate about the earth in the equatorial plane with a period equal to that of  
81 the earth's rotation on its axis, and thus appear to be at an approximately fixed longitude. The  
82 satellites are at about 35,900 km above the equator. Measurements from geostationary satellites  
83 sample diurnal changes. The term "polar-orbiting satellite" is often used as short-hand for "near-  
84 polar orbiting, sun-synchronous satellites". Such satellites orbit the earth at a height of 700-800  
85 km and have an inclination of  $\sim 98^\circ$ , meaning when they cross the equator, they travel in the

86 direction of  $\sim 98^\circ$  measured from east. The choice of altitude and inclination is determined by the  
87 effects of the earth's equatorial bulge on its gravity field, and results in the plane in which the  
88 satellite orbits precessing in space once per year meaning the satellite passes overhead at a given  
89 latitude at about the same times in a day, once going north (in the ascending arc) and again going  
90 south (in the descending arc), hence the "sun-synchronous" aspect. This has the advantage that  
91 measurements of the same place are taken at about the same local time, but it means that diurnal  
92 changes are poorly resolved by a single satellite. Details of earth satellite orbits are given by  
93 Montenbruck and Gill (2000)

94 Since significant progress in knowledge and understanding are often stimulated by developments  
95 of new or improved instruments, we include a section on the development of satellite instruments  
96 and on improvements in the accuracy of the satellite retrievals of SST. The remarkable  
97 contributions these instruments have made to further our understanding of the oceans, air-sea  
98 interactions, and the climate system, are dealt with in a wealth of papers in the primary literature  
99 and in many books (e.g. Robinson, 2004; Robinson, 2010; Martin, 2014) and encyclopedias (e.g.  
100 Njoku, 2014).

101 In this review, a Historical Background section is followed by a discussion of the meaning of  
102 "SST" and a summary of the techniques of satellite radiometers to derive retrievals of SST. The  
103 satellite radiometers used over the last half century are then presented, leading to a discussion of  
104 the instruments and approaches used to assess the accuracies of the satellite-derived SSTs. There  
105 follows a brief explanation of the various processing levels of the derived SSTs in which the data  
106 are delivered to users. Two regions, the Mediterranean Sea and the Arctic Ocean, are highlighted  
107 as examples of where deriving accurate SST retrievals is challenging but where satellite data  
108 have produced significant results. Three specific applications of satellite-derived SST with direct

109 societal benefit are then briefly discussed: Numerical Weather Prediction, Ocean Heat Content  
110 and its relationship to severe storms, and sea-level rise. The relatively new field of Operational  
111 Oceanography, in which satellite-derived SSTs have immediate applications, is introduced,  
112 followed by the contribution of accurate SSTs from satellites to a longer term application, that of  
113 generating Climate Data Records. Synergistic analyses of satellite-derived SSTs with other  
114 remotely sensed data are then discussed. The role of the Group for High-Resolution SST  
115 (GHRSSST) in coordinating research and operational applications of SST is presented before a  
116 discussion of the facilities at various data centers from where users can access satellite data. The  
117 review concludes with an outlook into anticipated developments in the foreseeable future.  
118 For more information than is possible in this review, the interested reader is referred to, for  
119 example, Chapters 7 and 8 of Robinson (2004), Chapters 7 to 9 of Martin (2014), and Robinson  
120 (2010).

## 121 **2 Historical Background**

122 It is generally accepted that one of the first depictions of a strong SST signal is the Franklin-  
123 Folger chart of the Gulf Stream published in 1768 (Figure 1; Franklin et al., 1768). Benjamin  
124 Franklin, who was deputy Postmaster General of the American colonies and was based in  
125 London, had wondered why sailing ships going to America took longer than the ships coming  
126 from the colonies. His cousin, Timothy Folger, a whaling captain, told Franklin that this was  
127 because of the strong current flowing to the east and was well known to local navigators, but  
128 apparently not to captains of ships crossing the Atlantic Ocean. The temperature gradients at the  
129 sides of the “Gulph Stream,” named in recognition of its origin in the Gulph of Florida, were  
130 known to be good areas for fishing and whaling (Lacouture, 1995). Although the Franklin-Folger

131 chart is the first recognized graphical representation of the Gulf Stream, it had been remarked  
132 upon by the Spanish Explorer, Juan Ponce de León, in 1513 when he landed and named Florida,



133 near present-day St. Augustine (Lacouture, 1995).

134 *Figure 1. An extract of the Franklin-Folger Map of the currents of the North Atlantic showing the*  
135 *position of the strong surface current named here as the Gulph Stream. From the Library of Congress*  
136 *(<https://www.loc.gov/resource/g9112g.ct000753/>).*

137 The history of knowledge about the analogous current in the Pacific Ocean, the Kuroshio, is  
138 much longer, going back to the seventh century (Kawai, 1998) with evidence of the current being  
139 based on flotsam and hapless castaways being washed up on islands having come from the south.  
140 The connection with SST was not made until much later, but was known by the mid-nineteenth  
141 century when mention of warm waters of the Kuroshio was made in ships' log books (Kawai,  
142 1998).

143 The depiction of the Gulf Stream in the Franklin-Folger map is remarkably congruent with the  
144 mean position of the Gulf Stream, as now known, but the current is not constant in position or  
145 strength. Measurements taken from ships were indicative of a very spatially and temporally  
146 variable current, which defied simple representation as a synoptic feature (Fuglister, 1955;  
147 Fuglister, 1963); the same is true of the Kuroshio (Fuglister, 1955).

148 It was not until the advent of infrared (IR) remote sensing from satellites that the spatial  
149 complexity of the surface signature of the Gulf Stream was revealed (Legeckis, 1975). Infrared  
150 scanning radiometers on geostationary satellites were capable of making images of the earth's  
151 disk at half hourly intervals, even in the 1970's. These provided frequent images for compositing  
152 cloud-free sections over a day or so to reduce the obscuration of the sea surface by clouds over  
153 the Gulf Stream (Legeckis, 1975) and to reveal strong features elsewhere, such as Tropical  
154 Instability Waves in the eastern equatorial Pacific (Legeckis, 1977). But it was the higher  
155 resolution and superior sensitivity of IR radiometers on polar-orbiting satellites that gave a better  
156 depiction of the SST features, not only of the Gulf Stream (Legeckis, 1979), but of many other  
157 strong SST gradients associated with upper ocean currents and eddies (Legeckis and Gordon,  
158 1982; Legeckis, 1978).



### 159 **3 Sea-Surface Temperature**

160 Although there have been marine observations since the mid-eighteenth-century (Worley et al.,  
161 2005) and there are records of the near-surface temperature for nearly two centuries using  
162 thermometers in a bucket of sea water hauled onto the deck of ships, it is generally recognized  
163 that the reliable time series of measurements began in the mid 1850's (Rayner et al., 2006). With  
164 time the measurement approaches improved and at about the same time as quantitative retrievals  
165 of SST from IR radiometers on satellites began, arrays of drifting buoys carrying thermometers  
166 and satellite data transmission were being deployed in significant numbers. Subsurface  
167 temperatures from these buoys were used to assess the accuracy of the satellite-derived SSTs,  
168 and while differences had a standard deviation of  $\sim 0.5$  K (McClain et al., 1985), details of the  
169 vertical structure of the near-surface temperature could be ignored. But, as the differences  
170 between satellite-derived SSTs and in situ measurements diminished, the temperature structure  
171 took on a new importance.

172 Although SST is not a single variable, it is considered by many to be the temperature within the  
173 mixed layer (approximately the upper 10 m). Air-sea fluxes of heat, moisture and momentum, as  
174 well as ocean turbulence means the temperature variation through the "mixed layer" can be  
175 complex and variable. This complexity and variability need to be considered when comparing or  
176 combining measurements of SST from different satellites and in situ sensors. To facilitate such  
177 activities, a set of definitions of SST were developed by the GHRSSST Science Team (Section  
178 13). These definitions achieve the closest possible agreement between what is defined and what  
179 can be measured, taking into account our current understanding of near surface thermal  
180 variability. The definitions are in agreement with the Climate and Forecast (CF) metadata  
181 convention and are now used across GHRSSST-format SST products. The definitions are shown

182 schematically in Figure 2 and are briefly summarized below. Further details on their derivation  
 183 are discussed by Minnett and Kaiser-Weiss (2012).

184 Five different SST definitions are specified: (1) The interface temperature ( $SST_{int}$ ) – the  
 185 temperature at the air-sea interface on molecular scales; (2) the skin sea surface temperature  
 186 ( $SST_{skin}$ ) - the temperature measured by an IR radiometer typically operating at wavelengths 3.7-  
 187 12  $\mu\text{m}$  (chosen for consistency with the majority of IR satellite measurements), which represents  
 188 the temperature within the conductive diffusion-dominated sub-layer at a depth of  $\sim 10\text{-}20\ \mu\text{m}$ ;  
 189 (3) the subskin sea surface temperature ( $SST_{subskin}$ ) - the temperature at the base of the

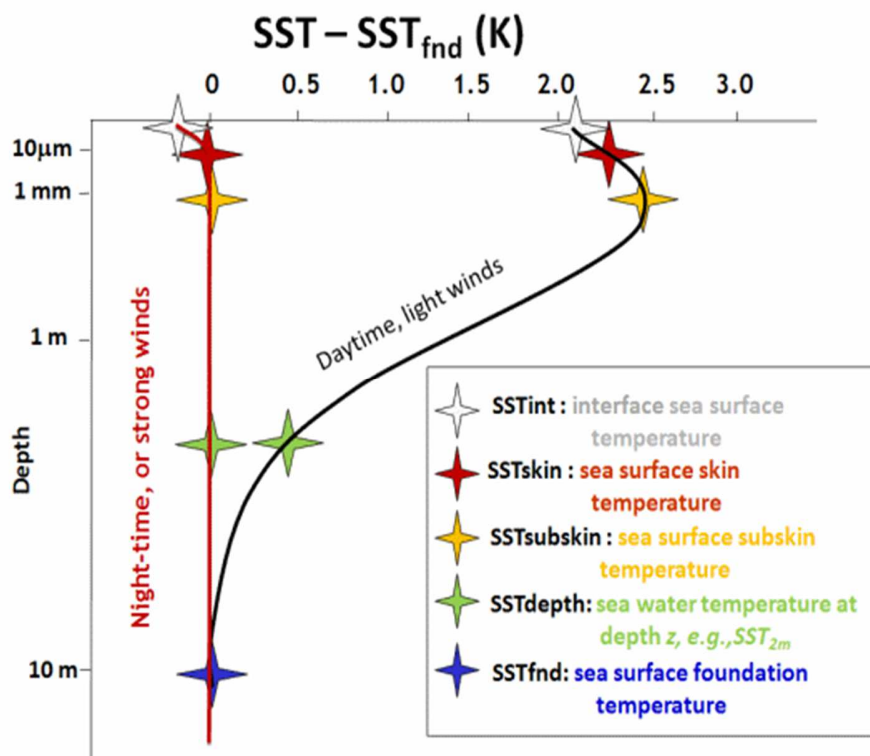


Figure 1. Near-surface oceanic temperature gradients. From Minnett and Kaiser-Weiss (2012)

190 conductive laminar sub-layer of the ocean surface, which for practical purposes can be well  
191 approximated to the measurement of surface temperature by a microwave radiometer operating  
192 in the 6-11 GHz frequency range; (4) the surface temperature at depth ( $SST_z$  or  $SST_{depth}$ ) - all  
193 measurements of water temperature beneath  $SST_{subskin}$ ; and (5) the foundation temperature  
194 ( $SST_{fnd}$ ) - the temperature free of diurnal temperature variability, i.e.,  $SST_{fnd}$  is defined as the  
195 temperature at the first time of the day when the heat gain from the solar radiation absorption  
196 exceeds the heat loss at the sea surface.

### 197 **3.1 Thermal skin effect**

198 The ocean surface is nearly everywhere and under nearly all conditions warmer than the  
199 atmosphere in contact with it, resulting in a heat flow from the ocean to atmosphere. The  
200 upwards flow of heat in the water is accomplished in the top hundred micrometers or so of the  
201 water (Wong and Minnett, 2018) by molecular conduction as the air-sea density difference and  
202 near surface viscous layer on the aqueous side of the interface suppress the turbulent heat  
203 transfer (Soloviev and Lukas, 2014). Thus, there is a vertical temperature gradient in the water  
204 just beneath the interface leading to decreasing temperature closer to the interface; this is referred  
205 to as the thermal skin layer. The IR emission from the sea surface emerges from a thin layer, an  
206 electromagnetic skin layer, that is of comparable thickness in the IR (Bertie and Lan, 1996) to  
207 the thermal skin layer (Wong and Minnett, 2018). The radiance emitted by the sea surface and  
208 measured by an IR radiometer is nearly always characteristic of a temperature lower than that  
209 measured by an in situ thermometer (Donlon et al., 2002; Minnett et al., 2011). The average  
210 temperature drop across the thermal skin layer is  $\sim 0.17$  K, with much larger values seen at very  
211 low winds (ibid), so, given the target accuracy of satellite-derived SSTs for climate change  
212 studies of 0.1 K (Ohring et al., 2005), the variable thermal skin effect should be taken into

213 account, and retrievals of SST in the IR should be considered as  $SST_{\text{skin}}$ . The electromagnetic  
214 skin depths at microwave frequencies used to derive SST are greater (see Figure 2 of Minnett  
215 and Kaiser-Weiss, 2012) so even though the thermal skin layer is embedded in the microwave  
216 electromagnetic skin layer, the microwave-derived SST is not an  $SST_{\text{skin}}$  and can be considered  
217 as an approximation to  $SST_{\text{subskin}}$ .

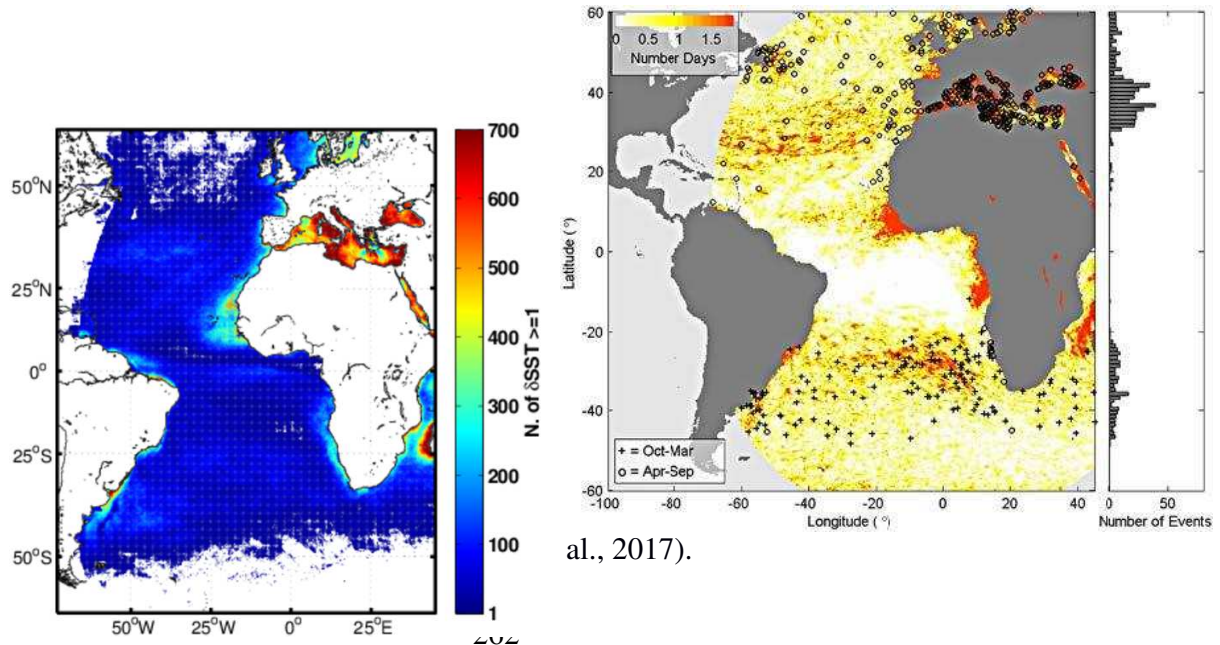
### 218 **3.2 Diurnal variability**

219 A significant part of the solar radiation entering the ocean is absorbed at the top few meters.  
220 During day-time and in the absence of strong enough winds to drive vertical mixing of heat,  
221 diurnal warming causes a relatively shallow warm layer to be formed (Figure 2).

222 Driven by solar heating, diurnal variability of SST occurs under moderately low wind speeds in  
223 all ocean basins. While in situ observations provided the first reported cases of diurnal variability  
224 (e.g. Stommel et al., 1969; Halpern and Reed, 1976; Kaiser, 1978), SST retrievals from space  
225 resulted in a significant increase of diurnal cycle characterization and understanding. Diurnal  
226 warming has been identified in the Arctic (Eastwood et al., 2011), the North and Baltic Sea  
227 (Karagali et al., 2012), various regions of the Atlantic Ocean (Figure 3; Cornillon and Stramma,  
228 1985; Stramma et al., 1986; Price et al., 1987; Gentemann and Minnett, 2008; Le Borgne et al.,  
229 2012a; Karagali and Høyer, 2014), the Mediterranean Sea (Deschamps and Frouin, 1984; Böhm  
230 et al., 1991; Buongiorno Nardelli et al., 2005; Merchant et al., 2008a; Marullo et al., 2014a), the  
231 Tropics (Clayson and Weitlich, 2007; Marullo et al., 2010) and Tropical Warm Pool (Zhang et  
232 al., 2016a; Zhang et al., 2016b), the Gulf of California (Flament et al., 1994; Ward, 2006), the  
233 Indian and South Pacific Ocean (Gentemann and Minnett, 2008) and the Arabian Sea (Stuart-  
234 Menteth et al., 2005b). Advances in space-borne SST retrievals allowed basin-scale studies of  
235 diurnal warming spanning several years and extended comparisons with in situ observations

236 (Stuart-Menteth et al., 2003; Gentemann and Minnett, 2008; Castro et al., 2014; Karagali and  
237 Høyer, 2014), with detailed characterization of number of occurrences, peak warming time and  
238 seasonal patterns. The abundance of SST retrievals from space and improvements in  
239 understanding of the diurnal cycle allowed for numerical simulations to reproduce the diurnal  
240 variability of the upper ocean layer, first developed shortly after the first observational evidence  
241 was reported. Based on parametrizations of solar heating of the upper ocean (Woods et al.,  
242 1984), Woods and Barkmann (1986) modelled the response of a layered ocean to daily and  
243 seasonal modulation of solar heating. Price et al. (1986) developed a mixed layer model using  
244 observational evidence from a measurement campaign. A simplified version of this model was  
245 developed a decade later by Fairall et al. (1996) and similar approaches were adopted by Zeng  
246 and Beljaars (2005), Schiller and Godfrey (2005), and Gentemann et al. (2009). A simpler  
247 approach to reproducing the diurnal variability was adopted through parameterizations derived  
248 from wind and surface warming observations (Webster et al., 1996; Clayson and Curry, 1996;  
249 Kawai and Kawamura, 2002; Gentemann et al., 2003; Stuart-Menteth et al., 2005a; Filipiak et  
250 al., 2010). A selection of these models has been intercompared in various regions (Karagali and  
251 Høyer, 2013; Zhang et al., 2018). Furthermore, turbulence closure models solving the equations  
252 for the distribution of heat, momentum, and salt across the water column, have been found to  
253 successfully reproduce diurnal SST signals (Kantha and Clayson, 1994; Hallsworth, 2005;  
254 Karagali et al., 2017). Identification and characterization of diurnal variability in all ocean basins  
255 promoted not only attempts for its numerical simulation but also impact studies to assess the  
256 importance of accounting for the formation of diurnal warm layers in large scale modelling  
257 systems. The implications associated with the lack of a properly resolved SST daily cycle in  
258 atmospheric, oceanic and climate models have been evaluated in terms of heat budget errors in

259 the Tropics (Danabasoglu et al., 2006; Bellenger and Duvel, 2009; Ham et al., 2010; Clayson and  
 260 Bogdanoff, 2013), the Mediterranean Sea (Marullo et al., 2016), and the North Sea (Fallmann et



al., 2017).

263 *Figure 3. Left: Spatial extent of hours of diurnal heating of SST  $\geq 1$  K (defined as the difference between*  
 264 *a given daytime hourly SST value and the corresponding foundation temperature of the previous night)*  
 265 *from SEVIRI hourly retrievals for 2006–2011. White areas indicate zero occurrences. After Karagali and*  
 266 *Høyer (2014). Right: Location of diurnal events over 5 K (black ‘+’ and ‘o’). Events generally occur in*  
 267 *the summer. The background color shows the days in a year (on average) that wind speed was  $< 1$  ms $^{-1}$  at*  
 268 *14:00 LMT. From Gentemann et al. (2008) with permission.*

## 269 4 Satellite Retrieval of Sea-Surface Temperature

270 The spectral distribution of radiation emitted by the sea surface at absolute temperature,  $T$ , is  
 271 given by Planck’s Function:

$$272 B_{\lambda}(T) = 2hc^2 \lambda^{-5} (e^{hc/(\lambda kT)} - 1)^{-1} \quad (1)$$

273 where  $h$  is Planck's constant,  $c$  is the speed of light in a vacuum,  $k$  is Boltzmann's constant, and  $\lambda$   
274 is the wavelength. Planck's Function is for a perfectly emitting surface, a blackbody, whereas all  
275 natural surfaces emit imperfectly with the ratio of emitted radiance to Planck's function being the  
276 emissivity,  $\epsilon$ , which is a function of the wavelength of the emitted radiation and the angle of  
277 emission relative to normal to the surface,  $\theta$ . The tilting of the facets of the sea surface by wind  
278 generated waves (Cox and Munk, 1954) introduces an apparent wind speed dependence of  $\epsilon$   
279 (Hanafin and Minnett, 2005; Nalli et al., 2008b; Nalli et al., 2008a). The emissivity of seawater  
280 at IR wavelengths where measurements of SST are made is high ( $\sim 0.985$  at  $\lambda = 10 \mu\text{m}$  at an  
281 emission angle of  $40^\circ$  and  $0.970$  at  $55^\circ$ ; Hanafin and Minnett, 2005) and exhibit small apparent  
282 wind speed dependence, at least for emission angles  $< 60^\circ$ . An important property of Planck's  
283 Function is that the emitted radiance at any wavelength increases as the emitting temperature  
284 increases. Thus, a measurement of radiance at a known wavelength can be used to derive the  
285 emitting temperature through Equation 1.

## 286 **4.1 SST retrievals in the Infrared**

287 The temperatures derived from the radiance measurements of satellite radiometers, using  
288 Planck's Function (Equation 1, modulated by the spectral response of the radiometer), are called  
289 brightness temperatures, and because of the effects of the intervening atmosphere these are not  
290 the same as would be measured by a radiometer of comparable accuracy just above the sea  
291 surface. The initial step in deriving SST from brightness temperatures requires the confident  
292 identification of pixels that include radiance from clouds, or aerosols, before clear-sky  
293 atmospheric correction algorithms can be applied.

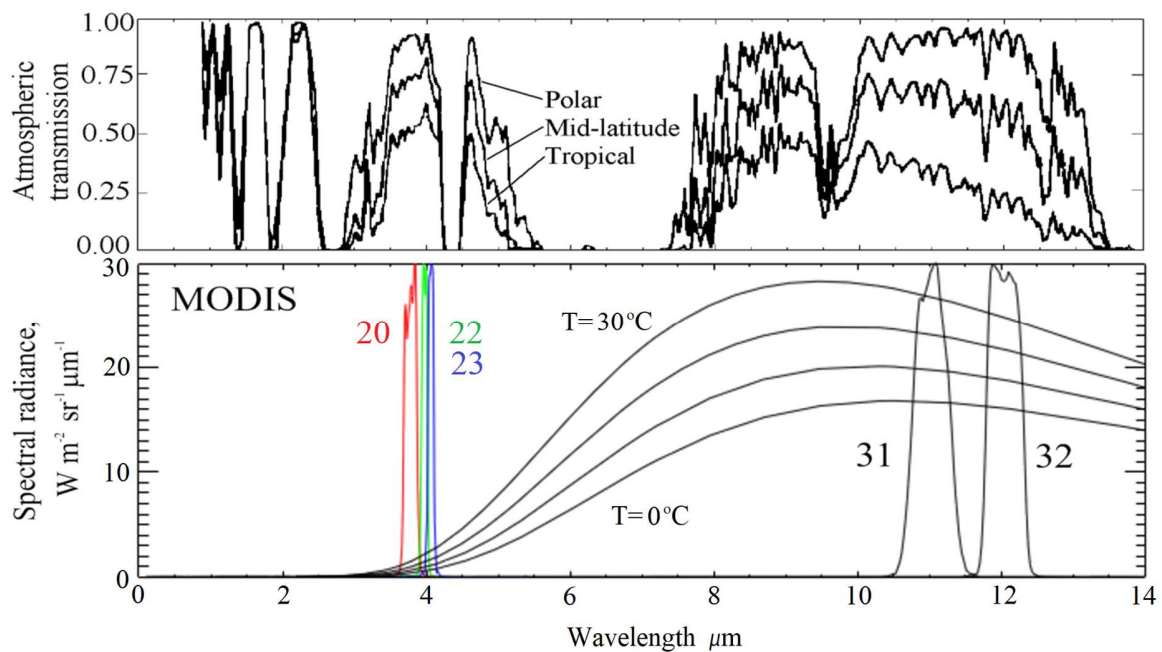
### 294 **4.1.1 Atmospheric transmission**

295 As the IR radiation propagates through the atmosphere to reach the satellite sensors, the photons  
296 may interact with the components of the atmosphere. As in the visible, IR radiation does not  
297 propagate unhindered through clouds, and, even in cloud-free conditions, the photons can be  
298 absorbed or scattered by molecules and aerosols, and the atmospheric components emit photons  
299 into the beam that reaches the satellite radiometer. The transmissivity of the clear-sky  
300 atmosphere in the IR is very variable with wavelength and with the concentrations of  
301 atmospheric gases. The term “atmospheric window” is used to describe wavelength intervals  
302 where the atmosphere is relatively transparent and it is measurements by satellite radiometers in  
303 these intervals that permit the estimation of SST from top-of-atmosphere measurements.

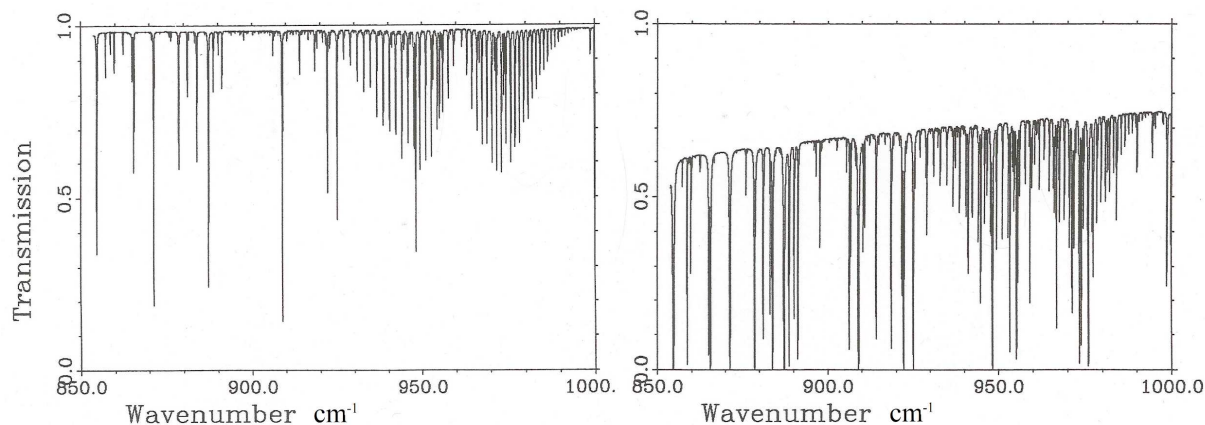
304 In the IR, the peak of Planck’s Function at temperatures typical of the SST is close to  $\lambda = 10 \mu\text{m}$ ,  
305 where the atmosphere is relatively transparent. Figure 4 shows the spectral dependence of the  
306 atmospheric transmission for three characteristic atmospheres derived from a radiative transfer  
307 model with relatively coarse spectral resolution. The lower panel of Figure 4 shows the spectral  
308 radiance calculated for four temperatures - 0, 10, 20, and 30 °C with the relative spectral  
309 response functions (RSRs), normalized to a maximum value of 1 for five bands of the  
310 MODerate-resolution Imaging Spectroradiometer (MODIS, see Section 5.1.4) on the *Aqua*  
311 satellite. The RSRs are defined by transmission filters and the responsivity of the detectors. The  
312 spectrum of the radiance measured at the top of the atmosphere depends on the product of the  
313 value of the RSR, the intensity of the emitted radiance at the sea surface, and the atmospheric  
314 transmission at each wavelength. The signal generated is the integral across wavelength of the  
315 top-of-atmosphere spectrum. A second atmospheric window used for IR remote sensing of SST  
316 is in the mid-IR between  $\lambda = 3.5$  to  $4.1 \mu\text{m}$ . At these wavelengths, the signal is much smaller than  
317 in the “thermal infrared” at  $\lambda = 9.5$ - $13 \mu\text{m}$ , but the sensitivity to changes in temperatures is much



318 higher, giving these measurements advantage for accurate and sensitive SST estimation.  
 319 However, the low radiance means these measurements are very susceptible to contamination by  
 320 reflected and scattered solar radiation and so SST can only be derived using measurements in the  
 321 mid-IR window when conditions limit solar effects, which usually means only at night.  
 322 The transmission of dry, cold polar atmospheres is high in both transmission windows, but as the  
 323 water vapor increases, the transmission decreases so that more of the signal originates in the  
 324 atmosphere and less at the surface. Figure 4 shows in broad terms the regional variations in the



325  
 326 *Figure 4. Spectral dependence of the atmospheric transmission for wavelengths of electromagnetic*  
 327 *radiation from about 1 to 14 μm, for three characteristic atmospheres (above), and (below) the black-*  
 328 *body emission for temperatures of 0, 10, 20 and 30°C, and the relative spectral response functions of the*  
 329 *bands of MODIS on Aqua used to derive SST. The upper panel is adapted from Llewellyn-Jones et al.*  
 330 *(1984) and the lower panel is taken from Kilpatrick et al. (2015).*



331  
 332 *Figure 5. Simulated spectra of atmospheric transmission in the thermal IR transmission window for dry*  
 333 *winter conditions (left) and moister summer conditions (right) at the same location (66°N, 2°E) in the*  
 334 *Norwegian Sea. The atmospheric conditions were given by radiosondes. Note the units on the abscissa*  
 335 *are in wavenumber units; 850 cm<sup>-1</sup> corresponds to  $\lambda = 12 \mu\text{m}$  and 1000 cm<sup>-1</sup> to  $\lambda = 10 \mu\text{m}$ .*

336 clear-sky atmospheric transmission, but there are significant seasonal variations at any location.  
 337 An example of seasonal variations is given in Figure 5, which shows the atmospheric  
 338 transmission spectra in the 10 – 12  $\mu\text{m}$  range derived by a high spectral resolution radiative  
 339 transfer model (Závody et al., 1995). The atmospheric water vapor and temperature profiles were  
 340 those measured by radiosondes launched from Ocean Weather Ship Mike at 66°N, 2°E in  
 341 February (left) and in July (right). The February conditions are very dry and cold, and the  
 342 atmospheric transmission is high; the narrow lines to lower transmission are the signatures of  
 343 quantized molecular absorption of photons propagating upwards. The July conditions are moister  
 344 and while the same line absorption is apparent, the baseline is not at high transmission as in  
 345 February and shows a gradient with wavenumber. This baseline transmission is caused by the  
 346 anomalous water vapor continuum absorption (Shine et al., 2012).

347

348 **4.1.2 Cloud screening**

349 Clear sky conditions are required for the derivation of SST from IR measurements so the  
350 identification and exclusion of cloud-contaminated pixels is critical for accurate retrievals.  
351 Historically, identification of clouds in IR measurements from satellites has been driven  
352 primarily by binary tests in a decision tree based on brightness temperature (BT) uniformity, BT  
353 minima, and comparisons with lower-resolution gap-free reference fields (Kilpatrick et al., 2001;  
354 Kilpatrick et al., 2015). The efficacy of these tests often decreases near ocean thermal fronts, at  
355 cloud edges, in the presence of small cirrus clouds, and low-level, uniform stratus clouds when  
356 cloud temperature can be close to that of the sea surface particularly at high latitudes. This  
357 reliance on stringent uniformity thresholds often has the unintended consequence of  
358 misidentifying strong SST frontal regions as clouds. Differences in detecting clouds between day  
359 when visible reflectance can be used and at night, when it cannot, lead to systematic erroneous  
360 irregularities in the cloud masks (Liu and Minnett, 2016; Liu et al., 2017).

361 An alternative, probabilistic approach to cloud identification in IR imagery based on Bayes'  
362 Theorem was developed by Merchant et al. (2005). Joint probability distributions of BTs in two  
363 IR channels were derived by radiative transfer simulations in clear sky conditions, and of cloudy  
364 conditions by visual inspection of satellite imagery. Radiative transfer simulations with weather  
365 prediction model output to give the atmospheric state are used to give an expectation of clear-sky  
366 BTs which are compared with probability distributions of cloudy measurements, the measured  
367 BTs are assigned a probability of having been influenced by clouds. This approach has been  
368 widely used for several satellite missions including for the (A)ATSR series (Merchant et al.,  
369 2012), the NOAA GOES (Geostationary Operational Environmental Satellite; Maturi et al.,

370 2008), and Himawari-8 satellite (Kurihara et al., 2016) of the Japan Meteorological Agency  
371 (JMA).

372 To address the specific cases where the decision-tree approach to cloud screening resulted in  
373 erroneous classification (Liu and Minnett, 2016; Liu et al., 2017), a new algorithm has been  
374 developed, called the Alternating Decision Tree (ADT) (Freund and Mason, 1999; Kilpatrick et  
375 al., 2019). Unlike in the decision tree approach where a pixel identified as being cloud-free has  
376 to pass every test, in the ADT the output of each test is considered in determining the likelihood  
377 of a pixel being identified as being clear or cloudy. The threshold values and the weighting given  
378 to each test were determined by a Machine Learning algorithm (Hall et al., 2009) applied to a  
379 subset of matchup data in four conditions: night-time, daytime, moderate sun-glitter and strong  
380 sun-glitter. When applied to MODIS and VIIRS (Visible and Infrared Imaging Radiometer Suite;  
381 see Section 5.1.6) data, the ADT algorithm improves on the decision tree approach for all metrics  
382 considered (Kilpatrick et al., 2019).

### 383 **4.1.3 Correction of clear-sky atmospheric effects**

384 The differential atmospheric transmission across the “atmospheric windows” at  $\lambda = 3.5 - 4.1 \mu\text{m}$   
385 and  $\lambda = 9.5 - 12.5 \mu\text{m}$  were recognized early on as a potential mechanism for providing a  
386 correction for the effect of the cloud-free atmosphere (McMillin, 1975). By placing two distinct  
387 spectral channels in a window, the BT measured in each would be different, being lower in the  
388 channel with lower atmospheric transmissivity, and the BT difference would be indicative of the  
389 attenuation of the IR signal intensity, caused primarily by water vapor in the  $\lambda = 9.5 - 12.5 \mu\text{m}$   
390 window but which is much less influential in the shorter wavelength window. Linearization of  
391 Planck’s Function and the radiative transfer equation leads to a simple expression in which the

392 BT difference is related to the drop in temperature from the  $SST_{skin}$  and one of the BTs  
393 (McMillin and Crosby, 1984; McMillin and Crosby, 1985; Barton, 1995):

$$394 \quad SST = aT_i + \gamma (T_i - T_j) + c \quad (2)$$

395 where  $T_i$  and  $T_j$  are the BTs measured in the two channels,  $c$  is an offset, and  $\gamma$  is the “differential  
396 absorption” coefficient of McMillin (1975). Equation 2 is called the Multi-Channel SST  
397 (MCSST) algorithm. The coefficients are dependent on the atmospheric state at the time of the  
398 measurement, particularly the profiles of temperature and water vapor, and can be determined by  
399 a simple regression analysis of collocated, coincident measurements (matchups) of BTs and in  
400 situ measurements, or by using radiative transfer simulations. The statistical approach requires a  
401 large number of matchups in conditions that sample the global atmospheric and SST variability  
402 (McClain et al., 1985). The temporal and spatial variability of the SST fields are inherent in the  
403 matchups. To limit undesirable consequences in determining both the coefficients in the MCSST  
404 and the accuracy of the retrieved SSTs, restricted time and spatial intervals are applied: typically  
405 10 km and less than an hour (Minnett, 1991). The radiative transfer approach to determine the  
406 coefficients requires an accurate radiative transfer model to predict the spectra of the emitted IR  
407 radiation at the satellite height (Závody et al., 1995) through a representative set of atmospheric  
408 profiles, generally derived from radiosonde profiles (Minnett, 1986; Minnett et al., 1987),  
409 modulated by the relative spectral response function of the channels of the IR radiometer in  
410 question to produce simulated BTs (Llewellyn-Jones et al., 1984).

411 Missing from the MCSST algorithm is provision for the effects of increasing path lengths. This  
412 was subsequently accommodated by adding a term of the form  $(\sec(\theta)-1)$ , where  $\theta$  is the satellite  
413 zenith angle measured at the surface, scaled by an additional coefficient. The characteristic of the  
414 errors in the derived SSTs indicated a regional dependence on the split window brightness

415 temperature differences suggestive that this difference is not sufficiently accurate in representing  
 416 the effects of water vapor. Given that there is a strong correlation between the atmospheric water  
 417 vapor content and SST, scaling the differential absorption coefficient with SST produced a very  
 418 robust algorithm called the Non-Linear SST algorithm (Walton et al., 1998; Walton, 2016),  
 419 which is based on the slightly non-linear combination of top-of-atmosphere brightness  
 420 temperatures measured in the 10-12  $\mu\text{m}$  wavelength interval where the atmosphere is relatively  
 421 transmissive:

$$422 \quad SST = a_0 + a_1 * T_{11} + a_2 * (T_{11} - T_{12}) * T_{\text{sfc}} + a_3 * (\sec(\theta) - 1.0) * (T_{11} - T_{12}) \quad (3)$$

423 where  $T_n$  are brightness temperatures measured in the channels at  $n \mu\text{m}$  wavelength,  $T_{\text{sfc}}$  is a ‘first  
 424 guess’ estimate of the SST in the area, and  $\theta$  is the satellite zenith angle.

425 While Equation 3 can be used both during day and night, more accurate night-time retrievals are  
 426 feasible using the measurements in the mid-IR transmission window. For sensors such as VIIRS,  
 427 the night-time algorithm takes the form:

$$428 \quad SST_{\text{triple}} = a_0 + a_1 * T_{11} + a_2 * (T_{3.7} - T_{12}) * T_{\text{sfc}} + a_3 * (\sec(\theta) - 1) \quad (4)$$

429 For MODISs, which have two narrow bands in the mid-IR transmission window, the most  
 430 accurate night-time algorithm has been found to be:

$$431 \quad SST4 = a_0 + a_1 * T_{3.95} + a_2 * (T_{3.95} - T_{4.05}) + a_3 * (\sec(\theta) - 1) \quad (5)$$

432 where the symbols have the same meaning as in Equation 2 but coefficients  $a_0 - a_3$  are of course  
 433 different (Kilpatrick et al., 2015).

434 More complex forms of the atmospheric correction algorithm have been developed using  
 435 additional channels, such as  $\lambda = 8.6 \mu\text{m}$  (Petrenko et al., 2014).

436 There are two approaches for deriving the coefficients: numerical simulations of the BT  
437 measurements (Llewellyn-Jones et al., 1984), and collocated and contemporaneous match-ups  
438 with in situ measurements (Kilpatrick et al., 2001; Kilpatrick et al., 2015). To attempt to  
439 accommodate the seasonal and regional variations in the atmospheric water vapor distributions,  
440 sets of coefficients that depend on month of the year and latitude bands can be used (Minnett,  
441 1990; Kilpatrick et al., 2001; Kilpatrick et al., 2015.). Since the information about the  
442 atmospheric water vapor is contained in the BT differences, for radiometers with large NE  $\Delta T$   
443 (Noise Equivalent Temperature Difference) or large digitization noise, the difference itself may  
444 be very noisy. Smoothing over a cluster of pixels, such as the clear-sky pixels in a 5x5 pixel  
445 array, improves the accuracy of the SST retrievals even at full resolution, making use of the fact  
446 that atmospheric properties generally change over longer distances than those of the SST  
447 (Barton, 1989; Coll et al., 1993). Indeed, in conditions of a very dry atmosphere, such as in the  
448 Arctic, the brightness temperature difference may be dominated by noise, and a single channel  
449 correction may be more effective (Vincent et al., 2008b).

450 The statistical approach to atmospheric correction generally works well when the conditions for  
451 a particular retrieval are close to the mean of those that are used to derive the coefficient set, but  
452 in conditions that deviate from these, such as at high latitudes, errors tend to be larger (Szczo drak  
453 et al., 2014). An approach that makes specific use of the atmospheric conditions was pioneered  
454 by Merchant et al. (2008b) using an Optimal Estimation (OE) approach in which the prior  
455 information about the expected state of a system is represented by a state vector  $\mathbf{x}_a = (SST_{skin},$   
456  $TWV)$  where  $TWV$  is total atmospheric column water vapor. The a priori values of  $SST_{skin}$  and  
457  $TWV$  can be taken from a number of sources, including weather forecast models, or reanalysis  
458 fields such as from ECMWF. Vector  $\mathbf{x}_a$  constitutes an input to a forward model  $F$  to simulate

459 “prior observations”  $\mathbf{y}_a = \mathbf{F}(\mathbf{x}_a)$ . The model  $\mathbf{F}$  is generally a radiative transfer model and the prior  
 460 observations are calculated radiances in the satellite radiometer channels. These simulated  
 461 radiances are then adjusted to match the measured channel radiance within uncertainties  
 462 determined by the radiometer characteristics, primarily the NE $\Delta$ T and other residual instrumental  
 463 artifacts if present. The adjustment is an inverse problem, as discussed by Rodgers (2000) and  
 464 followed by Merchant et al. (2008b) and Merchant et al. (2009c):

$$465 \quad \hat{\mathbf{z}} = \mathbf{z}(\mathbf{x}_a) + (\mathbf{K}^T \mathbf{S}_\varepsilon^{-1} \mathbf{K} + \mathbf{S}_a^{-1})^{-1} \mathbf{K}^T \mathbf{S}_\varepsilon^{-1} (\mathbf{y}_o - \mathbf{F}(\mathbf{x}_a)) \quad (6)$$

466 where  $\hat{\mathbf{z}}$  is a two-element vector containing the retrieved SST<sub>skin</sub> and TWV. The matrix of partial  
 467 derivatives (or the Jacobian),  $\mathbf{K}$ , for the state vector is defined by:

$$468 \quad \mathbf{K} = \left[ \frac{\partial \mathbf{F}(\mathbf{x}_a)}{\partial \mathbf{z}} \right] = \begin{bmatrix} \partial y_i / \partial x_1 & \partial y_i / \partial x_2 \\ \partial y_j / \partial x_1 & \partial y_j / \partial x_2 \end{bmatrix} \quad (7)$$

469  $\mathbf{S}_\varepsilon$  is the combined covariance matrix of the prior and satellite observations, and  $\mathbf{S}_a$  is the  
 470 covariance matrix of the two element prior reduced state vector. Merchant et al. (2008b) assumed  
 471 the covariance matrices to be diagonal. Application of the OE atmospheric correction to MODIS  
 472 data, using the Line-by-Line Radiative Transfer Model (LBLRTM) of Clough et al. (2005) and  
 473 atmospheric state vectors derived from the ERA-Interim reanalysis fields of the ECMWF (Dee et  
 474 al., 2011), resulted in SST retrieval accuracies that were better than those of the standard NLSST  
 475 correction, but not for all retrievals that were not identified as highest quality, meaning  
 476 confidently cloud-free, and for satellite zenith angles  $< 45^\circ$  (Szczo drak, 2017; pers. com).

477 A further development of the physical retrieval method to correct for the effects of the  
 478 intervening atmosphere has recently been developed by Koner et al. (2015). Called the Modified  
 479 Total Least Squares (MTLS) method, it builds on earlier work to derive trace gas concentrations  
 480 from satellite measurements (Koner and Drummond, 2008). The technique has been applied to



481 SST retrievals from the GOES-13 imager (Section 5.4.3) (Koner et al., 2015) and to MODIS on  
482 Aqua (Koner and Harris, 2016), and produces satellite-derived SSTs that compare better with  
483 drifting buoy measurements than those derived using other approaches.

## 484 **4.2 SST retrievals in the Microwave**

485 Planck's function (Equation 1) gives the spectral distribution of radiance emitted by a blackbody  
486 at a given temperature; it is highly non-linear in wavelength. But, at long wavelengths, where  $hc$   
487  $\ll \lambda kT$ , spectral radiance is a linear function of wavelength and using a Taylor expansion,  
488 Planck's function reduces to the Rayleigh-Jean Law:

$$489 \quad T = \lambda^4 B_\lambda(T) (2kc)^{-1} \quad (8)$$

490 As in the IR, the  $B_\lambda(T)$  measured by passive microwave radiometers is related to the  
491 thermodynamic temperature ( $T$ ) by the emissivity  $\epsilon(\lambda)$ :

$$492 \quad B_\lambda(T) = \epsilon(\lambda) T \quad (9)$$

493 As the radiation passes through the atmosphere it is absorbed, scattered, and re-emitted, so the  
494 satellite measurement is:

$$495 \quad B_\lambda(T) = \text{surface emission} + \text{atmospheric emission} + \text{atmospheric emission reflected at the sea}$$
$$496 \quad \text{surface} + \text{emission from the surface, atmosphere and space scattered by the atmosphere} + \text{surface}$$
$$497 \quad \text{reflected space emission}$$

498 A wind-speed dependent effective emissivity can also account for wave shadowing and surface  
499 emission being reflected from another facet of a roughened surface (Nalli et al., 2008a; Nalli et  
500 al., 2008b). The  $B_\lambda(T)$  signal measured in the range of microwave frequencies used for earth

501 observation depends on several varying parameters, including but not restricted to SST (Figure  
502 6).

503 Algorithms for deriving SST from passive microwave (PMW) measurements fall into two  
504 primary types, radiative transfer model (RTM) based algorithms and statistical algorithms. RTM  
505 simulations require instrument information (azimuth and earth incidence angles, frequency,  
506 polarization) and environmental data (SST, sea surface salinity, wind speed, wind direction,  
507 atmospheric profiles of temperature, pressure, water vapor density, and liquid cloud water  
508 density) to simulate the top of atmosphere (TOA) BTs.

509 Comparisons of the simulated and measured TOA BTs normally result in differences that can be  
510 attributed to errors in the RTM parameterizations or measurement errors (imperfect calibration,  
511 channel contamination, etc.), which require ‘ad-hoc’ corrections to the geophysical retrievals  
512 (Hilburn, 2009; Meissner and Wentz, 2012). The statistically based algorithms differ in that  
513 some of the calibration issues (up to ~1 K) or instrument issues may be accounted for by the  
514 nature of the statistical algorithm which is developed using satellite TOA BT measurements  
515 collocated with in situ and model observations (Shibata, 2006; Pearson et al., 2018; Nielsen-  
516 Englyst et al., 2018).

517 Both types of algorithms have their strengths and weaknesses. RTM-based algorithms clearly tie  
518 the physics of the observation to the geophysical retrieval allowing for identification of  
519 instrument calibration errors, and have a clear development path forward to improve future  
520 retrievals. Additionally, these algorithms can be used to develop realistic errors models, but such  
521 error estimates depend on the accuracy of the model and the data used to derive it. Statistically  
522 based algorithms are simpler to implement and can be more accurate as the coefficient derivation  
523 process can account for errors in calibration or other offsets in channel temperatures.

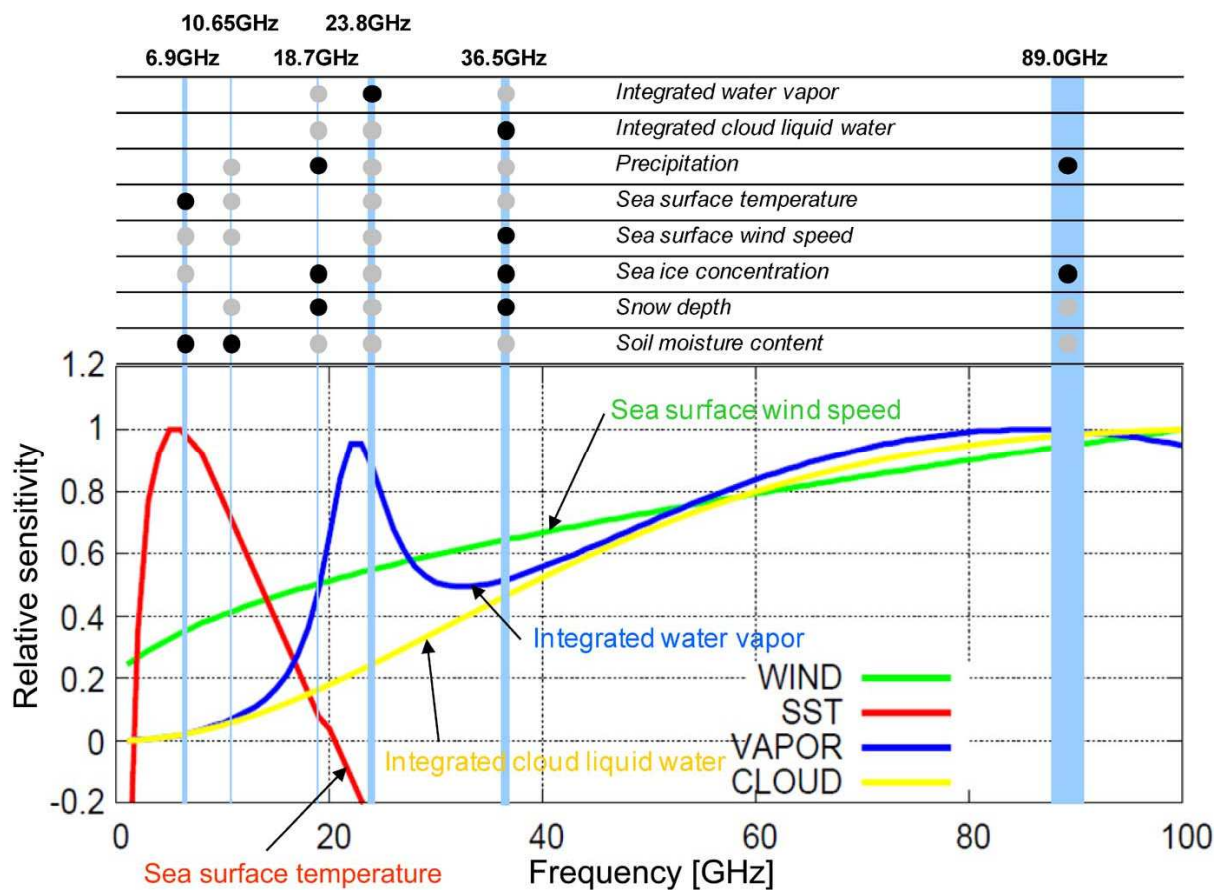


Figure 2. Schematic of relative sensitivity in BT (normalized by the maximum value) for some geophysical parameters for measurements at an incidence angle of  $55^\circ$  as a function of frequency. Typical primary and secondary frequency bands for retrieving each geophysical parameter are shown by black and gray circles. Note that atmospheric contribution was neglected for ocean surface parameters, and oxygen absorption was not included for atmospheric parameters. From Imaoka et al. (2010), with permission.

524 Regardless of the algorithm type used to determine SST, removing erroneous data from the

525 satellite retrievals ensures that estimated errors are accurate. Cases where the satellite PMW  
526 SST retrievals are contaminated by radio-frequency interference (RFI) from ground-based  
527 sources, geostationary satellites, and communication satellites, need to be identified and flagged  
528 as being untrustworthy (Gentemann and Hilburn, 2015). Cases where the SST retrievals are  
529 affected by rain, strong winds, sea ice, sunglint, and near land or sea ice as these retrievals have  
530 contributions from emission that enter through the antenna sidelobes, must also be identified and  
531 flagged. Precipitation, wind speed, and sea ice are geophysical variables derived from the same  
532 PMW measurements and these are used to flag erroneous SST values. The extent of sidelobe  
533 contamination is determined by calculating the distance to land or sea ice. Sunglint effects are  
534 present when the specular reflection angle is within  $20 - 25^\circ$  (depending on wind speed) of the  
535 solar angle at the surface. RFI can be difficult to identify, and the effects are usually identified  
536 using a mix of known ground-station locations and observation reflection vectors to known  
537 geostationary satellite emitters. Satellite to satellite RFI can be identified using a double  
538 difference method or estimated retrieval errors (Gentemann et al., 2010; Gentemann and Hilburn,  
539 2015).

540 PMW SSTs have been retrieved from the Tropical Rainfall Measuring Mission (TRMM)  
541 Microwave Imager (TMI; Section 5.5.2) from December 1997 to 2015, but the low-inclination  
542 orbit limited retrievals to  $< 40^\circ$  latitude. From June 2002 - 2011, Aqua's Advanced Microwave  
543 Scanning Radiometer - Earth Observing System (AMSR-E; Section 5.5.3) provided global PMW  
544 SST observations. From 2003, WindSat (Section 5.5.4) also measured PMW SST, and was  
545 joined by AMSR-2 (Section 5.5.7) in 2012, and Global Precipitation Mission (GPM) Microwave  
546 Imager (GMI; Section 0) in 2014. These last three radiometers are still in operation, but beyond  
547 their expected lifespan. The radiometers are described in more detail below.

### 548 **4.3 SST sensitivity**

549 The main focus of the development of SST retrieval algorithms has been to improve the absolute  
550 accuracy of the retrievals, but another important aspect is how well the derived SST fields  
551 represent local or larger scale spatial variability, or time series of retrieved SSTs represent time  
552 changes, such as diurnal warming and cooling. An ideal retrieval scheme would have zero  
553 sensitivity to water vapor variations, and a sensitivity to changes in the SST of unity. However,  
554 retrieval algorithms are imperfect and these targets are not achieved.

555 The sensitivities may be determined by radiative transfer modelling to simulate the satellite  
556 measurements through prescribed atmospheric conditions and surface temperatures, which can  
557 be adjusted in numerical experiments. As expected, the SST sensitivity to water vapor is  
558 dependent on the vapor distribution, being greater in the tropics and equatorial regions (Merchant  
559 et al., 2009b), and on the water vapor distribution in the vertical (Minnett, 1986). Using the  
560 AVHRR (Section 5.1.2) Pathfinder dataset (Kilpatrick et al., 2001), Merchant et al. (2009b)  
561 demonstrated that in nearly all cases the sensitivity of retrieved SST to actual SST variation is <  
562 1.0, with the global average being 0.93. The minimum sensitivity was found to occur where  
563 atmospheric water vapor column content is high, specifically in the equatorial Atlantic and  
564 Pacific Oceans, especially the Tropical Warm Pool where the sensitivity may be < 0.5.

565 Similarly, estimates of the amplitude of diurnal heating deduced from satellite-derived SST may  
566 be smaller than the real amplitude if the temporal sensitivity of the satellite data is < 1.0  
567 (Merchant et al., 2009b; Merchant et al., 2013). Zhang et al. (2018) compared diurnal heating  
568 signals in the Tropical Warm Pool region in geostationary satellite measurements from the  
569 Multifunctional Transport Satellite-1R (MTSAT-1R; Puschell et al., 2002) with in situ  
570 measurements from drifting buoys (Section 6) from the In situ SST Quality Monitor (iQuam)

571 data set (Xu and Ignatov, 2014; <https://www.star.nesdis.noaa.gov/sod/sst/iquam/>), which, with  
572 measurements at a depth of ~20 cm, were taken to be a good representation of the real diurnal  
573 heating amplitude (Gentemann et al., 2009). The resulting estimate of the satellite-derived SST  
574 sensitivity was found to be 0.60 ( $\pm 0.05$ ), meaning that remotely-sensed diurnal heating  
575 amplitudes in the Tropical Warm Pool are significantly underestimated.

## 576 **5 History of instrument development**

577 Throughout the history of science, major advances in knowledge and understanding of  
578 phenomena have followed new measurements often taken using new or improved instruments.  
579 The development of satellite oceanography, including the derivation of SST fields from  
580 spacecraft is no exception.

581 There are several common characteristics of satellite scanning radiometers used to derive  
582 quantitative measurements of SST: a mechanism to generate imagery - a rotating plane mirror in  
583 the IR or a rotating offset-paraboloid reflector in microwave radiometers; effective detectors; and  
584 a process for real-time, in-flight calibration of the measurements. Both rotating mirrors and  
585 reflectors direct the IR or microwave radiation into the radiometers. Calibration is based on  
586 measurements of two targets at known temperatures, one of which is often cold space on the  
587 anti-solar side of the spacecraft. A two-point, on-orbit calibration accounts for the linear  
588 response of the detectors, and the smaller, nonlinear response of some IR detectors is based on  
589 pre-launch characterization (Minnett and Smith, 2014), or by periodic “warm-up - cool-down”  
590 on-orbit temperature cycling of the internal black-body (Xiong et al., 2012; Minnett and Smith,  
591 2014).

592 Infrared detectors insert noise into their measurements, and the lower the temperature of the  
593 detector, the lower the noise level. Therefore, IR radiometers require cooled detectors, typically  
594 operating from 53 K (-220 °C) to 183 K (-90 °C) to reduce the NE $\Delta$ T to <0.1K (Xiong et al.,  
595 2012; Minnett and Smith, 2014).

596 Here we provide an overview of satellite instruments that have brought us to our current  
597 capabilities to measure SST from space. The list cannot be exhaustive, but we include those  
598 sensors that have resulted in major advances, or have introduced significant technological  
599 developments to the field. Included are relevant dates and instrument characteristics, including  
600 surface spatial resolution. The references included for each sensor provide the interested reader  
601 with guidance to more detailed descriptions. For further details on past, current and planned  
602 satellites and instruments, the reader is referred to the World Meteorological Organization  
603 (WMO) Observing Systems Capability Analysis and Review (OSCAR) Tool ([https://www.wmo-](https://www.wmo-sat.info/oscar/)  
604 [sat.info/oscar/](https://www.wmo-sat.info/oscar/)).

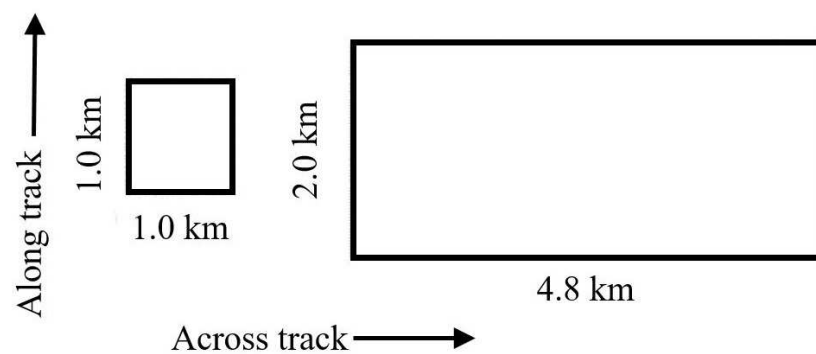
605 Where possible, we include assessments of accuracy to illustrate improvements resulting from  
606 instrumental and algorithmic developments. These estimates are specific to the retrieval  
607 algorithms as well as to the instrument calibration and performance, and also to the methods used  
608 in the assessments, including environmental variability consequent on different spatial and  
609 temporal sampling of the satellite SST fields and the reference measurements.

## 610 **5.1 Infrared instruments in low earth orbit**

611 The initial motivation for flying earth-viewing IR imaging radiometers on satellites was to  
612 provide pictures of clouds to assist weather forecasters. During the sunlit part of each orbit,  
613 detectors in the visible part of the electromagnetic spectrum provided the required information,

614 but at night IR radiometers were needed. Even though the sensitivities of the early IR detectors  
615 were poor compared to those in modern instruments, they were sufficient to reveal patterns in the  
616 cloud free parts of the images that were correctly interpreted as being indicative of spatial  
617 variability in the SST.

618 The spatial resolution at the sea surface of IR imaging radiometers is generally given at the  
619 subsatellite point, but because of beam spreading caused by longer path lengths the pixel size  
620 grows for measurements taken away from nadir and because of the curvature of the earth's  
621 surface the increase in size is not symmetric with growth in the across-track (scan) direction  
622 becoming greater than in the along-track direction (Figure 7).



623  
624 *Figure 7. A schematic of a MODIS 1km pixel growth from nadir to the edge of swath. The total swath*  
625 *width is 2330 km and comprises 1354 pixels. At the swath edges, the satellite zenith angle is ~65°.*

### 626 **5.1.1 Early Radiometers**

627 Starting in 1964, only seven years after the launch of the first artificial satellite, Sputnik, NASA  
628 began to launch research and development satellites called Nimbus. The Nimbus satellites were  
629 sun-synchronous and stabilized so that instruments on board could be directed to the Earth



630 throughout the orbits. The instruments were mostly prototypes, but once demonstrated to be  
631 successful successive versions were flown, often with incremental improvements.

632 Included in the instrument suite of Nimbus-1 was the High Resolution Infrared Radiometer  
633 (HRIR) which had a single IR channel, responsive to the 3.4 – 4.2  $\mu\text{m}$  wavelength range, and  
634 having a spatial resolution of 8.6 km at the sub-satellite point with a swath extending from  
635 horizon to horizon. Because of solar contamination, these data were restricted to use only at  
636 night. The clear-sky parts of the images were used to describe variations in SST (Allison and  
637 Kennedy, 1967). The Nimbus-1 mission lasted only about one month, but Nimbus-2, launched in  
638 May 1966, functioned for about six months. The data were transmitted in analogue form and  
639 were generally displayed as photo-facsimiles in gray tones, or printed by a line-printer and  
640 contoured by hand. These were interpreted in terms of a relative SST, and sharp gradients were  
641 identified as boundaries between currents or delineating fronts and used to describe their  
642 responses to changes in atmospheric forcing, such as winds in the Arabian Sea (LaViolette and  
643 Chabot, 1968) and Persian Gulf (Szekielda et al., 1972), or boundary currents and coastal  
644 upwelling (Warnecke et al., 1971). A third HRIR, which included a visible channel, was on  
645 Nimbus-3 launched in 1969.

646 A two channel radiometer, the Scanning Radiometer (SR) developed from the HRIR but with an  
647 IR channel in the 10.5 – 12.5  $\mu\text{m}$  atmospheric window, first flew on the NOAA TIROS-M  
648 (Television Infrared Observation Satellite-M) launched in January 1970 into a sun-synchronous  
649 orbit at an altitude of 1470 km. The spatial resolution was 3.6 km at the subsatellite point. The  
650 longer IR wavelength is essentially unaffected by scattered and reflected solar radiation, so the  
651 SR IR channels were also used during the day. TIROS-M was followed by five operational  
652 satellites, NOAA-1 to -5 launched from December 1970 to July 1976, each carrying an SR.

653 A further development of the SR, the Very High Resolution Radiometer (VHRR) flew on  
654 NOAA-2, launched in October, 1972, having channels very similar to the SR but with a spatial  
655 resolution at the subsatellite point of 0.9 km and a much reduced NE $\Delta$ T of ~0.5 K the VHRR  
656 permitted greatly improved depiction of the SST in cloud-free areas. On-board data recording  
657 also allowed data to be retained out of sight of ground stations and then subsequently transmitted  
658 to a receiving station as they come into range. These technological improvements supported

659 many investigations into ocean thermal fronts and associated features (Legeckis, 1978, and  
660 references therein).



661  
662 *Figure 8. VHRR IR image 4531 from NOAA 4 was obtained on November 12, 1975. The Gulf Stream*  
663 *north of Cape Hatteras and south of Cape Cod appears as the warmest (darkest) water. The large*  
664 *amplitude meanders as well as two warm core eddies are evident south of Cape Cod and Long Island.*  
665 *(Legeckis, 1978).*

666 Figure 8 shows the thermal structure of the Gulf Stream off Cape Cod, USA, taken from the  
667 HRIR on NOAA- 4 in November 1975 (Legeckis, 1978). The complexity of the fronts associated  
668 with the Gulf Stream is apparent, and explains the fact that ship-based surveys of the area defied  
669 simple interpretation (Fuglister, 1955), simply as a consequence of inadequate sampling of  
670 mesoscale current structure, and satellite imagery resolved which of multiple possible  
671 interpretations of ship-based measurements was correct.

### 672 **5.1.2 The Advanced Very High Resolution Radiometer (AVHRR)**

673 The satellite instrument that has contributed the longest to the study of SST is the AVHRR that  
674 first flew on TIROS-N launched in late 1978 (Cracknell, 1997). AVHRRs have flown on  
675 successive satellites from NOAA-6 to NOAA-19. AVHRRs are on satellites in near-polar, sun-  
676 synchronous orbits with an orbital period of about 100 min. There have been two NOAA  
677 AVHRRs operational at any given time, with at-launch local equator-crossing times of about  
678 2.30 a.m. and p.m. and about 7.30 a.m. and p.m. The overpass times drift with the time on orbit  
679 (e.g. Figure 1 of Bhatt et al., 2016). EUMETSAT, the European Organisation for the  
680 Exploitation of Meteorological Satellites, also flies AVHRRs on its three Metop satellites (Klaes  
681 et al., 2007) with a maintained descending equator crossing time at 9:30 a.m.

682 The AVHRRs on TIROS-N and NOAA-6 had only four channels and had limited capability for  
683 the derivation of SST because they lacked the “split-window” channels, numbered 4 and 5 ( $\lambda =$   
684 10.8 and 12.0  $\mu\text{m}$ ) which were on subsequent five-channel AVHRRs starting with NOAA-7,  
685 launched in June 1981. As with earlier IR imaging radiometers (Barton, 1985), SST retrieval  
686 from the AVHRRs without multiple IR bands was accomplished using a simple linear  
687 relationship to the measured BT, but the variability of the marine atmosphere introduced much  
688 scatter into this relationship. It was recognized early that a promising way forward was to make

689 simultaneous measurements in two IR channels in which the atmospheric transmission was  
690 different (Anding and Kauth, 1970; McMillin, 1975; McMillin and Crosby, 1984; McMillin and  
691 Crosby, 1985; inter alia), leading to atmospheric correction algorithms given in Section 4.1.3.  
692 However, in very constrained conditions, a tailored single channel atmospheric correction may  
693 produce more accurate SST retrievals than a multichannel retrieval, an example being the very  
694 dry, cold Arctic atmosphere over the North Water Polynya (Vincent et al., 2008b; Vincent et al.,  
695 2008a).

696 The current version, AVHRR/3, has six channels: 1 and 2 at  $\lambda = \sim 0.65$  and  $\sim 0.85$   $\mu\text{m}$ , measuring  
697 reflected sunlight are used to image clouds during the daytime part of each orbit. Channels 4 and  
698 5, also on all AVHRRs, are in the atmospheric window close to the peak of the SST thermal  
699 emission and are used to derive SSTs. Channel 3 is in the mid-IR atmospheric window ( $\lambda = 3.7$   
700  $\mu\text{m}$ ), also measures surface emission, modified by its propagation through the atmosphere, and  
701 hence is used to derive SST, but at this wavelength there is a significant component of reflected  
702 and scattered sunlight rendering these measurements suitable for SST determination only at  
703 night. The  $\lambda = 3.7$   $\mu\text{m}$  channel data of the early AVHRRs had noise that introduced a “herring-  
704 bone” effect in brightness temperature images at a level that made the quantitative use of the data  
705 very difficult (Dudhia, 1989; Warren, 1989), but research into reducing the excessive noise has  
706 shown success (Simpson and Yhann, 1994; Karlsson et al., 2017). The sixth channel of the  
707 AVHRR/3, first launched on NOAA-15 in May 1998, at  $\lambda \sim 1.6$   $\mu\text{m}$  was designated 3a with the  
708 earlier  $\lambda = 3.7$   $\mu\text{m}$  channel being renamed 3b, provides superior discrimination of cloud over  
709 snow, ice and bright desert during the day. Given limited telemetry bandwidth, measurements  
710 from only one of these two channels are transmitted to ground, with 3a data being taken during  
711 the daytime part of the orbit, and 3b at night. Infrared channels of the AVHRRs are calibrated

712 using measurements of an onboard blackbody plate, the temperature of which is monitored by  
713 five thermometers, and a measurement of space away from the sun providing a source of  
714 radiance very close to zero. The AVHRR/3s also incorporated several improvements, including  
715 better thermal stability of the blackbody used in the calibration of the IR channels (Trishchenko  
716 et al., 2002). The improved blackbody shielding reduced the temperature gradients that were  
717 found across the blackbody (Brown et al., 1985), which, since they exhibited orbital variations,  
718 were suggestive of stray light from the sun being incident on the blackbody. Although the  
719 AVHRR/3s on NOAA-15, -18 and -19 are still operation, these satellites are not in maintained  
720 orbits so the equator crossing time drifts (see  
721 [https://www.star.nesdis.noaa.gov/smcd/emb/vci/VH/vh\\_avhrr\\_ect.php](https://www.star.nesdis.noaa.gov/smcd/emb/vci/VH/vh_avhrr_ect.php)) with the result that the  
722 on-board thermal environment may move out of that in which the sensors were designed to  
723 operate, with a consequent degradation in accuracy of their measurements (see  
724 <https://www.star.nesdis.noaa.gov/sod/sst/3s/>).

725 The images in each channel are constructed by scanning the AVHRR field of view across the  
726 Earth's surface by a rotating plane mirror with its surface inclined at 45° to its axis which lies in  
727 the direction of flight. The rate of rotation, 6 Hz, is such that successive scan lines are contiguous  
728 at the surface directly below the satellite. The width of the swath (~2700 km) results in overlap  
729 of the edges of successive orbits so the whole Earth is sampled without gaps each day. The  
730 spatial resolution at nadir is 1.1 km and 6.15 x 2.27 km<sup>2</sup> (across-track x along track) at the edge  
731 of swath.

732 An important and exhaustive reprocessing of the AVHRR SST data stream from the AVHRR on  
733 NOAA-7, in 1981, to the present including those on the Metop satellites, has been recently  
734 completed by Merchant et al. (2019). Their objective was to produce a consistent data set for the

735 entire period that would be suitable for climate applications. For periods with overlap with the  
736 ATSR (Section 5.1.3) series of dual view radiometers, the infrared measurements from the most  
737 reliable channels of these were used as references to which the AVHRR data could be  
738 harmonized using radiative transfer modelling with atmospheric profiles given by the ERA-  
739 Interim data set (Dee et al., 2011). For AVHRR data prior to the first ATSR on ERS-1, in 1991,  
740 periods of overlap between successive AVHRRs on NOAA polar-orbiting satellites were used,  
741 but were thus far found insufficient to achieve adequate harmonization; additional reconciliation  
742 of the AVHRR SSTs to in situ sources was therefore applied prior to 1991. Thus, the resulting  
743 SST fields have a high degree of independence from in situ measurements, such as those from  
744 drifting buoys, from 1991 onwards. In addition to recalibrating the AVHRR data using improved  
745 understanding of the shortcomings of the AVHRR calibration procedures (Mittaz et al., 2019;  
746 Giering et al., 2019), the harmonization approach takes into account differences in the spectral  
747 response functions of each of the sensors, including those in the ATSR series, to produce  
748 empirical relationships to correct the residual errors in the individual AVHRR radiance  
749 measurements. A consistent Bayesian cloud screening algorithm has been applied to the data  
750 from all sensors (Bulgin et al., 2018). Apart from a few regions and periods, associated with  
751 episodes of sensor instability, stratospheric aerosols or desert dust, especially prior to ATSR data  
752 being available, the derived SSTs are accurate, having a median evaluated uncertainty of 0.18 K,  
753 at the pixel level. Long term stability, relative to drifting buoy measurements, is within 0.003 K  
754 yr<sup>-1</sup> of zero, thus meeting the stability requirement of an SST CDR (Ohring et al., 2005).

755

756

757

758 **5.1.3 The Along-Track Scanning Radiometer (ATSR) Series**

759 Instead of relying on the spectral dependence of atmospheric transmission to correct for the  
760 effects of the cloud- and aerosol-free atmosphere, measuring BTs at wavelengths in the  
761 atmospheric windows of the sea surface through two different atmospheric path lengths permits a  
762 direct measurement of the effect of the atmosphere on the top-of-atmosphere radiance. The pairs  
763 of such measurements must be made in quick succession, so that the SST and atmospheric  
764 conditions do not change in the time interval, and this is the basis of the Along-Track Scanning  
765 Radiometer (ATSR) series of IR radiometers. Following two ATSRs on ERS-1 and ERS-2, the  
766 Advanced ATSR (AATSR) was flown on Envisat (Louet and Bruzzi, 1999; Dubock et al., 2001),  
767 launched on 1 March 2002 for a decade-long mission. The AATSR had the same IR channels as  
768 the earlier ATSRs, but had additional channels in the visible part of the spectrum.

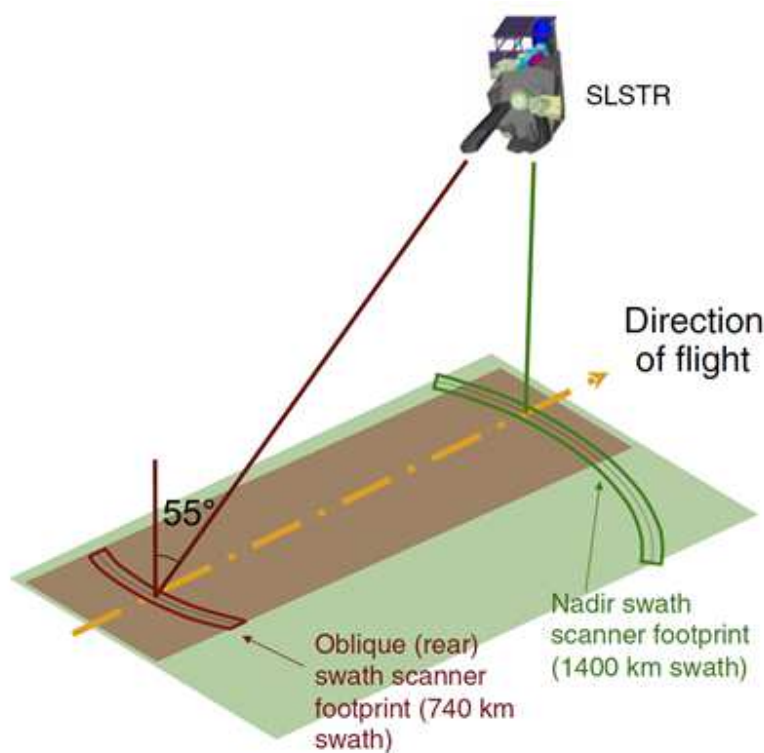
769 The ATSRs had IR channels in the atmospheric windows comparable to those of AVHRR. The  
770 axis of rotation of the scan mirror is inclined from the vertical by the half-angle of a cone,  
771  $\sim 23.5^\circ$ , so the swath passes through the subsatellite point sweeping out a curved path on the sea  
772 surface. Half a mirror revolution later, the field of view was about 900 km ahead of the sub-  
773 satellite track in the center of the 'forward view' (Prata et al., 1990). The field of view returns to  
774 the sub-satellite point, which has moved 1 km ahead of the starting point. Thus the pixels  
775 forming the successive swaths through the nadir point are contiguous. The nadir point overlays  
776 the center of the forward view after about 2 min. The scan geometry from the height of polar-  
777 orbiting satellites carrying the ATSRs,  $\sim 785$  km, results in a swath width of  $\sim 500$  km. The nadir  
778 measurement is through a single thickness of the atmosphere, and the slant path to the center of  
779 the forward view is almost double that, resulting in colder measured BTs for the same SST. The



780 differences in the BTs between the forward and nadir swaths are direct measurements of the  
 781 effect of the atmosphere. The atmospheric correction algorithm takes the form:

$$SST = c_0 + \sum_i c_{n,i} T_{n,i} + \sum_i c_{f,i} T_{f,i} \quad (10)$$

783 where the subscripts  $n$  and  $f$  refer to measurements from the nadir and forward views,  $i$  indicates  
 784 two or three atmospheric window channels and the set of  $c$  are coefficients (Závody et al., 1995).  
 785 As with the atmospheric correction algorithm for other IR radiometers, an Optimal Estimation  
 786 approach has been developed for the dual-view radiometers (Embury and Merchant, 2012;  
 787 Embury et al., 2012) which has become the basis of a 20-yr time series intended to be of climate



788 quality (Merchant et al., 2012; Berry et al., 2018).

789 *Figure 9. Scan geometry of the SLSTR. The dual-view measurements are made by an inclined conical*  
 790 *scan, which covers the same swath through two different atmospheric path lengths. The oblique swath is*

791 *limited to 740 km by geometrical constraints. Interleaved between successive conical scans, a wider,*  
792 *single view swath is obtained. (Reprinted with permission from Donlon et al., 2012a).*

793 The current generation of dual view radiometers, the Sea and Land Surface Temperature  
794 Radiometer (SLSTR; Donlon et al., 2012a; Smith et al., 2014) flying on Sentinel 3a launched on  
795 16 February 2016 and Sentinel 3b launched on April 25, 2018, includes a quasi-linear scan  
796 through nadir to extend the spatial coverage (Figure 9). In the extended scan, the atmospheric  
797 correction algorithm is based on a multi-channel formulation.

798 The coefficients of the atmospheric correction algorithms are derived by radiative transfer  
799 simulations, and have an explicit latitudinal dependence (Závody et al., 1995). Accurate  
800 calibration of the measured radiances is achieved using two onboard blackbody cavities, situated  
801 between the apertures for the nadir and oblique views being scanned during each rotation of the  
802 mirror (Prata et al., 1990). One blackbody is at the ambient temperature of the instrument,  
803 ~262.7 K, while the other is heated to ~301.6 K (Smith et al., 2012; Minnett and Smith, 2014)  
804 resulting in the measured brightness temperatures of the sea surface being straddled by the  
805 calibration temperatures.

#### 806 **5.1.4 The Moderate Resolution Imaging Spectroradiometer (MODIS)**

807 The Moderate Resolution Imaging Spectroradiometer (MODIS) is a 36-band imaging radiometer  
808 on the NASA Earth Observing System (EOS) satellites Terra, launched in December 1999, and  
809 Aqua, launched in May 2002. Included in the innovations in the design of MODIS are (i)  
810 multiple detectors - ten - for each spectral band so that ten lines of pixels are measured  
811 simultaneously across the swath, (ii) a dual-sided scan mirror, and (iii) several advances to  
812 ensure the calibration, both radiometric and spectral, of the measurements. For calibration of the  
813 IR measurements, a grooved plate blackbody target with twelve embedded thermometers was

814 developed, and the measurements of this along with those of cold space provided a two-point  
815 radiance calibration. The swath width of MODIS, at 2330 km, is narrower than that of AVHRR,  
816 with the result that a single day's coverage is not entire, but the gaps from one day are filled in  
817 on the next. The spatial resolution of the IR bands is 1 km at nadir. Further details of the ocean  
818 remote sensing of MODIS are given by Esaias et al. (1998). MODIS is much more complex than  
819 other radiometers used for deriving SST, but uses the same atmospheric transmission windows.  
820 The two bands in the 10–12  $\mu\text{m}$  wavelength interval have bandwidths of  $\sim 0.5 \mu\text{m}$ , which are  
821 about half of those of the AVHRR and ATSR series. MODIS also has three narrow bands in the  
822 3.7–4.1  $\mu\text{m}$  window, which, although limited by solar effects during the day, produce more  
823 accurate retrievals of SST during the night. Several of the other MODIS bands contribute to  
824 improving the SSTs by better identification of residual cloud and aerosol contamination  
825 (Kilpatrick et al., 2015; Kilpatrick et al., 2019).

### 826 **5.1.5 Visible Infrared Imaging Radiometer Suite (VIIRS)**

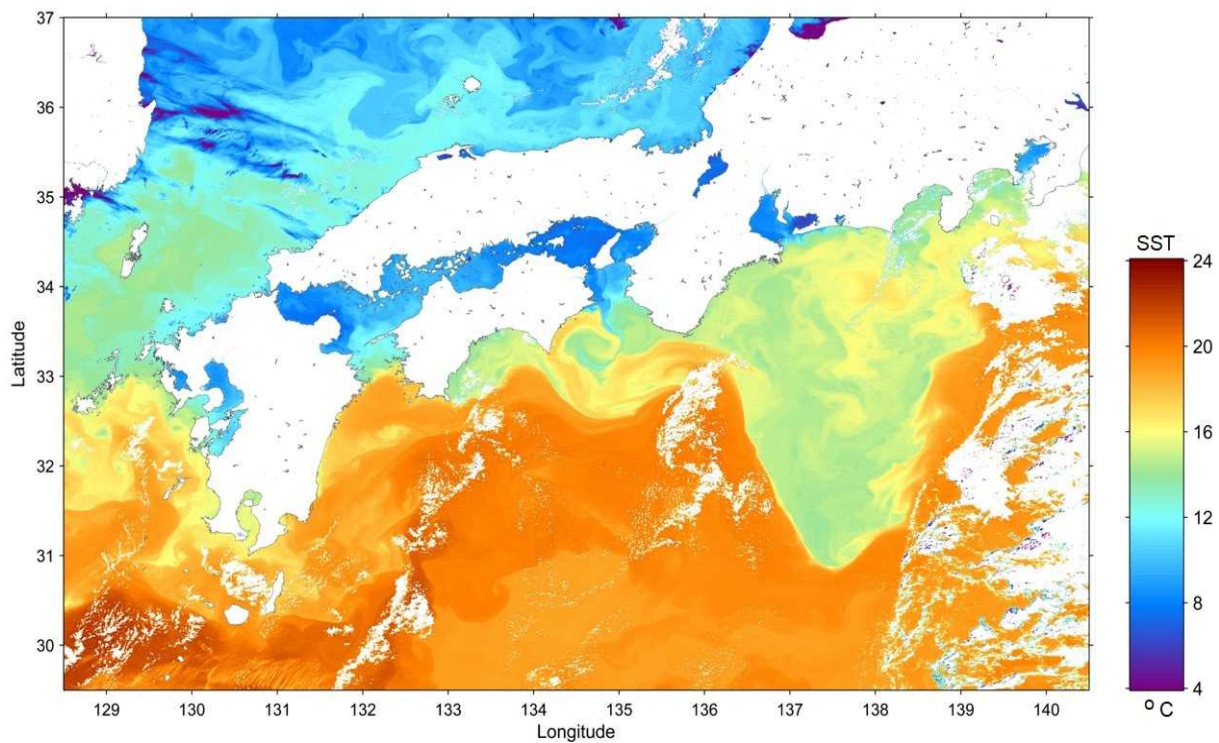
827 The replacement of the AVHRRs on the NOAA polar-orbiting satellites is the Visible Infrared  
828 Imaging Radiometer Suite (VIIRS), which built on experience gained from MODIS, including  
829 sixteen detectors for each band and the grooved blackbody for calibration. The paddle-wheel  
830 scan mirror of MODIS was not used, but instead the rotating telescope fore-optics as on  
831 SeaWiFS (Sea-Viewing Wide Field-of-View Sensor) was adopted, with a “half-angle mirror” to  
832 prevent image rotation across the swath that would otherwise occur as a result of using multiple  
833 detectors. The first VIIRS was launched on the Suomi-National Polar-orbiting Partnership  
834 satellite (S-NPP) on October 28, 2011, and the second was launched on November 18, 2017, on  
835 NOAA-20. VIIRS has 22 channels in the visible and IR parts of the electromagnetic spectrum;  
836 the channels are a subset of those of MODIS. The spatial resolution at the sea-surface is 0.75 km

837 at nadir, and VIIRS has an innovative approach of aggregating rectangular pixels, each having an  
838 aspect ratio of 3:1 in the along-track direction, to reduce the growth of pixel size across the swath  
839 away from nadir (Schueler et al., 2013; Gladkova et al., 2016). The IR bands used for SST  
840 measurements are the standard two in the  $\lambda = 10\text{--}12\ \mu\text{m}$  interval, and two in the  $\lambda = 3.7\text{--}4.1\ \mu\text{m}$   
841 atmospheric transmission window for use at night. VIIRS has a higher resolution IR band, 375  
842 m at nadir, that has a spectral response from  $\lambda = 10.6\text{--}12.4\ \mu\text{m}$ , essential using the entire  
843 atmospheric transmission window. While the spectral width of this band and the absence of  
844 another high-resolution band in this window prevents the use of an atmospheric correction  
845 algorithm to produce SSTs at the high resolution, an approach has been developed applying the  
846 atmospheric correction derived using the 750 m bands. This approach permits the use of VIIRS  
847 SSTs to investigate submesoscale processes at the ocean surface (Cornillon et al., 2014). NOAA-  
848 20 is the first of four planned satellites each carrying a VIIRS, providing SSTs into the late  
849 2030's.

#### 850 **5.1.6 Second-generation Global Imager (SGLI)**

851 The Japanese Global Change Observation Mission (GCOM) currently comprises two satellites:  
852 GCOM-W (Water) launched in 2012 into the A-Train, a series of satellites carrying  
853 complementary instruments in the same orbit facilitating the analysis of measurements from  
854 diverse instruments (L'Ecuyer and Jiang, 2010), and GCOM-C (Climate) launched in December,  
855 2017. GCOM-C is in a sun-synchronous polar orbit with an ascending node time of 22:30. Both  
856 GCOM satellites have instruments with SST capability as GCOM-W carries the Advanced  
857 Microwave Scanning Radiometer-2 (AMSR2) described below (Section 5.5.7) and GCOM-C  
858 carries the Second-generation Global Imager (SGLI), which is an imaging radiometer in the  
859 visible and IR. SGLI comprises two sensors: the Visible and Near Infrared Radiometer (VNR)

860 and the Infrared Scanning Radiometer (IRS). The IRS includes two split-window channels at  $\lambda =$   
861  $10.78 \mu\text{m}$  and  $11.97 \mu\text{m}$  with a resolution of 250 m at nadir and a swath width of 1400 km. The  
862 high resolution SSTs are expected to be of particular value in studying coastal processes. The  
863 SST fields derived from the split window bands are clean (Figure 10) and initial comparisons  
864 with in situ temperatures from iQuam (Xu and Ignatov, 2014) during October 2018 indicate a  
865 mean difference for highest quality SGLI SSTs of  $-0.063 \text{ K}$  during the day and  $-0.181 \text{ K}$  during



866 the night, with standard deviations of  $0.333 \text{ K}$  and  $0.619 \text{ K}$  and robust standard deviations of  
867  $0.284 \text{ K}$  and  $0.287 \text{ K}$ . (Y. Kurihara, 2018, pers. comm.). The relatively high nighttime standard  
868 deviations are attributed to imperfections in the cloud screening algorithms (ibid.).

869 *Figure 10. SST in the vicinity of Japan derived from SGLI on 27 February 2018, showing complex*  
870 *structure both inshore and offshore, and the sharp temperature contrast with the waters of the Kuroshio*  
871 *to the south. From Tanaka et al., 2018, with permission.*

872 **5.1.7 Multichannel Visible Infrared Scanning Radiometer (MVISR)**

873 The Chinese Meteorological Administration (CMA) has developed a series of meteorological  
874 satellites called FengYun, meaning “wind and cloud” and commonly abbreviated to FY, that  
875 comprise both sun-synchronous polar-orbiters and geostationary satellites. FY1-A was launched  
876 in 1988 into polar orbit but was very short lived. FY-1B was launched in September 1990 and  
877 functioned for about one year, followed by FY1-C in 1999 which completed a five-year mission,  
878 with overlap with FY-1D, launched in 2002, that functioned for nearly a decade. The FY-1C and  
879 -D series carried the Multichannel Visible Infrared Scanning Radiometer (MVISR), which had  
880 10 channels, most of which were in the visible and near-IR but included three in IR atmospheric  
881 windows:  $\lambda = 3.75 \mu\text{m}$ ,  $10.8 \mu\text{m}$  and  $12.0 \mu\text{m}$ . These had the potential to be used in SST  
882 retrievals, but the relatively high NE  $\Delta T$ s (0.4 K at 300 K at  $\lambda = 3.75 \mu\text{m}$ ; 0.22 K at 300 K at  $\lambda =$   
883  $10.8$  and  $12.0 \mu\text{m}$ ), as well as the difficulty of accessing the data by non-Chinese researchers  
884 limited the MVISR applications. The spatial resolution was 1.1 km at the subsatellite point.

885 **5.1.8 FY-3 Visible and Infra-Red Radiometer (VIRR)**

886 The current series of FY polar-orbiters, FY-3, carry the Visible and Infra-Red Radiometer  
887 (VIRR) with IR bands similar to those of the MVISR. FY-3A was launched in 2008 and  
888 functioned until 2015; FY-3B, -3C and -3D are operating at the time of writing. Comparisons  
889 with the global iQuam buoy temperatures from May to July, 2014, yielded mean differences of  
890  $-0.26$  K during the day and  $0.06$  K at night, with standard deviations of  $0.54$  K and  $0.56$  K (Wang  
891 et al., 2014). The VIRR was replaced on FY-3D by a much more capable instrument, the  
892 Medium Resolution Spectral Imager-2 (MERSI-2) with 25 channels, including one at  $\lambda = 3.80$   
893  $\mu\text{m}$  with surface resolution of 1 km at nadir, and two at  $\lambda = 10.8 \mu\text{m}$  and  $\lambda = 12.0 \mu\text{m}$  with spatial

894 resolution of 250 m at the subsatellite point. A further four FY-3 satellites are planned to extend  
895 the series beyond 2027.

896

### 897 **5.1.9 HY-1 China Ocean Colour & Temperature Scanner (COCTS)**

898 The Chinese State Ocean Administration has sponsored the development of the polar-orbiting  
899 ocean satellites called Hai Yang, meaning “Ocean” and referred to as the HY series. HY-1A and  
900 -1B were small satellites, launched in 2002 and 2007, and carried two imagers: the Coastal Zone  
901 Imager with four visible channels and the China Ocean Colour & Temperature Scanner  
902 (COCTS), a ten-channel imager with eight in the visible and near IR, and two in the thermal IR,  
903  $\lambda = 10.85 \mu\text{m}$  and  $11.95 \mu\text{m}$ , with a spatial resolution at nadir of 1.1 km. Comparisons with  
904 temperatures measured by buoys in the North-East Asian Regional Global Ocean Observing  
905 System revealed mean differences of 1.22 K and a standard deviation of 1.78 K with the HY-1B  
906 COCTS SST retrievals using a standard NLSST algorithm (Lei and Cong, 2013). When new  
907 coefficients for the NLSST were calculated using the matchups between COCTS BTs, and buoy  
908 data, the mean difference was removed and the standard deviation reduced to 1.35 K. The HY-  
909 1C was launched in September 2018, and a further three satellites are planned to provide data  
910 beyond 2029.

### 911 **5.2 Hyperspectral IR imagers**

912 For most of the period of satellite retrievals of SST, IR radiometers have provided measurements  
913 in discrete spectral bands defined by filters. For SST determination, the channels were selected in  
914 spectral intervals where the atmosphere is relatively transparent. But, hyperspectral IR  
915 radiometers that measure the full or significant parts of the spectrum of IR emission at orbital

916 height have also been flown. In spectral regions where the atmospheric transmission is low, the  
917 measurements are primarily of atmospheric emission, and can be used to derive atmospheric  
918 soundings, cloud properties, and trace gas concentrations. In the high-transmission atmospheric  
919 window spectral regions, surface temperatures can be derived. There are two types of imaging  
920 hyperspectral IR radiometers: those using diffraction gratings, and those based on Fourier-  
921 Transform interferometry. Both split the incoming spectrum of IR radiation into numerous  
922 spectral intervals, each very much narrower than those derived by filters in more conventional  
923 multispectral radiometers, so to retain a usable signal-to-noise ratio the field-of-view of the  
924 radiometer is increased to typically ~12 km, with an increase in the signal integration time. The  
925 decrease in the spatial resolution is a hindrance to deriving accurate SSTs given the need to  
926 identify confidently clear sky pixels.

### 927 **5.2.1 Atmospheric Infrared Sounder (AIRS)**

928 The Atmospheric Infrared Sounder (AIRS; Aumann et al., 2003) on the NASA satellite Aqua,  
929 launched in May, 2002, is a grating spectrometer that samples three intervals of the IR spectrum:  
930  $\lambda = 3.75$  to  $4.59 \mu\text{m}$ ,  $\lambda = 6.20$  to  $8.22 \mu\text{m}$ , and  $\lambda = 8.80$  to  $15.37 \mu\text{m}$ , with a total of 2378  
931 channels. The width of the AIRS scan is 1650 km. In principle, the high spectral resolution of  
932 AIRS should make it a good sensor for  $\text{SST}_{\text{skin}}$  derivation as some of the spectral regions with  
933 the highest atmospheric transmission are included in the measurements, such as wavenumber  
934  $2616 \text{ cm}^{-1}$  ( $\lambda = 3.823 \mu\text{m}$ ), but this does not seem to have been exploited by the community. One  
935 reason might be the relatively poor spatial resolution ( $13 \times 13 \text{ km}^2$  at nadir) which limits the  
936 opportunities to finding clear-sky pixels.

### 937 **5.2.2 Infrared Atmospheric Sounding Interferometer (IASI)**



938 An important instrument on the three Metop polar-orbiting satellites of EUMETSAT (Klaes and  
939 Holmlund, 2014) is the Infrared Atmospheric Sounding Interferometer (IASI). Metop-A was  
940 launched in 2006, -B in 2012 and -C in 2018. The IASI (Blumstein et al., 2004; Simeoni et al.,  
941 2004) is a Fourier-Transform IR Interferometer (Michelson and Morely, 1887; Griffiths and de  
942 Haseth, 1986) having a spectral range of  $\lambda = 3.62$  to  $15.5 \mu\text{m}$  with 8461 spectral samples. The  
943 IASI calibration, which uses an internal blackbody target and a measurement of cold space, has  
944 been determined to be well-specified (Hewison and König, 2008) and stable (Aumann and  
945 Pagano, 2008), and consequently the IASIs have been selected as reference instruments by the  
946 Global Space-Based Inter-Calibration System (GSICS; Hewison et al., 2013). A comparison of  
947 best quality Metop-A IASI SST<sub>skin</sub> retrievals with subsurface temperatures from drifting buoys  
948 resulted in a mean difference of  $-0.16$  K with a standard deviation of  $0.33$  K (O'Carroll et al.,  
949 2012), and a three-way analysis of IASI and AVHRR (also on Metop-A) and drifters resulted in  
950 a standard deviation attributable to IASI of  $0.28$  K (ibid).

### 951 **5.3 High resolution imagers**

952 The majority of IR imaging radiometers on polar orbiting satellites have surface resolution of  
953 typically  $1 \text{ km}^2$  and broad swaths that provide global, or near global, coverage in a day. For some  
954 purposes, usually associated with land surface applications a much higher spatial resolution is  
955 required, and radiometers developed for these applications may also be used to derive SST  
956 provided there is a mechanism to correct for atmospheric effects and the IR measurements are  
957 well calibrated. To achieve high spatial resolution, coverage is sacrificed resulting in a much  
958 reduced swath width.

#### 959 **5.3.1 Landsat**

960 The Landsat series of satellites have been in operation since 1972 carrying instruments designed  
961 to support monitoring and studying land surfaces. As such, these instruments have high spatial  
962 resolution. The imagers in the first satellites were limited to measurements in the visible, but  
963 with the Thematic Mapper (TM) on Landsat-4 and -5, launched in 1982 and 1984, a thermal IR  
964 channel ( $\lambda = 10.4 - 12.5 \mu\text{m}$ ) was added. Landsat-6 had a launch failure. This IR channel is also  
965 included in the Enhanced TM+ (ETM+) on Landsat-7, launched in 1999, with a surface  
966 resolution of 60m at nadir in the IR and a swath 183 km wide. The ETM+ is still in operation.  
967 Landsat-8 (formerly called the Landsat Data Continuity Mission, LDCM), was launched on 11  
968 February 2013, with two instruments: the Operational Land Imager (OLI) that operates in the  
969 visible through the short-wave IR; and the Thermal Infrared Sensor (TIRS), a two-channel  
970 radiometer ( $\lambda = 10.3 - 11.3 \mu\text{m}$  and  $\lambda = 11.5 - 12.5 \mu\text{m}$ ) with a spatial resolution of 100 m at  
971 nadir and an 185 km swath.

972 The TM and ETM+ IR measurements are calibrated on orbit by scanning a calibration wand in  
973 the field of view that serves as a warm blackbody at a controlled temperature and a cold shutter  
974 (Markham et al., 1997; Barsi et al., 2016). The TIRS on-orbit calibration uses measurements of  
975 cold space and of a blackbody at a known temperature with a correction for the non-linearity of  
976 the detector responses based on pre-launch calibration (Montanaro et al., 2014). However,  
977 evidence of stray light contamination was found that required a further correction (Wang et al.,  
978 2017). The large aperture of the TIRS renders accurate calibration very challenging, and it was  
979 recognized that comparisons with measurements of other spacecraft sensors, such as MODIS  
980 (Section 5.1.4) and GOES Imager (Section 5.4.3) would be a valuable approach (Wang et al.,  
981 2017; Wang and Ientilucci, 2018).

982 The high resolution of the TIRS measurements has been exploited in coastal waters, for example,  
983 to study inshore water quality (Trinh et al., 2017) and thermal discharge of cooling water from  
984 nuclear power stations (Wang et al., 2016).

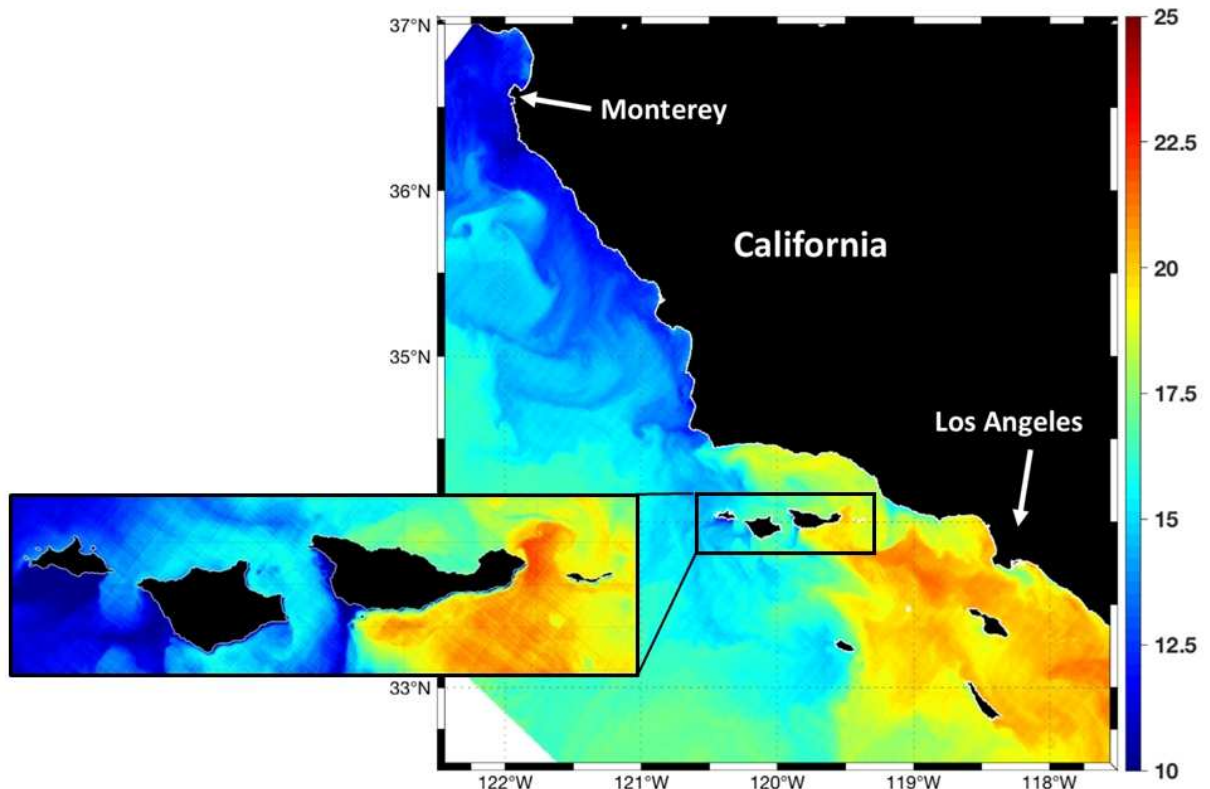
### 985 **5.3.2 ASTER**

986 The Advanced Spaceborne Thermal Emission and Reflection Radiometer (ASTER) is a Japanese  
987 imaging radiometer on the Terra satellite. ASTER has 14 spectral channels spanning the visible  
988 to the thermal IR, including two split-window channels centered at  $\lambda = 10.65$  and  $11.30 \mu\text{m}$  with  
989 bandwidths of  $0.667$  and  $0.593 \mu\text{m}$  (Yamaguchi et al., 1998). The ASTER optical system for the  
990 IR channels is a whiskbroom scanner, with the visible and short-wave IR channels being  
991 pushbroom imagers. The IR channels have a spatial resolution of  $90 \text{ m}$  at nadir (Yamaguchi et  
992 al., 1999). ASTER does not operate continuously, but “scenes” are gathered with dimensions  
993 about  $60 \times 60 \text{ km}^2$  according to a pre-programmed scheme; about 600 scenes can be gathered on  
994 one day (ibid). Unlike the IR measurements from most other imaging radiometers that are  
995 calibrated using two internal blackbody targets at different temperatures, or one blackbody target  
996 and a view of cold space (Minnett and Smith, 2014), the geometry of the ASTER optics prevents  
997 such an approach and instead the IR measurements are calibrated with a full-aperture blackbody  
998 that can be held at constant temperatures from  $270$  to  $340 \text{ K}$ . The blackbody is viewed before and  
999 after each scene (Tonooka et al., 2005; Hook et al., 2007). Although ASTER was designed for  
1000 land surface and cloud measurements, its high spatial resolution and calibrated IR channels  
1001 allows it to provide useful SST retrievals, especially in coastal areas (e.g. Matsuoka et al., 2011).

### 1002 **5.3.3 ECOSTRESS**

1003 Developed for land surface applications, the ECOsystem Spaceborne Thermal Radiometer  
1004 Experiment on Space Station (ECOSTRESS) also has a capability to derive SSTs. ECOSTRESS

1005 was launched to the International Space Station (ISS) on 29 June 2018 and installed on there on  
1006 July 2. Following the commissioning phase, ECOSTRESS became operational on August 20,  
1007 2018. The ISS orbit has an inclination of  $51.64^\circ$  and thus high latitudes are not accessible to  
1008 ECOSTRESS. The orbit is not sun-synchronous and successive arcs of the orbit drift west (at the  
1009 Equator) by about  $22.9^\circ$  of longitude, meaning that over about two months a full diurnal cycle is  
1010 sampled. ECOSTRESS is an infrared imaging radiometer with five spectral bands in atmospheric  
1011 transmission windows ( $\lambda = 8.29, 8.78, 9.20, 10.49, 12.09 \mu\text{m}$ ) each having a spatial resolution at  
1012 nadir of  $38 \text{ m} \times 68 \text{ m}$ . From the altitude of  $\sim 400 \text{ km}$  of the International Space Station (ISS) the  
1013 swath is  $402 \text{ km}$  wide (Hulley and Hook, 2018). Each infrared band has 256 detectors that sweep  
1014 out lines of pixels in a whisk-broom fashion, similar to MODIS (Section 5.1.4). Calibration is  
1015 accomplished with two on-board blackbody targets at  $300 \text{ K}$  and  $340 \text{ K}$  that are scanned each mirror  
1016 rotation (ibid).



1017

1018 *Figure 11. ECOSTRESS composite of two Level-2 images of SST derived with the Land Surface*  
 1019 *Temperature (LST) retrieval algorithm, acquired on September 16, 2018 at 13:04 and 13:05 UTC. Colder*  
 1020 *SSTs are associated with upwelling north of Santa Barbara. The enlargement shows fine-scale SST*  
 1021 *gradients around the Channel Islands National Marine Sanctuary – note the color scale has been*  
 1022 *stretched to cover 14°C to 22°C to show the fine-scale detail. The western islands (San Miguel, Santa*  
 1023 *Rosa) experience much cooler ocean temperatures than the eastern islands due to differences in*  
 1024 *upwelling, winds and currents. Image credit: Daniel Otis, Institute for Marine Remote Sensing (IMaRS),*  
 1025 *College of Marine Science, University of South Florida. Reproduced from*  
 1026 *<https://ecostress.jpl.nasa.gov/gallery/viewgalleryimage> with permission.*

1027 Figure 11 shows an example of coastal SST from ECOSTRESS derived using a land surface  
 1028 temperature retrieval algorithm, revealing high-resolution variability indicating the potential of  
 1029 ECOSTRESS to make contributions to coastal research.

1030 As yet there has been no concerted effort to determine the accuracy of the ECOSTRESS SST<sub>skin</sub>  
1031 retrievals, but work is underway (Hulley et al., 2019), including using the facilities at Lake Tahoe  
1032 and the Salton Sea as has been done for ASTER and MODIS (Hook et al., 2007; Tonooka et al.,  
1033 2005). Preliminary analysis of four months of comparisons indicate that the RMSE is < 1K (G. C.  
1034 Hulley, 2019, pers. comm.).

#### 1035 **5.4 Geostationary satellite instruments**

1036 The early geostationary earth observation satellites were “spin-stabilized” meaning they spin  
1037 about an axis parallel to that of the rotation of the earth. Thus an image of the earth’s disk, as  
1038 visible from geostationary orbit, is built as the sensor scans the earth’s disk longitudinally, with  
1039 latitudinal sampling being achieved through a stepped motion of the sensor’s scan mirror. There  
1040 are several advantages to spin-stabilization, but a major disadvantage is the small part of each  
1041 revolution when the earth is in view. Three-axis stabilized spacecraft, as used for GOES-8 in  
1042 1994 and subsequent satellites in the GOES series, rotates on its axis parallel to the earth’s axis  
1043 at the same rate as the earth. Thus, a single side of the satellite remains facing the earth, and  
1044 instruments mounted on this face of the satellite view the earth all the time. The current Meteosat  
1045 series, the European geostationary satellites, are spin-stabilized but the third generation will be 3-  
1046 axis stabilized with the first planned for launch in 2021 and the series expected to reach into the  
1047 late 2030s.

1048 The potential contributions of imagery from geostationary orbit to improve weather nowcasting  
1049 and forecasting were recognized early in the satellite era, and the first imagers on geostationary  
1050 earth observation satellites were sensitive to radiation in the visible part of the spectrum. The  
1051 first was the spin-scan cloud camera (SSCC) on the Applications Technology Satellite-1 (ATS-1)  
1052 launched in 1966 and which functioned for seven years. In 1974, the three-axis stabilized

1053 satellite ATS-6 was launched carrying the Geosynchronous Very High Resolution Radiometer  
 1054 (GVHRR) that included the first IR channel that permitted cloud imaging at night and estimation  
 1055 of cloud-top temperature, and thereby cloud-top height. The spectral width of the IR channel was  
 1056 10.5-12.5  $\mu\text{m}$ . The ATS-6 mission ended in 1979, ending the deployment of last 3-axis stabilized  
 1057 geosynchronous satellites until 1994.

1058 Some details of currently operational geostationary satellites are summarized in Table 1.

Table 1. Positions of geostationary satellites with an SST retrieval capability.

| Name        | Date launched    | Longitude | Notes   |
|-------------|------------------|-----------|---|
| GOES-16     | 19 November 2016 | 75.2°W    | GOES-E. Operational on 18 December, 2017.             |
| GOES-17     | 1 March 2018     | 137.2°W   | GOES-W. Operational on 12 February 2019.              |
| Meteosat-8  | 28 August 2002   | 41.5°E    | Moved on 4 July 2016 for Indian Ocean coverage.       |
| Meteosat-9  | 21 December 2005 | 3.5°E     | As backup for Meteosat-10 or Meteosat -11.            |
| Meteosat-10 | 15 July 2012     | 9.5°E     | Moved on 21 January 2013 for rapid scans over Europe. |
| Meteosat-11 | 15 July 2015     | 0°        | Operational on 20 February 2018.                      |
| Himawari-8  | 7 October 2014   | 140.7°E   | Operational on 7 July 2015.                           |

|                |                  |          |   |
|----------------|------------------|----------|---|
| Himawari-9     | 2 November 2016  | 140.7°E  | On standby as operational replacement for Himawari-8.                     |
| FengYun-2E     | 23 December 2008 | 86.5°E   | Operational on 1 July 2015  |
| FengYun-2F     | 13 January 2012  | 112.0°E  | On standby as operational replacement; used now for regional scanning     |
| FengYun-2G     | 31 December 2014 | 99.5°E   | Relocated from 105°E on 16 April 2018.                                    |
| FengYun-2H     | 5 June 2018      | 79.0°E   | Operational on 1 January 2019.  |
| FengYun-4A     | 10 Dec 2016      | 105.0°E  | Operational on 1 May 2018.  |
| INSAT-3D       | 25 July 2013     | 82.0 E   | Operational on 15 January 2014.   |
| INSAT-3DR      | 8 September 2016 | 74.0 E   | Operational on 11 October 2016.   |
| GEO-KOMPSAT-1  | 27 June 2010     | 128.25°E | Also referred to as Cheollian-1 and COMS-1. Operational on April 1, 2011. |
| GEO-KOMPSAT-2A | 4 December 2018  | 128.2° E | In commissioning. Expected to become operational in July 2019.            |

The longitude of each satellite may vary throughout its lifetime, being moved according to operational requirements. The information shown here are taken from the WMO OSCAR tool (<https://www.wmo-sat.info/oscar/>) or the web-pages of the satellite operators.



---

The satellites shown are those in operation at the time of writing. For past and planned satellites, please see the text.

1059

#### 1060 **5.4.1 VISSR and VAS**

1061 In 1974, the first model of the Visible Infrared Spin-Scan Radiometer (VISSR) was launched on  
1062 the spin-stabilized Synchronous Meteorological Satellite -1 (SMS-1; McClain, 1980). VISSR  
1063 had one IR channel occupying the 10.5-12.6  $\mu\text{m}$  wavelength interval and was the first to have  
1064 on-board IR calibration (Hursen and Ross, 1996). The spatial resolution of the IR channel at the  
1065 subsatellite point was 7 km and produced a full-disk image of the Earth each 30 minutes. Having  
1066 just a single IR channel prevented a split-window type atmospheric correction algorithm to  
1067 derive SST, but nevertheless, the VISSR brightness temperature images elucidated many upper  
1068 ocean processes, including westward propagating tropical instability waves (Legeckis, 1977).  
1069 The VISSR was the principal instrument on five US satellites: SMS-1 and -2, GOES -1, -2 and -  
1070 3, four Japanese satellites: Himawari-1 to -4 (also known as Geostationary Meteorological  
1071 Satellite, GMS-1 to -4).

1072 An important development of the VISSR was the VISSR Atmospheric Sounder (VAS) that first  
1073 flew on GOES-4, launched in 1980. VAS included a filter wheel in front of the detectors that  
1074 resulted in there being 12 channels in the IR that were selected at wavelengths to permit  
1075 sounding of the atmospheric temperature and humidity (Menzel et al., 1981). In addition to the  
1076 10.5-12.6  $\mu\text{m}$  wavelength band inherited from VISSR, VAS had two additional channels, one in  
1077 the 3.9  $\mu\text{m}$  window and the other at 12.6  $\mu\text{m}$  where the atmosphere is relatively transparent but  
1078 has a marked sensitivity to water vapor variations (Section 4.1.1). Measurements in these three

1079 channels permitted a multi-channel atmospheric correction to estimate SST (Bates and Smith,  
1080 1985).

### 1081 **5.4.2 SEVIRI**

1082 The main payload of the current European Meteosats is the Spinning Enhanced Visible and  
1083 Infrared Imager (SEVIRI), having 12 spectral channels of which 8 are in the IR having an  
1084 instantaneous field of view (IFOV) of 4.8 km at the surface at nadir, over-sampled to give a pixel  
1085 resolution of 3 km at the subsatellite point (European Space Agency, 1999; Aminou, 2002;  
1086 Schmid, 2012). With a rotation rate of 100 rpm, the SEVIRI provides full disk images every 15  
1087 minutes. The primary location of Meteosat is at 0°E above the Equator, which is now occupied  
1088 by Meteosat-11. Meteosat-10 is currently at 9.5°E producing rapid scans of a section of the  
1089 earth's disk of limited latitudinal range primarily covering Europe every 5 minutes. Meteosat-9 is  
1090 now at 3.5°E as a backup for -10 and -11, and Meteosat-8 is at 41.5°E to provide coverage over  
1091 the Indian Ocean. Some of the IR channels of SEVIRI, those at  $\lambda = 3.92 \mu\text{m}$ ,  $10.8 \mu\text{m}$  and  $12.0$   
1092  $\mu\text{m}$ , are suitable for accurate SST retrievals.

### 1093 **5.4.3 The GOES Imager**

1094 The GOES Imager (Hursen and Ross, 1996) has flown on the GOES 8-15 satellites (Menzel and  
1095 Purdom, 1994) from 1994 to the present; GOES-15 is still operating, but is scheduled to be  
1096 decommissioned in July 2019. There are two GOES operational spacecraft - one at nominally  
1097 75°W, called GOES-East, and the other at 135°W, GOES-West. The image of the Earth's disk is  
1098 constructed by scanning the field of view of the radiometer along horizontal lines by an  
1099 oscillating mirror, with latitudinal increments of the scan line resulting from tilting the axis of the  
1100 scan mirror between longitudinal scans. The spatial resolution of the IR channels is 4 km at the  
1101 subsatellite point (Maturi et al., 2008). A full-disk image is produced every 30 min, and limited

1102 areas where rapidly evolving meteorological features are occurring, can be imaged in  
1103 correspondingly shorter time intervals. The GOES Imager is a five-channel instrument, of which  
1104 three on earlier satellites (GOES-8 to GOES-11) were suitable for SST retrieval:  $\lambda = 3.9\mu\text{m}$ ,  $10.7$   
1105  $\mu\text{m}$  and  $11.95\mu\text{m}$ . On GOES-12, which became operational in 2003, and subsequent satellites,  
1106 the channel at  $\lambda = 11.95\mu\text{m}$  was moved to  $13.35\mu\text{m}$ , thereby compromising the feasibility of  
1107 using split-window atmospheric corrections to derive SSTs, although an algorithm using the  $\lambda =$   
1108  $3.9\mu\text{m}$  after a correction for solar contamination was developed (Merchant et al., 2009a).

#### 1109 **5.4.4 Advanced Himawari Imager (AHI) and the Advanced Baseline Imager (ABI)**

1110 The first of a new generation of geostationary meteorology satellites of the JMA, Himawari-8  
1111 (Bessho et al., 2016), began operation on July 7<sup>th</sup> 2015; it is located at  $140.7^\circ\text{E}$  above the equator  
1112 and replaced the earlier MTSAT-2 (Multifunction Transport Satellite-2, or Himawari-7).

1113 MTSAT-2 carried a five-channel imager with IR channels for SST at  $\lambda = 3.75\mu\text{m}$ ,  $10.8\mu\text{m}$  and  
1114  $12.0\mu\text{m}$ , with a 4 km spatial resolution at nadir. Himawari-8 carries the first of a new type of  
1115 visible and IR imager for geostationary satellites, the Advanced Himawari Imager (AHI). The  
1116 AHI has 16 spectral channels of which five are in the IR and can be used for SST retrievals:  $\lambda =$   
1117  $8.60\mu\text{m}$ ,  $10.45\mu\text{m}$ ,  $11.20\mu\text{m}$ , and  $12.35\mu\text{m}$ , with one at  $\lambda = 3.85\mu\text{m}$  available for use at night.  
1118 The IR bands have a spatial resolution of 2 km at nadir. The AHI provides full disk images of  
1119 most of the Pacific Ocean and eastern Indian Ocean as rapidly as every 10 minutes, with smaller  
1120 areas being sampled more frequently as required.

1121 The first of a new series of NOAA geostationary satellites, called GOES-R while in development  
1122 and renamed GOES-16 once declared operational on December 16<sup>th</sup> 2017, is located above  
1123  $75.2^\circ\text{W}$ . GOES-17, operational since February 12<sup>th</sup> 2019, is located above  $137.2^\circ\text{W}$ . This series  
1124 of geostationary satellites, each with a planned lifetime of 10 years, is expected to operate into

1125 the mid-2030s, carries the Advanced Baseline Imager (ABI), which has very similar capabilities  
1126 to those of the AHI, including IR bands suitable for the derivation of SST, at  $\lambda = 3.90 \mu\text{m}$ ,  $8.50$   
1127  $\mu\text{m}$ ,  $10.3 \mu\text{m}$ ,  $11.2 \mu\text{m}$ , and  $12.3 \mu\text{m}$ .

1128 The AHI and ABI represent a significant development in the derivation of SST from  
1129 geostationary orbit.

#### 1130 **5.4.5 FengYun-2 Stretched Visible Infrared Spin Scan Radiometer**

1131 The Chinese, spin-stabilized geostationary satellites are the FengYun-2 (FY-2) series, with FY-  
1132 2A having been launched in 1997 to a position above  $105^\circ\text{E}$ , where it operated for a little less  
1133 than one year. It was succeeded by FY-2B in 2000 which functioned until 2004. These two  
1134 satellites carried the S-VISSR (Stretched-VISSR) with a single IR channel at  $\lambda = 10.5 - 12.5 \mu\text{m}$ .  
1135 The FY-2C, launched in 2004 to a position at  $123^\circ\text{E}$ , and subsequent satellites of this series  
1136 carried an enhanced S-VISSR with a channel at  $\lambda = 3.75 \mu\text{m}$  and split-window channels at  $\lambda =$   
1137  $10.8 \mu\text{m}$  and  $12.0 \mu\text{m}$ , permitting multi-channel atmospheric corrections to derive SST. The on-  
1138 board calibration of the FY-2C S-VISSR IR bands was checked by comparing their BTs with  
1139 those of MODIS on Terra and AIRS by Jiang et al. (2009) who reported that while the S-VISSR  
1140 calibration was stable, there were significant temperature dependent offsets between the IR  
1141 channels of the three instruments, which are largely consistent between S-VISSR and the two  
1142 reference radiometers. Currently there are four FY-2s in operation: FY-2E at  $86.5^\circ\text{E}$ , FY-2F at  
1143  $112^\circ\text{E}$ , FY-2G at  $105^\circ\text{E}$ , and FY-2H launched in June 2018, at  $79^\circ\text{E}$ .

#### 1144 **5.4.6 FengYun-4 Advanced Geostationary Radiation Imager**

1145 The first of the next-generation Chinese geostationary satellites, the FY-4 series (Yang et al.,  
1146 2017) was launched in December 2017 into a position at  $105^\circ\text{E}$ . The FY-4s are three-axis  
1147 stabilized satellites and one of the six instruments making up their payload is the Advanced

1148 Geostationary Radiation Imager (AGRI) with 14 channels, including two at  $\lambda = 3.75 \mu\text{m}$  – one  
1149 with spatial resolution of 4 km and an NE $\Delta$ T of 0.2 K at 300 K, and the other with a surface  
1150 resolution of 2 km with an NE $\Delta$ T of 0.7 K at 300 K – and two split window channels at  $\lambda = 10.7$   
1151  $\mu\text{m}$  and 12.0  $\mu\text{m}$  with 4 km spatial resolution and NE $\Delta$ Ts of 0.2 K at 300 K. A full disk scan can  
1152 be made by AGRI every 5 minutes. Seven FY-4 satellites are planned which will extend beyond  
1153 2040.

#### 1154 **5.4.7 Communication Ocean Meteorological Satellite (COMS) Meteorological Imager**

1155 To provide ocean and meteorological measurements in the vicinity of the Korean Peninsula, a  
1156 geostationary satellite was launched in June 2010 to 128.25°E. Called the Communication Ocean  
1157 Meteorological Satellite (COMS), it has subsequently been renamed GEO-KOMPSAT 1  
1158 (Geostationary Korea Multi-Purpose Satellite) and is also referred to as Cheollian-1, it is three-  
1159 axis stabilized and serves three objectives: monitoring ocean color, providing meteorological  
1160 imagery, including IR bands that can be used for SST derivation, and for communications. The  
1161 Meteorological Imager (MI) is a development of the imager flown on MTSAT-2 with five bands  
1162 including at  $\lambda = 3.75 \mu\text{m}$ , 10.8  $\mu\text{m}$  and 12.0  $\mu\text{m}$  (Cho and Youn, 2006). Following adjustment of  
1163 the calibration of the MI IR channels after comparison with IASI measurements in the  
1164 framework of the Global Space-based Inter-Calibration System (GSICS; Section 11), the SSTs  
1165 derived using an NLSST atmospheric correction algorithm compared much better with in situ  
1166 measurements from drifters in the western Pacific Ocean and eastern Indian Ocean with daytime  
1167 differences of -0.062 K in the mean and root-mean-square error of 0.666 K, and night-time  
1168 values of -0.020 K and 0.809 K (Park et al., 2015).

1169 The next-generation satellites comprise of two satellites operating together; GEO-KOMPSAT-  
1170 2A was launched on December 4<sup>th</sup> 2018, and -2B is scheduled for launch in October 2019. GEO-

1171 KOMPSAT-2A carries an Advanced Meteorological Imager (AMI), which is very similar to the  
1172 AHI and ABI. GEO-KOMPSAT-2B will be for monitoring ocean color, atmospheric ozone and  
1173 other trace gases.

#### 1174 **5.4.8 INSAT-3 Imager**

1175 The Indian Space Research Organisation (ISRO) has been launching satellites into geostationary  
1176 orbit since 1982. These Indian National Satellites (INSATs) include telecommunication satellites  
1177 as well as those for earth observation. The early series of satellites carried the Very High  
1178 Resolution Radiometer (VHRR), with a single IR channel at  $\lambda = 11.6 \mu\text{m}$  thus not permitting  
1179 correction for the atmosphere to derive SSTs. INSAT-3D, launched in 2013 above 82°E,  
1180 included an Imager with IR channels at  $\lambda = 3.82 \mu\text{m}$ ,  $10.8 \mu\text{m}$ ,  $12.0 \mu\text{m}$ , with a 4 km resolution at  
1181 the subsatellite point. INSAT-3DR (Repeat) with the same payload was launched to 74°E in  
1182 2016, with INSAT-3DS (Second Repeat) scheduled for launch in 2022. Comparisons with the  
1183 iQuam drifter data in the seas around India, revealed mean differences ranging from  $-0.16 \text{ K}$  to  
1184  $-0.20 \text{ K}$ , being worse in the Arabian Sea at  $-0.27 \text{ K}$  with greater values during the monsoon  
1185 season (Tyagi et al., 2018).

#### 1186 **5.5 Microwave Instruments**

1187 Imaging microwave radiometers are confined to satellites with orbital altitudes typical of those in  
1188 polar orbits, or at lower altitudes, as the spatial resolution is limited by the size of an antenna that  
1189 can be deployed on a spacecraft, typically 2m or less in diameter. Since the sensitivity of the  
1190 emitted radiation from the sea surface in microwave frequencies to SST variations is at 6 to 10  
1191 GHz,  $\lambda = 5 \text{ cm}$  to  $3 \text{ cm}$ , (Figure 6; Wilheit, 1979) and so the diffraction-limited surface  
1192 resolution is tens of km ( $35 \times 62 \text{ km}^2$  at 7 GHz for a 2 m diameter parabolic reflector at a height

1193 of 700 km, and 24 x 42 km<sup>2</sup> at 10 GHz). Measurements are usually taken at both horizontal and  
1194 vertical polarizations. A further consequence of the diffraction limitation of microwave  
1195 measurements of SST is the presence of significant side-lobes (e.g. Kawanishi et al., 2003)  
1196 which, in the vicinity of land, permits the leakage of terrestrial emission from a high emissivity  
1197 source into the signal from the sea surface, with low emissivity, resulting in a degradation in the  
1198 accuracy of the SST retrievals within ~100 km of coastlines. A further loss of SST retrievals is  
1199 caused by the presence of heavy rain. Since the angular dependence of the apparent surface  
1200 emissivity of sea water is large and dependent on the wind speed (Wilheit, 1979), there would be  
1201 a strong variation in the BT signal across the swath of a linearly scanning microwave radiometer,  
1202 so to avoid this complicating factor, satellite microwave radiometers use a conical scan with a  
1203 constant angle of incidence of the field of view at the sea-surface, typically 50°-55°. As a  
1204 consequence, the swath width of microwave radiometers with SST capabilities is typically less  
1205 than 1600 km from polar orbit, resulting in large gaps between successive orbits but these are  
1206 generally filled in over two to three days.

### 1207 **5.5.1 Scanning Multichannel Microwave Radiometer (SMMR)**

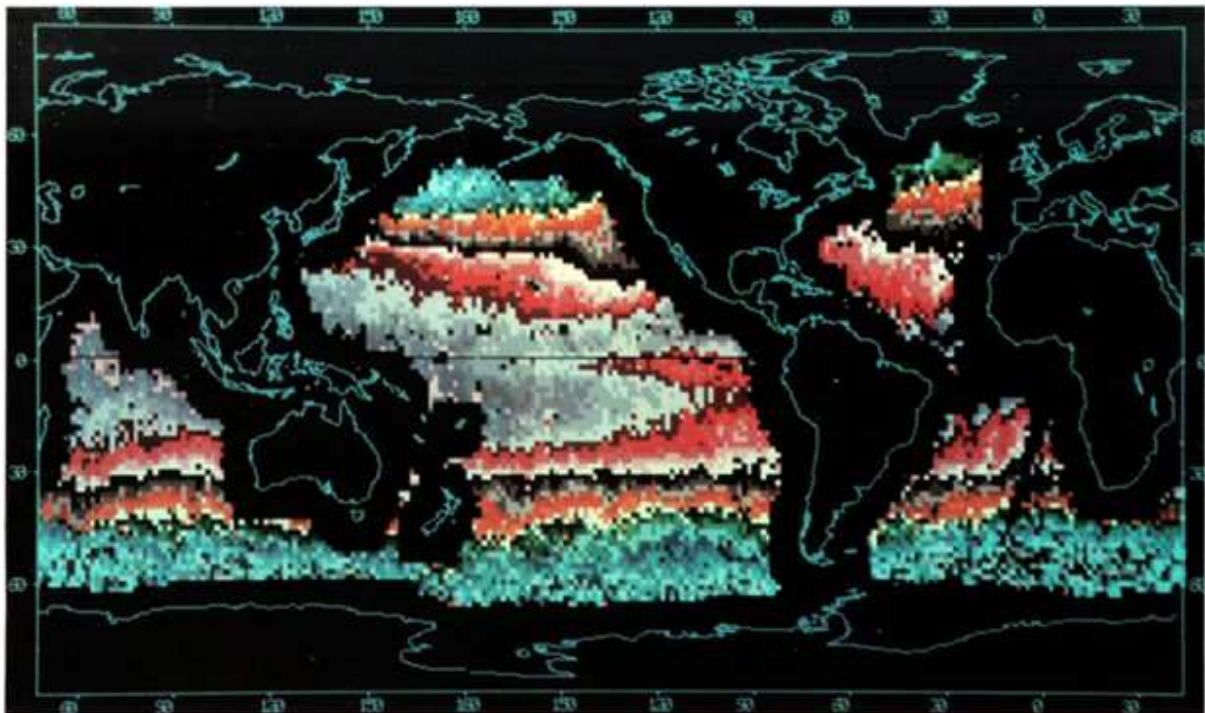
1208 Two models of the SMMR (Gloersen and Barath, 1977) were flown, one on SeaSat in a drifting  
1209 orbit from June to October, 1978, and the other on Nimbus-7 in a sun-synchronous orbit from  
1210 1978 to 1994, with SMMR operations ending in 1988. Both had channels with SST sensitivity at  
1211 6.6 GHz and 10.7 GHz, but with a relatively small antenna at 60cm diameter, the surface  
1212 resolution was 95 x 160 km<sup>2</sup> at 6.6 GHz and 60 x 100 km<sup>2</sup> at 10.7 GHz. Prabhakara et al. (1983)  
1213 attempted to assess the accuracy of the Nimbus-7 SMMR brightness temperatures at 6.6 GHz to  
1214 represent the SST, as measured from ships, and confirmed the confusing influence of variations  
1215 in wind speed and cloud liquid water. They derived empirical corrections which resulted in

1216 useful maps of SST being derived that indicated oceanographic patterns, such as the cool tongue  
1217 of surface water in the equatorial eastern Pacific Ocean. A comparison with SMMR SSTs  
1218 derived with corrections for water vapor, liquid water and wind speed through combinations of  
1219 different channels and polarizations, and SSTs derived from drifting buoys deployed as part of  
1220 the FGGE (First Global GARP Experiment, where GARP is the Global Atmospheric Research  
1221 Program) during 1979 in the southern hemisphere revealed differences of ~0.6 K in the mean and  
1222 a standard deviation of ~1.76 K (Gloersen et al., 1984). Figure 12 shows the global SST field  
1223 derived from the SMMR on Nimbus-7 for June 1979.

#### 1224 **5.5.2 TRMM Microwave Imager (TMI)**



1225 The Tropical Rainfall Measuring Mission (TRMM) satellite (Kummerow et al., 1998), a joint  
1226 mission of NASA and the Japan Aerospace Exploration Agency (JAXA) launched in 1997,  
1227 carried the TRMM Microwave Imager (TMI), which was a nine-channel microwave radiometer.  
1228 The channels were centered at five frequencies: 10.65, 19.35, 21.3, 37.0, and 85.5 GHz, with  
1229 four of them being measured in both horizontal and vertical polarizations. The 10.65 GHz  
1230 channels confer a sensitivity to SST in the higher SST range found in the tropics, a capability  
1231 that had been absent since the SMMR. The TMI complemented AVHRR IR SSTs by providing



1232 SSTs in the tropics where persistent clouds can be a problem for IR retrievals. The TMI swath  
1233 width was only 759 km due to the low altitude of the orbit, and the low inclination of the TRMM  
1234 orbit limited SST measurements to within  $38.5^\circ$  of the equator. The beam width of the 10.65  
1235 GHz channels produced an approximately elliptical footprint of  $37 \times 63 \text{ km}^2$ , but the data were  
1236 over-sampled to produce 104 pixels across the swath. Although originally planned for a three-  
1237 year mission, TRMM ended in April, 2015, after providing SSTs for 17 years.

1238 *Figure 12. Global SST's from SMMR, June 1979. Plate 1 of Gloersen et al., 1984.*

### 1239 **5.5.3 Advanced Microwave Scanning Radiometer for EOS (AMSR-E)**

1240 The Japanese Advanced Microwave Scanning Radiometer for EOS (AMSR-E) was part of the  
1241 payload of the NASA satellite Aqua. It was a twelve-channel, six-frequency, microwave  
1242 radiometer that measured brightness temperatures at 6.925, 10.65, 18.7, 23.8, 36.5, and 89.0 GHz  
1243 with vertical and horizontal polarization. AMSR-E had a parabolic reflector 1.6 m in diameter  
1244 that rotated at 40 rpm to scan across the surface in a cone with an incidence angle of 55°,  
1245 producing a swath width of 1445 km. As with other microwave radiometers, before and since,  
1246 the calibration used the cosmic background radiation and an on-board warm target. The spatial  
1247 resolution of the 6.9 GHz measurements was 74 km x 43 km but increased with increasing  
1248 frequency, reaching 8.2 km x 14 km at 36.5 GHz (Kawanishi et al., 2003). The derivation of  
1249 SST from microwave radiometer data requires the combination of measurements at different  
1250 frequencies and therefore different footprint sizes (Gentemann et al., 2010) so the effective  
1251 footprint size of the SST retrievals is not self-evident. A recent study (Boussidi et al., 2019)  
1252 using  $SST_{skin}$  retrievals from MODIS on Aqua within the swath of AMSR-E has produced a  
1253 reference footprint for the AMSR-E with 40 km x 60 km being the full-width defined as the  
1254 point at which the magnitude has fallen to about  $e^{-1}$  of its central value (P. Cornillon (2019) pers.  
1255 comm.). But many microwave-derived SST fields are produced at higher spatial resolution,  
1256 indicating these fields are oversampled. The AMSR-E was decommissioned in October 2011  
1257 when the mechanism to rotate the antenna failed, after providing nearly a decade of valuable  
1258 measurements.

1259 In three-way comparisons with AMSR-E, AATSR and drifting buoys, O'Carroll et al. (2008)  
1260 determined the AMSR-E SST observations have an uncertainty of ~0.42 K, comparable to the

1261 results of a subsequent analysis by Lean and Saunders (2013) who expressed their results as  
1262 standard deviations for the years 2003 to 2009, ranging from 0.462 K to 0.500 K, with higher  
1263 values in later years. In a three-way analysis including MODIS SSTs along with AMSR-E SSTs,  
1264 Gentemann (2014) reported standard deviations of AMSR-E SSTs of 0.48 K. All of these three-  
1265 way analyses were done using AMSR-E L2 (see Section 7 below) SST product distributed by  
1266 Remote Sensing Systems (<http://www.remss.com/missions/amsr/>), with a 25 km retrieval grid.  
1267 More recent versions were used in the later analyses. Comparable analyses using AMSR-E SSTs  
1268 derived using different algorithms at different processing centers would not necessarily produce  
1269 identical results.

#### 1270 **5.5.4 WindSat**

1271 The US Navy launched a sun-synchronous polar-orbiting satellite called Coriolis in January 2003  
1272 into a terminator orbit, having equator crossing times of 6 a.m. and 6 p.m. Coriolis carries the  
1273 WindSat microwave radiometer with bands at 6.8, 10.7, 18.7, 23.8, and 37.0 GHz. The 6.8 and  
1274 10.7 GHz channels are sensitive to SST. The conically-scanning 1.8 m reflector produces a  
1275 swath of ~1000 km width with a native resolution of 39 x 71 km<sup>2</sup> of the low frequency channel  
1276 (Gaiser et al., 2004). Meissner and Wentz (2007) assessed the accuracies of WindSat SSTs by  
1277 comparing global fields with those of AMSR-E and found a mean difference of -0.08 K with a  
1278 standard deviation of 0.56K, and in a smaller, regional comparison with M-AERI SST<sub>skin</sub> an  
1279 RMS of 0.27 K. Comparisons between SSTs from WindSat and moored buoys in the Tropical  
1280 Pacific Ocean resulted in an RMS difference of 0.36 K (Zhang et al., 2016c).

#### 1281 **5.5.5 OceanSat-1 Multi-frequency Scanning Microwave Radiometer (MSMR)**

1282 A series of sun-synchronous satellites for marine research was begun by the Indian Space  
1283 Research Organisation (ISRO) in 1999 with the launch of OceanSat-1 with a Multi-frequency

1284 Scanning Microwave Radiometer (MSMR), which included channels at 6.6 GHz and 10.65 GHz,  
1285 conferring an SST capability. The swath width was 1360 km. Comparisons with temperatures  
1286 measured from five moored buoys in the Arabian Sea and the Bay of Bengal showed differences  
1287 of  $-0.67$  K with a standard deviation of 2.0 K; there were significant differences between day  
1288 and night comparisons with the daytime values being better, and also with season as defined by  
1289 the monsoon, with monsoonal values being better (Parekh et al., 2007). A more extensive  
1290 comparison using drifting buoys in the Indian Ocean revealed a mean difference of  $-0.48$  K with  
1291 a standard deviation of 1.15 K (Muraleedharan et al., 2004). Although there were subsequent  
1292 OceanSat missions, none included microwave radiometers.

#### 1293 **5.5.6 HY-2 microwave radiometer (MWI).**

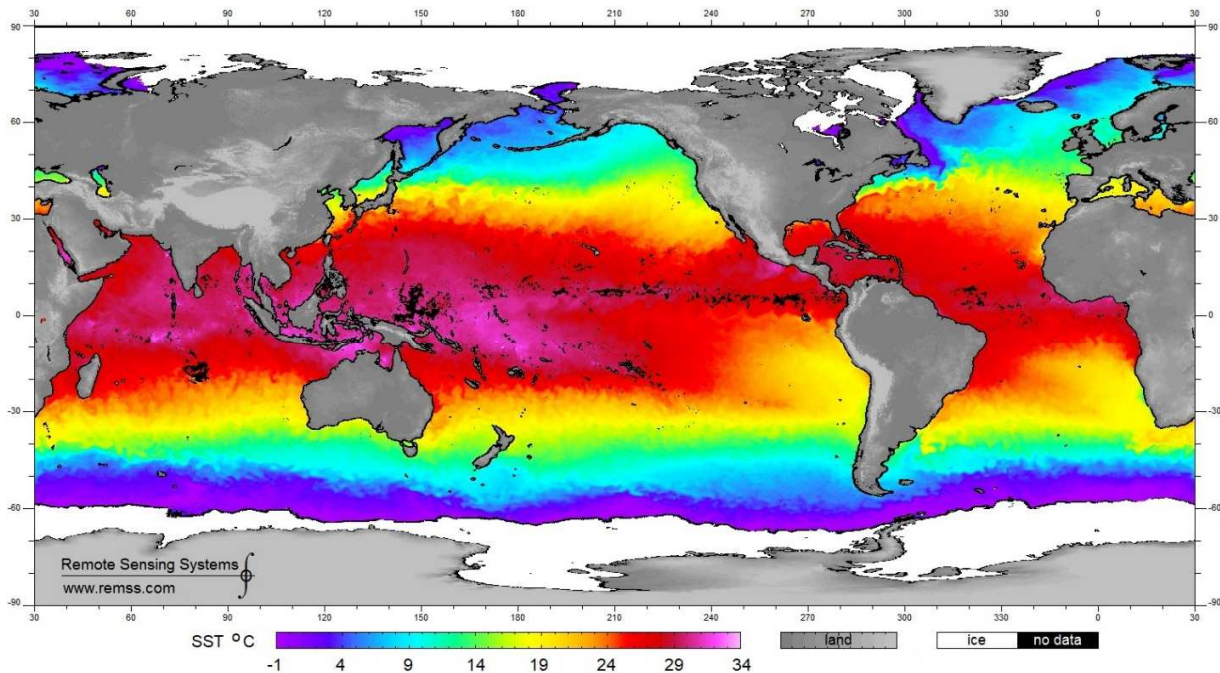
1294 A complementary series of satellites to the Chinese HY-1 polar orbiters, the HY-2 series, has  
1295 microwave radars (altimeter and scatterometer) and a microwave radiometer (MWI). HY-2A was  
1296 launched in 2011 and -2B in October, 2018. The MWI has dual-polarized, low frequency  
1297 channels at 6.6 GHz and 10.7 GHz thereby giving an SST capability. The surface resolution is 80  
1298  $\times$  120 km<sup>2</sup> and 50  $\times$  75 km<sup>2</sup>, respectively. Comparisons with temperatures measured by drifting  
1299 and moored buoys from NDBC (US National Data Buoy Center) gave a mean difference of  $-0.49$   
1300 K with a standard deviation of 1.63 K, and with near-surface temperatures from Argo profilers  
1301 (Roemmich et al., 2009) a mean difference of  $-0.28$  K and 1.68 K (Zhao et al., 2014).

#### 1302 **5.5.7 Advanced Microwave Scanning Radiometer 2**

1303 The second generation Advanced Microwave Scanning Radiometer (AMSR2) was launched on  
1304 May 17, 2012, on the Japanese Global Change Observation Mission-Water “Shizuku” (GCOM-  
1305 W1; Heygster et al., 2017; Kachi et al., 2017). GCOM-W1 is in the A-Train series of satellites  
1306 with an ascending node at 13:30 (L’Ecuyer and Jiang, 2010). The diameter of the AMSR-2

1307 reflector is 2.0 m, and, like AMSR-E, its rotation traces a conical scan with an angle of incidence  
1308 of 55° at the surface. The channels of AMSR2 are the same as for AMSR-E with the addition of  
1309 a 7.3 GHz channel to mitigate radiofrequency interference in the SST retrievals (Gentemann and  
1310 Hilburn, 2015). An example of global SST derived from AMSR2 measurements is shown in  
1311 Figure 13.

1312 Comparisons with in situ measurements of temperatures from drifting and moored buoys were  
1313 found by Gentemann and Hilburn (2015) to give mean discrepancies of -0.04 K with a standard  
1314 deviation of 0.55 K, with a small latitudinal dependence, and by Hihara et al. (2015) to be 0.21 K  
1315 in the mean with an RMS of 0.49 K through comparisons with the TRITON moorings in the  
1316 Western Tropical Pacific Ocean. Hihara et al. (2015) acknowledged the high mean difference  
1317 could be a consequence of diurnal heating in the daytime comparisons whereas Gentemann and  
1318 Hilburn (2015) removed daytime comparisons for wind speeds  $<6 \text{ ms}^{-1}$  to avoid the effects of  
1319 diurnal heating.



1320

1321 *Figure 13. Global SST distribution derived by compositing AMSR2 measurements over three days ending*  
 1322 *21 November 2018. Credit: Wentz, F.J., T. Meissner, C. Gentemann, K.A. Hilburn, J. Scott, 2014:*  
 1323 *Remote Sensing Systems GCOM-W1 AMSR2 Environmental Suite on 0.25° grid, Version V.8. Remote*  
 1324 *Sensing Systems, Santa Rosa, CA. Available online at [www.remss.com/missions/amsl](http://www.remss.com/missions/amsl). Accessed 24*  
 1325 *November 2018.*

### 1326 **5.5.8 The Global Precipitation Measurement Microwave Imager**

1327 Even before the end of the successful TRMM mission (Section 5.5.2), a follow-on satellite was  
 1328 being developed with a similar, but improved, suite of sensors. As with TRMM, the new  
 1329 satellite, the Global Precipitation Measurement (GPM; Smith et al., 2007) Core Observatory was  
 1330 planned to be in a drifting orbit so that over time diurnal variations would be sampled. The new  
 1331 satellite was launched on February 27<sup>th</sup>, 2014, into an orbit with an altitude of 407 km and an  
 1332 inclination of 65°. The GPM Core Observatory carries a Microwave Imager (GMI; Draper et al.,

1333 2015), a conical-scanning radiometer covering a swath width of 550 miles (885 km) with thirteen  
1334 channels from 10.65 GHz to 183.31 GHz. The 10.65 GHz channels, with horizontal and vertical  
1335 polarization, have sensitivity to SST variations, but only for warm water, SST  $> \sim 13^{\circ}\text{C}$ , as at  
1336 colder temperatures the sensitivity decreases and the noise level increases (Gentemann et al.,  
1337 2010).

## 1338 **6 Validation**

1339 As with all measurements, the success of the application of satellite-derived SSTs to research  
1340 and to operational endeavors relies on an accurate and confident assessment of errors and  
1341 uncertainties. As indicated in the previous section, such estimates of accuracy are generally  
1342 derived by comparison with in situ measurements, and this requires the validating measurement  
1343 to be of greater accuracy and lower uncertainty than the satellite data. The first satellite SST  
1344 validation was reported by Allison and Kennedy (1967) from the Nimbus 1 High Resolution  
1345 Infrared Radiometer (HRIR). But, it was not until the launch of the first AVHRR on TIROS-N  
1346 that SST was routinely produced from space-based measurements. The initial validation of  
1347 AVHRR SSTs, using the split-window MCSST atmospheric correction algorithm produced  
1348 standard deviations of  $\sim 0.5$  K at best (Strong and McClain, 1984), with mean differences of up to  
1349 several tenths of a degree depending on the source of the validating data (McClain et al., 1985)  
1350 and at these levels of accuracy, the contribution of the inaccuracy from the validating sensor and  
1351 from the method of validation were not considered important, so the statistics of the comparisons  
1352 were deemed to be an assessment of the accuracy of the satellite retrievals. As satellite sensors  
1353 improved, along with the cloud screening and atmospheric correction algorithms, the differences  
1354 between satellite-derived and in situ temperatures became much smaller, these other

1355 contributions could no-longer be ignored. It was realized these contributions should be taken into  
1356 account to determine a more meaningful estimate of the accuracy of the satellite retrievals of  
1357 SST (see, for example, Corlett et al., 2014).

1358 In situ measurements are available from many platforms (e.g. drifting buoys, moored buoys,  
1359 ships, Argo floats). Each have different characteristics and also different performances, as  
1360 presented by Castro et al. (2012) and Xu and Ignatov (2010) for drifting and moored buoys, and  
1361 by Atkinson et al. (2014), for many other different types. Drifting buoys are the most commonly  
1362 used type as they have several advantages: good geographical coverage, shallow measurement  
1363 depth - typically 20 cm - and availability in near-real time through the GTS (Global  
1364 Telecommunication Service). Argo floats, whose number has been increasing in recent years,  
1365 have been recommended for climate studies; however, the uppermost measurement depth is  
1366 about 5 meters and relatively few are at the surface close to the time of overpass of a given  
1367 satellite. The moorings of the Global Tropical Moored Buoy Array (GT MBA; McPhaden et al.,  
1368 2010) provided long-term consistent measurements until the unfortunate degradation of the  
1369 GT MBA in 2014 and are so far the best way to estimate the stability of satellite SST records  
1370 (Merchant et al., 2012).

1371 Given that the source of the IR radiation reaching the satellite is the skin of the ocean, the  
1372 variable size of the thermal skin effect (Donlon et al., 2002; Minnett et al., 2011; Wong and  
1373 Minnett, 2018) and variable diurnal heating decouple the  $SST_{skin}$  from the subsurface  
1374 temperatures measured by in situ thermometers. Using well-calibrated IR radiometers on ships to  
1375 measure the  $SST_{skin}$  provide validation measurements that avoid the contributions from  
1376 variations in the temperature gradients across the thermal skin layer and possible diurnal heating.



1377 Two types of shipboard radiometers that have been continuously deployed for many years for the  
1378 validation of satellite derived  $SST_{skin}$  are the Marine-Atmospheric Emitted Radiance  
1379 Interferometer (M-AERI; Minnett et al., 2001) and the Infrared SST Autonomous Radiometer  
1380 (ISAR; Donlon et al., 2008). The M-AERI is a Fourier Transform Infrared Interferometer  
1381 (Griffiths and de Haseth, 1986) that measures the spectra of IR emission from the ocean surface  
1382 and the atmosphere from  $\lambda = \sim 3 \mu m$  to  $\sim 18 \mu m$  in  $\sim 2700$  samples, with accurate internal  
1383 calibration using two SI-traceable blackbody cavities, one of which is heated and the other is at  
1384 ambient temperature. A gold-plated scan mirror directs the field of view of the interferometer to  
1385 the ocean and the atmosphere (needed to correct the sky radiance reflected at the sea surface) and  
1386 to the two blackbodies. A rain sensor is used to move the mirror to a “safe” position directed at  
1387 one of the blackbodies when rain or sea spray is detected.  $SST_{skin}$  is derived from measurements  
1388 around  $\lambda = 7.7 \mu m$  (Smith et al., 1996; Minnett et al., 2001) where the effects of cloud variability  
1389 in the reflected sky radiance is much smaller than in the thermal IR atmospheric window at  $\lambda =$   
1390  $10-12 \mu m$ , but where the emission depth at the ocean surface is very similar to those at  
1391 wavelengths of the thermal window (Bertie and Lan, 1996). Running two M-AERIs side by side  
1392 on a section from Hawaii to New Zealand produced  $SST_{skin}$  values from each instrument that  
1393 were different by 0.005 K with a standard deviation of 0.077 K for 890 measurement pairs  
1394 (Minnett et al., 2001). A recently revised error model of M-AERI  $SST_{skin}$  retrievals gives, for  
1395 example, a median value for the total error of 0.041K for 4600 retrievals during a recent research  
1396 cruise in the Mediterranean Sea.

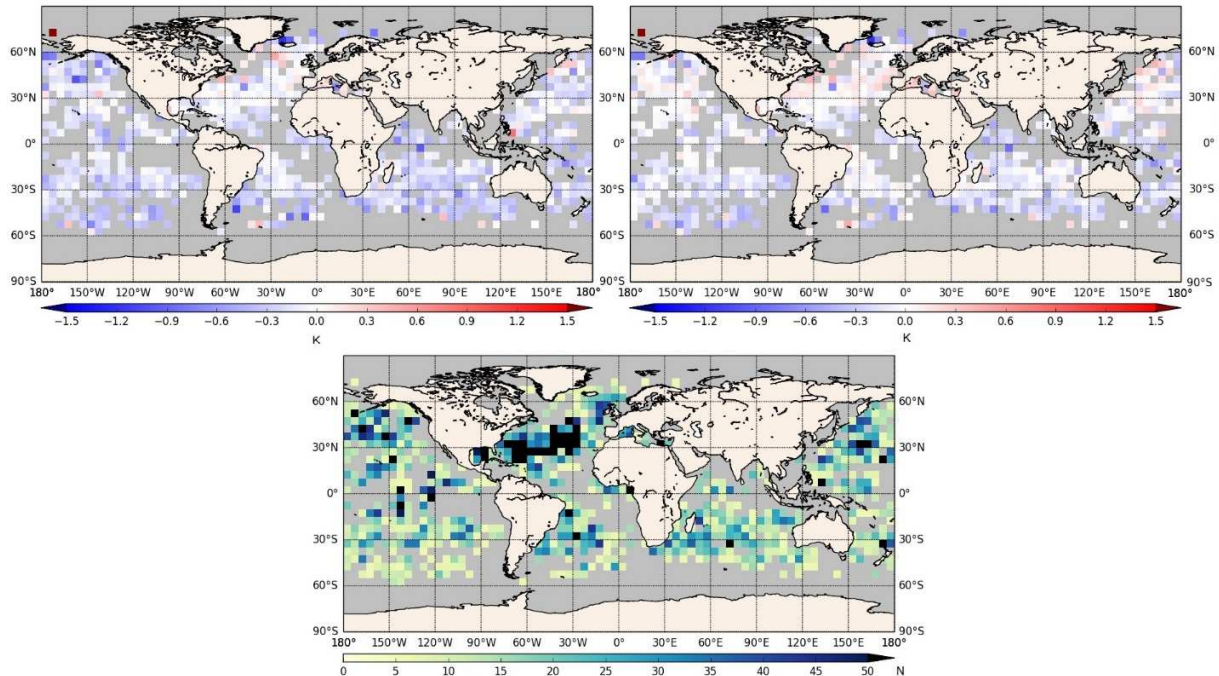
1397 The ISAR operates on the same principle but uses a filter to define the wavelength passband of  $\lambda$   
1398  $= 9.6-11.5 \mu m$ . However, this choice of a wavelength interval where the atmosphere is very  
1399 transparent in the IR increases the sensitivity of the  $SST_{skin}$  retrievals to errors introduced by

1400 cloud variability as, with all ship radiometers, the sky and sea view measurements are made  
1401 sequentially. An analysis of at-sea measurements from the Scanning Infrared Sea Surface  
1402 Temperature Radiometer (SISTeR; described by Donlon et al. (2014)), which has very similar  
1403 measurement and operating principles to the ISAR, Donlon and Nightingale (2000) found cases  
1404 where variable cloud fields could lead to errors in the  $SST_{skin}$  of  $\pm 0.25$  K and greater were  
1405 possible. Nevertheless, an analysis of 12 years of  $SST_{skin}$  retrievals from ISAR from ships  
1406 crossing the Bay of Biscay shows that 77.6% of the data are accurate within 0.1 K (Wimmer and  
1407 Robinson, 2016). Donlon et al. (2014) give a more complete review of shipboard IR radiometry  
1408 for satellite-derived SST validation.

1409 Various approaches are used to control the quality of in situ data. Gross error checks, e.g. a 5 K  
1410 cut-off relative to climatology, are commonly applied. The so-called blacklist approach is an  
1411 automatic scheme that detects the platforms having anomalous statistics and blacklist them:  
1412 UKMO makes a monthly blacklist by comparing drifting buoy SSTs and ship SSTs to those of  
1413 OSTIA (Operational Sea Surface Temperature and Sea Ice Analysis; Donlon et al., 2012b), OSI  
1414 SAF (Ocean and Sea Ice Satellite Application Facility of EUMETSAT) updates its blacklist  
1415 every 10 days, using night-time SST differences between satellites and buoys, considering two  
1416 satellites for a given buoy, when available (Marsouin et al., 2015). The in situ SST Quality  
1417 Monitor (iQuam) developed at NOAA (Xu and Ignatov, 2014) is an elaborate scheme that  
1418 routinely processes the in situ data (drifters, ships, tropical and coastal moorings) available on  
1419 the GTS. Quality flags are assigned to each measurement through multiple tests, Bayesian and  
1420 basic (e.g. track check, SST spike check). Files with quality controlled SSTs are available online  
1421 (<https://www.star.nesdis.noaa.gov/sod/sst/iquam2/>).

1422 Satellite-derived SST retrievals have been validated using several approaches: satellite-derived  
1423 SST compared with in situ SST considered as a reference (Walton et al., 1998; Kilpatrick et al.,  
1424 2001; Le Borgne et al., 2012a; Høyer et al., 2012; Marsouin et al., 2015; Kilpatrick et al., 2015),  
1425 three-way analyses using two satellite-derived SSTs and one in situ SST (O'Carroll et al., 2008;  
1426 O'Carroll et al., 2012; Gentemann, 2014) and a satellite-derived SST field compared to another  
1427 satellite-derived SST field or an SST analysis (Dash et al., 2012; Le Borgne et al., 2012b). The  
1428 first two approaches, based on collocated, coincident satellite and in situ data (matchups), aim to  
1429 assess the SST accuracy, while the third approach may reveal defects or artifacts, undetected or  
1430 hardly detected with matchups.

1431 The assessment of satellite-derived SST accuracy is usually performed through the analysis of



1432 statistics computed on a set of collocated matchups between satellite-derived retrievals and in  
1433 situ measurements. Statistics are computed globally or regionally and on time intervals ranging  
1434 from daily to multi-annual depending on the data availability and the goal pursued (e.g.  
1435 Marsouin et al., 2015). Mean and standard deviation are broadly used. In more recent years,  
1436 robust statistics (Merchant and Harris, 1999) have been implemented more systematically  
1437 because they provide an estimate of the accuracy that is less sensitive to outliers (cloud  
1438 contamination or erroneous in situ value, for instance) and is therefore more representative of the  
1439 accuracy of the retrieval algorithm (Figure 14).

1440 *Figure 14. Maps of the differences between Metop-B AVHRR and drifting buoys temperatures at night for*  
1441 *October 2018. Top left: Mean differences (mean = -0.16 K, standard deviation = 0.53 K); top right:*  
1442 *Median differences (median = -0.05 K, robust standard deviation = 0.39 K); bottom: number of matchups*

1443 *in 5° latitude x longitude bins – bins with < 5 matchups are excluded from the analysis. There are 14560*  
1444 *cases. (Data produced by the OSI SAF; quality index data from 3 to 5 have been used.)*

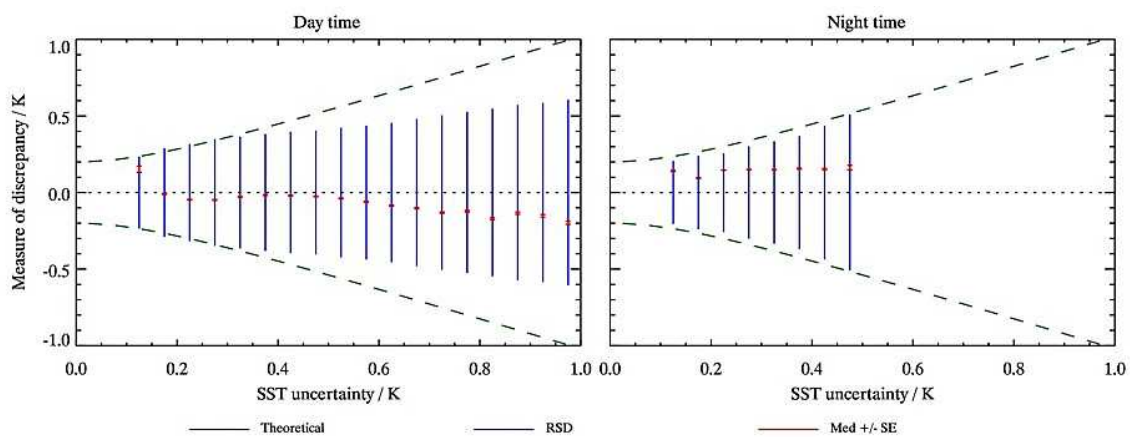
1445 Statistics are often computed using daytime and night-time data separately because the cloud-  
1446 screening and atmospheric correction algorithms usually differ and also because daytime  
1447 comparisons to in situ measurements may be complicated by potential diurnal warming of the  
1448 surface of the ocean (Section 3.2), of which the geographical extent and depth are very difficult  
1449 to predict accurately. Also, the spatial resolution of the satellite-derived SST (pixel size) and the  
1450 depth of the in situ measurement may significantly impact the accuracy assessment. This is  
1451 particularly true in the presence of horizontal thermal fronts and other regions of high spatial  
1452 variability, such as close to the coast or in the vicinity of sea ice.

1453 The constraining time and space intervals applied to matchups should be as small as possible.  
1454 These intervals are determined by the geographical zone, the coverage by in situ data, satellite  
1455 SST temporal and spatial resolution and the need to obtain enough matchups. The time interval is  
1456 mostly 2 or 3 hours, with values varying from 30 minutes in AVHRR Pathfinder, MODIS and  
1457 VIIRS matchups (Kilpatrick et al., 2001; Kilpatrick et al., 2015) based on ship measurements of  
1458 temperature variability (Minnett, 1991), to 4 hours (Walton et al., 1998). The spatial intervals  
1459 vary from the satellite radiometer resolution (typically 1 km at subsatellite, to 2 x 5 km<sup>2</sup> at the  
1460 swath edges) to 25 km (Walton et al., 1998). Research is continuing to define an optimal set of  
1461 space and time intervals. Sub-pixel variability within 1-km MODIS SSTs was estimated to have  
1462 a mean value of order 0.1 K by Castro et al. (2017). The spatial variability within a satellite SST  
1463 pixel was further examined by Castro et al. (2018).

1464 While it is convenient to state the accuracy of SSTs derived from a particular satellite radiometer  
1465 and associated algorithms in terms of a mean error, often referred to as a bias, or a median error

1466 and a standard deviation (or robust standard deviation), there are multiple factors that contribute  
 1467 to inaccuracies in the satellite-derived SSTs. Some are reasonably well defined, such as the  
 1468 atmospheric path length that increases in a simple fashion across the swath leading to less  
 1469 accurate retrievals as the satellite zenith angle increases (Kilpatrick et al., 2015), while others  
 1470 less so, such as anomalous atmospheres (Minnett, 1986; Szczodrak et al., 2014). Thus, the error  
 1471 for the retrieval for each pixel should be constructed on a statistical expectation based on the  
 1472 conditions at the time of the satellite measurements. This is formulated in the GHRSSST Sensor  
 1473 Specific Error Statistics (SSESs; Donlon et al., 2007).

1474 Recently a new type of validation specifically aimed at assessing Climate Data Records has  
 1475 emerged, where both the SST and its uncertainty are validated (Figure 15). For this the  
 1476 uncertainty in the SST is not estimated from the comparison to the in situ data but is instead  
 1477 estimated from a theoretical basis through an uncertainty model (e.g., Bulgin et al., 2016). Using  
 1478 the approach defined in Corlett et al. (2014), the distribution of satellite-in situ SST differences  
 1479 offers a way to assess the magnitude of the uncertainty derived from the theoretical model (Lean  
 1480 and Saunders, 2013; Bulgin et al., 2016; Nielsen-Englyst et al., 2018).



1481

1482 *Figure 15. Example of validation of an uncertainty model for ESA SST\_CCI VI.1 NOAA-18 AVHRR SST*  
1483 *products for (left) day time and (right) nighttime. Match-ups to drifting buoys are binned in terms of the*  
1484 *product uncertainty; vertical blue lines indicate the measured dispersion for each uncertainty level and*  
1485 *red dots indicate the standard error for each uncertainty level and also provide an indication of the*  
1486 *number of match-ups. The dashed green lines indicated the theoretical dispersion of uncertainties*  
1487 *(assuming an average drifting buoy measurement uncertainty of 0.2 K) if the product uncertainty*  
1488 *estimates (and uncertainty models) are accurate. The agreement at night time is very good but the day*  
1489 *time results show the product uncertainties were overestimated. (Corlett, G., 2018.*  
1490 *Uncertainty\_validation\_example.jpg. [https://doi.org/10.6084/m9.figshare.7286168.v2.](https://doi.org/10.6084/m9.figshare.7286168.v2))*

1491 This new approach to SST retrieval, uncertainty estimation and validation is resilient to the  
1492 significant variations in both type and coverage of in situ SST across the years. It also offers a  
1493 way to check the stability in time of the uncertainty of the retrieved SST, which is of prime  
1494 importance for climate studies. The GHRSSST Climate Data Assessment Framework (CDAF;  
1495 Merchant et al., 2014) gives guidelines on how to assess the stability and also on the criteria of  
1496 selection of in situ data. The CDAF was developed from the methods given in Merchant et al.  
1497 (2012) using the GTMBA; the method has recently been applied to drifter and Argo match-ups  
1498 in addition to the GTMBA (Berry et al., 2018).

1499 SST data producers usually assess their products in near real time or in a slightly delayed mode  
1500 and often share results of their assessment with users through websites. More comprehensive  
1501 online tools, such as the Summary Quality Monitor (SQUAM; Dash et al., 2010;  
1502 <https://www.star.nesdis.noaa.gov/sod/sst/squam/>) and the Monitoring & Evaluation of Thematic  
1503 Information from Space (METIS; <http://metis.eumetsat.int/>) enable interactive comparisons  
1504 between various SST products (in situ, satellite and analysis). New open source software

1505 developments such as Felyx (Taberner et al., 2013) offer community tools for diagnostics and  
1506 match-up generation.

## 1507 **7 Data Processing Progression: L2 – L3 – L4**

1508 After the SST values are retrieved from the satellite measurements, they are usually presented in  
1509 three different data levels, called Level 2 (L2), Level 3 (L3), and Level 4 (L4) analyses  
1510 (Parkinson et al., 2006). These levels are the most common forms in which the satellite-based  
1511 SST data are archived and delivered to their “consumers”, from fishermen needing the most  
1512 recent SST imagery to scientists studying long-term temperature trends as well as to the  
1513 computers downloading the daily inputs for weather forecasting models. The three analysis  
1514 formats differ in the way that the SST samples are averaged, interpolated, and combined with  
1515 other SST data. The NASA definitions of the different data levels are summarized in Table 2,  
1516 although others exist varying in details and often refined for the characteristics of particular  
1517 sensors. The extent of averaging, interpolation, and combination increases from L2 to L3 to L4.  
1518 The L3 and L4 data sets are "gridded", meaning that the SST values are presented on a grid of  
1519 prescribed geolocations (latitude and longitude coordinates, usually at a regular interval) to  
1520 facilitate data use (such as visual displays). On the other hand, in general, the L2 data sets are not  
1521 gridded, maintaining the original geolocation of each SST retrieval. An exception is the re-  
1522 gridding of SST pixels derived from instruments on several geostationary satellites, for example  
1523 the ABI fixed-grid SST fields (Harris Corporation, 2018). L2 fields are the most authentic  
1524 representation of the satellite SST retrievals. Among the ocean surface parameters monitored  
1525 from satellites, SST is unique in the large number of concurrent observations (both in spatial  
1526 coverage and number of sensors and platforms), and the L3 and L4 analyses of SST are the



1527 device with which these heterogeneous data are coalesced. The higher-level analyses, in  
 1528 particular, could attempt to achieve more complete spatial coverage through multi-modality (IR,  
 1529 microwave, in situ) and higher accuracy through averaging of multiple coincident samples.  
 1530 Different versions of Level 3 fields are given in Table 3. The typical L3 and L4 data sets are also  
 1531 significantly more compact than their L2 counterparts in terms of data volume (i.e., total file  
 1532 size).

1533 The L2 form is the standard format for the individual sensor data set, comprising the retrieved  
 1534 SST value, geolocation, and sample time for each SST sample. Most L2P data sets contain a  
 1535 wealth of additional information for each sample, including an estimate for uncertainty in the  
 1536 retrieval (typically, a standard deviation), and an array of quality flags that, for example, reflect  
 1537 the atmospheric conditions like cloud cover affecting the retrieval procedure, and the

Table 2, NASA Definitions of Data Levels

|          |  |
|----------|--|
| Level 0  | Reconstructed, unprocessed instrument/payload data at full resolution; any and all communications artifacts, e.g., synchronization frames, communications headers, duplicate data removed.   |
| Level 1A | Reconstructed, unprocessed instrument data at full resolution, time- referenced, and annotated with ancillary information, including radiometric and geometric calibration coefficients and georeferencing parameters, e.g., satellite ephemeris, computed and appended but not applied to the Level 0 data. |
| Level 1B | Level 1A data that have been processed to sensor units (not all instruments have Level 1B data products).  |

Table 3, GHRSSST Refinement of Definitions of Data levels

---

|         |  |
|---------|--|
| Level 2 | Derived geophysical variables at the same resolution and location as the Level 1 source data.                  |
| Level 3 | Variables mapped on uniform space-time grids, usually with some completeness and consistency.                  |
| Level 4 | Model output or results from analyses of lower level data, e.g., variables derived from multiple measurements. |

After Parkinson et al., 2006

See also <https://science.nasa.gov/earth-science/earth-science-data/data-processing-levels-for-eosdis-data-products>.

|                              |  |
|------------------------------|--|
| Level 2P (L2P)               | As L2 with uncertainty information as Sensor Specific Error Statistics derived from coincident satellite and reference measurements taken at the surface. Includes auxiliary fields for each pixel to help interpreting the SST data – sometimes refers to as Dynamic Flags. |
| Level-3 Uncollated (L3U)     | L2 data granules remapped to a space grid without combining any observations from overlapping orbits.  |
| Level-3 Collated (L3C)       | SST measurements combined from a single instrument into a space-time grid. Multiple passes/scenes of data can be combined. Adjustments may be made to input SST data.  |
| Level-3 Super-collated (L3S) | SST measurements combined from multiple instruments into a space-time grid. Multiple passes/scenes of data are combined. Adjustments may be made to input SST data.  |

After <https://www.ghrsst.org/ghrsst-data-services/products/>

1538 atmospheric parameter values used in the retrieval and quality control procedures. An estimate of  
1539 the difference between the derived SST and the foundation temperature is also typically given  
1540 with every sample to facilitate oceanographic application of SST. Unlike most in situ SST data,  
1541 the satellite retrieval should not be considered to be a point measurement of ocean surface  
1542 temperature. The satellite measurement is already an average over the sensor “footprint” which is  
1543 a surface area several km<sup>2</sup> in the IR and many hundred km<sup>2</sup> in the microwave. The geocenter

1544 reported in an L2 data set is hence an estimate of the center of the footprint. Moreover, sensor-  
1545 level averaging is also applied mostly for reduction of instrumental noise. For example, the data  
1546 from AVHRR, with a native spatial resolution of  $\sim 1 \text{ km}^2$ , are acquired in three formats: High  
1547 Resolution Picture Transmission (HRPT), Local Area Coverage (LAC), and Global Area  
1548 Coverage (GAC). The HRPT data are full-resolution data transmitted to a ground station as they  
1549 are collected. The LAC data are also full-resolution data, but the acquisition is recorded by an  
1550 on-board tape recorder for subsequent transmission during a ground station overpass. The GAC  
1551 data are derived from an on-board sample averaging, where four out of every five samples along  
1552 the scan line are used to compute an average value, and the data from only every third scan line  
1553 are processed, yielding an approximate 4 km resolution at nadir. Further binning and averaging  
1554 of these pixels by some agencies (e.g. the US Naval Oceanographic Office) result in the final  
1555 GAC data resolution of these products of approximately 9 km.

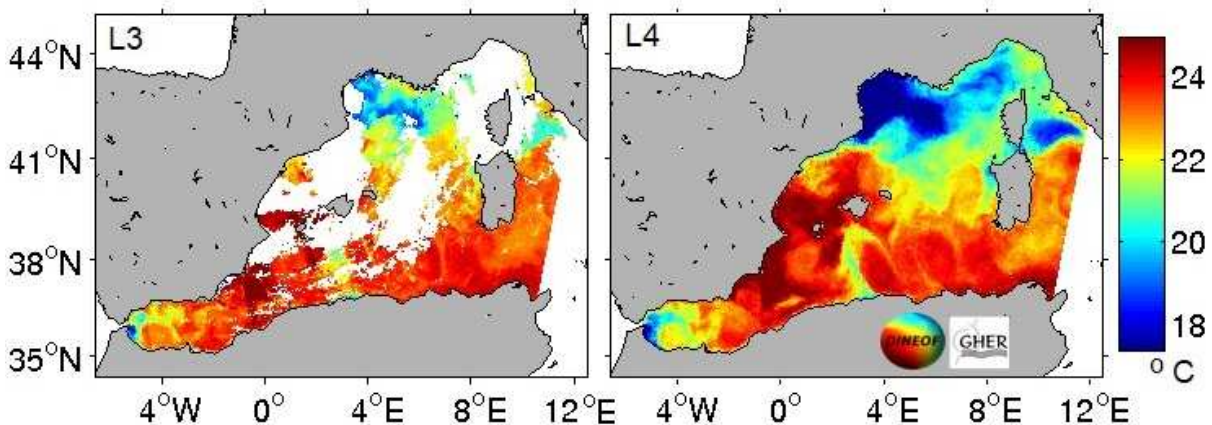
1556 Unlike the general L2 form, both the L3 and L4 analyses are gridded and are so designed to  
1557 provide measurement-based SST values at a regular interval in space and time. Many L3 and L4  
1558 data sets today are given at a daily frequency, typically at noon UTC. A popular spatial interval  
1559 is  $1/4^\circ$  in latitude and longitude, although finer grid spacings are also in use today while coarser  
1560 grids can be found in long-term data sets that extend coverage back into the pre-satellite era.  
1561 Typical contents of L3 and L4 data sets include the latitude and longitude coordinates of the grid,  
1562 interpolated SST values over the grid-points, and an accompanying estimate of uncertainty for  
1563 the SST values. Almost all of the L3 and most L4 SST analyses are derived from L2 data sets,  
1564 with some L4 analyses ingesting L3 data as their inputs. The L2 samples are heavily quality  
1565 controlled using the accompanying quality flags and other auxiliary data, typically much less  
1566 than half of the available samples being selected. The traditional method for gridding is to sort

1567 the selected L2 samples based on their geolocation and time into space-time bins defined by the  
1568 given spatial grid and time interval. The SST value of a bin is then computed as a weighted  
1569 average of the values of all samples in the bin (with the weights typically defined by the inverse  
1570 of the uncertainty variances). Gridding methods more sophisticated than this "bin-average"  
1571 method are also in use today, as described below.

1572 The main difference between the L3 and L4 forms is the data void: some L3 grid locations can  
1573 be absent of data (marked as voids), while all L4 grid locations are filled with data. The data void  
1574 in L3 data sets is typically inherited from the input L2 data. The grid bins without L2 samples  
1575 simply become a void in L3. In satellite-based SST, the most significant data void in terms of the  
1576 area affected is the cloud masking of IR SSTs. An L3 analysis can be derived from a single L2  
1577 data set or a combination of several data sets (Table 3). An example of the latter is the AVHRR  
1578 Pathfinder SST data set which combines the AVHRR GAC data from NOAA-7, 9, 11, 14, 16,  
1579 17, and 18 satellites in order to produce a long-term data set with cross-satellite consistency  
1580 (Kilpatrick et al., 2001; Casey et al., 2010).

1581 Most of the L4 SST analyses are a combination of multiple lower level SST data sets, which are  
1582 often used in a complementary manner. In particular, large and persistent IR data voids can be  
1583 filled with data from microwave sensors which are less prone to cloud and water vapor  
1584 contamination than IR sensors which nevertheless tend to provide higher horizontal resolutions.  
1585 Data voids typically remain after binning of the combined data sets. There are two common ways  
1586 to fill such voids: spatial interpolation and temporal extension. In the latter, the temporal extent  
1587 of each bin is increased to more than a day (for a daily analysis), resulting in temporally  
1588 overlapping bins that could collect from more samples to fill the bin. The assumption behind this  
1589 technique is that the SST does not vary much during the binning duration, and for a 1/4-degree

1590 grid such an assumption is practically acceptable for a temporal bin length of a week or so  
 1591 (Reynolds and Smith, 1994). A common method for spatial interpolation, on the other hand, is  
 1592 the Bayesian statistical estimation based on a given prior distribution for the global SST field  
 1593 derived from some climatological mean field and/or empirical correlations over the ocean  
 1594 surface (Reynolds and Smith, 1994; Thiébaux et al., 2003; Donlon et al., 2012b). Bin-averaging  
 1595 mentioned previously is performed as part of this spatial interpolation procedure. Approaches  
 1596 based on principal component analysis or empirical orthogonal functions (Figure 16) can be also  
 1597 *Figure 16. An example of L3 to L4 SST interpolation using DINEOF (Data Interpolating Empirical*  
 1598 *Orthogonal Functions); (left): original VIIRS SST<sub>skin</sub> data on 8 October 2018 and (right): DINEOF L4*  
 1599 *SST<sub>skin</sub> reconstruction.*



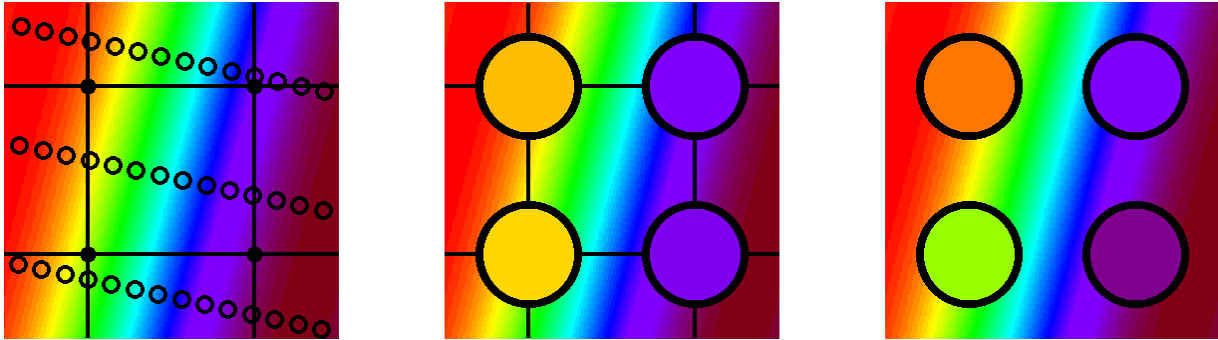
1600 used to obtain a spatio-temporal interpolation of the data (e.g. Kaplan et al., 1997; Alvera-  
 1601 Azcárate et al., 2005; Alvera-Azcárate et al., 2009). In order to combine SST retrievals and  
 1602 measurements from multiple types of sensors (IR, microwave, in-situ) in a coherent fashion,  
 1603 inter-sensor bias fields are often computed empirically in advance to reduce the persistent  
 1604 discrepancy among certain data sets (Donlon et al., 2012b).  
 1605 Currently, at least ten near real-time L4 analysis data sets of the daily global SST are in existence  
 1606 (Dash et al., 2010) reflecting their demand in operations such as weather forecasting. The

1607 ensemble variance in the analyzed SST values among the existing L4 data sets has turned out to  
1608 be a better predictor for the difference between the in-situ SST observations and analyzed SST  
1609 represented by the ensemble median value (Martin et al., 2012) than the formal uncertainty  
1610 estimated for many of the individual analyses. The ensemble median itself has also shown  
1611 consistently to be one of the most accurate SST analyses (at 1/4-degree resolution) in terms of  
1612 comparison to the in situ observations (Dash et al., 2012; Fiedler et al., 2019), and comparisons  
1613 of individual L4 fields with the median to which they contribute reveal the spatial and temporal  
1614 characteristics of the deviations from the median (ibid). These results indicate great practical  
1615 potential for L4 ensemble statistics, and that scientific investigations into their accuracy and  
1616 mechanism behind it are appropriate. At present, satellite remotely sensed SST data sets are  
1617 uniquely positioned to allow such statistical study due to the existence of multiple independent  
1618 analyses.

1619 There are other topics of investigation to improve SST analyses. One is the common practice of  
1620 ignoring the correlations among the L2 samples during interpolation, a practice which tends to  
1621 yield inadequate estimation of analysis uncertainty that reflects mostly the area density of the  
1622 samples (Kaplan et al., 2003). Treating neighboring L2 samples as independent observations  
1623 during Bayesian interpolation can also lead to numerical conditioning issues (due to discrepancy  
1624 in bin weights between densely observed areas of the ocean surface and those without data)  
1625 leading to visible artifacts in the analyzed SST fields, which turn out to be preventable simply by  
1626 using a constant positive correlation value among all samples in every bin (Chin et al., 2014).  
1627 This implies potential for improvements in the Bayesian interpolation procedure used for L4  
1628 (and L3) analyses. In particular, the prior distribution may need to be adaptable to the density of  
1629 the L2 samples to be ingested. Another common practice to be improved may be the bin-average

1630 method itself. In standard bin-averaging, every L2 sample in a bin assumes the geolocation of the  
1631 bin, effectively being “moved” to the center of the bin and truncating the geolocation values  
1632 associated with the L2 sample. Truncation of sub-grid geolocation can smear ocean features such  
1633 as SST fronts in an L4 analysis (Figure 17), but smearing can be mitigated significantly by the  
1634 use of non-constant (e.g., cubic) polynomials as the kernel function for interpolation (Chin et al.,  
1635 2014). The bin-averaging procedure is equivalent to using a piecewise constant function as the  
1636 kernel, which is the only "polynomial" that cannot encode sub-grid geolocation information.  
1637 Finally, the daily frequency commonly used is likely not frequent enough to capture the sub-10  
1638 km scale SST features observable in the 1-km resolution L2 data sets. A sub-daily time window  
1639 is found more appropriate to form an analysis at such a high horizontal resolution (Chin et al.,  
1640 2017). A sub-daily analysis would be affected more directly by the diurnal SST variability than  
1641 the current daily analyses, which tend to simply avoid the samples from areas of strong daytime  
1642 warming (Donlon et al., 2012b; Chin et al., 2017). In summary, the technical issues noted here  
1643 are especially relevant to analysis of high-resolution SST data and represent future topics of SST  
1644 analysis: lopsided data density, fast-evolving sub-grid features, and diurnal variability. Handling  
1645 of inter-sensor biases and inter-sample correlations, which have already been addressed as  
1646 mentioned above, can also be considered as among the open issues in general SST analyses.



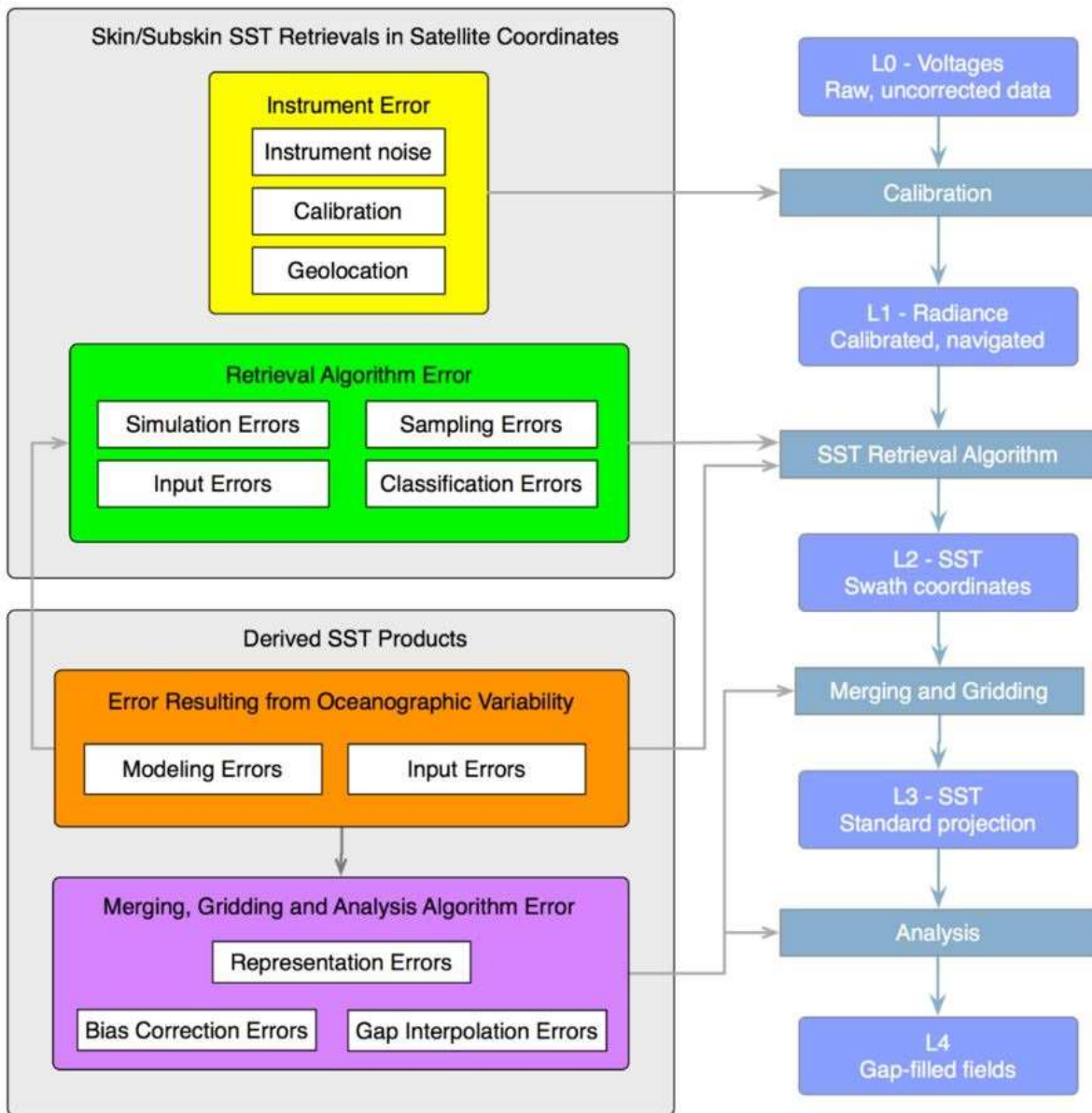


1647 *Figure 17. Demonstration of a “gridless” interpolation and importance of avoiding truncation of*  
 1648 *geolocation data. Left: observations (open circles) are typically averaged at a nearest grid-point (closed*  
 1649 *circles) effectively truncating the subgrid portion of the location parameters. Center: such bin-averaging*  
 1650 *(colors inside big circles) can distort spatial information like the orientation of the front (background),*  
 1651 *due to the nearest-neighbor approximation of geolocation data. Right: a gridless interpolation method*  
 1652 *tends to ingest the observations at their original locations, reducing the distortion in front orientation,*  
 1653 *even at a low resolution shown.*

1654 Finally, advances in computer power have ushered in a new approach to analysis of SST data,  
 1655 namely *data assimilation*. As noted above, majority of the L4 SST data products available today  
 1656 are daily analyses reporting  $T_{\text{fnd}}$  (Figure 2). Applications in weather forecasting requires instead  
 1657  $\text{SST}_{\text{skin}}$  at the interface of ocean and atmosphere sampled multiple times a day (e.g., every 3 or 6  
 1658 hours). Current operational practices often involve separate procedures interpolating the existing  
 1659 daily L4 SST data in time and estimating the skin temperature from the foundation temperature  
 1660 based on models of diurnal solar heating of ocean surface and associated measurements of  
 1661 insolation parameters and ocean surface winds. Recent increases in computational speed and  
 1662 storage, however, have enabled integration of these procedures into the forecast model itself,  
 1663 allowing direct assimilation of the L2 SST samples instead of their analyzed versions. An SST  
 1664 analysis would also be made a by-product of such a data-assimilative integrated forecast system,  
 1665 and such L4 analyses are packaged as emerging SST data products (e.g. Miyazawa et al., 2017;

1666 Li et al., 2019). Some of these systems have also integrated the traditional SST retrieval  
1667 procedures (e.g., in a Radiative Transfer Model), so that the brightness temperature  
1668 measurements from satellite sensors instead of the L2 retrievals could directly be ingested into a  
1669 model of ocean surface to provide a L4 SST analysis (Li et al., 2019). An advantage of using  
1670 ocean circulation dynamics to interpolate L2 data into L4 analyses via data assimilation is its  
1671 potential to estimate the finer scale structures in a dynamically consistent way. In contrast,  
1672 traditional interpolation schemes, such as Bayesian optimal interpolation, tends to smooth out the  
1673 finer scale features. An integrated dynamical model, however, must also manage the variety of  
1674 types and scales of data they ingest in order to balance the consistency and representativeness of  
1675 their dynamical parameters. For example, while ocean circulation models are still refining their  
1676 dynamics to resolve the location where the Gulf Stream separate from the American coastline  
1677 into the North Atlantic Ocean (Ezer, 2016; Chassignet and Xu, 2017), the existing traditional  
1678 SST analyses can usually pinpoint the separation point in general, and it remains to be seen if  
1679 assimilation of SST (or associated brightness temperature) data would have enough numerical  
1680 and dynamical influence to sufficiently correct the modeled three-dimensional circulation pattern,  
1681 i.e., the course of the modeled Gulf Stream. As such issues are resolved, we should see more  
1682 and more components of traditional SST analysis as well as retrieval procedures incorporated  
1683 into dynamical forecast/nowcast systems, which could in turn become important sources of SST  
1684 analysis data products.

1685 The progression of satellite data through the processing levels makes the SST fields more  
1686 accessible for many users but comes at a cost as each step leads to the accumulation of errors and  
1687 uncertainties from many sources, as illustrated in Figure 18 (Wu et al., 2017). L2 is where  
1688 uncertainties in SST retrievals are derived by comparison with independent measurements in



1689 *Figure 18. Error budget framework with sources of errors and uncertainties (left column) and how they*  
 1690 *accumulate in the progression to L4 gap-filled SST fields (right column). From Wu et al. (2017),*  
 1691 *reproduced through CC BY 4.0.*

1692 cloud-free conditions, but L4 fields are used to initialize climate models and in other climate  
 1693 studies. The accuracy assessed for SST fields from the same satellite radiometer, but at different  
 1694 Levels, is likely to be different; the uncertainties may be reduced at higher Levels by averaging

1695 multiple measurements in a grid cell, but may be increased due to additional processing steps and  
1696 assumptions, and where L2 data are missing. Thus, the L2 SSESs may not be appropriate for L4  
1697 fields (Liu and Minnett, 2016; Liu et al., 2017).

## 1698 **8 Examples of regional studies**

1699 Clearly a great strength of satellite remote sensing of SST is the global sampling at high temporal  
1700 and spatial resolution and thus the contributions of satellite-derived SSTs to studies of processes  
1701 and particular regions have been very significant. Here we focus on two regions each presenting  
1702 particular challenges but clearly benefiting from satellite data: the Mediterranean Sea and the  
1703 Arctic Ocean. The Mediterranean Sea is a nearly landlocked sea with the atmosphere above it  
1704 frequently influenced by continental air masses, including very dry, aerosol laden air from north  
1705 Africa, which pose particular challenges to the derivation of SST in the IR. Nevertheless, the  
1706 Mediterranean Sea is an important component of the global thermohaline circulation and given  
1707 that it is less cloudy than many other regions, it continues to be a focus of research that  
1708 incorporates analysis of satellite-derived SSTs. The Arctic Ocean, on the other hand, is a cloudy  
1709 region which thus presents problems for the accurate retrievals of IR SSTs, as does the fact that  
1710 the Arctic is an extreme case in the distributions of global atmospheric properties. Furthermore,  
1711 because of difficulties in access and the harshness of the conditions for both researchers and  
1712 instruments, the area is poorly sampled by in situ sensors placing a greater reliance on satellite  
1713 remote sensing. The key role of the Arctic in the climate system also warrants a significant  
1714 research effort.

1715

1716

## 1717 **8.1 Mediterranean Sea**

1718 The Mediterranean Sea is the most famous among the “mediterranean seas”. It is a mid-latitude  
1719 semi-enclosed marginal sea that exchanges water and heat with the Atlantic Ocean through the  
1720 shallow Strait of Gibraltar. The Mediterranean Sea is a concentration basin with an inflow of  
1721 fresher (S ~36.2) and warmer (T ~15.0°C) Atlantic water in the upper layer and outflow of saltier  
1722 (S ~38.4) and colder (T ~13.5°C) Mediterranean water in the lower layer through the Strait of  
1723 Gibraltar. On an annual mean basis, the Mediterranean Sea loses buoyancy to the atmosphere  
1724 through both an excess of evaporation over precipitation and a negative heat budget (Lacombe et  
1725 al., 1981). The combination of all these air-sea exchanges as well as deep and intermediate water  
1726 formation contributes to sustaining a basin-wide thermohaline circulation cell that can be viewed  
1727 as a reduced version of the large-scale oceanic conveyor (Broecker, 1991). In this sense, as  
1728 suggested by Robinson and Golnaraghi (1993), the Mediterranean Sea can be considered as a  
1729 “small-scale ocean” where “many processes which are fundamental to the general circulation of  
1730 the world ocean also occur within the Mediterranean, either identically or analogously”. The  
1731 direct consequence is that the Mediterranean Sea can be considered as a natural laboratory where  
1732 field and numerical experiments can be conducted in more favorable dimensional and  
1733 environmental conditions than for the global ocean. Satellite oceanography researchers also  
1734 benefited from these favorable conditions; in particular sea surface temperature remote sensing  
1735 has produced the longest record of valuable scientific results and practical applications.

1736 The first satellite Mediterranean Sea application, recoverable from the web, was published in  
1737 *Oceanologica Acta* in 1979 (Albuissou et al., 1979) and reported a first comparison between  
1738 NOAA-4 VHRR and Aries airborne radiometer in the Gulf of Lions on August 3 and 6, 1976.  
1739 They concluded that thermographic maps derived from VHRR data could enable users to

1740 determine the relative SST and study horizontal thermal gradients and their spatial distribution.  
1741 Determining spatial thermal gradients and then detecting thermal fronts was the first most  
1742 important result of the IR satellite remote sensing of the Mediterranean Sea during the 1980s,  
1743 when a whole generation of Mediterranean oceanographers was fascinated by the possibility to  
1744 observe, week after week, the evolution of the Mediterranean thermal fronts in the SATMER  
1745 bulletin (SATMER, Bulletin Mensuel de Renseignements Oceanographiques Obtenus a Partir  
1746 de Mesures Satellitaires Meteorologiques sur la Mediterranee et l'Atlantique Nord-Est,  
1747 Direction de la Meteorologie Nationale, Paris, France, 1984-1987).

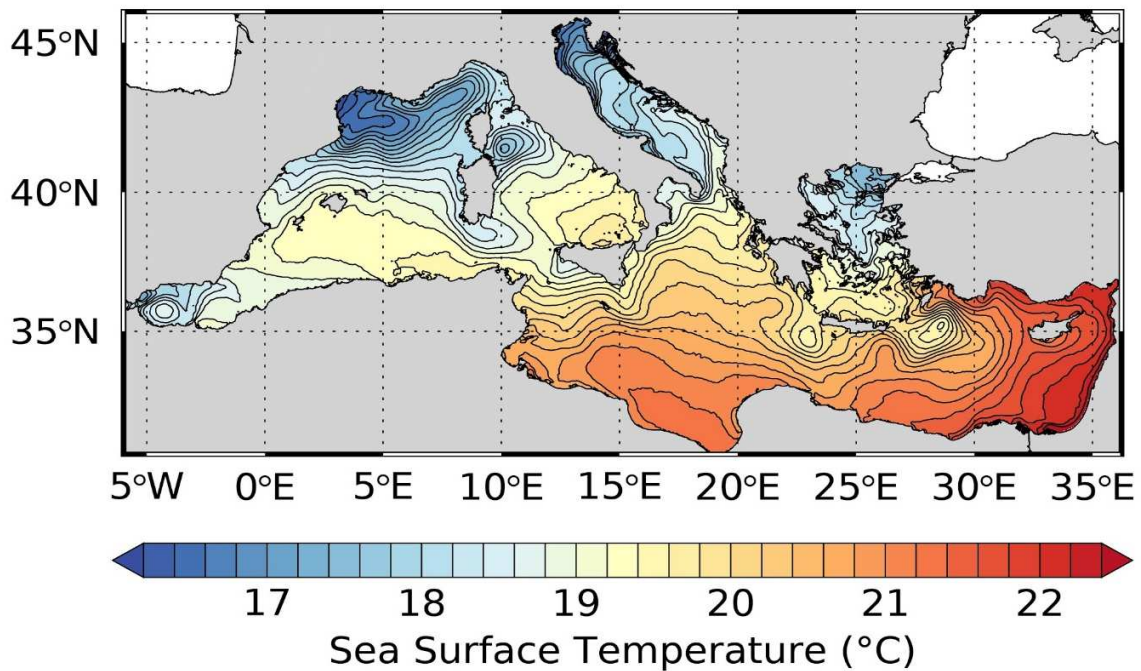
1748 Mollo-Christensen et al. (1981) reported one of the first applications of IR imagery of fronts, in  
1749 their case off Cape Hatteras, to infer upper ocean dynamics. In the following year Crépon et al.  
1750 (1982) demonstrated that a time series of thermal IR images obtained by the VHRR on NOAA-5  
1751 to detect thermal fronts in the Ligurian Sea can be used to determine the mean wavelength and  
1752 phase velocity of the low-frequency waves associated with the evolution of the fronts. These  
1753 waves were interpreted as large-amplitude baroclinic waves, finding a fairly good agreement  
1754 with simulations using a two-layer ocean model. Additional studies of the Ligurian Sea based on  
1755 IR images from the VHRR on NOAA-5 were reported by Millot and Wald (1980) and Wald and  
1756 Nihous (1980).

1757 A few years later, TIROS-N AVHRR thermal images from November 1979, were used to detect  
1758 thermal fronts and measure wavelengths of the meanders of the Ligurian Current, relating them  
1759 to the occurrence of baroclinic instabilities and small scale eddies detected during a field  
1760 experiment (see Fig. 6 of Marullo et al. (1985)).

1761 One of the first attempts to derive absolute values of SST from AVHRR data, considering the  
1762 particular environmental conditions of the Mediterranean Sea, was proposed by Dalu et al.

1763 (1985). Their algorithm was based on radiative transfer model simulations and considered the  
1764 specific Mediterranean conditions for water vapor absorption in the thermal IR. Validation was  
1765 performed for a limited number of samples acquired in a field campaign in the Adriatic Sea.  
1766 Since that time things have improved, moving from the laborious and expensive analysis of a  
1767 relatively small set of images ingested from magnetic tapes to the time series analysis of years of  
1768 daily or even hourly acquisitions downloaded from web-based servers. This was possible thanks  
1769 to the initiatives of national and international institutions and agencies that undertook to archive,  
1770 preserve and freely distribute petabytes of high level processed SST maps worldwide (Section  
1771 14). In the specific case of the Mediterranean Sea a crucial role has been played by European  
1772 operational oceanography efforts which, in the 1990's, selected the Mediterranean Sea to  
1773 develop a first prototype of observation and forecasting system. In this framework, MFSP  
1774 (Mediterranean Forecasting System Pilot Project) the MFSTEP (Mediterranean Forecasting  
1775 System Toward Environmental Predictions) project and the first SST L4 operational products  
1776 specific to the Mediterranean Sea were developed (Buongiorno Nardelli et al., 2003) and  
1777 assimilated in near-real time in the Mediterranean Forecasting System (Pinardi et al., 2003). Of  
1778 course, the Mediterranean Sea had been included in global L4 analyses since the 1990's  
1779 (Reynolds and Marsico, 1993; Reynolds and Smith, 1994). The outcome of this European effort  
1780 is now the CMEMS (Copernicus Marine Environment Monitoring Service) which has made the  
1781 last 36 years of SST L4 data available to a wider community of scientific users. Figure 19 shows  
1782 the mean Mediterranean SST field derived from the average of all the CMEMS reprocessed daily  
1783 SSTs maps from 1982 to 2017.

1784 Before that time several attempts had been made that used a relatively long series of acquisitions  
1785 to increase the knowledge of the description and the understanding of the Mediterranean



1786 *Figure 19. Mean Sea Surface Temperature field in the Mediterranean Sea from 1982 to 2017 derived*  
 1787 *from CMEMS reprocessing.*

1788 circulation following the thermal signatures of eddies and currents. Today, such things can  
 1789 appear trivial but then, for the first time, baroclinic instabilities evolving along the Algerian  
 1790 Current in small-scale eddies traveling northward to meet the Balearic Front, it became apparent  
 1791 that a new era for the exploration of the sea had started.

1792 This kind of approach, either based on time series of several full resolution AVHRR images or  
 1793 on the NASA PO.DAAC (Section 14.1) AVHRR Pathfinder SST Archive (18 km resolution at  
 1794 that time), produced interesting results and new understanding of the Mediterranean circulation  
 1795 as a result of combining previous information based on in situ observations and satellite thermal  
 1796 IR images (e.g. Marullo et al., 1999a; Marullo et al., 1999b; Hamad et al., 2005; Millot and  
 1797 Taupier-Letage, 2005). Such research has definitively proved that the key element that made  
 1798 possible the great progress in the knowledge and understanding of the Mediterranean Sea



1799 dynamics was the jump from the use of a few thermal images, produced by individual  
1800 researchers, like the “icing on the cake” of analyses based on other data or models, to the  
1801 analysis of long time series of maps, centrally and uniformly produced in dedicated facilities.  
1802 This pioneering work has opened the way to the more recent studies that made use of space-  
1803 based IR remote sensing observations for advanced Mediterranean Sea investigations. In fact,  
1804 starting from the beginning of this millennium, a consistent number of publications appeared  
1805 dealing with basin-scale investigations and focusing on time scales ranging from hourly to  
1806 interannual. A first re-analysis of the AVHRR SST maps of the Mediterranean Sea, starting from  
1807 1985, was published in 2007 (Marullo et al., 2007). This analysis also presented a validation of  
1808 the product including the optimal interpolation scheme applied to produce the series of L4 SSTs  
1809 and the evaluation of the stability of biases with respect to in situ data. With the lengthening of  
1810 the series, remote sensing scientists began to glimpse the possibility of addressing the field of  
1811 climatology. Since SST forms the longest, quality controlled and continuous series of satellite-  
1812 derived ocean data, the possibility to estimate linear (at least) trends over large areas of the basin  
1813 was considered a golden opportunity to promote, with modest effort, satellite oceanography  
1814 (Nykjaer, 2009; Shaltout and Omstedt, 2014; Pastor et al., 2018). At the time of writing, one  
1815 more year of L4 Mediterranean SST maps is about to be released by CMEMS (Section 14.3),  
1816 extending the time series started in 1982 to the end of 2018: 37 years of quality controlled  
1817 consistent SST data. This implies that not only significant linear and nonlinear trends (covering  
1818 the positive phase of Atlantic Multidecadal Oscillation, AMO) can be evaluated but also that  
1819 interesting oscillatory modes in the range of periods from quasi-biennial to ENSO can and have  
1820 been detected (Skiriris et al., 2012).

1821 On shorter time scales, investigations to study the SST diurnal cycle have also benefited from  
1822 satellite-derived SSTs. This has been feasible also thanks to the contribution of geostationary  
1823 satellites making it possible to observe the Mediterranean Sea surface with frequencies  
1824 compatible with the resolution of the diurnal cycle (more than 4 times per day as suggested by  
1825 Sykes et al. (2011). Particular attention has been paid to the Mediterranean Sea, as it is one of the  
1826 world ocean regions where extreme diurnal warming events are more frequent (Figure 3;  
1827 Gentemann et al., 2008; Karagali and Høyer, 2014). This particular interest produced a series of  
1828 publications that highlighted the contribution of high frequency satellite observation to  
1829 reconstruct the variability of the diurnal SST cycle in the Mediterranean Sea to understand the  
1830 physical mechanisms that modulate the intensity of diurnal warming events (among several:  
1831 Merchant et al., 2008a; Le Borgne et al., 2012a; Marullo et al., 2014b; Marullo et al., 2016).

## 1832 **8.2 The Arctic Ocean**

1833 A defining feature of the Arctic Seas is the seasonal or perennial presence of a floating sea ice  
1834 pack, formed locally during winter or advected by winds or currents. Where sea ice exists, the  
1835 underlying ocean mixed layer is generally at or very close to the freezing point, except in leads  
1836 and polynyas on calm, sunny days when the ocean may become warm within a surface melt layer  
1837 (Richter-Menge et al., 2001; Vincent et al., 2008b). The lateral extent of Arctic sea ice has  
1838 always been greater in winter than in summer, but in the past few decades dramatic summer  
1839 melt-back (e.g., Cavalieri and Parkinson, 2012) has led to a large increase in the area of  
1840 seasonally ice-free Arctic waters (Steele and Ermold, 2015; Haine and Martin, 2017). Thus,  
1841 until recently, the topic of SST in much of the Arctic Seas was relatively uninteresting: the ocean  
1842 remained at or near the freezing point all year round. This is not the case now, as ocean surface

1843 warming has become evident in many areas of the Arctic (Steele et al., 2008; Eastwood et al.,  
1844 2011).

1845 When the ice retreats, what exactly causes the ocean to warm? In the western Arctic Ocean,  
1846 Steele et al. (2010) analyzed model output to determine that the largest forcing by far was net  
1847 surface heating, largely from solar radiation; areas within ~ 100 km of Alaska were also  
1848 influenced by lateral heat flux convergence, i.e. warm currents moving northward from the North  
1849 Pacific Ocean via Bering Strait. Heat flux from below the mixed layer in summer is essentially  
1850 nil, owing to strong stratification in the estuarine-like Arctic Ocean. The partition is likely  
1851 different in the highly advective eastern Arctic Ocean near the Atlantic Water inflow, which is  
1852 where the bulk of the Arctic Ocean's subsurface heat content enters (e.g., Smedsrud et al., 2013).  
1853 In the Northeast Water Polynya in western Fram Strait, Minnett (1995) found the summertime  
1854 surface heat budget of the open water to be dominated by the radiative terms, as was also the  
1855 case in the North Water Polynya (Hanafin and Minnett, 2001). Given that clouds modulate the  
1856 incoming solar radiation and the net IR flux at the ocean surface, Arctic clouds play a crucial role  
1857 in determining the evolution of the SST (Minnett, 1999; Hanafin and Minnett, 2001).

1858 Warming in the Arctic Seasonal Ice Zone (SIZ) has some unique properties. The western Arctic  
1859 is very strongly stratified by freshwater inputs from rivers, net precipitation less evaporation,  
1860 relatively fresh inflows from the North Pacific Ocean via the Bering Strait, and (seasonally) from  
1861 sea ice melt (Aagaard and Carmack, 1989). The result is mixed layers in the summer SIZ that  
1862 are 20 m thick or shallower (Peralta-Ferriz and Woodgate, 2015). In fact, winds in early-  
1863 midsummer are generally quite weak, so that stratification can extend right to the surface  
1864 (Randelhoff et al., 2017). These conditions lead also to diurnal warming in summer even at high  
1865 latitudes (Eastwood et al., 2011). Later in the summer, surface winds accelerate and mix warm

1866 SSTs downward, even while the net air-sea heat flux is still weakly downward (Steele and  
1867 Dickinson, 2016).

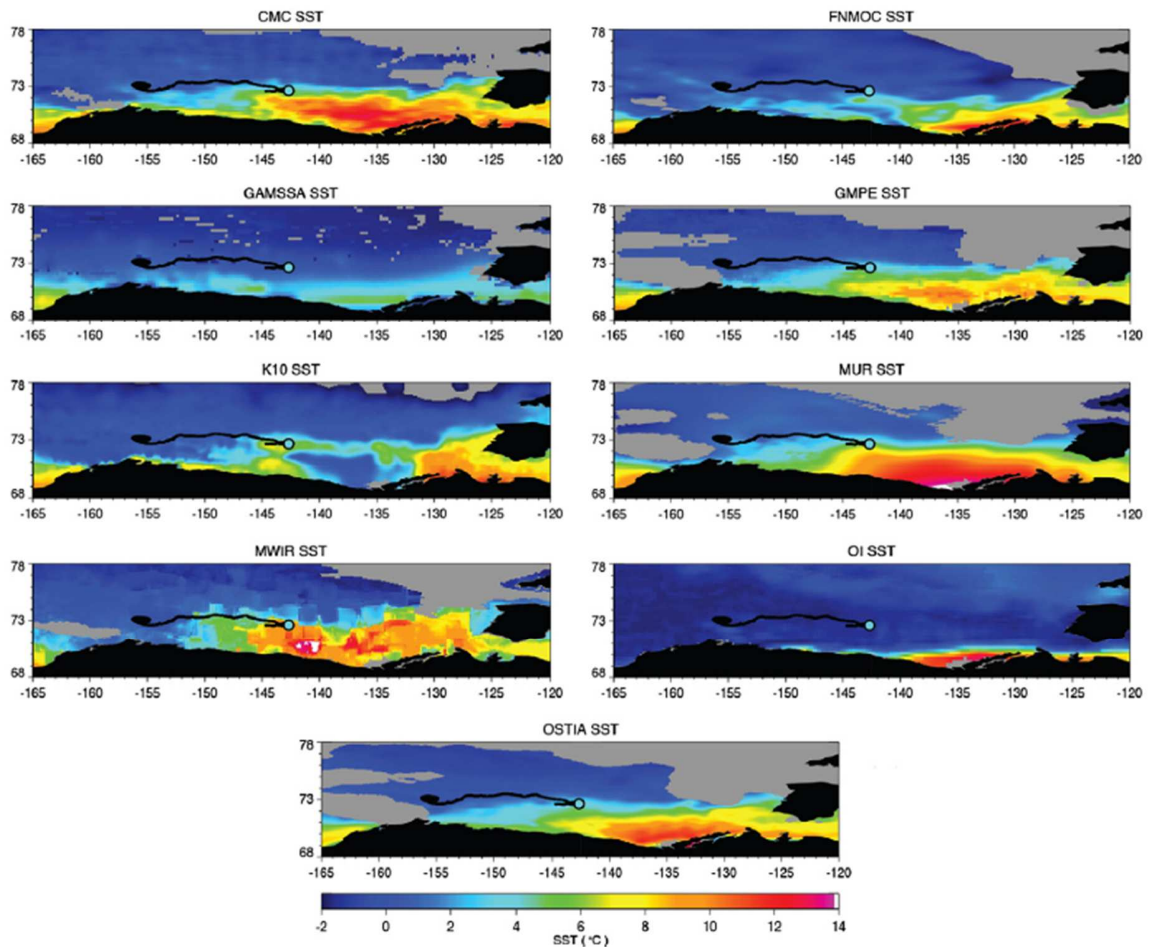
1868 Warming of seasonally ice-free Arctic waters has a number of impacts, e.g., on the marine  
1869 ecosystem (e.g., Feng et al., 2018), on coastal terrestrial ecosystems (Uma et al., 2017), and on  
1870 the atmospheric boundary layer (especially in fall when this heat is fluxed upward; Screen et al.,  
1871 2013). This seasonal ocean surface warming in turn affects both the details of ice retreat (Steele  
1872 and Ermold, 2015) and ice advance (Stroeve et al., 2016; Smith et al., 2018).

1873 In situ measurement of SST and upper ocean conditions in the Seasonal Ice Zone (SIZ) is not  
1874 easy, given the short period in which field work is generally possible (i.e., late summer open  
1875 water for ship-based work, and late winter pre-melt ice cover for aircraft-based work).

1876 Traditional Arctic autonomous drifting buoys have been deployed on thick ice floes to maximize  
1877 survival, which explicitly avoids the SIZ. A unique program focused on the SIZ is the  
1878 University of Washington's UpTempO (Upper Temperature of the polar Oceans) buoy program,  
1879 which deploys surface drifters with a thermistor string in the SIZ

1880 (<http://psc.apl.washington.edu/UpTempO/>). These buoys have been successful in measuring the  
1881 vertical extent of seasonal warming, the presence of diurnal warming, and the process of fall  
1882 cooling that sometimes allows a portion of summer heat to survive through winter under the  
1883 mixed layer. Buoy data from two years in the Beaufort Sea have also been used to evaluate the  
1884 performance of a large suite of global gridded SST products (Figure 20; Castro et al., 2016).

1885 More work is needed on this subject, i.e. in different areas and different seasons. Other  
1886 autonomous SST-measuring platforms are also being used in the SIZ, such as wave- and sea-  
1887 gliders, saildrones, and even profiling floats.



1888

1889 *Figure 20. Comparison of selected L4 SST analyses in the Beaufort Sea on 13 August 2012 (DOY 226).*  
 1890 *The color scale has been fixed to facilitate comparisons between products, and the trajectory of one of the*  
 1891 *drifting buoys (Louis 2012-03) has been plotted over the images with the circle showing the position of*  
 1892 *the buoy for that particular day and the color indicating the corresponding buoy temperature. The gray*  
 1893 *areas indicate that the respective ice mask has been applied, if available. Note that no ice mask is shown*  
 1894 *in the OISST since the ice and water masks were mistakenly inverted during this period and the buoy*  
 1895 *location was inaccurately flagged as ice covered. The anomalously low OISST temperature at the buoy*  
 1896 *location is a result of the improper masking. From Castro et al. (2016), with permission.*

1897 Remote sensing of SST in the Arctic Seas is challenging, owing to the frequent and extensive  
1898 summer cloud cover which hides the surface from IR satellite sensors. A further problem in the  
1899 IR is the varying length of the sunlit part of the day round the year. In sunlit conditions,  
1900 measurements in the mid-infrared window cannot be used because of scattering and reflection of  
1901 sunlight, with the consequence that in summer, there is a limited opportunity for matchups with  
1902 in situ data from the drifting buoys at high latitudes at night to generate coefficients for the  
1903 atmospheric correction algorithms, and for assessing the accuracy of the derived SSTs. These  
1904 issues in the IR enhance the role that microwave SST products should play in this region,  
1905 although their lower resolution is limiting, especially early in the ice retreat season when open  
1906 water areas are small. A positive note is that polar-orbiting satellites take many images per day  
1907 at high Arctic latitudes, a capability that could allow for more detailed examination of diurnal  
1908 warming and other processes, but one that has not been fully exploited to date.

1909 What should global, gridded SST products provide in ice-covered waters? One option is to  
1910 provide a foundation or mixed layer temperature, which (since it is in contact with ice) will be  
1911 the freezing point of seawater. This is the traditional approach, where most products assume a  
1912 value of  $-1.8^{\circ}\text{C}$ , appropriate for salinities of  $\sim 34$ . That is, a satellite sea ice extent mask is used to  
1913 determine where to create “synthetic observations” of SST at this value, which are then blended  
1914 in various ways with the true observed values in the open water to the south. A few products  
1915 recognize the estuarine nature of the Arctic Seas, which results in large spatial variability of sea  
1916 surface salinity. This means that the freezing point varies by up to perhaps 0.5 K over the region.  
1917 There is also temporal variability, owing to recent Arctic Ocean freshening and large changes in  
1918 salinity (Rabe et al., 2011). Furthermore, the algorithms for blending of synthetic freezing SSTs  
1919 and open water observed values across the Marginal Ice Zone (MIZ) likely requires some

1920 updating in most products, as the MIZ has changed dramatically in recent years (Strong and  
1921 Rigor, 2013).

1922 Another option for a global gridded product might be to produce a blend of open water SST and  
1923 ice/snow surface temperature in icy conditions. Some products are in fact available that provide  
1924 this blend, which is most appropriate for, e.g., providing a lower boundary condition for  
1925 atmospheric models. This can be difficult, however, in areas with mixed ice and open water.  
1926 Further, ice/snow surface temperature is much more highly variable (spatially and temporally)  
1927 relative to SST, owing to their lower thermal inertia.

1928 In summary, deriving SST in seasonally ice-free Arctic waters is a new, relevant and exciting  
1929 field, one that will only grow as the ice cover continues to shrink. These waters still suffer from a  
1930 severe lack of in situ data for satellite validation, although new observational strategies are on the  
1931 horizon. Ocean surface warming in the Arctic Seas is both a response to, and an active  
1932 participant in, the large changes in sea ice cover we have seen and will likely continue to see in  
1933 coming years.

## 1934 **9 Examples of Applications**

1935 There are many global and regional applications of satellite-derived SSTs, such as forecasting  
1936 and monitoring El-Niño-Southern Oscillation events (McPhaden, 2012), better understanding of  
1937 atmospheric boundary layer response to SST variability (Perlin et al., 2014), assisting with  
1938 efficient fisheries and monitoring ecosystem changes (Stuart et al., 2011), monitoring thermal  
1939 stress threats to coral reefs (Mumby et al., 2004; Hedley et al., 2016), seeking signals that  
1940 indicate changes in large-scale ocean phenomena (Liu and Minnett, 2015) and a warming climate  
1941 (Casey and Cornillon, 2001; Good et al., 2007), better understanding air-sea fluxes of heat and

1942 moisture (Bentamy et al., 2011) and of CO<sub>2</sub> (Olsen et al., 2004; Wickramaratna et al., 2008;  
1943 Wanninkhof et al., 2013), but here we focus on three applications that have very specific societal  
1944 benefits: weather forecasting, development of severe storms, and sea level rise.

## 1945 **9.1 Numerical Weather Prediction**

1946 Accurate sea surface temperature data is vital for Numerical Weather Prediction (NWP) from a  
1947 few days, to seasonal forecasts covering several weeks, to longer term climate variability. Most  
1948 NWP systems use single (daily) spatially complete L4 SST analysis fields (e.g. OSTIA, Donlon  
1949 et al., 2012b) as a boundary condition for constraining the atmospheric model (Thiébaux et al.,  
1950 2003). Here we begin the discussion of contributions of SST fields to NWP with a focus on the  
1951 use of daily fields, and then present results of the recent development at the US National Centers  
1952 for Environmental Prediction (NCEP) to generate and use global SST fields at 6-hourly intervals.

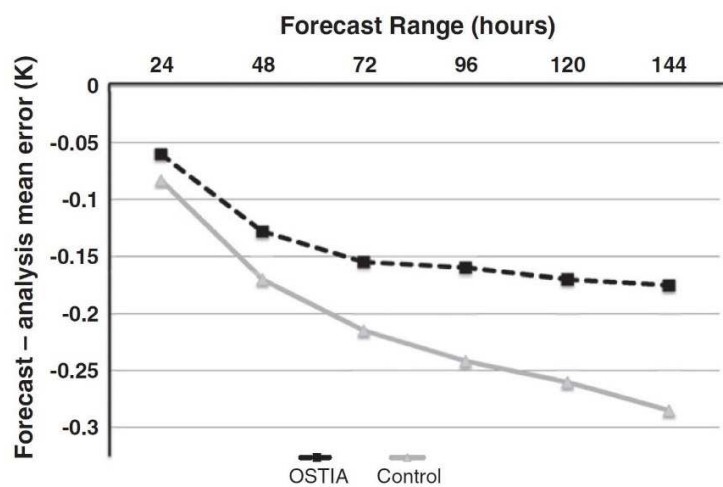
### 1953 **9.1.1 Daily SST fields**

1954 Most L4 SST analyses used for NWP applications are smoothed to avoid shocks in the NWP  
1955 model. Invariably L4 SST fields are of a temperature at an unknown depth – many aim to be a  
1956 foundation temperature – and so near surface temperature gradients not considered in the  
1957 forecast results in larger errors. Consequently, the error characteristics of L4 SST analyses are  
1958 often not well understood and are not represented in subsequent applications. A more detailed  
1959 review of the use of SST analyses in operational systems is given in Beggs (2010). SST patterns  
1960 are dynamic and strong gradients in SST can impact the evolution of many atmospheric  
1961 phenomena through its influence on surface winds (Song et al., 2006; Small et al., 2008; Perlin et  
1962 al., 2014). For example, the benefits of OSTIA were shown in Donlon et al. (2012b), where the  
1963 higher resolution of OSTIA reduced NWP forecast errors compared to a legacy SST product, by



1964 resolving, for example, small scale changes in the Arctic SSTs due to above average sea-ice loss  
 1965 in the summer of 2007 (Figure 21). Seasonal patterns of SST change more slowly but strong  
 1966 signals associated with the El Niño, for example, can impact global weather patterns. Here, SST  
 1967 anomalies – the difference from a climatological mean – in the Niño 3.4 region are more useful  
 1968 in predicting changes (see, for example, Arribas et al., 2011).

1969



1970

1971 *Figure 21. An example of the improvement in the NWP forecasting skill when a more realistic SST field is*  
 1972 *used as the bottom marine boundary. The mean error in temperature at 850 hPa in the Northern*  
 1973 *Hemisphere when using old AVHRR and in situ low resolution SST data as a bottom boundary condition*  
 1974 *(grey line) and high resolution SST data from the OSTIA system (black line). The trial period was from*  
 1975 *1st August 2007 until 31st August 2007. (From Donlon et al. (2012b), with permission).*

1976 A key requirement for NWP application is timeliness. For example, an SST analysis may be up  
 1977 to 48 hours old when used in an NWP system at 00z if the timeliness of the SST analysis is not  
 1978 optimized for the NWP production time. Further, for reanalysis applications the recent satellite  
 1979 based SST analyses need to be aligned with the historical SST record from in situ measurements.

1980 Also, NWP requires global SST data to be stable over time and robust to changes in the satellite  
1981 constellation.

### 1982 **9.1.2 Six-hourly SST fields.**

1983 One SST analysis, referred to as the NSST (Near-Surface Sea Temperature) analysis, has been  
1984 developed within the NCEP Global Forecast System (GFS), an integrated operational NWP  
1985 system, to improve the resolution of diurnal heating and cooling by producing 6-hourly fields. In  
1986 the history of the NCEP GFS since 1980, the thermal lower boundary condition has been  
1987 provided by weekly OI SST (Reynolds, 1988; Reynolds and Marsico, 1993; Reynolds and Smith,  
1988 1994) initially, then daily RTG SST (Thiébaux et al., 2003) since 2015, and then 6-hourly NSST  
1989 since 2017 (Li et al., 2019). Increasing the temporal resolution to capture diurnal variability in  
1990 the SST is intended to improve the satellite radiance measurement assimilation over water  
1991 surfaces.

1992 One of the fundamental issues in SST analysis is the definition of the analysis variable. The  
1993 foundation temperature,  $SST_{\text{fnd}}$  (Figure 2), is widely used in analyses such as OSTIA (Donlon et  
1994 al., 2012b), the Canadian Meteorological Centre (CMC) analysis (Brasnett, 1997; Brasnett,  
1995 2008) and the Multi-Scale Ultra-High Resolution (MUR) fields (Chin et al., 2017). In the NCEP  
1996 NSST, the analysis variable,  $T_f$ , is defined as the sea temperature at the base ( $z = z_w$ ) of the  
1997 diurnal warming layer. Thus,  $T_f$  is slightly different from  $SST_{\text{fnd}}$  and evolves with time. The  
1998 NSST profile,  $T(z)$ , incorporating diurnal warming and skin-layer cooling physics is simulated  
1999 or parameterized in the atmospheric model to provide a prognostic lower thermal boundary  
2000 condition for both atmospheric and radiative transfer models. Therefore, at a specific time,  
2001  $T(z) = T_f(z_w) + T'_w(z) - T'_c(z)$ , where,  $T'_w(z)$  and  $T'_c(z)$  are the simulated diurnal warming  
2002 profile and skin-layer cooling profile respectively (Li et al., 2019).

2003 The SST for air-sea fluxes calculation and skin-depth (or wavelength) dependent thermal lower  
2004 boundary condition for the Community Radiative Transfer Model (CRTM; Han et al., 2006; Zou  
2005 et al., 2016) over water surface can be provided when the NSST profile is available. For  
2006 example,  $SST = T(0) = T_f(z_w) + T'_w(0) - T'_c(0)$ .

2007 The  $T_f$ , an oceanic variable, as one of the analysis variables is incorporated into the atmospheric  
2008 data assimilation system of GFS. All observations, including satellite radiances and in situ sea  
2009 water temperature, are assimilated directly (without retrieval for satellite observations) with  
2010 observation operators and their Jacobians provided by a Radiative Transfer Model and NSST  
2011 model.

2012 The major difference between NSST and the other SST analyses is in the way of handling the  
2013 challenge that all the observations are indirect. In NSST, all observations are assimilated directly,  
2014 including satellite radiances and in situ sea temperatures. In the other SST analyses, the radiances  
2015 are converted to sea water temperature retrieval first, and the observations with diurnal warming  
2016 signals are discarded according to some criterion. Additionally, NSST is able to take advantage  
2017 of the well-established quality control and bias correction of the satellite radiances in the  
2018 frequently-updated atmospheric data assimilation system. It is also a step towards the future  
2019 coupled data assimilation.

2020 The validation of NSST can be roughly divided into two stages: the first is to compare to RTG SST fields,  
2021 the previous one used in operational GFS; and the second to compare to other SST analyses with the  
2022 major goal being to understand the causes of differences and then find possible ways to improve the  
2023 analysis. The Analysis (A) and Background (B) are the  $T_f$  analysis or background plus the diurnal  
2024 warming amount at the observed depth. The observed depth,  $z_{ob}$ , is assumed to be 20 cm for drifting  
2025 buoys,  $T_w^{'bg}(z_{ob})$ , in NSST and used in the validation here. The Observation – Background (O – B)

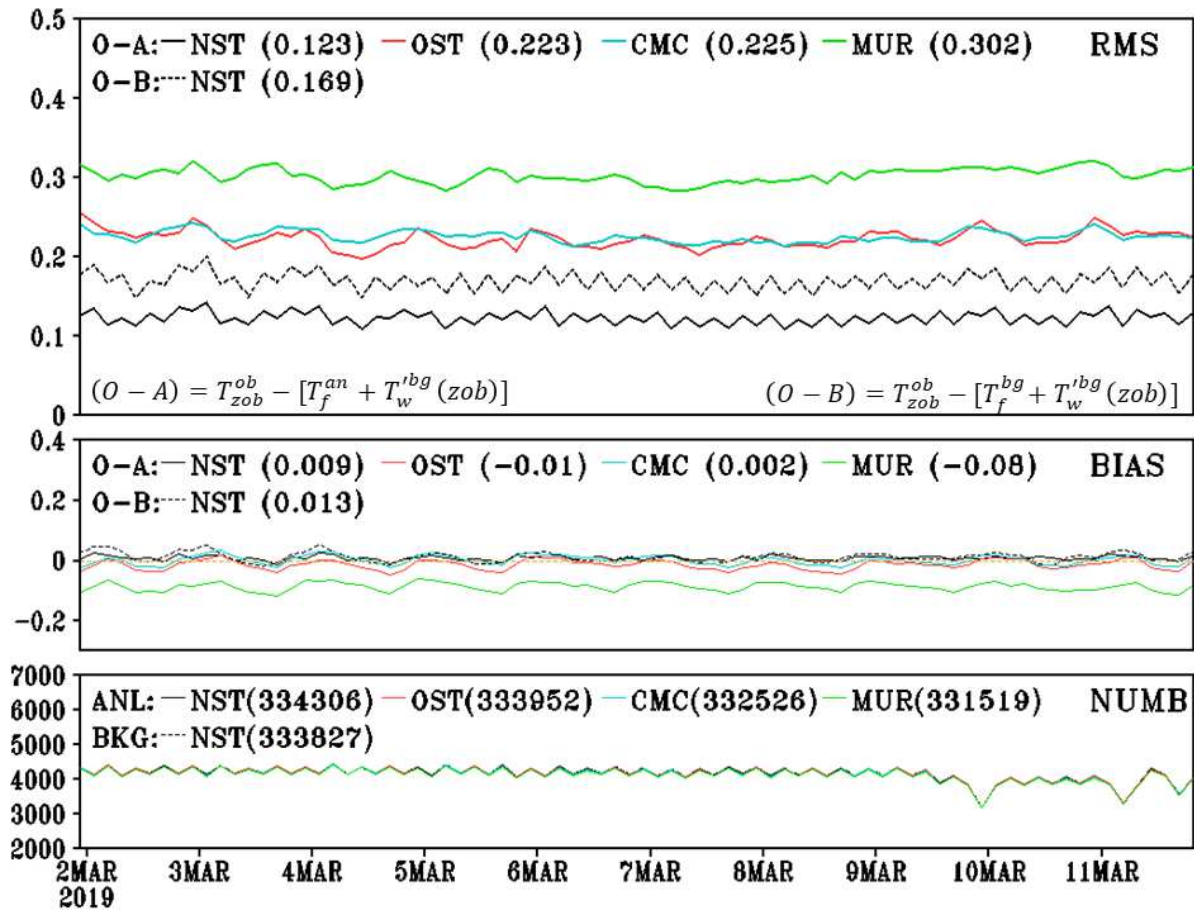
2026 statistics for both in situ and satellite data have indicated improvement, with positive impacts on weather  
2027 prediction being seen especially in the tropics. Here, verification against drifting buoy observations is  
2028 reported. The statistics are calculated using 6-hour samples for a 10-day period. NSST is analyzed 6-  
2029 hourly and the other three, OSTIA, CMC and MUR fields, are analyzed daily. The horizontal resolution  
2030 of the NSST product is about 25 km, but the analysis increment is generated at about 50 km grid spacing.  
2031 For the comparison, the other three products are interpolated to NSST resolution with identical 4  
2032 consecutive 6-hourly analyses. For every 6-hour interval, the analyses at the NSST resolution are  
2033 interpolated to the observed location to generate the O – A fields; O – B is available for NSST only. The  
2034 drifting buoy observations are from the diagnostic files of the NCEP NSST analysis, the same quality  
2035 control as NSST is applied to the other three analyses.

2036 It is illustrative to see how well the OSTIA, CMC and MUR  $SST_{\text{fnd}}$  analyses compare to the  
2037 drifting buoy observations which of course include diurnal warming and cooling signals. Figure  
2038 22 shows the verification of four SST analyses, NSST, OSTIA, CMC and MUR, against global  
2039 drifting buoy measurements. The (O – A) RMS difference is 0.123 K, 0.223 K, 0.225 K and  
2040 0.302 K for this 10-day period. The bias is nearly zero for NSST, OSTIA and CMC; MUR is  
2041 slightly too warm. There is no significant difference in the observation counts. As expected, the  
2042 NSST (O – B) is generally worse than (O – A). The basic features are stable with time, based on  
2043 comparisons over much longer periods (not shown; Li et al., 2019).

2044 In Figure 23 the calculated diurnal warming at the observation depth,  $T_w^{'bg}(zob)$ , is not applied  
2045 to the analysis or background. As is reasonable, this leads to larger RMS differences and smaller  
2046 numbers of data counts. The bias increases from nearly zero to 0.070 K, 0.046 K and 0.061 K  
2047 for NSST, OSTIA and CMC respectively. However, for MUR the negative bias is reduced from  
2048 -0.08 K to -0.02 K. For small areas (not shown), the conclusions are basically the same, and the

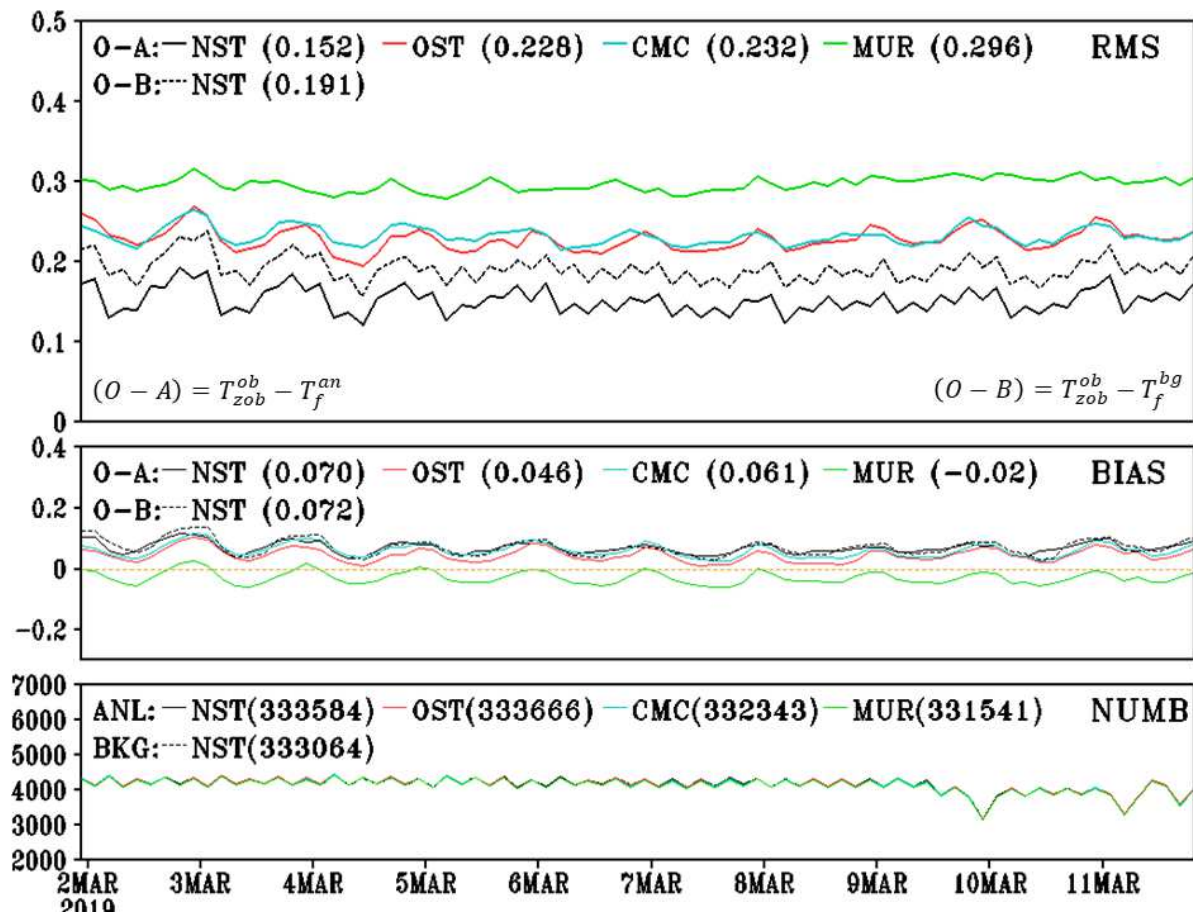
2049 difference due the inclusion of  $T_w^{'bg}(zob)$  is larger over more active diurnal warming area, such  
 2050 as tropics.

2051



2052

2053 *Figure 22. 3-hourly verification against drifting buoys of four SST analyses. Global data for March 2,*  
 2054 *2019 to March 11, 2019. The solid curves are for  $O - A = T_{zob}^{ob} - [T_f^{an} + T_w^{'bg}(zob)]$ , black: NCEP*  
 2055 *NSST (NST); red: OSTIA (OST); blue: CMC; green: MUR. The upper, middle and lower panel is for bias,*  
 2056 *root mean square and used counts respectively. The black dashed curve is  $(O - B) = T_{zob}^{ob} - [T_f^{bg} +$*   
 2057  *$T_w^{'bg}(zob)]$  for NSST.*



2058

2059 *Figure 23. As Figure 22 but excluding the diurnal warming at the observed depth in the analysis*  
 2060 *and background fields.*

2061 The validation has been repeated using other in situ observation platforms, including fixed buoys  
 2062 and ships. In comparison to temperatures measured from ships, NSST is significantly worse than  
 2063 OSTIA and CMC, and this is due to too large an observation error attributed to ship data. A  
 2064 smaller ship observation error will be used in the NSST in the future. From the inter-comparison  
 2065 with the other SST analyses, it has been found the NSST has issues in certain circumstances,  
 2066 particularly where observation coverage is poor. Improvements to the NSST production are  
 2067 underway, including the use of more observations especially microwave satellite radiances, using  
 2068 a more advanced background error correlation length and the better use of the SST climatology.

2069 It should be pointed out, drifting buoy temperature measurements are ingested in all four  
2070 analyses discussed here, and the fitness of the analyses to this observation depends on the  
2071 weights given to these and to the background temperatures. Therefore, the (O – A) statistics are  
2072 not the only metrics of the quality evaluation, and (O – B) is a better metric. A metric to evaluate  
2073 the fit to satellite observations needs to be established even though it is acknowledged that it is  
2074 not likely to be straightforward.

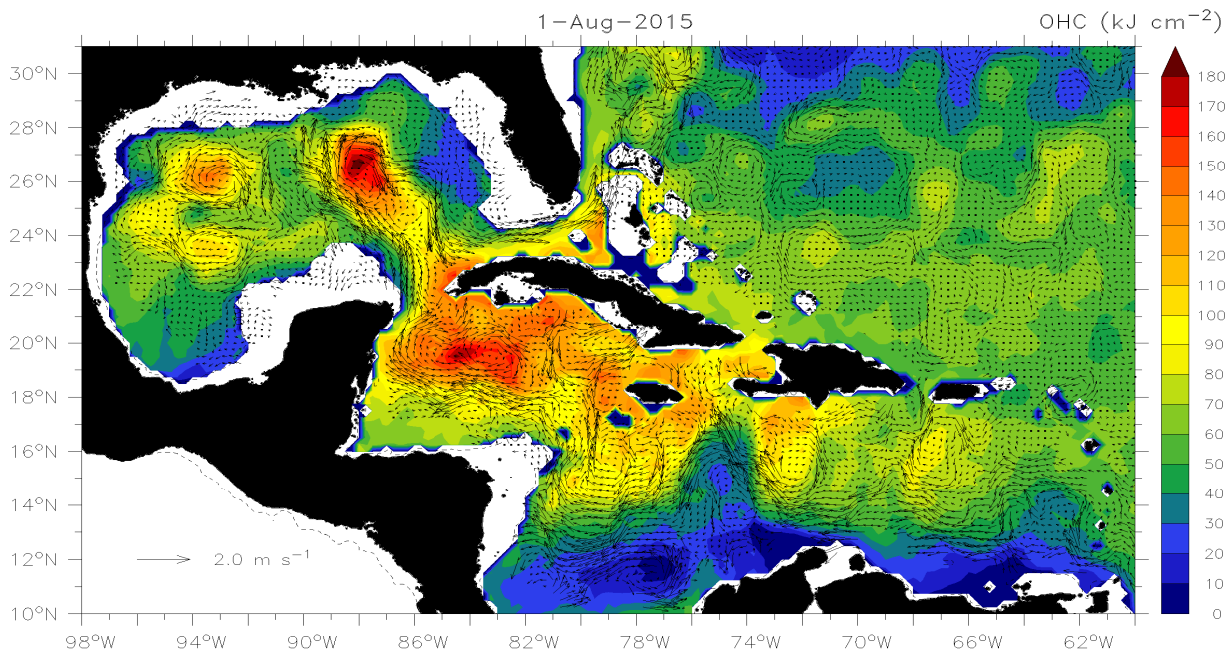
2075 As NWP systems become more complex and move towards coupled ocean-atmosphere models  
2076 (Miller et al., 2017) then the requirements for SST products increase. In a coupled system the  
2077 SST is first assimilated into an ocean model, which then exchanges fluxes with the atmospheric  
2078 model. Also, diurnally varying SST analysis systems are being developed (While et al., 2017) to  
2079 reduce errors due to timeliness and for validation of coupled models. In the future, operational  
2080 forecast centers will move to direct radiance assimilation to allow a more consistent atmospheric  
2081 and oceanic processing across all sky conditions (Geer et al., 2018). However, SST will remain  
2082 an essential diagnostic as it can be independently validated (see Section 6).

## 2083 **9.2 Ocean Heat Content and Severe Storms**

2084 The connection between high SST and Atlantic hurricanes has been long recognized as the ocean  
2085 was seen as a source of heat to sustain a hurricane (Malkus and Riehl, 1960). In 1948, Palmen,  
2086 used arguments based on atmospheric stability to conclude that SSTs > 27-28°C are needed for  
2087 hurricane formation, and Miller (1958) found a relationship between SST and storm intensity,  
2088 also noting that hurricanes in the Atlantic Ocean were unlikely to form over SSTs below 26-  
2089 27°C. Merrill (1988) reported that SST >30°C were needed for the development of a severe  
2090 hurricane. Before quantitative retrievals of SST from satellites, a climatological SST field or  
2091 sparse data from ship-based meteorological reports had to be used. Making use of cloud images

2092 from early meteorological satellites, Ramage (1974) described the life-cycles of three typhoons  
2093 in the South China Sea in 1970, and although he noted that SST  $>30^{\circ}\text{C}$  was found in the area, the  
2094 resolution and sampling of the SSTs caused him to conclude the SST “bore no apparent direct  
2095 relationship to the typhoon intensity changes” but he did note that the SST was cooler after the  
2096 passage of a storm.

2097 Of course, it is not just the SST itself that is critical to the development of severe storms, but the  
2098 ocean heat content (OHC) that is available to the storms through air-sea exchanges at the surface.  
2099 Variations in the upper ocean heat content, derived by integrating the vertical temperature profile  
2100 from the surface to some depth, usually taken to be the depth of the  $26^{\circ}\text{C}$  isotherm, was shown  
2101 by Shay et al. (2000) to be critical in understanding the development of Hurricane Opal in the  
2102 Gulf of Mexico in 1995, highlighting the influence of the Loop Current and warm core eddies  
2103 (Hong et al., 2000). The OHC can be estimated using SSH fields and sea-surface height

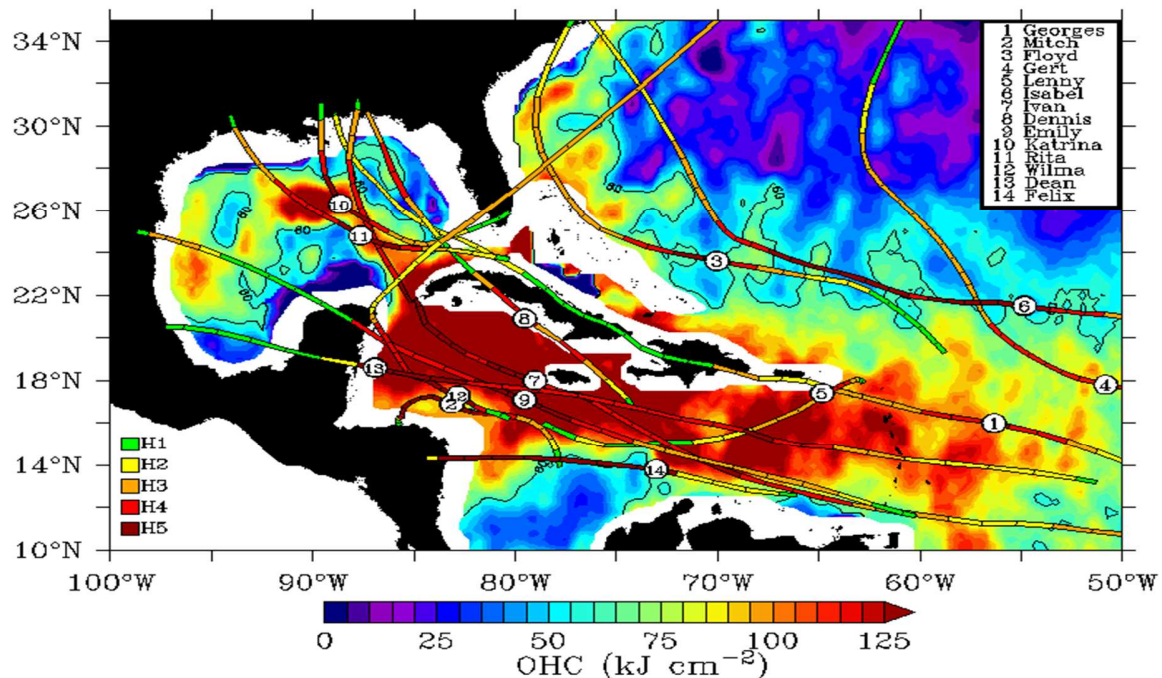


2104 anomalies (SSHA) derived from satellite altimetry (Shay et al., 2000).



2105 *Figure 24. OHC estimate (relative to 26°C: color bar) and geostrophic velocity vectors from space-based*  
2106 *measurements of satellite altimetry and SST on 1 August 2015 in the Intra-American Seas.*

2107 Figure 24 shows OHC in the Intra-American Seas (IAS), with high OHC in the Loop Current  
2108 and the warm anticyclonic eddy field having provided additional thermal energy to major  
2109 hurricanes over the past decade such as Hurricane Katrina in 2005, Hurricane Harvey in 2017,  
2110 and Hurricane Michael in 2018. Some of the strongest North Atlantic Ocean basin hurricanes  
2111 have occurred over the warm pool regime in the IAS (Figure 25). This variability points to the  
2112 importance of the OHC on hurricane intensity in the IAS. Examination of these hurricanes  
2113 relative to OHC (Meyers et al., 2014) shows that they often reach maximum intensity over the  
2114 high-OHC Subtropical Water of the Caribbean Sea, Florida Current, Gulf of Mexico Loop  
2115 Current, or Gulf Stream, often weakening just before landfall (Rappaport et al., 2010).  
2116 Approximately 70% of hurricanes with maximum winds  $> 120$  knots ( $62 \text{ ms}^{-1}$ ) experience  
2117 eyewall replacement cycles (ERCs) after reaching maximum intensity levels. Hurricanes  
2118 subsequently weaken due to the combination of



2119 *Figure 25. Tracks and positions of maximum intensity for fourteen of the strongest hurricanes 1998-2011,*  
 2120 *plotted over OHC relative to the 26°C isotherm for September 2005.*

2121 ERCs increasing shear, and movement over lower-OHC water. Hurricanes striking the US  
 2122 Atlantic Eastern Seaboard encounter similar oceanic environments passing over the Gulf Stream  
 2123 and then cooler shelf waters. Such behavior in hurricanes has become much clearer now that  
 2124 there is an evaluated OHC product available for forecasting.

2125 A novel application of OHC maps and their daily progression is in predicting the behavior and  
 2126 migration of large predatory fish. While it has been understood for many years that ocean  
 2127 thermal fronts are a preferred environment for large marine predators, using tagged tunas Luo et  
 2128 al. (2015) were able to demonstrate that the large horizontal variations in OHC are a potent  
 2129 predictor of fish behavior, even when the surface manifestation of fronts is weak.

### 2130 **9.3 Sea level**

2131 As the global population continues to grow, the largest rate of growth is found in coastal areas  
2132 where there is an influx of people from the hinterland as well as continuing urbanization, which  
2133 are expected to continue (Neumann et al., 2015). Many of the world's largest cities are in the  
2134 coastal areas, often located in large deltas with low-lying surroundings, with ~10% of the global  
2135 population living on land within 10m of sea level (McGranahan et al., 2007). The greatest  
2136 increase in coastal populations are in Asia, especially southeast Asia (Neumann et al., 2015). In  
2137 addition to the loss of habitat by permanent submergence of low-lying coastal areas by the  
2138 inexorably rising sea, coastal populations are vulnerable to other events exacerbated by rising  
2139 sea-levels, including storm surges, tidal flooding, more persistent river flooding following  
2140 extreme rain events, and flooding by tsunamis. Some events may be rare, but when they occur  
2141 they can be devastating to both human populations and ecosystems (see the references in  
2142 Neumann et al., 2015).

2143 Measurements from tide gauges and satellite altimeters leave no doubt that sea-levels are rising,  
2144 and that this increase in sea level is expected to accelerate (Nerem et al., 2018). There are two  
2145 contributing factors to sea-level rise: increases in mass resulting from run-off from melting land  
2146 ice, especially from Greenland and Antarctica (Rignot et al., 2011), and increases in volume as  
2147 the ocean temperature increases and expands (Nicholls and Cazenave, 2010). Although there are  
2148 significant regional variations in the rate of sea-level rise (Cazenave and Nerem, 2004) and some  
2149 are caused by large scale phenomena such as ENSO (Cheng et al., 2008), the thermosteric  
2150 expansion can be monitored using global satellite-derived SST fields with ocean and climate  
2151 models (e.g. Han et al., 2010).

## 2152 **10 Operational Oceanography**

2153 The high variability of ocean properties and the need for the assessment of the state of the marine  
2154 environment require a continuous monitoring of the ocean environment at unprecedented  
2155 resolution and quality. To respond to these requirements, Operational Oceanography (OO)  
2156 became a branch of ocean science that routinely makes available high quality observational and  
2157 model data for both fundamental studies and practical applications. Operational oceanography  
2158 depends critically on the near real time availability of high quality satellite and in-situ data with a  
2159 sufficiently dense space and time sampling. Observations are required to constrain ocean models  
2160 through data assimilation and also to validate them. As a consequence, the evolution of OO that  
2161 occurred in the last two decades strongly intersected with the evolution of the satellite observing  
2162 systems, computer technology and improvement of models. Satellite retrievals of SST were the  
2163 first high space and time resolution data available in real time. SST data were used to constrain  
2164 ocean models through data assimilation and/or to serve downstream applications (Le Traon et al.,  
2165 2015). The first prototype of the OO system was developed in Europe, in the late 90's when the  
2166 implementation of operational oceanography in the world ocean was still at its infancy (Pinaridi  
2167 and Woods, 2002; Pinaridi et al., 2003). The prototype was the Mediterranean observing and  
2168 modeling system for operational oceanography developed by Mediterranean Forecasting System  
2169 Pilot Project (MFSPP) that, starting from October 1998, was able to provide Near Real Time  
2170 (NRT) observational data and 5-day forecasts of currents for the entire Mediterranean basin.  
2171 During the MFSPP, a system for the acquisition and processing in NRT of satellite data  
2172 (AVHRR at that time) was developed and became operational, providing NRT data and products  
2173 to users (Buongiorno Nardelli et al., 2003). The SST processing system at that time included all  
2174 the steps required to transform AVHRR L0 data into L4 SST analyses: the reception of the L0  
2175 raw telemetry AVHRR data stream via HRPT stations, L2 SST retrieval from IR measurements,

2176 automatic cloud screening, data quality control, L3 merging data of SSTs (5 to 6 satellite passes  
2177 were available over the areas of interest) to produce daily L3 SSTs, a production of the daily-  
2178 weekly L4 analysis using optimal interpolation techniques (Santoleri et al., 1991; Marullo et al.,  
2179 1999a; Marullo et al., 1999b; Buongiorno Nardelli et al., 2003). During, MFSP for the first time  
2180 NRT SST were assimilated in MFS general circulation modeling every week and used to correct  
2181 the atmospheric forcing to improve ocean forecasts. This prototype observing and modeling  
2182 system was operational from October 1998 to the end of 2001, demonstrating the importance of  
2183 an OO system at basin scale. Successive upgrades of the various components of the  
2184 oceanographic system, including an SST component, were developed in the following years  
2185 (Pinardi et al., 2003; Pinardi and Coppini, 2010).

2186 At the same time, the Global Ocean Data Assimilation Experiment (GODAE) concept was  
2187 developed with the aim to conduct a 10-year international demonstration of the feasibility and  
2188 utility of real-time, global ocean forecasting (Bell et al., 2009). Thanks to the MSF success and  
2189 GODAE effort, other OO projects started in Europe and worldwide. To respond to operational  
2190 SST requirements of the modelling community, several international projects were launched:  
2191 such as Medspiration by ESA, OSI SAF by EUMETSAT and the international GODAE High  
2192 Resolution Sea Surface Temperature Pilot Project was established (GHRSSST-PP, subsequently  
2193 renamed the Group for High Resolution Sea Surface Temperature (GHRSSST) (Section 13)) in  
2194 2001 (Donlon et al., 2009). The GODAE OceanView (GOV) has maintained strong links with  
2195 satellite oceanography communities and major progress has been made over the past 10 years to  
2196 develop and optimize the use of satellite observations for operational oceanography. The  
2197 GHRSSST partners offered, and continue to offer, a suite of tailored global high-resolution SST

2198 products, in near-real-time, on a daily basis, to support operational forecast systems and the  
2199 broader scientific community.

2200 The establishment of a political framework for the Global Earth Observation System of Systems  
2201 (GEOSS; Lautenbacher, 2006) and the accompanying Earth Observation Summits have been the  
2202 backdrop to the formation of a significant European contribution to GEOSS. The Global  
2203 Monitoring for Environment and Security (GMES) initiative, subsequently renamed the  
2204 Copernicus program, has been established in the course of the last decade to fulfill the growing  
2205 need expressed by European policy-makers to access accurate and timely information to better  
2206 manage the environment, understand and mitigate the effects of climate change and ensure civil  
2207 security. MyOcean Projects implemented the European GMES Marine Core Service for the  
2208 2009-2015 period, and developed and tested in pre-operational mode the first concerted and  
2209 integrated pan-European capacity for ocean monitoring and forecasting. The main results and  
2210 recommendations of the GHRSSST have been reflected in the design of the MyOcean sub-  
2211 systems devoted to the development and production of satellite SST data (SST-TAC, Thematic  
2212 Assembly Centre). The SST-TAC was developed, implemented and is now part of CMEMS. The  
2213 SST-TAC is maintaining the operational chains for the production, validation and dissemination  
2214 of the multi-sensor SST Level 3 data (more precisely L3S data) and L4 products for a total of 18  
2215 products covering the global ocean and the European Seas (North Atlantic, Baltic, Arctic,  
2216 Mediterranean and Black Sea). Currently, the L3S and L4 data are built from all available  
2217 GHRSSST L2P IR measurements, and correspond to daily (night-time) gridded super-collated  
2218 (multi-sensor) and optimally interpolated satellite SST estimates at High spatial Resolution (10  
2219 to 5 km) and Ultra-High spatial Resolution (1 km, as in the Mediterranean Sea, Buongiorno  
2220 Nardelli et al., 2015) and hourly L4 SST products.

2221 The other important impact of OO has been its role in defining the requirements for the space  
2222 component. In fact, climate, science and OO applications share the same backbone system.  
2223 Operational oceanography has, however, specific requirements for near real time and space  
2224 resolution. Operational oceanography requirements have been detailed in several papers and used  
2225 by space agencies to define space segment and the characteristics of the latency and accuracy of  
2226 operational data. For example, the needs of an ocean observing system was used to define the  
2227 Sentinel-3 mission, dedicated to global ocean observations (Drinkwater, 2005; Donlon et al.,  
2228 2012a). This role is still crucial and recently CMEMS has revised the space component  
2229 requirements to take into account the evolving user requests. In particular, continuity of the  
2230 present capability of the Copernicus Sentinel missions (Desnos et al., 2014) should be ensured  
2231 and the request of a European passive microwave mission for high spatial resolution ocean  
2232 surface temperature should be considered (CMEMS, 2017; Le Traon et al., 2019).

2233

## 2234 **11 Climate Data Record**

2235 The concept of a Climate Data Record (CDR) was formally introduced in a National Academy of  
2236 Sciences report (NRC, 2000) as being “*a data set designed to enable study and assessment of*  
2237 *long-term climate change, with ‘long-term’ meaning year-to-year and decade-to-decade change.*  
2238 *Climate research often involves the detection of small changes against a background of intense,*  
2239 *short-term variations... The production of CDRs requires repeated analysis and refinement of*  
2240 *long-term data sets, usually from multiple data sources.” The report emphasized the need for  
2241 “Data Stability,” reasoning that “because natural signals are often small, it is difficult to ascribe  
2242 particular events or processes to climate change... [so that] long-term, high-quality*

2243 *measurements are needed to discern subtle shifts in Earth’s climate. Such measurements require*  
2244 *an observing strategy emphasizing a strong commitment to maintaining data quality and*  
2245 *minimizing gaps in coverage.” The Report states that “long-term studies such as those needed for*  
2246 *documenting and understanding global climate change require not only that a remote sensing*  
2247 *instrument be accurately characterized and calibrated but also that its characteristics and*  
2248 *calibration be stable over the life of the mission”. Data Continuity “includes the continuous and*  
2249 *accurate characterization of the properties that affect the construction of the time series. The*  
2250 *most useful data for climate research purposes are time series that are continuous and for which*  
2251 *the characterization of error, in terms of precision and bias, is known. Such errors should be*  
2252 *minimized as much as possible in order to detect the often small, climate-related signal.”*

2253 The Committee on Earth Observation Satellites (CEOS) has declared SST to be an Essential  
2254 Climate Variable (ECVs; Bojinski et al., 2014) that has a high impact on the requirements of the  
2255 UNFCCC (United Nation Framework Convention on Climate Change) and the IPCC  
2256 (Intergovernmental Panel on Climate Change). SST derived from satellite measurements offers  
2257 the best source of global, repeated fields, along with accompanying uncertainty characteristics.  
2258 Compared to some other ECVs, satellite-derived SST can more readily produce a CDR as  
2259 temperature is a base variable of the SI system (International System of Units; Taylor and  
2260 Thompson, 2008) and as such, traceability to SI temperature standards is much more  
2261 straightforward to achieve than other CDRs. An unbroken chain of calibration to an SI  
2262 temperature reference for each source of satellite-derived SSTs is an important factor in  
2263 generating SST CDRs with data from multiple satellite missions (Minnett and Corlett, 2012).  
2264 The required accuracy for satellite remote sensing of SST for climate research and applications is  
2265 very stringent, but it is a good target as in striving to achieve it we will generate data sets that can



2266 contribute to many research activities. The target accuracy,  $\pm 0.1$  K with a decadal stability of  
2267 0.04 K (Ohring et al., 2005), is very challenging not only to achieve but also to demonstrate  
2268 convincingly whether these targets have been attained. Determining the accuracies of satellite-  
2269 derived SST<sub>skin</sub> by comparing them with independent measurements from using ship-board  
2270 radiometers (Donlon et al., 2014), by being a comparison of “like-with-like,” removes much of  
2271 the error and uncertainty attendant when using subsurface temperature measurements taken from  
2272 drifting or moored buoys (Minnett, 2003; Minnett and Smith, 2014). However, the number of  
2273 ship-board radiometers is small, whereas the number of drifting and moored buoys is large, so  
2274 that an optimal way forward to assess the accuracies of satellite-derived SSTs is to use both  
2275 (Minnett and Corlett, 2012).

2276 In recognition of the need to improve the consistency and the calibration of different satellite  
2277 instruments providing measurements used to derive climate-relevant variables, including SST,  
2278 the Global Space-based Inter-Calibration System (GSICS) was set up in 2005 by the WMO and  
2279 the Coordination Group for Meteorological Satellites (CGMS) with membership of a number of  
2280 national space agencies and meteorological agencies (<https://gsics.wmo.int/en>). The objectives of  
2281 GSICS include ensuring the satellite radiometers are tested and calibrated pre-launch to SI-  
2282 standards, the radiometers be intercalibrated on orbit with specific radiometers that have been  
2283 identified to be stable and well calibrated, and that archives of satellite data can be reprocessed to  
2284 produce stable and improved long-term data sets (Goldberg et al., 2011). Currently, the on-orbit  
2285 reference radiometers are the IASIs (Section 5.2.2) on the Metop polar-orbiters (Hewison et al.,  
2286 2013). A further aspect of GSICS is the monitoring of the satellite radiance measurements using  
2287 NWP fields (Saunders et al., 2013).

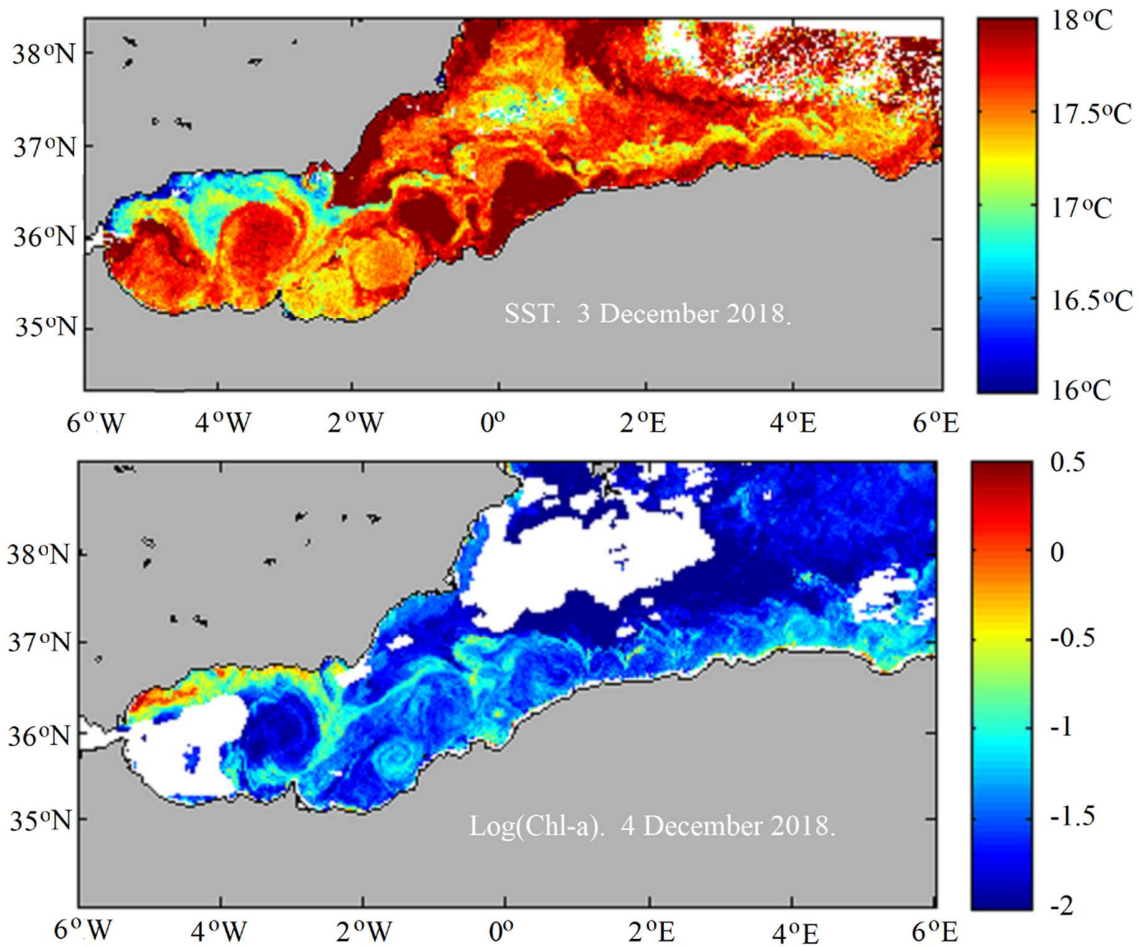
2288 The assessment of accuracies of satellite-derived SSTs using ship-board radiometers also  
2289 contributes to establishing an unbroken chain of calibration to SI Standards (Minnett and Corlett,  
2290 2012). The internal calibration accuracies of the ship radiometers have been checked periodically  
2291 through a series of international workshops involving reference instruments provided by national  
2292 metrology laboratories, the National Institute of Standards and Technology (NIST) in the USA,  
2293 and the National Physical Laboratory (NPL) in the UK. The format of the workshops comprises  
2294 assessment of calibrations of ship-board radiometers using metrology standard blackbody  
2295 calibration targets, and an assessment of the accuracies of blackbody calibration facilities used  
2296 by individual researchers in their laboratories through measurements of national standard  
2297 radiometers. (Kannenbergh and Palluconi, 1998; Rice et al., 2004; Barton et al., 2004;  
2298 Theocharous et al., 2019).

## 2299 **12 Synergy with other remotely-sensed variables**

2300 The relation between SST and other oceanic variables has long been exploited to obtain a better  
2301 understanding of the processes controlling the ocean, to assess the spatial and temporal scales of  
2302 variability of these processes, and to study the ocean dynamics at these scales. Physical and  
2303 biogeochemical processes are closely coupled in the ocean, with SST being a key variable that  
2304 allows a link to be made between these different disciplines. Figure 26 shows SST and  
2305 chlorophyll-a concentration in the western Mediterranean Sea on 3 and 4 December 2018  
2306 respectively. The fields of eddies and fronts are clearly visible in the images, showing the link  
2307 between ocean dynamics, SST and primary production. Multivariate studies of the state of the  
2308 ocean have been performed ever since such satellite-based retrievals have been available, often  
2309 in combination with in situ data in order to understand the vertical expression of the processes

2310 observed at the surface. Santoleri et al. (2002), for example, studied the circulation patterns in  
2311 the Mediterranean Sea using a combination of altimeter, SST and chlorophyll-a data. The results  
2312 were compared with in situ data in the Algerian basin and Adriatic Sea, and contributed to  
2313 explaining mesoscale dynamics in these basins. Smyth et al. (2001) linked SST and chlorophyll-  
2314 a imagery with Lagrangian measurements to study the biological response to upwelling at wind-  
2315 induced offshore filaments. Access to real-time satellite imagery allowed the optimization of  
2316 field sampling stations.

2317 It is well known that upwelling-favorable winds bring deep, cold, nutrient-laden waters to the  
2318 surface, which favor the development of phytoplankton blooms visible from space through their  
2319 chlorophyll-a content. The joint study of SST and chlorophyll-a using satellite data supported,  
2320 for example, the study of the evolution of biological patterns in time and their link to SST  
2321 structures during an El Niño event in 1997 off the Chile coast (Thomas et al., 2001). Using  
2322 satellite winds in addition to SST and chlorophyll-a, Murtugudde et al. (2004) also showed the  
2323 influence of atmospheric patterns on ecosystem response for the El Niño event of 1997. As the



2324

2325 *Figure 26. SST on 3 December, 2018 (top) and Chlorophyll-a concentration (units  $\log(\text{mg m}^{-3})$ ) on 4*  
 2326 *December, 2018 (bottom), western Mediterranean Sea, derived from measurements of MODIS on Aqua.*

2327 satellite time series becomes longer, studies showing interannual variability in the relation  
 2328 between SST and chlorophyll-a concentration in the Pacific Ocean, related to changes in El Niño  
 2329 events, has become feasible (e.g. Thomas et al., 2012). On a smaller scale, Mauri and Poulain  
 2330 (2001) used SST and chlorophyll-a satellite data to study circulation patterns in the northern  
 2331 Adriatic Sea, identifying a link between river plume dynamics and wind events. More recently,  
 2332 Brando et al. (2015) used satellite-derived turbidity and SST data to track river plume water in  
 2333 the northern Adriatic after a major flood event. The use of multiple satellite variables might also

2334 lead to improved SST analyses, as the correlation between variables can be used to infer missing  
2335 information about, for example, length scales of variability. Alvera-Azcárate et al. (2007)  
2336 performed a multivariate analysis using SST, chlorophyll-a and winds to study an  
2337 upwelling/downwelling event in the West Florida Shelf, and demonstrated that using jointly  
2338 these three variables led to improved SST analyses. Li and He (2014) performed a similar  
2339 analysis to study the multi-year relationship between chlorophyll-a and SST and the dynamics at  
2340 the Gulf of Maine.

2341 Ocean dynamics, expressed at the surface in the form of currents, fronts and eddies, have also  
2342 very often a clear SST signature. The relation between sea surface height and SST can be  
2343 therefore also used in studies aimed at describing the ocean circulation. Earlier studies (e.g.  
2344 Carnes et al., 1994; Knudsen et al., 1996; Vazquez-Cuervo et al., 1996; Santoleri et al., 2002)  
2345 had already pointed out the potential of exploiting the synergy between these variables. The joint  
2346 use of SST and sea surface height, used to derive OHC (Section 9.2), can also help in deriving  
2347 information about the ocean dynamics, such as improved representations of ocean currents  
2348 (González-Haro and Isern-Fontanet, 2014; Rio et al., 2016). Recently, Rio and Santoleri (2018)  
2349 demonstrated that the use of the information contained in high resolution SST maps leads to  
2350 improved determination of surface velocities at spatial scales not resolved by the altimeter  
2351 systems (i.e., below 150 km) but also at larger scales, where the geostrophic equilibrium might  
2352 not be the unique or dominant process of the ocean circulation.

2353 The data of SMOS (Soil Moisture Ocean Salinity; Drinkwater et al., 2009), Aquarius (Lagerloef  
2354 et al., 2008) and SMAP (Soil Moisture Active Passive; Entekhabi et al., 2010; Piepmeier et al.,  
2355 2017) have recently produced global measurements of sea-surface salinity (SSS). The relation  
2356 between SST and SSS provides information about water mass formation and circulation patterns

2357 (e.g. Reul et al., 2014; Buongiorno Nardelli et al., 2016). The close relationship between SSS and  
2358 SST is also used to improve the spatial resolution and to reduce noise in the satellite-derived SSS  
2359 fields (Olmedo et al., 2018).

2360 The evolution of satellite sensors, with more accurate data and higher spatial resolutions being  
2361 resolved over the last decade, have led to works linking the meso- and submesoscale variability  
2362 in different ocean variables. For example, Cotroneo et al. (2016) studied the evolution of a  
2363 mesoscale eddy detaching from the Algerian current (Mediterranean Sea) using a combination of  
2364 satellite SST and chlorophyll-a data with in situ high-resolution glider data, allowing them to  
2365 study the dynamics of this structure and its impact on biochemistry. Pascual et al. (2017)  
2366 performed a multiplatform experiment in the western Mediterranean Sea using satellite and in  
2367 situ data to study meso- and submesoscale processes at an intense front. Satellite SST data were  
2368 used to determine the strategy to sample an eddy at the Alboran Sea, and also to describe the  
2369 physical and biogeochemical variability of this region, in combination with in situ data from  
2370 gliders, drifters and Argo profilers.

### 2371 **13 The Group for High-Resolution Sea-Surface Temperature (GHRSSST)**

2372 Since 2002, research into many aspects of SST, primarily satellite remote sensing of SST, and  
2373 the transition of research results into operations has benefited from the actions of the GHRSSST  
2374 which plays a key role in coordinating international SST-related activities. The GHRSSST is made  
2375 up of scientists and operational practitioners from universities, research institutes, space agencies  
2376 and operational forecast centers from many countries. GHRSSST works closely with the  
2377 Committee on Earth Observation (CEOS) SST Virtual Constellation (SST-VC). The group  
2378 started out as the Global Ocean Data Assimilation Experiment (GODAE; Bell et al., 2009) High

2379 Resolution SST Pilot Project (GHRSSST-PP; Donlon et al., 2007) and transitioned to GHRSSST  
2380 following the completion of GODAE. GODAE had set the GHRSSST-PP the challenge of  
2381 providing global near-real time (within 6 hours) < 10 km and 6-12 hr resolution products with an  
2382 accuracy better than 0.4 K (Smith and Koblinsky, 2001). In response, GHRSSST established  
2383 several practical steps to meet the GODAE requirements.

2384 To provide data with sufficient sampling, a merging of all available data sources (satellite and in  
2385 situ) was required. For this, GHRSSST established a series of three key standards: first, GHRSSST  
2386 recognized the need to standardize the definition of SST itself, as data labelled “SST” would be  
2387 coming from measurements made at different depths and times (Section 3) using different  
2388 measuring techniques; second, to ease comparison, joint analysis, and merging SST data from  
2389 different sources, a common data format (the GHRSSST Data Specification, or GDS;  
2390 [https://www.ghrsst.org/governance-documents/ghrsst-data-processing-specification-2-0-revision-](https://www.ghrsst.org/governance-documents/ghrsst-data-processing-specification-2-0-revision-5/)  
2391 [5/](https://www.ghrsst.org/governance-documents/ghrsst-data-processing-specification-2-0-revision-5/)) was required; and third, an international framework (the Regional/Global Task Sharing, or  
2392 RGT/S) was needed to coordinate SST data production from diverse sources and distribution to  
2393 users. These standards have allowed GHRSSST to ensure that data products meeting the  
2394 requirements of GODAE are now available from its contributing entities.

2395 As well as providing uniformity of file structure, the GDS also identified the process of  
2396 transforming data across different levels (Section 7). In addition, it also specifies both a quality  
2397 level and an uncertainty (in the form of single Sensor Error Statistics, SSES), information that is  
2398 now becoming more common across all Earth observation domains through initiatives such as  
2399 the Quality Assurance Framework for Earth Observation (QA4EO; Fox, 2010). Indeed, this  
2400 information is vital for producing higher level products as it offers a way to quantitatively merge  
2401 data from multiple sources.

2402 As SST datasets become more diverse and satellite data volumes grow (with the new generation  
2403 of geostationary satellites for example), the role of GHRSSST is arguably more important now  
2404 than when the group was initiated. To address these new challenges, the Group is currently  
2405 evolving the RGT/S framework to ensure seamless data provision to users well into the future.  
2406 Information on the GHRSSST project may be accessed through the main home page at  
2407 <http://www.ghrsst.org>.

## 2408 **14 Data handling, data sources and archives**

2409 In the half century of satellite remote sensing of SST, the methods available to distribute data to  
2410 operational centers and researchers has undergone a revolution. Initially, data were mailed from  
2411 receiving stations to researchers on computer readable 9-track magnetic tapes and the processing  
2412 of the data was a challenge, not least how to display imagery in a cost-effective but scientifically  
2413 useful fashion, often as photographic prints. The growth in data volume that began with the ERS  
2414 series in the early 1990s and more so with the NASA Earth Observing System in the early  
2415 2000's led to the formation of large data processing and archive centers, which coincided with  
2416 the development of the Internet and the ability to deliver large datasets on a computer-to-  
2417 computer basis using unified protocols. Currently, data access and remote processing and  
2418 analysis of satellite-derived SSTs is no longer the daunting challenge it used to be, and many  
2419 tools are available to researchers that facilitate the exploitation of large data sets in a wide range  
2420 of applications.

2421 Considerable progress has been made in providing users with a single point of entry for all SST  
2422 data sets. The GHRSSST page: <https://www.ghrsst.org/ghrsst-data-services/services/> provides an  
2423 overview of how to access the near real time (PO.DAAC; <http://podaac.jpl.nasa.gov>) and the



2424 historical L2 to L4 data (NODC; <https://data.nodc.noaa.gov/ghrsst/> or  
2425 <ftp://ftp.nodc.noaa.gov/pub/data.nodc/ghrsst/>). Yet, the numerous GHRSSST data sets, while  
2426 providing users with many sources, also creates the need to integrate information and tools that  
2427 allow users to make informed decisions about which data set to use. This will be a major  
2428 challenge for the future.

#### 2429 **14.1 Physical Oceanography Distributed Active Archive Center (PO.DAAC)**

2430 The Physical Oceanography Distributed Active Archive Center (PO.DAAC) located at the Jet  
2431 Propulsion Laboratory/California Institute of Technology, and NOAA's National Centers for  
2432 Environmental Information (NCEI, and its forerunners) have been the lead centers for the  
2433 distribution and management of SST products. The original NOAA/NASA Pathfinder AVHRR  
2434 data set (Kilpatrick et al., 2001) was archived and distributed through the PO.DAAC. Processing  
2435 of the data set was done at the University of Miami with the PO.DAAC undertaking post-  
2436 processing from L2 to L3 for distribution and archival. This was a major breakthrough in setting  
2437 a standard for data providers and data managers working together to provide efficient  
2438 distribution and tools and services for data extraction.

2439 The AVHRR Pathfinder project led to a breakthrough in how to distribute high volume data. At a  
2440 4 km global spatial resolution, it required the implementation of new technologies for subsetting  
2441 and extracting data on regional scales. The 4 km spatial global resolution made it prohibitive for  
2442 users to download and easily work with the global data. This led to a breakthrough in  
2443 implementing data format standards which included all the data processed and formatted in the  
2444 Format HDF). The PO.DAAC developed an interface and distribution tool  
2445 known as PO.DAAC OceanESIP Tool (POET). This tool facilitated the subsetting of the

2446 Pathfinder data set. Additionally, it gave the user the flexibility to choose several output formats,  
2447 including ASCII and ArcGIS (a tradename of a Geographical Information System). The POET  
2448 tool was a major step forward in data distribution in several ways: 1) allowing data subsetting; 2)  
2449 implementing data interoperability standards through a common format (HDF); 3) flexibility in  
2450 allowing users different output formats for implementation in their own tools and software  
2451 programs. The model used for the NOAA/NASA Pathfinder project was instrumental in moving  
2452 forward with the GHRSSST (Section 13).

2453 Following on the success of the NOAA/NASA Pathfinder project the GHRSSST project was one  
2454 of the first to implement the common data format Network Common Data Form (NetCDF). The  
2455 goal of satellite derived SST data sets to be implemented in a common data format with  
2456 compliant standards allowed for interoperability among all the satellite derived SST data sets.  
2457 This also allowed for a unique cooperation between NASA and NOAA to allow users access to  
2458 both near real time and historical data. The GHRSSST Data Specification Document (GDS)  
2459 provided the framework for all data providers to process data into common formats, including  
2460 specifications for data levels (Table 3). Implementation of tools such as the Thematic Real-Time  
2461 Environmental Distributed Data Services (THREDDS), OPeNDAP, and the Live Access Server  
2462 (LAS) allowed users to easily extract and subset data in both space and time. All the tools allow  
2463 for subsetting of data and use the OPeNDAP protocol. Additionally, LAS allows the user to  
2464 visualize the data, along with the extraction of time series at particular locations, as well as  
2465 generate Hovmöller diagrams for both longitude and latitude. Other functionality with LAS,  
2466 allows the user to save the data in netCDF, CSV, ASCII, or ArcGrid. The THREDDS server  
2467 allows the user to aggregate the extracted data into one file. This is very useful when a user is  
2468 extracting several years of data that consist of daily files. Issues with extracting large amounts of

2469 data were not due to the tool, but primarily the data format. These issues included tools timing  
2470 out and/or having to submit multiple jobs to access the desired data over a certain period of  
2471 time. A major breakthrough that occurred was the transition from NetCDF version 3 to NetCDF  
2472 version 4, which allowed for internal compression, thus eliminating the need to decompress data  
2473 before reading. Users could then extract and access larger amounts of data. Both LAS and  
2474 THREDDS would have timeout issues with data sets such as the MUR SST data set, which is  
2475 formed of files of daily, global gridded data at 1km resolution. Conversion to NetCDF4 allowed  
2476 users to easily access the entire time series of these data sets. This was critical for MUR, with  
2477 data available since 2002, and the AVHRR\_OI, with data availability since 1981. Overall, each  
2478 tool provides advantages, depending on the user need, with OPeNDAP being a primary protocol  
2479 used in both THREDDS and LAS. The THREDDS server primarily uses the NetCDF JAVA  
2480 libraries, thus the conversion to NetCDF4 improved accessibility of the GHRSSST data.

2481 Effective June 3, 2019, NASA has retired their standard FTP protocol for data and information  
2482 access. For more information on using the replacement service, PO.DAAC Drive, to access data  
2483 please see: [https://podaac.jpl.nasa.gov/announcements/2019-02-13\\_REMINDER\\_PO.DAAC\\_](https://podaac.jpl.nasa.gov/announcements/2019-02-13_REMINDER_PO.DAAC_FTP_RETIREMENT)  
2484 [FTP\\_RETIREMENT](https://podaac.jpl.nasa.gov/announcements/2019-02-13_REMINDER_PO.DAAC_FTP_RETIREMENT).

2485 As the GHRSSST data sets span increasingly longer time periods and with the availability of high  
2486 resolution (<10km) SSTs, challenges remain in distribution. These include implementing new  
2487 methodologies for allowing users to extract large amounts of data in their particular areas of  
2488 interest. Some examples of the challenges include extracting the NOAA/NCEI AVHRR\_OI SST  
2489 fields dating back to 1981 (Banzon et al., 2014). Another example is the daily MUR SST (Chin  
2490 et al., 2017) which has 1 km global spatial resolution and dates back to June 1, 2002. Data from  
2491 the Visible Infrared Imaging Radiometer Suite (VIIRS; Section 5.1.5) has sub-kilometer

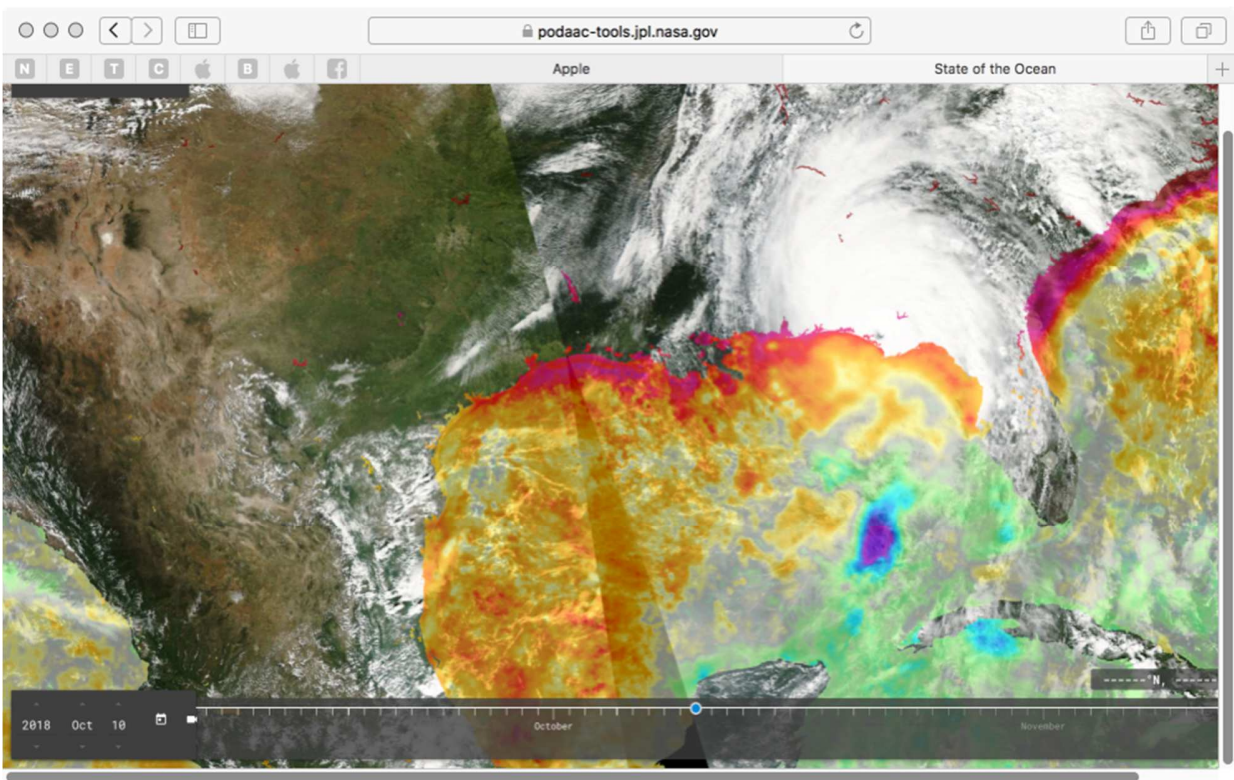
2492 resolution. As these data sets are applied to coastal regions, for example, allowing users  
2493 flexibility in applying quality flags and filtering is critical, interfaces that give users flexibility in  
2494 filtering and gridding data will be a major challenge for the future.

2495 Future directions for the GHRSSST project and data management include a restructuring of the  
2496 GHRSSST Regional/Global Task Sharing Network (R/GTS) to a more federated approach. Data  
2497 will be accessible through a centralized catalog. Data providers will have primary responsibility  
2498 for maintaining data distribution and access. This would include implementation of THREDDS  
2499 and OPeNDAP servers. Even with restructuring, many challenges remain. Many of these have to  
2500 do with the access of higher resolution and longer time periods of data. A major challenge will  
2501 not only be managing data, but also information. The management of information needs to  
2502 include documentation of error sources and uncertainties. This will be critical as an increasing  
2503 number of satellite-derived SST products become available to the user community.

2504 Part of the challenges will be in transitioning to cloud based technology that would allow for  
2505 accessing and manipulating large amounts of data. This is critical as high resolution data sets  
2506 such as VIIRS are available over longer periods of time. Cloud-based technologies will allow for  
2507 users to implement their own algorithms for gridding and optimal interpolation. A major hurdle  
2508 to the user community will be implementing software on the cloud that allows for functionality  
2509 beyond the traditional downloading of data and processing on a laptop. Cloud based solutions are  
2510 currently being developed by both NOAA and NASA to prepare for these future challenges.

2511 Additional challenges include the visualization of multiple data sets and accessing such data sets  
2512 in near real time. The example in Figure 27 shows an image of the SST anomaly derived from  
2513 the MUR SST data set (Chin et al., 2017). The image was generated using NASA's State of the  
2514 Ocean Tool (SOTO) (<http://podaac.jpl.nasa.gov/soto>). The SST anomaly is overlaid on a true

2515 color image from MODIS on Aqua. Blue colors indicate the surface cooling from the passage of  
2516 Hurricane Michael which made landfall on October 10<sup>th</sup>, 2018. Adding functionality to future  
2517 tools that allow for not only data extraction, but also data manipulation and derivation of  
2518 statistics will be a large focus of future development. This work will build on the groundbreaking  
2519 web interfaces of the SST Quality Monitor (SQUAM; Dash et al., 2010) and the in-Situ Quality



2520 Monitor (iQuam; Xu and Ignatov, 2014).

2521

2522 *Figure 27. The SST anomaly derived from the Multi-Scale Ultra-High Resolution (MUR) SST overlaid on*  
2523 *a true color image from MODIS on Aqua. Clearly visible (blue colors) is the cooling of the Gulf of*  
2524 *Mexico as Hurricane Michael made landfall on October 10<sup>th</sup>, 2018. Image provided by*  
2525 *JPL/Caltech/PO.DAAC.*

2526

2527 **14.2 Ocean and Sea Ice Satellite Application Facility (OSI SAF)**

2528 The Ocean and Sea Ice Satellite Application Facility (OSI SAF) is part of the EUMETSAT  
2529 ground segment. Its primary aim is to provide users with sea surface parameters in near real time  
2530 derived mostly from European meteorological satellites, and among these parameters is SST  
2531 computed from IR radiometers on board polar orbiting and geostationary satellites.

2532 Currently OSI SAF is distributing hourly L3C SST products derived from three geostationary  
2533 satellites: Meteosat-8 above the Indian Ocean (41.5°E), Meteosat-11 in 0° position and GOES-16  
2534 (75.2°W); and L2P and L3C from instruments on two polar orbiting satellites: AVHRR on  
2535 Metop-B (global and regional) and VIIRS on S-NPP (North Atlantic region). All products are  
2536 delivered in NetCDF-4 format compliant with the GHRSSST GDS v2. Near real-time and  
2537 historical OSI SAF data can be accessed by several means including EUMETCast or FTP  
2538 servers. Some products are also archived and available at the EUMETSAT Data Center (EDC)  
2539 and at the PO.DAAC. Details on how to access OSI SAF products can be found on the "Access  
2540 to data" page at [https:// www.osi-saf.org](https://www.osi-saf.org).

2541 OSI SAF is also performing reprocessing activities. For instance, it has recently released an  
2542 MSG SST data record (2004-2012) which was created using state of the art methodologies.

2543 Future OSI SAF activities are strongly tied to the future EUMETSAT meteorological satellite  
2544 programs and as such will aim at providing the best possible SST products for the new  
2545 generation sensors expected in the next few years: Metop-Second Generation and Meteosat Third  
2546 Generation.

2547

2548

### 2549 **14.3 Copernicus Marine Environment Monitoring Service (CMEMS)**

2550 The Copernicus Marine Environment Monitoring Service (CMEMS) is one of the six pillar  
2551 services of the EU Copernicus program. CMEMS provides regular and systematic reference  
2552 information on the ocean and sea ice state for the global ocean and the European regional seas  
2553 ([www.cmems.org](http://www.cmems.org)). CMEMS today provides about 160 different products derived from  
2554 observations and models which include 18 different SST products (see CMEMS catalogue at  
2555 [www.marine.copernicus.eu](http://www.marine.copernicus.eu)) and serves a wide range of users and applications with more than  
2556 15000 users are now registered for the service. SST observations are a fundamental pillar of the  
2557 CMEMS added value chain that goes from observation to information and users (Le Traon et al.,  
2558 2019). SST is the most downloaded observational product of CMEMS. Users require both global  
2559 and regional products designed for specific European regions. These data are produced by  
2560 CMEMS-SST-TAC (Thematic Assembling Centre) both for dissemination to external users and  
2561 for use internally within CMEMS. CMEMS SST products are available in near real time and  
2562 operationally assimilated by CMEMS global and regional modeling forecasting systems to  
2563 produce ocean reanalysis and forecasts (Bell et al., 2000; Lellouche et al., 2018; Oddo et al.,  
2564 2009). The CMEMS SST products are global and regional L3 multi-sensor SST and L4 analysis  
2565 products, and are produced ingesting all L2 data provided by Space Agencies, using an ad hoc  
2566 processing chain developed by the CMEMS SST-TAC. The processing chain includes  
2567 additional quality checks of upstream data, bias adjustment among sensors, and interpolation  
2568 techniques (e.g. Donlon et al., 2012b; Buongiorno Nardelli et al., 2013). SST L4 products at  
2569 regional scales are characterized by improved spatial resolution with respect to global products  
2570 reaching 1 km resolution, as for L4 Mediterranean SST (Buongiorno Nardelli et al., 2015).

2571 Multi-year reprocessed Products (MYP) are also produced and distributed by CMEMS, which  
2572 are consistent time series covering the period 1982 to the present (Pisano et al., 2016). MYP  
2573 SSTs are required to provide consistent descriptions of the ocean state over the past decades and  
2574 are used by CMEMS to produce ocean monitoring indicators available on the web and to  
2575 contribute to the Ocean State Report published every year (von Schuckmann et al., 2018). MYP  
2576 SSTs are also assimilated by global and regional CMEMS MFCs (Monitoring and Forecasting  
2577 Centers) to produce ocean reanalysis of the two decades. The SST TAC is responsible for  
2578 ensuring the quality of their products by planning and implementing validation of their products,  
2579 instigating quality control checks of incoming data streams and then monitoring the quality of  
2580 the data produce

2581 d. The SST TAC makes a continuous effort to include any new sources of data that are proven to  
2582 improve the quality of the CMEMS output products, such as newly available satellite sensors.  
2583 These new data sets, for example the SLSTR data from both Sentinel 3A and Sentinel 3B  
2584 missions, are included in all regional and global products. Interaction with users is another  
2585 important component of the CMEMS, for example via provision of quality information  
2586 documents and user manuals and by responding to queries received through the CMEMS service  
2587 desk.

## 2588 **15 Outlook**

2589 The outlook for the next decade and longer is very good, with continuation of current SST-  
2590 capable satellite missions and the first launches of new radiometers. Data processing and  
2591 distribution capabilities will no doubt continue to expand and provide increasingly effective  
2592 support for research and operations, and the combination of improved sensors and algorithms



2593 will result in more accurate SST fields. A detailed discussion of requirements and  
2594 recommendations to ensure continuing our SST capability through the next decade is given by  
2595 O’Carroll et al. (2019).

## 2596 **15.1 Satellite instruments**

2597 We can confidently expect the continuation of VIIRS on the NOAA polar orbiters, SLSTR on  
2598 Sentinel 3 series and several other IR radiometers described in Section 5 through the next decade  
2599 and beyond. Similarly, the new generation of instruments on the current GOES and Himawari  
2600 and on the new GEO-KOMPSAT-2 geostationary satellites will continue to provide valuable  
2601 data.

2602 In addition, new satellite series carrying radiometers with SST capabilities are planned to be  
2603 launched in the next decade into both sun-synchronous polar and geostationary orbits. The first  
2604 of the EUMETSAT Polar System - Second Generation (EPS-SG) polar-orbiters is planned for  
2605 launch in 2022 and will carry a new class of visible and IR imager, METImage (Wallner et al.,  
2606 2017) and the Infrared Atmospheric Sounding Interferometer - New Generation, IASI-NG  
2607 (Bermudo et al., 2014; Crevoisier et al., 2014), both being significant developments of their  
2608 predecessors on the Metop series. METImage will have 20 spectral channels, including a set of  
2609 IR that correspond to those of MODIS for  $SST_{skin}$  retrievals, but with 500 m surface resolution at  
2610 nadir with a 2670 km swath. IASI-NG will have improved spectral resolution and better  
2611 radiometric accuracy than the IASI, but will have the same surface resolution of 12 km.

2612 Complementing the AHI, ABI and AMI on Japanese, US, and Korean geostationary satellites,  
2613 EUMETSAT will launch the first of Meteosat Third Generation -Imaging (MTG-Im) three-axis  
2614 stabilized satellites in 2021 with the Combined Flexible Imager (CFI) as part of its payload. CFI  
2615 will have 16 channels, with surface resolution of 1 km in the visible and near-IR, and 2 km in the

2616 IR, including SST channels at  $\lambda = 3.8 \mu\text{m}$ ,  $10.5 \mu\text{m}$ , and  $12.3 \mu\text{m}$  (Ouaknine et al., 2013; Durand  
2617 et al., 2015). Full Disc Scans will have a basic repeat cycle of 10 minutes, and a European  
2618 Regional-Rapid-Scan will have a repeat cycle of 2.5 minutes. When the CFI becomes  
2619 operational, the globe will be sampled from geostationary orbit by new generation imagers at 2  
2620 km resolution at nadir and 10-minute temporal resolution. The constellation of satellites with  
2621 microwave sensors with SST capability remains fragile and vulnerable to instrument failure. A  
2622 major breakthrough would be the development of a high-resolution microwave sensor, such as  
2623 the Copernicus Imaging Microwave Radiometer (CIMR) which is a candidate mission within the  
2624 European Copernicus Expansion program (Kilic et al., 2018). The proposed CIMR would have  
2625 channels at 1.4, 6.9, 10.65, 18.7, and 36.5 GHz giving it sensitivity to SST and also SSS, wind  
2626 speed and sea ice concentration. The CIMR design is a conically scanning microwave radiometer  
2627 with 7 m antenna, giving a spatial resolution of 15 km, about three times better than that of  
2628 AMSR-2, and an ability to retrieve SST within 35 km of the coast.

## 2629 **15.2 Validating sensors**

2630 The drifting buoy array used in the validation of satellite-derived SSTs have evolved during the  
2631 last three decades. At first, the common drifter type was based on the ARGOS system for geo-  
2632 location and data transmission, SST resolution was 0.1K and position and SST measurements  
2633 were asynchronous. The migration to a new drifter type, called HRSST-1, began around 2010  
2634 and is almost completed. HRSST-1 buoys transmit their data through Iridium satellites, are geo-  
2635 located by GPS, SST resolution is 0.01K and position and SST measurements are synchronous.  
2636 Simultaneously, another drifter type, called HRSST-2, characterized by a digital SST probe  
2637 better calibrated, has been developed and tested. HRSST-2 buoys are not all the same, some of  
2638 them have additional improvements such as two SST probes, at 0.17 m and 0.48 m, or a careful

2639 insulation of the SST sensor from anything other than sea water (Poli et al., 2018). HRSST-2  
2640 buoys provide a more accurate SST and information on its representativeness, which is very  
2641 useful when comparing satellite and buoy SST. With more than 60 buoys deployed so far and  
2642 100 buoys expected in the next three years, HRSST-2 buoys are not sufficient by themselves for  
2643 satellite SST operational validation, but they will significantly contribute to the validation of  
2644 future instruments.

2645 It is hoped that the current suite of ship-radiometers (Section 6) will continue to be deployed to  
2646 provide SI-traceable assessments of the satellite-derived  $SST_{skin}$  accuracy and thereby contribute  
2647 to the SST CDR. The fact that reliable, well-calibrated ship-board radiometers capable of  
2648 providing  $SST_{skin}$  values are few in number, but slowly increasing, means that in the foreseeable  
2649 future the data for assessing the accuracy of satellite-derived  $SST_{skin}$  will be comparatively  
2650 sparse. Efforts are made to mount the radiometers on research ships for cruises in areas where  
2651 conditions are particularly challenging for the cloud-screening and atmospheric correction  
2652 algorithms (e.g. Minnett, 2010). Examples are at high latitudes where the atmospheric conditions  
2653 are extreme in the global distributions of atmospheric temperature and humidity and where  
2654 drifting buoys are few, or upwelling regions where air-sea temperature differences are generally  
2655 different from the global distribution and from where the surface divergence tends to advect  
2656 drifters. Additionally, atmospheric aerosols pose particular challenges to the algorithms (Díaz et  
2657 al., 2001; Bogdanoff et al., 2015; Luo et al., 2019 ) and areas with frequent contamination by  
2658 aerosols, such as Saharan dust outflows over the tropical and equatorial north-east and south-east  
2659 Atlantic Ocean and Arabian Sea (Prospero and Carlson, 1972; Prospero, 1999; Prospero et al.,  
2660 2002), or smoke from forest fires, such as of southwest Africa (Adebiyi et al., 2015) and around  
2661 Indonesia require further investigation. There is an additional imperative to studying the effects

2662 of aerosols on the accuracies of infrared-derived  $SST_{skin}$  as the reduction in surface insolation  
2663 resulting from aerosol scattering of sunlight reduces the SST and near-surface heat content  
2664 (Delworth et al., 2005; Rajeev et al., 2008; Martínez Avellaneda et al., 2010). The activities of  
2665 those operating ship-board radiometers are coordinated through the International SST Fiducial  
2666 Reference Measurement (FRM) Radiometer Network (ISFRN; see [http://www.shipborne-  
2668 radiometer.org/](http://www.shipborne-<br/>2667 radiometer.org/)), which issues guidelines on the specifications of ship-board radiometers, on best  
2669 practices to mount instruments on ships, and the preferred format of data to facilitate easy data  
2670 exchange (Ships4SST, 2019). It is in this format, referred to as L2R, that radiometer  
2671 measurements should be submitted to the ESA Felyx system (Taberner et al., 2013) for  
2672 generating match-ups with satellite radiometer measurements.

2672 The recent, rapid development of reliable and stable unmanned aerial vehicles (UAVS,  
2673 commonly referred to as “drones”) has introduced a new potential method for validating  
2674 satellite-derived  $SST_{skin}$ . This has spurred the recent development of lightweight miniaturized  
2675 self-calibrating radiometers with low power requirements, such as the Ball Experimental Sea  
2676 Surface Temperature (BESST) Radiometer (Emery et al., 2014). Such radiometers offer a cost-  
2677 effective method of validating satellite data in remote or rarely accessed areas. The BESST was  
2678 installed on a Boeing ScanEagle UAV ([https://en.wikipedia.org/wiki/Boeing\\_Insitu\\_ScanEagle](https://en.wikipedia.org/wiki/Boeing_Insitu_ScanEagle))  
2679 for the MIZOPEX study in the Arctic Marginal Ice Zone and the measurements have been  
2680 analyzed to quantify  $SST_{skin}$  variability within individual MODIS pixels (Castro et al., 2017).

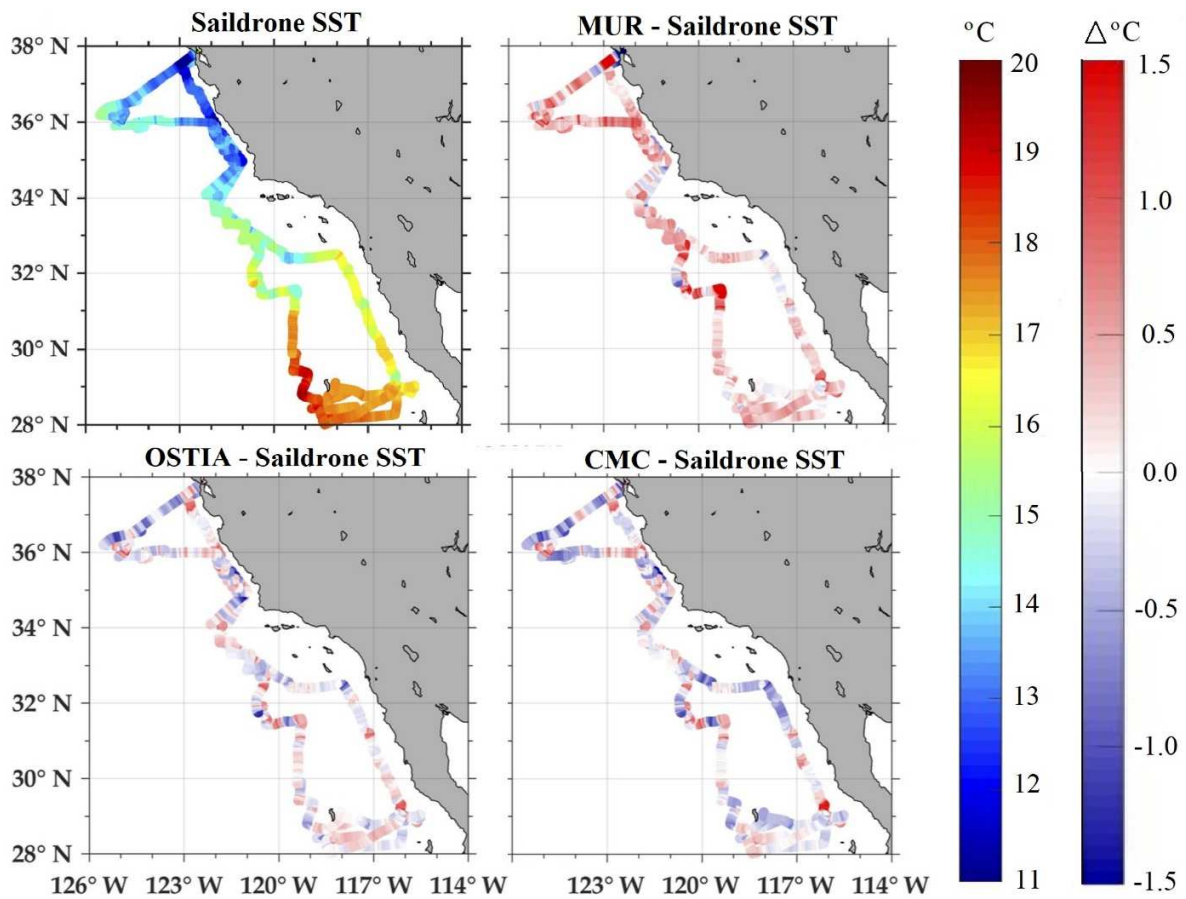
2681 A further recent development that is contributing to the validation of satellite-derived SSTs is the  
2682 growing use of robotic Autonomous Surface Vehicles, such as Sailables (Voosen, 2018) and  
2683 Wave Gliders (Manley and Willcox, 2010) as many are fitted with near-surface thermometers, In  
2684 a recent deployment, from April 11, 2018-June 11, 2018, of a Sailable off California and

2685 Mexico (Figure 28), additional self-recording thermometers were installed on the hull and keel.  
2686 The great advantage of such approaches is the possibility of post-cruise calibration of the  
2687 sensors, and since they are not disposable platforms, more expensive and accurate sensors can be  
2688 deployed than are usually used on drifting buoys. A comparison between subsurface  
2689 temperatures measured by a SeaBird 56 temperature sensor on the Saildrone and L2 SST<sub>skin</sub>  
2690 derived from measurements from MODIS on Terra and Aqua, and from VIIRS on Suomi-NPP  
2691 produced very promising results (Gentemann et al., 2019). The SSTs measured by the Saildrone  
2692 CTD at 0.6 m depth throughout the deployment are shown in Figure 28, along with differences  
2693 between these temperatures and those in three widely-used GHRSSST L4 SST products: MUR  
2694 (Chin et al., 2017), OSTIA (Donlon et al., 2012b), and CMC (Brasnett, 1997; Brasnett and  
2695 Surcel-Colan, 2016). Such co-located satellite-derived SSTs and Saildrone measurements  
2696 provide estimates of mean differences, root mean square differences (RMSD) and correlations  
2697 (Table 4). Overall, the differences were close to zero, except for the MUR data which shows  
2698 warm biases offshore. The high correlations of 0.96 and greater are consistent with the L4 fields  
2699 reproducing a significant part of the coastal variability in this area.

2700 In the summer of 2019, a fleet of six Saildrones was deployed in the Alaskan sector of the Arctic  
2701 Ocean in a collaboration between NOAA's Pacific Marine Environmental Laboratory (PMEL)  
2702 and a NASA-sponsored component of a US National Oceanographic Partnership Program  
2703 (NOPP) project called the Multi-sensor Improved Sea-Surface Temperature (MISST). As with  
2704 the 2018 Saildrone deployment, the two MISST Saildrones carry additional sub-surface  
2705 thermometers, and also a pair of infrared radiometers, one viewing the sea-surface ahead of the  
2706 Saildrone, and the other viewing the sky to provide data for the correction of reflected sky

2707 radiation to permit the retrieval of  $SST_{skin}$  from the Saildrone. It is anticipated that similar  
2708 Saildrone deployments will be made in the summers of the next several years.

2709



2710

2711 *Figure 28: The track of the Saildrone deployment from April 11, 2018-June 11, 2018 (top left), colored by*  
2712 *the measured SST, as indicated by the temperature scale at right. Other panels show the differences*  
2713 *between three L4 satellite-derived SST fields and the Saildrone measurements, colored according to the*  
2714 *temperature difference scale at far right. After Vazquez-Cuervo et al. (2019).*

2715 As with UAVs carrying radiometers, ASVs can make high-resolution measurements along their  
2716 track.

2717

Table 4: Statistics of differences between L4 satellite-derived SST fields and Saildrone measurements (After Vazquez-Cuervo et al., 2019).

| <b>Parameter</b> | <b>Bias (K)</b> | <b>RMSD (K)</b> | <b>Correlation<br/>(R)</b> | <b>Signal-to-Noise<br/>Ratio</b> |
|------------------|-----------------|-----------------|----------------------------|----------------------------------|
| CMC              | -0.03           | 0.43            | 0.97                       | 4.3                              |
| OSTIA            | 0.04            | 0.39            | 0.98                       | 5.0                              |
| MUR              | 0.32            | 0.42            | 0.97                       | 4.4                              |

The Signal to Noise Ratio indicates that the signal, as defined by each of the satellite derived data sets, is significantly larger than the noise, as defined by the differences between the satellite derived product and Saildrone

### 2718 **15.3 Gridded SST analyses**

2719 For the gridded (L3 and L4) SST analyses in the near future, wider availability of 1-km and  
 2720 higher spatial resolution L2 input data sets such as VIIRS, SGLI, SLSTR, and METimage, and  
 2721 new-generation geostationary imagery could lead to new practices in data interpolation. The  
 2722 analysis interval would need to be shortened to a sub-daily level to avoid aliasing of the sub-10  
 2723 km scale SST features which tend to evolve faster than their mesoscale counterparts.

2724 The current NOAA 5 km Geostationary-Polar SST Analyses are generated on a daily basis for  
 2725 day and night, nighttime and diurnally corrected L4 products (Maturi et al., 2017). The  
 2726 availability of new, rapidly-sampled SST retrievals from geostationary satellites complemented  
 2727 by high latitude sampling from the new polar-orbiting sensors will support the development of a

2728 unified methodology to investigate the global characteristics of diurnal variability. This will  
2729 support the optimal integration of diurnal variability in operational modelling systems, leading to  
2730 improved L4 SST analyses products that resolve the daily cycle. The analysis methodology could  
2731 build on that used in the current Geo-Polar Blended SST analysis (Maturi et al., 2017) but  
2732 applied at a higher resolution. This will provide detection of high resolution spatial and temporal  
2733 variability in coastal regions for the protection, restoration and management of coastal and ocean  
2734 resources through ecosystem-based management, and contribute a better understanding of  
2735 climate variability and change.

2736 Another aspect related to the generation of L4 SST fields, in addition to diurnal temperature  
2737 effects, is the drastic difference in L2 sample density between areas with and without sensor  
2738 coverage and this will need to be dealt with, perhaps by determining inter-sample correlations, to  
2739 avoid interpolation artifacts of numerical origin. The geolocation information in the L2 data sets  
2740 would also need to be fully accounted for, without truncating its sub-grid portion, to represent  
2741 SST features like front locations with higher fidelity.

#### 2742 **15.4 Ocean Heat Contents and Severe Storms**

2743 To improve our ability to resolve the sources and sinks of OHC in all ocean basins, at least three  
2744 radar altimeter missions are needed for sea surface height anomalies (SSHA) for adequate daily  
2745 sampling and to provide a realistic product for mesoscale oceanography needed for improved  
2746 forecasting of severe storms. Given that only 17-years of OHC are currently available, such  
2747 applied research efforts must continue over the next decade to build an evaluated data base,  
2748 useful also for climate studies. While OHC has been principally used during tropical cyclone  
2749 seasons, daily mapping also provides valuable data to address key science questions related to  
2750 climate, such as the extent of warming (or cooling) in the warm pools of the Atlantic and Pacific



2751 Oceans, thermodynamic processes in the equatorial wave guides associated with eastward  
2752 propagating Kelvin Waves, and linkages to the Madden-Julian Oscillation across the tropics.

2753 In the coastal regime, connections to the nation-wide array of high frequency surface current  
2754 radars and glider technologies will allow the derivation OHC closer to the coast. Thus, a more  
2755 complete picture will emerge of OHC variability for use in basic and applied research as well as  
2756 operations such as forecasting hurricane intensity change.

2757 Anticipated benefits include new understanding of upper ocean thermodynamics, dynamics and  
2758 air-sea processes relevant to tropical cyclone intensity forecasting, climate variability (e.g., SST  
2759 anomalies and OHC anomalies over various time and spatial scales), fisheries, coral reef  
2760 bleaching and air-sea fluxes. Over the longer term, the benefits will be for understanding climate  
2761 variability including SST and OHC anomalies across the ocean basins.

## 2762 **15.5 Data Distribution**

2763 In terms of data archive and distribution, the primary challenges for the future include allowing  
2764 access and manipulation to larger amounts of data over longer periods of time, developing cloud  
2765 technologies that allow users to implement their own processing algorithms (example cloud  
2766 masking/optimal interpolation), and visualization and extraction tools for near real time  
2767 applications. Data quality standards should be measured by two issues: 1) Adherence to metadata  
2768 standards that allow for interoperability, while maximizing implementation across a wide range  
2769 of tools and services and 2) access to validation (matchup databases) that allow users to assess  
2770 the quality of the data in their area of interest. Cloud technologies must be adopted cautiously,  
2771 as it will require major paradigm shifts in both accessing data and information. An associated  
2772 issue is ensuring that the user community is aware of new SST products, and of their strengths

2773 and weaknesses, so that new data sets that meet the users' requirements can be appropriately  
2774 exploited. Some further evolving aspects of data centers have already been discussed in Section  
2775 14.

## 2776 **16 Acknowledgements**

2777 PJM acknowledges support from the NASA Physical Oceanography Program. The contributions  
2778 by TMC and JV to this paper were carried out at the Jet Propulsion Laboratory (JPL), California  
2779 Institute of Technology, under a contract with the National Aeronautics and Space  
2780 Administration (NASA). MAS acknowledges support from ONR N00014-17-1-2545, NSF OPP-  
2781 1751363, and NASA 80NSSC18K0837. IK is supported by the Copernicus & Mercator-Ocean  
2782 through the Service Evolution Call 2 project DIVOST-COM.

2783 The authors thank Dr. C. J. Merchant for providing a preprint of the paper (Merchant et al.,  
2784 2019) to support the description (in Section 5.1.2) of the generation of the AVHRR time series of  
2785 consistent SSTs.

2786 Authors affiliated with NOAA state that their views, opinions, and findings contained in this  
2787 paper are their own and should not be construed as an official NOAA or U.S. Government  
2788 position, policy, or decision.

2789 Apologies to those whose work was not included here, even though it may have made a  
2790 significant contribution to the progress in the field, but were simply a casualty of limited space.

2791 Declarations of interest: none.

2792 The authors acknowledge with thanks the suggestions and comments from three reviewers as  
2793 these have resulted in an improved paper.

2794 **17 References**

- 2795 Aagaard, K., & Carmack, E.C. (1989). The role of sea ice and other fresh water in the Arctic  
 2796 circulation. *Journal of Geophysical Research* 94, 14485-14498.
- 2797 Adebisi, A.A., Zuidema, P., & Abel, S.J. (2015). The Convolution of Dynamics and Moisture  
 2798 with the Presence of Shortwave Absorbing Aerosols over the Southeast Atlantic. *Journal of*  
 2799 *Climate* 28, 1997-2024. 10.1175/jcli-d-14-00352.1
- 2800 Albuissou, M., Pontier, L., & Wald, L. (1979). A comparison between sea surface temperature  
 2801 measurements from satellite NOAA 4 and from airborne radiometer ARIES. *Oceanologica Acta*  
 2802 2, 1-4.
- 2803 Allison, L.J., & Kennedy, J.S. (1967). An Evaluation of Sea Surface Temperature as Measured  
 2804 by the Nimbus I High Resolution Infrared Radiometer, *NASA Technical Note*, NASA TN D-  
 2805 4078, (26 pp.). Washington DC, USA: NASA. Available at  
 2806 <https://ntrs.nasa.gov/archive/nasa/casi.ntrs.nasa.gov/19680000754.pdf>.
- 2807 Alvera-Azcárate, A., Barth, A., Beckers, J.-M., & Weisberg, R.H. (2007). Multivariate  
 2808 reconstruction of missing data in sea surface temperature, chlorophyll, and wind satellite fields.  
 2809 *Journal of Geophysical Research: Oceans* 112. doi:10.1029/2006JC003660
- 2810 Alvera-Azcárate, A., Barth, A., Rixen, M., & Beckers, J.M. (2005). Reconstruction of  
 2811 incomplete oceanographic data sets using empirical orthogonal functions: application to the  
 2812 Adriatic Sea surface temperature. *Ocean Modelling* 9, 325-346.  
 2813 <https://doi.org/10.1016/j.ocemod.2004.08.001>
- 2814 Alvera-Azcárate, A., Barth, A., Sirjacobs, D., & Beckers, J.M. (2009). Enhancing temporal  
 2815 correlations in EOF expansions for the reconstruction of missing data using DINEOF. *Ocean Sci.*  
 2816 5, 475-485. 10.5194/os-5-475-2009
- 2817 Aminou, D.M.A. (2002). MSG's SEVIRI instrument. *ESA Bulletin* 11, 15-17.
- 2818 Anding, D., & Kauth, R. (1970). Estimation of sea-surface temperature from space. *Remote*  
 2819 *Sensing of Environment* 1, 217-220.
- 2820 Arribas, A., Glover, M., Maidens, A., Peterson, K., Gordon, M., MacLachlan, C., Graham, R.,  
 2821 Fereday, D., Camp, J., Scaife, A.A., Xavier, P., McLean, P., Colman, A., & Cusack, S. (2011).  
 2822 The GloSea4 Ensemble Prediction System for Seasonal Forecasting. *Monthly Weather Review*  
 2823 139, 1891-1910. 10.1175/2010mwr3615.1
- 2824 Atkinson, C.P., Rayner, N.A., Kennedy, J.J., & Good, S.A. (2014). An integrated database of  
 2825 ocean temperature and salinity observations. *Journal of Geophysical Research: Oceans* 119,  
 2826 7139-7163. doi:10.1002/2014JC010053
- 2827 Aumann, H.H., Chahine, M.T., Gautier, C., Goldberg, M.D., Kalnay, E., L. M. McMillin,  
 2828 Revercomb, H., Rosenkranz, P.W., Smith, W.L., Staelin, D.H., Strow, L.L., & Susskind, J.  
 2829 (2003). AIRS/AMSU/HSB on the Aqua Mission: Design, science objectives, data products, and  
 2830 processing systems. *IEEE Transactions Geoscience and Remote Sensing* 41, 253-264.
- 2831 Aumann, H.H., & Pagano, T.S. (2008). Using AIRS and IASI data to evaluate absolute  
 2832 radiometric accuracy and stability for climate applications. In *Proceedings of Optical*  
 2833 *Engineering + Applications*, 7085, (5 pp): SPIE. doi:  
 2834 Banzon, V.F., Reynolds, R.W., Stokes, D., & Xue, Y. (2014). A 1/4°-Spatial-Resolution Daily  
 2835 Sea Surface Temperature Climatology Based on a Blended Satellite and in situ Analysis. *Journal*  
 2836 *of Climate* 27, 8221-8228. 10.1175/JCLI-D-14-00293.1

2837 Barsi, J.A., Markham, B.L., Czapla-Myers, J.S., Helder, D.L., Hook, S.J., Schott, J.R., & Haque,  
2838 M.O. (2016). Landsat-7 ETM+ radiometric calibration status. In Proceedings of SPIE Earth  
2839 Observing Systems XXI, 9972, (12 pp): SPIE. doi: 10.1117/12.2238625

2840 Barton, I.J. (1985). Transmission model and ground truth investigation of satellite derived sea  
2841 surface temperatures. *J. Climate and Appl. Met.* 24, 508-516.

2842 Barton, I.J. (1989). Digitization effects in AVHRR and MCSST data. *Remote Sensing of*  
2843 *Environment* 29, 87-89. [https://doi.org/10.1016/0034-4257\(89\)90081-3](https://doi.org/10.1016/0034-4257(89)90081-3)

2844 Barton, I.J. (1995). Satellite-derived sea surface temperatures: Current status. *Journal of*  
2845 *Geophysical Research* 100, 8777-8790.

2846 Barton, I.J., Minnett, P.J., Donlon, C.J., Hook, S.J., Jessup, A.T., Maillet, K.A., & Nightingale,  
2847 T.J. (2004). The Miami2001 infrared radiometer calibration and inter-comparison: 2. Ship  
2848 comparisons. *Journal of Atmospheric and Oceanic Technology* 21, 268-283.

2849 Bates, J.J., & Smith, W.L. (1985). Sea surface temperature: Observations from geostationary  
2850 satellites. *Journal of Geophysical Research: Oceans* 90, 11609-11618.  
2851 [10.1029/JC090iC06p11609](https://doi.org/10.1029/JC090iC06p11609)

2852 Beggs, H. (2010). Use of TIR from Space in Operational Systems. In V. Barale, J.F.R. Gower, &  
2853 L. Alberotanza (Eds.), *Oceanography from Space Revisited* (pp. 249-271). Dordrecht: Springer  
2854 Science+Business Media B.V. ISBN 978-90-481-8681-5. DOI: [https://doi.org/10.1007/978-90-](https://doi.org/10.1007/978-90-481-8681-5)  
2855 [481-8681-5](https://doi.org/10.1007/978-90-481-8681-5).

2856 Behrenfeld, M.J., & Falkowski, P.G. (1997). Photosynthetic Rates Derived from Satellite-based  
2857 Chlorophyll Concentration. *Limnol. Oceanogr.* 21, 1-20.

2858 Behrenfeld, M.J., O'Malley, R.T., Siegel, D.A., McClain, C.R., Sarmiento, J.L., Feldman, G.C.,  
2859 Milligan, A.J., Falkowski, P.G., Letelier, R.M., & Boss, E.S. (2006). Climate-driven trends in  
2860 contemporary ocean productivity. *Nature* 444, 752. [10.1038/nature05317](https://doi.org/10.1038/nature05317),  
2861 <https://www.nature.com/articles/nature05317#supplementary-information>

2862 Bell, M., J., Lefèbvre, M., Le Traon, P.-Y., Smith, N., & Wilmer-Becker, K. (2009). GODAE:  
2863 The Global Ocean Data Assimilation Experiment. *Oceanography* 22, 14.  
2864 <https://doi.org/10.5670/oceanog.2009.62>

2865 Bell, M.J., Forbes, R.M., & Hines, A. (2000). Assessment of the FOAM global data assimilation  
2866 system for real-time operational ocean forecasting. *Journal of Marine Systems* 25, 1-22.

2867 Bellenger, H., & Duvel, J.-P. (2009). An Analysis of Tropical Ocean Diurnal Warm Layers.  
2868 *Journal of Climate* 22, 3629-3646. [10.1175/2008JCLI2598.1](https://doi.org/10.1175/2008JCLI2598.1)

2869 Bentamy, A., Katsaros, K., & Queffelec, P. (2011). Satellite Air – Sea Fluxes. In D. Tang (Ed.),  
2870 *Remote Sensing of the Changing Oceans* (pp. 141-168): Springer Berlin Heidelberg. 978-3-642-  
2871 16540-5. [10.1007/978-3-642-16541-2\\_8](https://doi.org/10.1007/978-3-642-16541-2_8).

2872 Bentamy, A., Piollé, J.F., Grouazel, A., Danielson, R., Gulev, S., Paul, F., Azelmat, H., Mathieu,  
2873 P.P., von Schuckmann, K., Sathyendranath, S., Evers-King, H., Esau, I., Johannessen, J.A.,  
2874 Clayson, C.A., Pinker, R.T., Grodsky, S.A., Bourassa, M., Smith, S.R., Haines, K., Valdivieso,  
2875 M., Merchant, C.J., Chapron, B., Anderson, A., Hollmann, R., & Josey, S.A. (2017). Review and  
2876 assessment of latent and sensible heat flux accuracy over the global oceans. *Remote Sensing of*  
2877 *Environment* 201, 196-218. <https://doi.org/10.1016/j.rse.2017.08.016>

2878 Bermudo, F., Rousseau, S., Pequignot, E., & Bernard, F. (2014). IASI-NG program: A new  
2879 generation of Infrared Atmospheric Sounding Interferometer. In Proceedings of 2014 IEEE  
2880 Geoscience and Remote Sensing Symposium, (1373-1376 pp). doi:  
2881 [10.1109/IGARSS.2014.6946690](https://doi.org/10.1109/IGARSS.2014.6946690)

2882 Berry, D., Corlett, G., Embury, O., & Merchant, C. (2018). Stability Assessment of the (A)ATSR  
2883 Sea Surface Temperature Climate Dataset from the European Space Agency Climate Change  
2884 Initiative. *Remote Sensing* 10, 126.

2885 Bertie, J.E., & Lan, Z.D. (1996). Infrared intensities of liquids XX: the intensity of the OH  
2886 stretching band revisited, and the best current values of the optical constants of H<sub>2</sub>O (l) at 25°C  
2887 between 15,000 and 1 cm<sup>-1</sup>. *App. Spectroscopy* 50, 1047-1057.

2888 Bessho, K., Date, K., Hayashi, M., Ikeda, A., Imai, T., Inoue, H., Kumagai, Y., Miyakawa, T.,  
2889 Murata, H., Ohno, T., Okuyama, A., Oyama, R., Sasaki, Y., Shimazu, Y., Shimoji, K., Sumida,  
2890 Y., Suzuki, M., Taniguchi, H., Tsuchiyama, H., Uesawa, D., Yokota, H., & Yoshida, R. (2016).  
2891 An Introduction to Himawari-8/9 - Japan's New-Generation Geostationary Meteorological  
2892 Satellites. *Journal of the Meteorological Society of Japan. Ser. II* 94, 151-183.  
2893 10.2151/jmsj.2016-009

2894 Bhatt, R., Doelling, D.R., Scarino, B.R., Gopalan, A., Haney, C.O., Minnis, P., & Bedka, K.M.  
2895 (2016). A Consistent AVHRR Visible Calibration Record Based on Multiple Methods  
2896 Applicable for the NOAA Degrading Orbits. Part I: Methodology. *Journal of Atmospheric and*  
2897 *Oceanic Technology* 33, 2499-2515. 10.1175/jtech-d-16-0044.1

2898 Blumstein, D., Chalon, G., Carlier, T., Buil, C., Hebert, P., Maciaszek, T., Ponce, G., Phulpin,  
2899 T., Tournier, B., Simeoni, D., Astruc, P., Clauss, A., Kayal, G., & Jegou, R. (2004). IASI  
2900 instrument: technical overview and measured performances. In Proceedings of Proceedings of  
2901 Infrared Spaceborne Remote Sensing XII, SPIE Vol. 5543, Bellingham, WA, M. Strojnik (Ed.),  
2902 5543, (196-207 pp): SPIE. doi: doi: 10.1117/12.560907

2903 Bogdanoff, A.S., Westphal, D.L., Campbell, J.R., Cummings, J.A., Hyer, E.J., Reid, J.S., &  
2904 Clayson, C.A. (2015). Sensitivity of infrared sea surface temperature retrievals to the vertical  
2905 distribution of airborne dust aerosol. *Remote Sensing of Environment* 159, 1-13.  
2906 <http://dx.doi.org/10.1016/j.rse.2014.12.002>

2907 Böhm, E., Marullo, S., & Santoleri, R. (1991). AVHRR visible-IR detection of diurnal warming  
2908 events in the western Mediterranean Sea. *Int. J. remote sensing*. 12, 695-701.

2909 Bojinski, S., Verstraete, M., Peterson, T.C., Richter, C., Simmons, A., & Zemp, M. (2014). The  
2910 Concept of Essential Climate Variables in Support of Climate Research, Applications, and  
2911 Policy. *Bulletin of the American Meteorological Society* 95, 1431-1443. 10.1175/bams-d-13-  
2912 00047.1

2913 Boussidi, B., Cornillon, P., Puggioni, G., & Gentemann, C. (2019). Determining the AMSR-E  
2914 SST Footprint from Co-Located MODIS SSTs. *Remote Sensing* 11, 715.

2915 Brando, V.E., Braga, F., Zaggia, L., Giardino, C., Bresciani, M., Matta, E., Bellafiore, D.,  
2916 Ferrarin, C., Maicu, F., Benetazzo, A., Bonaldo, D., Falcieri, F.M., Coluccelli, A., Russo, A., &  
2917 Carniel, S. (2015). High-resolution satellite turbidity and sea surface temperature observations of  
2918 river plume interactions during a significant flood event. *Ocean Sci.* 11, 909-920. 10.5194/os-11-  
2919 909-2015

2920 Brasnett, B. (1997). A Global Analysis of Sea Surface Temperature for Numerical Weather  
2921 Prediction. *Journal of Atmospheric and Oceanic Technology* 14, 925-937. 10.1175/1520-  
2922 0426(1997)014<0925:Agaoss>2.0.Co;2

2923 Brasnett, B. (2008). The impact of satellite retrievals in a global sea-surface-temperature  
2924 analysis. *Quarterly Journal of the Royal Meteorological Society* 134, 1745-1760. 10.1002/qj.319

2925 Brasnett, B., & Surcel-Colan, D. (2016). Assimilating Retrievals of Sea Surface Temperature  
2926 from VIIRS and AMSR2. *Journal of Atmospheric and Oceanic Technology* 33, 361-375.  
2927 10.1175/jtech-d-15-0093.1

2928 Broecker, W.S. (1991). The great ocean conveyor. *Oceanography* 42, 79-89.

2929 Brown, O.B., Brown, J.W., & Evans, R.H. (1985). Calibration of advanced very high resolution  
 2930 radiometer infrared observations. *Journal of Geophysical Research: Oceans* 90, 11667-11677.  
 2931 10.1029/JC090iC06p11667

2932 Bulgin, C.E., Embury, O., Corlett, G., & Merchant, C.J. (2016). Independent uncertainty  
 2933 estimates for coefficient based sea surface temperature retrieval from the Along-Track Scanning  
 2934 Radiometer instruments. *Remote Sensing of Environment* 178, 213-222.  
 2935 <http://dx.doi.org/10.1016/j.rse.2016.02.022>

2936 Bulgin, C.E., Mittaz, J.P.D., Embury, O., Eastwood, S., & Merchant, C.J. (2018). Bayesian  
 2937 Cloud Detection for 37 Years of Advanced Very High Resolution Radiometer (AVHRR) Global  
 2938 Area Coverage (GAC) Data. *Remote Sensing* 10, 97.

2939 Buongiorno Nardelli, B., Droghei, R., & Santoleri, R. (2016). Multi-dimensional interpolation of  
 2940 SMOS sea surface salinity with surface temperature and in situ salinity data. *Remote Sensing of*  
 2941 *Environment* 180, 392-402. <http://dx.doi.org/10.1016/j.rse.2015.12.052>

2942 Buongiorno Nardelli, B., Larnicol, G., D'Acunzo, E., Santoleri, R., Marullo, S., & Le Traon,  
 2943 P.Y. (2003). Near Real Time SLA and SST products during 2-years of MFS pilot project:  
 2944 processing, analysis of the variability and of the coupled patterns. *Annales Geophysicae* 21, 103-  
 2945 121.

2946 Buongiorno Nardelli, B., Pisano, A., Tronconi, C., & Santoleri, R. (2015). Evaluation of  
 2947 different covariance models for the operational interpolation of high resolution satellite Sea  
 2948 Surface Temperature data over the Mediterranean Sea. *Remote Sensing of Environment* 164, 334-  
 2949 343. <https://doi.org/10.1016/j.rse.2015.04.025>

2950 Buongiorno Nardelli, B., S.Marullo, & Santoleri, R. (2005). Diurnal variations in AVHRR SST  
 2951 fields: A strategy for removing warm layer effects from daily images. *Remote Sensing of*  
 2952 *Environment*, 47-56.

2953 Buongiorno Nardelli, B., Tronconi, C., Pisano, A., & Santoleri, R. (2013). High and Ultra-High  
 2954 resolution processing of satellite Sea Surface Temperature data over Southern European Seas in  
 2955 the framework of MyOcean project. *Remote Sensing of Environment* 129, 1-16.  
 2956 <https://doi.org/10.1016/j.rse.2012.10.012>

2957 Carnes, M.R., Teague, W.J., & Mitchell, J.L. (1994). Inference of Subsurface Thermohaline  
 2958 Structure from Fields Measurable by Satellite. *Journal of Atmospheric and Oceanic Technology*  
 2959 11, 551-566. 10.1175/1520-0426(1994)011<0551:Iostsf>2.0.Co;2

2960 Casey, K.S., Brandon, T.B., Cornillon, P., & Evans, R. (2010). The Past, Present, and Future of  
 2961 the AVHRR Pathfinder SST Program. In V. Barale, J.F.R. Gower, & L. Alberotanza (Eds.),  
 2962 *Oceanography from Space: Revisited* (pp. 273-287). Dordrecht: Springer Netherlands. 978-90-  
 2963 481-8681-5. 10.1007/978-90-481-8681-5\_16.

2964 Casey, K.S., & Cornillon, P. (2001). Global and Regional Sea Surface Temperature Trends.  
 2965 *Journal of Climate* 14, 3801-3818.

2966 Castro, S., Emery, W., Wick, G., & Tandy, W. (2017). Submesoscale Sea Surface Temperature  
 2967 Variability from UAV and Satellite Measurements. *Remote Sensing* 9, 1089.  
 2968 doi:10.3390/rs9111089

2969 Castro, S.L., Monzon, L.A., Wick, G.A., Lewis, R.D., & Beylkin, G. (2018). Subpixel variability  
 2970 and quality assessment of satellite sea surface temperature data using a novel High Resolution  
 2971 Multistage Spectral Interpolation (HRMSI) technique. *Remote Sensing of Environment* 217, 292-  
 2972 308. <https://doi.org/10.1016/j.rse.2018.08.019>

2973 Castro, S.L., Wick, G.A., & Buck, J.J.H. (2014). Comparison of diurnal warming estimates from  
2974 unpumped Argo data and SEVIRI satellite observations. *Remote Sensing of Environment* 140,  
2975 789-799. <http://dx.doi.org/10.1016/j.rse.2013.08.042>

2976 Castro, S.L., Wick, G.A., & Emery, W.J. (2012). Evaluation of the relative performance of sea  
2977 surface temperature measurements from different types of drifting and moored buoys using  
2978 satellite-derived reference products. *J. Geophys. Res.* 117, C02029. 10.1029/2011jc007472

2979 Castro, S.L., Wick, G.A., & Steele, M. (2016). Validation of satellite sea surface temperature  
2980 analyses in the Beaufort Sea using UpTempO buoys. *Remote Sensing of Environment* 187, 458-  
2981 475. <http://dx.doi.org/10.1016/j.rse.2016.10.035>

2982 Cavalieri, D.J., & Parkinson, C.L. (2012). Arctic sea ice variability and trends, 1979-2010. *The*  
2983 *Cryosphere* 6, 881-889. 10.5194/tc-6-881-2012

2984 Cazenave, A., & Nerem, R.S. (2004). Present-day sea level change: Observations and causes.  
2985 *Reviews of Geophysics* 42. doi:10.1029/2003RG000139

2986 Chassignet, E.P., & Xu, X. (2017). Impact of Horizontal Resolution (1/12° to 1/50°) on Gulf  
2987 Stream Separation, Penetration, and Variability. *Journal of Physical Oceanography* 47, 1999-  
2988 2021. 10.1175/jpo-d-17-0031.1

2989 Cheng, X., Qi, Y., & Zhou, W. (2008). Trends of sea level variations in the Indo-Pacific warm  
2990 pool. *Global and Planetary Change* 63, 57-66. <https://doi.org/10.1016/j.gloplacha.2008.06.001>

2991 Chin, T.M., Vazquez-Cuervo, J., & Armstrong, E.M. (2014). On “Gridless” Interpolation and  
2992 Subgrid Data Density. *Journal of Atmospheric and Oceanic Technology* 31, 1642-1652.  
2993 10.1175/jtech-d-13-00219.1

2994 Chin, T.M., Vazquez-Cuervo, J., & Armstrong, E.M. (2017). A multi-scale high-resolution  
2995 analysis of global sea surface temperature. *Remote Sensing of Environment* 200, 154-169.  
2996 <https://doi.org/10.1016/j.rse.2017.07.029>

2997 Cho, Y.-M., & Youn, H.-S. (2006). Characteristics of COMS Meteorological Imager. In  
2998 Proceedings of SPIE Remote Sensing, 6361, (8 pp): SPIE. doi:  
2999 Clayson, C.A., & Bogdanoff, A.S. (2013). The Effect of Diurnal Sea Surface Temperature  
3000 Warming on Climatological Air–Sea Fluxes. *Journal of Climate* 26, 2546-2556. 10.1175/JCLI-  
3001 D-12-00062.1

3002 Clayson, C.A., & Curry, J.A. (1996). Determination of surface turbulent fluxes for the Tropical  
3003 Ocean-Global Atmosphere Response Experiment: Comparison of satellite retrievals and in situ  
3004 measurements. *Journal of Geophysical Research* 101, 28,515 - 528,528.

3005 Clayson, C.A., & Weitlich, D. (2007). Variability of Tropical Diurnal Sea Surface Temperature.  
3006 *Journal of Climate* 20, 334-352. 10.1175/JCLI3999.1

3007 Clough, S.A., Shephard, M.W., Mlawer, E.J., Delamere, J.S., Iacono, M.J., Cady-Pereira, K.,  
3008 Boukabara, S., & Brown, P.D. (2005). Atmospheric radiative transfer modeling: a summary of  
3009 the AER codes. *Journal of Quantitative Spectroscopy and Radiative Transfer* 91, 233-244.  
3010 doi:10.1016/j.jqsrt.2004.05.058

3011 Coll, C., Caselles, V., & Valor, E. (1993). Atmospheric correction and determination of sea  
3012 surface temperature in midlatitudes from NOAA-AVHRR data. *Atmospheric Research* 30, 233-  
3013 250. [https://doi.org/10.1016/0169-8095\(93\)90026-K](https://doi.org/10.1016/0169-8095(93)90026-K)

3014 Corlett, G.K., Merchant, C.J., Minnett, P.J., & Donlon, C.J. (2014). Assessment of Long-Term  
3015 Satellite Derived Sea Surface Temperature Records. In G. Zibordi, C.J. Donlon, & A.C. Parr  
3016 (Eds.), *Experimental Methods in the Physical Sciences, Vol 47, Optical Radiometry for Ocean*  
3017 *Climate Measurements* (pp. 639-677): Academic Press. 1079-4042.  
3018 <http://dx.doi.org/10.1016/B978-0-12-417011-7.00021-0>.

3019 Cornillon, P., G. Pan, & Schloesser, F. (2014). The Submesoscale from VIIRS Imagery-Band  
3020 (375 m) Sea Surface Temperature Fields. Presented at AGU Fall Meeting, San Francisco, CA,  
3021 USA. (<https://agu.confex.com/agu/fm14/webprogram/Paper4205.html>),  
3022 Cornillon, P., & Stramma, L. (1985). The distribution of diurnal sea surface warming events in  
3023 the Western Sargasso Sea. *J. Geophys. Res.* 90, 11,811-811, 815.  
3024 Cotroneo, Y., Aulicino, G., Ruiz, S., Pascual, A., Budillon, G., Fusco, G., & Tintoré, J. (2016).  
3025 Glider and satellite high resolution monitoring of a mesoscale eddy in the algerian basin: Effects  
3026 on the mixed layer depth and biochemistry. *Journal of Marine Systems* 162, 73-88.  
3027 <https://doi.org/10.1016/j.jmarsys.2015.12.004>  
3028 Cox, C., & Munk, W. (1954). Statistics of the sea surface derived from sun glitter. *Journal of*  
3029 *Marine Research* 13, 198-227.  
3030 Cracknell, A.P. (1997). *The Advanced Very High Resolution Radiometer* London, UK: CRC  
3031 Press, Taylor and Francis. ISBN 9780748402090  
3032 Crépon, M., Wald, L., & Monget, J.-M. (1982). Low-frequency waves in the Ligurian Sea during  
3033 December 1977. *Journal of Geophysical Research: Oceans* 87, 595-600.  
3034 Crevoisier, C., Clerbaux, C., Guidard, V., Phulpin, T., Armante, R., Barret, B., Camy-Peyret, C.,  
3035 Chaboureaud, J.P., Coheur, P.F., Crépeau, L., Dufour, G., Labonnote, L., Lavanant, L., Hadji-  
3036 Lazaro, J., Herbin, H., Jacquinet-Husson, N., Payan, S., Péquignot, E., Pierangelo, C., Sellitto,  
3037 P., & Stubenrauch, C. (2014). Towards IASI-New Generation (IASI-NG): impact of improved  
3038 spectral resolution and radiometric noise on the retrieval of thermodynamic, chemistry and  
3039 climate variables. *Atmos. Meas. Tech.* 7, 4367-4385. 10.5194/amt-7-4367-2014  
3040 Dalu, G., Viola, A., & Marullo, S. (1985). Sea surface temperature from AVHRR-2 data. *Il*  
3041 *Nuovo Cimento C* 8, 793-804. 10.1007/bf02558011  
3042 Danabasoglu, G., Large, W.G., Tribbia, J.J., Gent, P.R., Briegleb, B.P., & McWilliams, J.C.  
3043 (2006). Diurnal coupling in the tropical oceans of CCSM3. *Journal of Climate* 19, 2347-2365.  
3044 Dash, P., Ignatov, A., Kihai, Y., & Sapper, J. (2010). The SST Quality Monitor (SQUAM).  
3045 *Journal of Atmospheric and Oceanic Technology* 27, 1899-1917. 10.1175/2010jtecho756.1  
3046 Dash, P., Ignatov, A., Martin, M., Donlon, C., Brasnett, B., Reynolds, R.W., Banzon, V., Beggs,  
3047 H., Cayula, J.-F., Chao, Y., Grumbine, R., Maturi, E., Harris, A., Mittaz, J., Sapper, J., Chin,  
3048 T.M., Vazquez-Cuervo, J., Armstrong, E.M., Gentemann, C., Cummings, J., Piollé, J.-F., Autret,  
3049 E., Roberts-Jones, J., Ishizaki, S., Høyer, J.L., & Poulter, D. (2012). Group for High Resolution  
3050 Sea Surface Temperature (GHRSSST) analysis fields inter-comparisons—Part 2: Near real time  
3051 web-based level 4 SST Quality Monitor (L4-SQUAM). *Deep Sea Research Part II: Topical*  
3052 *Studies in Oceanography* 77–80, 31-43. 10.1016/j.dsr2.2012.04.002  
3053 Dee, D.P., Uppala, S.M., Simmons, A.J., Berrisford, P., Poli, P., Kobayashi, S., Andrae, U.,  
3054 Balmaseda, M.A., Balsamo, G., Bauer, P., Bechtold, P., Beljaars, A.C.M., van de Berg, L.,  
3055 Bidlot, J., Bormann, N., Delsol, C., Dragani, R., Fuentes, M., Geer, A.J., Haimberger, L., Healy,  
3056 S.B., Hersbach, H., Hólm, E.V., Isaksen, L., Kållberg, P., Köhler, M., Matricardi, M., McNally,  
3057 A.P., Monge-Sanz, B.M., Morcrette, J.J., Park, B.K., Peubey, C., de Rosnay, P., Tavolato, C.,  
3058 Thépaut, J.N., & Vitart, F. (2011). The ERA-Interim reanalysis: configuration and performance  
3059 of the data assimilation system. *Quarterly Journal of the Royal Meteorological Society* 137, 553-  
3060 597. 10.1002/qj.828  
3061 Delworth, T.L., Ramaswamy, V., & Stenchikov, G.L. (2005). The impact of aerosols on  
3062 simulated ocean temperature and heat content in the 20th century. *Geophysical Research Letters*  
3063 32. 10.1029/2005gl024457



3064 Deschamps, P.Y., & Frouin, R. (1984). Large diurnal heating of the sea surface observed by the  
3065 HCMR Experiment. *J. Phys. Oceanogr.* 14, 177-184.

3066 Desnos, Y., Borgeaud, M., Doherty, M., Rast, M., & Liebig, V. (2014). The European Space  
3067 Agency's Earth Observation Program. *IEEE Geoscience and Remote Sensing Magazine* 2, 37-46.  
3068 10.1109/MGRS.2014.2319270

3069 Díaz, J.P., Arbelo, M., Expósito, F.J., Podestá, G., Prospero, J.M., & Evans, R. (2001).  
3070 Relationship between errors in AVHRR-derived sea surface temperature and the TOMS Aerosol  
3071 Index. *Geophysical Research Letters* 28, 1989-1992.

3072 Dong, B., Dai, A., Vuille, M., & Timm, O.E. (2018). Asymmetric Modulation of ENSO  
3073 Teleconnections by the Interdecadal Pacific Oscillation. *Journal of Climate* 31, 7337-7361.  
3074 10.1175/jcli-d-17-0663.1

3075 Donlon, C., Berruti, B., Buongiorno, A., Ferreira, M.H., Féménias, P., Frerick, J., Goryl, P.,  
3076 Klein, U., Laur, H., Mavrocordatos, C., Nieke, J., Rebhan, H., Seitz, B., Stroede, J., & Sciarra, R.  
3077 (2012a). The Global Monitoring for Environment and Security (GMES) Sentinel-3 mission.  
3078 *Remote Sensing of Environment* 120, 37-57. 10.1016/j.rse.2011.07.024

3079 Donlon, C., Robinson, I.S., Reynolds, M., Wimmer, W., Fisher, G., Edwards, R., & Nightingale,  
3080 T.J. (2008). An Infrared Sea Surface Temperature Autonomous Radiometer (ISAR) for  
3081 Deployment aboard Volunteer Observing Ships (VOS). *Journal of Atmospheric and Oceanic*  
3082 *Technology* 25, 93-113.

3083 Donlon, C.J., K.S. Casey, I.S. Robinson, C.L. Gentemann, R.W. Reynolds, I. Barton, O. Arino,  
3084 J. Stark, N. Rayner, P. LeBorgne, D. Poulter, J. Vazquez-Cuervo, E. Armstrong, H. Beggs, D.  
3085 Llewellyn-Jones, P.J. Minnett, C.J. Merchant, & Evans, R. (2009). The GODAE High-  
3086 Resolution Sea Surface Temperature Pilot Project. *Oceanography* 22, 34-45.

3087 Donlon, C.J., Martin, M., Stark, J., Roberts-Jones, J., Fiedler, E., & Wimmer, W. (2012b). The  
3088 Operational Sea Surface Temperature and Sea Ice Analysis (OSTIA) system. *Remote Sensing of*  
3089 *Environment* 116, 140-158. 10.1016/j.rse.2010.10.017

3090 Donlon, C.J., Minnett, P.J., Gentemann, C., Nightingale, T.J., Barton, I.J., Ward, B., & Murray,  
3091 J. (2002). Toward improved validation of satellite sea surface skin temperature measurements for  
3092 climate research. *Journal of Climate* 15, 353-369. doi: 10.1175/1520-  
3093 0442(2002)015<0353:TIVOSS>2.0.CO;2

3094 Donlon, C.J., Minnett, P.J., Jessup, A., Barton, I., Emery, W., Hook, S., Wimmer, W.,  
3095 Nightingale, T.J., & Zappa, C. (2014). Ship-Borne Thermal Infrared Radiometer Systems. In G.  
3096 Zibordi, C.J. Donlon, & A.C. Parr (Eds.), *Experimental Methods in the Physical Sciences, Vol*  
3097 *47, Optical Radiometry for Ocean Climate Measurements* (pp. 305-404): Academic Press. 1079-  
3098 4042. <http://dx.doi.org/10.1016/B978-0-12-417011-7.00011-8>.

3099 Donlon, C.J., & Nightingale, T.J. (2000). The effect of atmospheric radiance errors in  
3100 radiometric sea-surface skin temperature measurements. *Applied Optics* 39, 2387-2392.

3101 Donlon, C.J., Robinson, I., Casey, K.S., Vazquez-Cuervo, J., Armstrong, E., Arino, O.,  
3102 Gentemann, C., May, D., LeBorgne, P., Piollé, J., Barton, I., Beggs, H., Poulter, D.J.S.,  
3103 Merchant, C.J., Bingham, A., Heinz, S., Harris, A., Wick, G., Emery, B., Minnett, P., Evans, R.,  
3104 Llewellyn-Jones, D., Mutlow, C., Reynolds, R.W., Kawamura, H., & Rayner, N. (2007). The  
3105 Global Ocean Data Assimilation Experiment High-resolution Sea Surface Temperature Pilot  
3106 Project. *Bulletin of the American Meteorological Society* 88, 1197-1213.

3107 Draper, D.W., Newell, D.A., Wentz, F.J., Krimchansky, S., & Skofronick-Jackson, G.M. (2015).  
3108 The Global Precipitation Measurement (GPM) Microwave Imager (GMI): Instrument Overview

3109 and Early On-Orbit Performance. *IEEE Journal of Selected Topics in Applied Earth*  
3110 *Observations and Remote Sensing* 8, 3452-3462. 10.1109/JSTARS.2015.2403303  
3111 Drinkwater, M.R., H.; Le Traon, P. Y.; Phalippou, L.; Cotton, D.; Johannesen, J.; Ruffini, G.;  
3112 Bahurel, P.; Bell, M.; Chapron, B.; Pinardi, N.; Robinson, I.; Santoleri, L.; Stammer, D. (2005).  
3113 Roadmap for a GMES Operational Oceanography Mission. In Proceedings of MERIS (A)ATSR  
3114 Workshop, ESRIN, Frascati, Italy, H. Lacoste (Ed.), ESA SP-597, (10 pp). doi:  
3115 Drinkwater, M.R., Kerr, Y., Font, J., & Berger, M. (2009). The Soil Moisture and Ocean Salinity  
3116 (SMOS) mission. *Bulletin of the European Space Agency* 137, 7-15.  
3117 Dubock, P., Spoto, F., Simpson, J., Spencer, D., Schutte, E., & Sontag, H. (2001). The Envisat  
3118 satellite and its integration. *ESA Bulletin* 106, 26-45.  
3119 Dudhia, A. (1989). Noise characteristics of the AVHRR infrared channels. *International Journal*  
3120 *of Remote Sensing* 10, 637-644. 10.1080/01431168908903904  
3121 Durand, Y., Hallibert, P., Wilson, M., Lekouara, M., Grabarnik, S., Aminou, D., Blythe, P.,  
3122 Napierala, B., Canaud, J.-L., Pigouche, O., Ouaknine, J., & Verez, B. (2015). The flexible  
3123 combined imager onboard MTG: from design to calibration. In Proceedings of SPIE Remote  
3124 Sensing, 9639, (14 pp): SPIE. doi: doi: 10.1117/12.2196644  
3125 Eastwood, S., Le Borgne, P., Péré, S., & Poulter, D. (2011). Diurnal variability in sea surface  
3126 temperature in the Arctic. *Remote Sensing of Environment* 115, 2594-2602.  
3127 <https://doi.org/10.1016/j.rse.2011.05.015>  
3128 Embury, O., & Merchant, C.J. (2012). A reprocessing for climate of sea surface temperature  
3129 from the along-track scanning radiometers: A new retrieval scheme. *Remote Sensing of*  
3130 *Environment* 116, 47-61. 10.1016/j.rse.2010.11.020  
3131 Embury, O., Merchant, C.J., & Filipiak, M.J. (2012). A reprocessing for climate of sea surface  
3132 temperature from the along-track scanning radiometers: Basis in radiative transfer. *Remote*  
3133 *Sensing of Environment* 116, 32-46. 10.1016/j.rse.2010.10.016  
3134 Emery, W.J., Good, W.S., Tandy, W., Izaguirre, M.A., & Minnett, P.J. (2014). A  
3135 Microbolometer Airborne Calibrated Infrared Radiometer: The Ball Experimental Sea Surface  
3136 Temperature (BESST) Radiometer. *Geoscience and Remote Sensing, IEEE Transactions on* 52,  
3137 7775-7781. 10.1109/TGRS.2014.2318683  
3138 Entekhabi, D., Njoku, E.G., Neill, P.E.O., Kellogg, K.H., Crow, W.T., Edelstein, W.N., Entin,  
3139 J.K., Goodman, S.D., Jackson, T.J., Johnson, J., Kimball, J., Piepmeier, J.R., Koster, R.D.,  
3140 Martin, N., McDonald, K.C., Moghaddam, M., Moran, S., Reichle, R., Shi, J.C., Spencer, M.W.,  
3141 Thurman, S.W., Tsang, L., & Zyl, J.V. (2010). The Soil Moisture Active Passive (SMAP)  
3142 Mission. *Proceedings of the IEEE* 98, 704-716. 10.1109/JPROC.2010.2043918  
3143 Esaias, W.E., Abbott, M.R., Barton, I., Brown, O.B., Campbell, J.W., Carder, K.L., Clark, D.K.,  
3144 Evans, R.H., Hoge, F.E., Gordon, H.R., Balch, W.M., Letelier, R., & Minnett, P.J. (1998). An  
3145 Overview of MODIS Capabilities for Ocean Science Observations. *IEEE Transactions on*  
3146 *Geoscience and Remote Sensing* 36, 1250-1265. doi: 10.1109/36.701076  
3147 European Space Agency (1999). *Meteosat Second Generation: The Satellite Development*. ESA  
3148 BR-153, (55 pp.). Noordwijk, The Netherlands: ESA ESTEC. Available at  
3149 <http://www.esa.int/esapub/br/br153/br153.pdf>.  
3150 Ezer, T. (2016). Revisiting the problem of the Gulf Stream separation: on the representation of  
3151 topography in ocean models with different types of vertical grids. *Ocean Modelling* 104, 15-27.  
3152 <https://doi.org/10.1016/j.ocemod.2016.05.008>

3153 Fairall, C., Bradley, E., Godfrey, J., Wick, G., Edson, J., & Young, G. (1996). Cool-skin and  
3154 warm-layer effects on sea surface temperature. *Journal of Geophysical Research*. 101, 1295-  
3155 1308.

3156 Fallmann, J., Lewis, H., Castillo, J.M., Arnold, A., & Ramsdale, S. (2017). Impact of sea surface  
3157 temperature on stratiform cloud formation over the North Sea. *Geophysical Research Letters* 44,  
3158 4296-4303. doi:10.1002/2017GL073105

3159 Feng, Z., Ji, R., Ashjian, C., Campbell, R., & Zhang, J. (2018). Biogeographic responses of the  
3160 copepod *Calanus glacialis* to a changing Arctic marine environment. *Global Change Biology* 24,  
3161 e159-e170. doi:10.1111/gcb.13890

3162 Fiedler, E.K., McLaren, A., Banzon, V., Brasnett, B., Ishizaki, S., Kennedy, J., Rayner, N.,  
3163 Roberts-Jones, J., Corlett, G., Merchant, C.J., & Donlon, C. (2019). Intercomparison of long-  
3164 term sea surface temperature analyses using the GHRSSST Multi-Product Ensemble (GMPE)  
3165 system. *Remote Sensing of Environment* 222, 18-33. <https://doi.org/10.1016/j.rse.2018.12.015>

3166 Filipiak, M., Merchant, C., Kettle, H., & Le Borgne, P. (2010). A statistical model for sea surface  
3167 diurnal warming driven by numerical weather prediction fluxes and winds. *Ocean Science*  
3168 *Discussions* 7

3169 Flament, P., Firing, M., Sawyer, M., & Trefois, C. (1994). Amplitude and horizontal structure of  
3170 a large diurnal sea surface warming event during the coastal ocean dynamics experiment.  
3171 *Journal of Physical Oceanography* 24, 124-139.

3172 Fox, N.P. (2010). QA4EO guide: A Guide to Establish a Quality Indicator on a Satellite Sensor  
3173 Derived Data Product (Version 4.0). QA4EO-QAEO-GEN-DQK-001, (7 pp.) Available at  
3174 Available online: [http://qa4eo.org/docs/QA4EO-QAEO-GEN-DQK-001\\_v4.0.pdf](http://qa4eo.org/docs/QA4EO-QAEO-GEN-DQK-001_v4.0.pdf) Accessed on  
3175 28 November 2018.

3176 Franklin, B., Folger, T., Wright, E., Halley, E., & Moll, H. (1768). Franklin-Folger chart of the  
3177 Gulf Stream. London: Mount and Page. <https://www.loc.gov/item/88696412/>. Retrieved from the  
3178 Library of Congress. Accessed November 1, 2017

3179 Freund, Y., & Mason, L. (1999). The alternating decision tree learning algorithm. In Proceedings  
3180 of Proceeding of the Sixteenth International Conference on Machine Learning, Bled, Slovenia, I.  
3181 Bratko, & S. Dzeroski (Eds.), (124-133 pp). doi:  
3182 Fuglister, F.C. (1955). Alternative analyses of current surveys. *Deep Sea Research (1953)* 2,  
3183 213-229. [https://doi.org/10.1016/0146-6313\(55\)90026-5](https://doi.org/10.1016/0146-6313(55)90026-5)

3184 Fuglister, F.C. (1963). Gulf stream '60. *Progress In Oceanography* 1, 265-373.  
3185 [https://doi.org/10.1016/0079-6611\(63\)90007-7](https://doi.org/10.1016/0079-6611(63)90007-7)

3186 Gaiser, P.W., St Germain, K.M., Twarog, E.M., Poe, G.A., Purdy, W., Richardson, D.,  
3187 Grossman, W., Jones, W.L., Spencer, D., Golba, G., Cleveland, J., Choy, L., Bevilacqua, R.M.,  
3188 & Chang, P.S. (2004). The WindSat spaceborne polarimetric microwave radiometer: sensor  
3189 description and early orbit performance. *Geoscience and Remote Sensing, IEEE Transactions on*  
3190 42, 2347-2361. 10.1109/TGRS.2004.836867

3191 Geer, A.J., Lonitz, K., Weston, P., Kazumori, M., Okamoto, K., Zhu, Y., Liu, E.H., Collard, A.,  
3192 Bell, W., Migliorini, S., Chambon, P., Fourrié, N., Kim, M.-J., Köpken-Watts, C., & Schraff, C.  
3193 (2018). All-sky satellite data assimilation at operational weather forecasting centres. *Quarterly*  
3194 *Journal of the Royal Meteorological Society* 144, 1191-1217. doi:10.1002/qj.3202

3195 Gentemann, C., Mazzini, P., Pianca, P., Scott, J.P., Akella, S., Minnett, P.J., Cornillon, P.,  
3196 Cetinić, I., Chin, T.M., Gomez-Valdes, Vazquez, J., Tsontos, V., Jenkins, R., De Halleux, S.,  
3197 Peacock, D., Mattias, T., & Cohen, N. (2019). Saildrone: adaptively sampling the marine  
3198 environment. *Bull. Amer. Met. Soc. In preparation.*

3199 Gentemann, C.L. (2014). Three way validation of MODIS and AMSR-E sea surface  
3200 temperatures. *Journal of Geophysical Research: Oceans* 119, 2583-2598.  
3201 10.1002/2013JC009716

3202 Gentemann, C.L., Donlon, C.J., Stuart-Menteth, A., & Wentz, F.J. (2003). Diurnal signals in  
3203 satellite sea surface temperature measurements. *Geophysical Research Letters* 30, 1140-1143.

3204 Gentemann, C.L., & Hilburn, K.A. (2015). In situ validation of sea surface temperatures from the  
3205 GCOM-W1 AMSR2 RSS calibrated brightness temperatures. *Journal of Geophysical Research:  
3206 Oceans* 120, 3567-3585. 10.1002/2014JC010574

3207 Gentemann, C.L., Meissner, T., & Wentz, F.J. (2010). Accuracy of Satellite Sea Surface  
3208 Temperatures at 7 and 11 GHz. *IEEE Transactions on Geoscience and Remote Sensing* 48, 1009-  
3209 1018. 10.1109/TGRS.2009.2030322

3210 Gentemann, C.L., & Minnett, P.J. (2008). Radiometric measurements of ocean surface thermal  
3211 variability. *Journal of Geophysical Research* 113, C08017. 10.1029/2007JC004540

3212 Gentemann, C.L., Minnett, P.J., LeBorgne, P., & Merchant, C.J. (2008). Multi-satellite  
3213 measurements of large diurnal warming events. *Geophysical Research Letters* 35, L22602.  
3214 10.1029/2008GL035730

3215 Gentemann, C.L., Minnett, P.J., & Ward, B. (2009). Profiles of Ocean Surface Heating (POSH):  
3216 a new model of upper ocean diurnal thermal variability. *Journal of Geophysical Research* 114,  
3217 C07017. 10.1029/2008JC004825

3218 Giering, R., Quast, R., Mittaz, J.P.D., Hunt, S.E., Harris, P.M., Woolliams, E.R., & Merchant,  
3219 C.J. (2019). A Novel Framework to Harmonise Satellite Data Series for Climate Applications.  
3220 *Remote Sensing* 11, 1002.

3221 Gladkova, I., Ignatov, A., Shahriar, F., Kihai, Y., Hillger, D., & Petrenko, B. (2016). Improved  
3222 VIIRS and MODIS SST Imagery. *Remote Sensing* 8, 79.

3223 Gloersen, P., & Barath, F.T. (1977). A Scanning Multichannel Microwave Radiometer for  
3224 Nimbus-G and SeaSat-A. *IEEE Journal of Oceanic Engineering* OE-2, 172-178.

3225 Gloersen, P., Cavalieri, D.J., Chang, A.T.C., Wilheit, T.T., Campbell, W.J., Johanessen, O.M.,  
3226 Katsaros, K.B., Kunzi, K.F., Ross, D.B., Staelin, D., Windsor, E.P.L., Barath, F.T.,  
3227 Gudmandsen, P., Langham, E., & Ramseier, R.O. (1984). A summary of results from the first  
3228 Nimbus-7 SMMR observations. *J. Geophys. Res.* 89, 5335-5344.

3229 Goldberg, M., Ohring, G., Butler, J., Cao, C., Datla, R., Doelling, D., Gärtner, V., Hewison, T.,  
3230 Iacovazzi, B., Kim, D., Kurino, T., Lafeuille, J., Minnis, P., Renaut, D., Schmetz, J., Tobin, D.,  
3231 Wang, L., Weng, F., Wu, X., Yu, F., Zhang, P., & Zhu, T. (2011). The Global Space-Based  
3232 Inter-Calibration System. *Bulletin of the American Meteorological Society* 92, 467-475.  
3233 10.1175/2010bams2967.1

3234 González-Haro, C., & Isern-Fontanet, J. (2014). Global ocean current reconstruction from  
3235 altimetric and microwave SST measurements. *Journal of Geophysical Research: Oceans* 119,  
3236 3378-3391. doi:10.1002/2013JC009728

3237 Good, S.A., Corlett, G.K., Remedios, J.J., Noyes, E.J., & Llewellyn-Jones, D.T. (2007). The  
3238 Global Trend in Sea Surface Temperature from 20 Years of Advanced Very High Resolution  
3239 Radiometer Data. *Journal of Climate* 20, 1255-1264. doi: 10.1175/JCLI4049.1

3240 Griffiths, P.R., & de Haseth, J.A. (1986). *Fourier Transform Infrared Spectrometry* New York:  
3241 John Wiley & Sons. 0-471-09902-3

3242 Haine, T.W.N., & Martin, T. (2017). The Arctic-Subarctic sea ice system is entering a seasonal  
3243 regime: Implications for future Arctic amplification. *Scientific Reports* 7, 4618. 10.1038/s41598-  
3244 017-04573-0

3245 Hall, M., Frank, E., Holmes, G., Pfahringer, B., Reutemann, P., & Witten, I.H. (2009). The  
3246 WEKA data mining software: an update. *SIGKDD Explor. Newsl.* 11, 10-18.  
3247 10.1145/1656274.1656278

3248 Hallsworth, S. (2005). Modelling the diurnal-variation of sea surface temperature using a one-  
3249 dimensional ocean turbulence model. Ph.D. Thesis, School of GeoSciences. University of  
3250 Edinburgh, Edinburgh, United Kingdom. pp. 187,

3251 Halpern, D., & Reed, R.K. (1976). Heat Budget of the Upper Ocean Under Light Winds. *Journal*  
3252 *of Physical Oceanography* 6, 972-975. 10.1175/1520-0485(1976)006<0972:Hbotuo>2.0.Co;2

3253 Ham, Y.-G., Kug, J.-S., Kang, I.-S., Jin, F.-F., & Timmermann, A. (2010). Impact of diurnal  
3254 atmosphere–ocean coupling on tropical climate simulations using a coupled GCM. *Climate*  
3255 *Dynamics* 34, 905-917. 10.1007/s00382-009-0586-8

3256 Hamad, N., Millot, C., & Taupier-Letage, I. (2005). A new hypothesis about the surface  
3257 circulation in the eastern basin of the mediterranean sea. *Progress In Oceanography* 66, 287-298.  
3258 <https://doi.org/10.1016/j.pocean.2005.04.002>

3259 Han, W., Meehl, G.A., Rajagopalan, B., Fasullo, J.T., Hu, A., Lin, J., Large, W.G., Wang, J.-w.,  
3260 Quan, X.-W., Trenary, L.L., Wallcraft, A., Shinoda, T., & Yeager, S. (2010). Patterns of Indian  
3261 Ocean sea-level change in a warming climate. *Nature Geoscience* 3, 546. 10.1038/ngeo901,  
3262 <https://www.nature.com/articles/ngeo901#supplementary-information>

3263 Han, Y., Delst, P.v., Liu, Q., Weng, F., Yan, B., Treadon, R., & Derber, J. (2006). JCSDA  
3264 Community Radiative Transfer Model (CRTM)—Version 1, NOAA Tech. Rep. NESDIS 122,  
3265 (40 pp. pp.). Camp Springs, MD.: NOAA. Available at

3266 Hanafin, J.A., & Minnett, P.J. (2001). Cloud forcing of surface radiation in the North Water  
3267 Polynya. *Atmosphere-Ocean* 39, 239-255.

3268 Hanafin, J.A., & Minnett, P.J. (2005). Infrared-emissivity measurements of a wind-roughened  
3269 sea surface. *Applied Optics*. 44, 398-411.

3270 Harris Corporation (2018). GOES-R Series Product Definition and Users' Guide, (720 pp.)  
3271 Available at <https://www.goes-r.gov/products/docs/PUG-L2+-vol5.pdf>.

3272 Hedley, J., Roelfsema, C., Chollett, I., Harborne, A., Heron, S., Weeks, S., Skirving, W., Strong,  
3273 A., Eakin, C., Christensen, T., Ticzon, V., Bejarano, S., & Mumby, P. (2016). Remote Sensing of  
3274 Coral Reefs for Monitoring and Management: A Review. *Remote Sensing* 8, 118.  
3275 10.3390/rs8020118

3276 Hewison, T.J., & König, M. (2008). Inter-calibration of Meteosat imagers and IASI. In  
3277 Proceedings of Proc. 2008 EUMETSAT Meteorological Satellite Conf, (52-59 pp): Citeseer. doi:  
3278 Hewison, T.J., Wu, X., Yu, F., Tahara, Y., Hu, X., Kim, D., & Koenig, M. (2013). GSICS inter-  
3279 calibration of infrared channels of geostationary imagers using Metop/IASI. *IEEE Transactions*  
3280 *on Geoscience and Remote Sensing* 51, 1160-1170.

3281 Heygster, G., Kachi, M., Kelly, R., & Liu, G. (2017). Guest Editorial The Global Change  
3282 Observation Mission—Water: Contributions to Global Water Cycle Science From the Advanced  
3283 Microwave Scanning Radiometer–2. *IEEE Journal of Selected Topics in Applied Earth*  
3284 *Observations and Remote Sensing* 10, 3835-3838. 10.1109/JSTARS.2017.2751758

3285 Hihara, T., Kubota, M., & Okuro, A. (2015). Evaluation of sea surface temperature and wind  
3286 speed observed by GCOM-W1/AMSR2 using in situ data and global products. *Remote Sensing*  
3287 *of Environment* 164, 170-178. <https://doi.org/10.1016/j.rse.2015.04.005>

3288 Hilburn, K. (2009). Including temperature effects in the F15 RADCAL correction, *Remote*  
3289 *Sensing Systems Tech. Rep.*, 51209, (11 pp.) Available at

3290 [ftp://rain.atmos.colostate.edu/FCDR/doc/F15/Hilburn\\_09\\_\\_Including\\_Temp\\_Effects\\_in\\_the\\_F1](ftp://rain.atmos.colostate.edu/FCDR/doc/F15/Hilburn_09__Including_Temp_Effects_in_the_F1)  
3291 [5\\_RADCAL\\_Corr\\_RSS\\_TechRep051209.pdf](#).

3292 Hong, X., Chang, S.W., Raman, S., Shay, L.K., & Hodur, R. (2000). The Interaction between  
3293 Hurricane Opal (1995) and a Warm Core Ring in the Gulf of Mexico. *Monthly Weather Review*  
3294 *128*, 1347-1365.

3295 Hook, S.J., Vaughan, R.G., Tonooka, H., & Schladow, S.G. (2007). Absolute Radiometric In-  
3296 Flight Validation of Mid Infrared and Thermal Infrared Data From ASTER and MODIS on the  
3297 Terra Spacecraft Using the Lake Tahoe, CA/NV, USA, Automated Validation Site. *Geoscience*  
3298 *and Remote Sensing, IEEE Transactions on* *45*, 1798-1807. 10.1109/TGRS.2007.894564

3299 Høyer, J.L., Karagali, I., Dybkjær, G., & Tonboe, R. (2012). Multi sensor validation and error  
3300 characteristics of Arctic satellite sea surface temperature observations. *Remote Sensing of*  
3301 *Environment* *121*, 335-346. <http://dx.doi.org/10.1016/j.rse.2012.01.013>

3302 Hulley, G., Hook, S., Radocinski, R., & Cawse-Nicholson, K. (2019). Stage-1 validation of the  
3303 ECOSTRESS Level-2 land surface temperature and emissivity products. *In preparation*.

3304 Hulley, G.C., & Hook, S.J. (2018). ECOSystem Spaceborne Thermal Radiometer Experiment on  
3305 Space Station Level-2 Land Surface Temperature and Emissivity Algorithm Theoretical Basis  
3306 Document (ATBD). JPL D-94643, (96 pp.). Pasadena, CA, USA: Jet Propulsion Laboratory,  
3307 California Institute of Technology. Available at  
3308 [https://ecostress.jpl.nasa.gov/downloads/atbd/ECOSTRESS\\_L2\\_ATBD\\_LSTE\\_2018-03-08.pdf](https://ecostress.jpl.nasa.gov/downloads/atbd/ECOSTRESS_L2_ATBD_LSTE_2018-03-08.pdf).

3309 Hursen, K.A., & Ross, R. (1996). GOES Imager: overview and evolutionary development. In  
3310 Proceedings of SPIE's 1996 International Symposium on Optical Science, Engineering, and  
3311 Instrumentation, 2812, (14 pp): SPIE. doi:  
3312 Imaoka, K., Kachi, M., Fujii, H., Murakami, H., Hori, M., Ono, A., Igarashi, T., Nakagawa, K.,  
3313 Oki, T., Honda, Y., & Shimoda, H. (2010). Global Change Observation Mission (GCOM) for  
3314 Monitoring Carbon, Water Cycles, and Climate Change. *Proceedings of the IEEE* *98*, 717-734.  
3315 10.1109/JPROC.2009.2036869

3316 Jha, B., Hu, Z.-Z., & Kumar, A. (2014). SST and ENSO variability and change simulated in  
3317 historical experiments of CMIP5 models. *Climate Dynamics* *42*, 2113-2124. 10.1007/s00382-  
3318 013-1803-z

3319 Jiang, G., Yan, H., & Ma, L. (2009). Intercalibration of SVISSR/FY-2C Infrared Channels  
3320 Against MODIS/Terra and AIRS/Aqua Channels. *IEEE Transactions on Geoscience and Remote*  
3321 *Sensing* *47*, 1548-1558. 10.1109/TGRS.2008.2005200

3322 Kachi, M., Maeda, T., Tsutsui, H., Ono, N., Kasahara, M., & Mokuno, M. (2017). Five years  
3323 observations of global water cycle by GCOM-W/AMSR2. In Proceedings of 2017 IEEE  
3324 International Geoscience and Remote Sensing Symposium (IGARSS), (5641-5643 pp). doi:  
3325 10.1109/IGARSS.2017.8128285

3326 Kaiser, J.A.C. (1978). Heat Balance of the Upper Ocean under Light Winds. *Journal of Physical*  
3327 *Oceanography* *8*, 1-12. 10.1175/1520-0485(1978)008<0001:Hbotuo>2.0.Co;2

3328 Kannenberg, R., & Palluconi, F. (1998). Joint Rosenstiel School of Marine and Atmospheric  
3329 Science (RSMAS) Committee on Earth Observation Satellites (CEOS) Validation Workshop.  
3330 *The Earth Observer* *10*, 38-42.

3331 Kantha, L.H., & Clayson, C.A. (1994). An improved mixed layer model for geophysical  
3332 applications. *Journal of Geophysical Research: Oceans* *99*, 25235-25266.  
3333 doi:10.1029/94JC02257

3334 Kaplan, A., Cane, M.A., & Kushnir, Y. (2003). Reduced space approach to the optimal analysis  
3335 interpolation of historical marine observations: Accomplishments, difficulties, and prospects,

3336 *Advances in the Applications of Marine Climatology: The Dynamic Part of the WMO Guide to*  
3337 *the Applications of Marine Climatology*, (199-216 pp.). Geneva, Switzerland: World  
3338 Meteorological Organization. Available at  
3339 Kaplan, A., Kushnir, Y., Cane, M.A., & Blumenthal, M.B. (1997). Reduced space optimal  
3340 analysis for historical data sets: 136 years of Atlantic sea surface temperatures. *Journal of*  
3341 *Geophysical Research: Oceans* 102, 27835-27860. 10.1029/97jc01734  
3342 Karagali, I., Høyer, J., & Hasager, C. (2012). SST diurnal variability in the North Sea and the  
3343 Baltic Sea. *Remote Sensing of Environment* 121, 159-170.  
3344 <https://doi.org/10.1016/j.rse.2012.01.016>  
3345 Karagali, I., & Høyer, J.L. (2013). Observations and modeling of the diurnal SST cycle in the  
3346 North and Baltic Seas. *Journal of Geophysical Research: Oceans* 118, 4488-4503.  
3347 doi:10.1002/jgrc.20320  
3348 Karagali, I., & Høyer, J.L. (2014). Characterisation and quantification of regional diurnal SST  
3349 cycles from SEVIRI. *Ocean Sci.* 10, 745-758. 10.5194/os-10-745-2014  
3350 Karagali, I., Høyer, J.L., & Donlon, C.J. (2017). Using a 1-D model to reproduce the diurnal  
3351 variability of SST. *Journal of Geophysical Research: Oceans* 122, 2945-2959.  
3352 doi:10.1002/2016JC012542  
3353 Karlsson, K.-G., Håkansson, N., Mittaz, J.P.D., Hanschmann, T., & Devasthale, A. (2017).  
3354 Impact of AVHRR Channel 3b Noise on Climate Data Records: Filtering Method Applied to the  
3355 CM SAF CLARA-A2 Data Record. *Remote Sensing* 9, 568.  
3356 Kawai, H. (1998). A brief history of recognition of the Kuroshio. *Progress In Oceanography* 41,  
3357 505-578. [https://doi.org/10.1016/S0079-6611\(98\)00024-X](https://doi.org/10.1016/S0079-6611(98)00024-X)  
3358 Kawai, Y., & Kawamura, H. (2002). Evaluation of the diurnal warming of sea surface  
3359 temperatures using satellite-derived marine meteorological data. *Journal of Oceanography* 58,  
3360 805-814.  
3361 Kawanishi, T., Sezai, T., Ito, Y., Imaoka, K., Takeshima, T., Ishido, Y., Shibata, A., Miura, M.,  
3362 Inahata, H., & Spencer, R.W. (2003). The Advanced Microwave Scanning Radiometer for the  
3363 Earth Observing System (AMSR-E), NASDA's contribution to the EOS for global energy and  
3364 water cycle studies. *Geoscience and Remote Sensing, IEEE Transactions on* 41, 184-194. doi:  
3365 10.1109/TGRS.2002.808331  
3366 Kilic, L., Prigent, C., Aires, F., Boutin, J., Heygster, G., Tonboe, R.T., Roquet, H., Jimenez, C.,  
3367 & Donlon, C. (2018). Expected Performances of the Copernicus Imaging Microwave Radiometer  
3368 (CIMR) for an All-Weather and High Spatial Resolution Estimation of Ocean and Sea Ice  
3369 Parameters. *Journal of Geophysical Research: Oceans* 123, 7564-7580.  
3370 doi:10.1029/2018JC014408  
3371 Kilpatrick, K.A., Podestá, G., Walsh, S., Williams, E., Halliwell, V., Szczodrak, M., Brown,  
3372 O.B., Minnett, P.J., & Evans, R. (2015). A decade of sea surface temperature from MODIS.  
3373 *Remote Sensing of Environment* 165, 27-41. <http://dx.doi.org/10.1016/j.rse.2015.04.023>  
3374 Kilpatrick, K.A., Podestá, G., Williams, E., Walsh, S., & Minnett, P.J. (2019). Alternating  
3375 Decision Trees for Cloud Masking in MODIS and VIIRS NASA Sea Surface Temperature  
3376 Products. *Journal of Atmospheric and Oceanic Technology* 36, 387-407. 10.1175/jtech-d-18-  
3377 0103.1  
3378 Kilpatrick, K.A., Podestá, G.P., & Evans, R.H. (2001). Overview of the NOAA/NASA  
3379 Pathfinder algorithm for Sea Surface Temperature and associated Matchup Database. *Journal of*  
3380 *Geophysical Research* 106, 9179-9198.

3381 Klaes, D.K., Cohen, M., Buhler, Y., Schluessel, P., Munro, R., Luntama, J.-P., Engeln, A.v.,  
3382 Clerigh, E., Bonekamp, H., Ackermann, J., & Schmetz, J. (2007). An Introduction to the  
3383 EUMETSAT Polar system. *Bulletin of the American Meteorological Society* 88, 1085-1096.  
3384 Klaes, K.D., & Holmlund, K. (2014). EUMETSAT programmes and plans. Presented at Proc.  
3385 SPIE 9218, Earth Observing Systems XIX, 92181D (September 25, 2014).  
3386 (<http://dx.doi.org/10.1117/12.2061020>).10.1117/12.2061020.  
3387 Knudsen, P., Andersen, O.B., & Knudsen, T. (1996). ATSR sea surface temperature data in a  
3388 global analysis with TOPEX/POSEIDON altimetry. *Geophysical Research Letters* 23, 821-824.  
3389 doi:10.1029/96GL00618  
3390 Koner, P., & Harris, A. (2016). Improved Quality of MODIS Sea Surface Temperature Retrieval  
3391 and Data Coverage Using Physical Deterministic Methods. *Remote Sensing* 8, 454.  
3392 Koner, P.K., & Drummond, J.R. (2008). Atmospheric trace gases profile retrievals using the  
3393 nonlinear regularized total least squares method. *Journal of Quantitative Spectroscopy and*  
3394 *Radiative Transfer* 109, 2045-2059. <https://doi.org/10.1016/j.jqsrt.2008.02.014>  
3395 Koner, P.K., Harris, A., & Maturi, E. (2015). A Physical Deterministic Inverse Method for  
3396 Operational Satellite Remote Sensing: An Application for Sea Surface Temperature Retrievals.  
3397 *IEEE Transactions on Geoscience and Remote Sensing* 53, 5872-5888.  
3398 10.1109/TGRS.2015.2424219  
3399 Kummerow, C., Barnes, W., Kozu, T., Shiue, J., & Simpson, J. (1998). The Tropical Rainfall  
3400 Measuring Mission (TRMM) Sensor Package. *Journal of Atmospheric and Oceanic Technology*  
3401 15, 809-817.  
3402 Kurihara, Y., Murakami, H., & Kachi, M. (2016). Sea surface temperature from the new  
3403 Japanese geostationary meteorological Himawari-8 satellite. *Geophysical Research Letters* 43,  
3404 1234-1240. 10.1002/2015GL067159  
3405 L'Ecuyer, T.S., & Jiang, J.H. (2010). Touring the atmosphere aboard the A-Train. *Phys. Today*  
3406 63, 36-41.  
3407 Lacombe, H., Gascard, J., Gonella, J., & Bethoux, J. (1981). Response of the Mediterranean to  
3408 the water and energy fluxes across its surface, on seasonal and interannual scales. *Oceanologica*  
3409 *Acta* 4, 247-255.  
3410 Lacouture, J. (1995). The Gulf Stream Charts of Benjamin Franklin and Timothy Folger.  
3411 *Historic Nantucket* 44, 82-86.  
3412 Lagerloef, G., Colomb, F.R., Vine, D.L., Wentz, F., Yueh, S., Ruf, C., Lilly, J., Gunn, J., Chao,  
3413 Y., deCharon, A., G. Feldman, & Swift, C. (2008). The Aquarius/SAC-D Mission: Designed to  
3414 meet the salinity remote-sensing challenge. *Oceanography* 21, 68-81.  
3415 <http://dx.doi.org/10.5670/oceanog.2008.68>  
3416 Lautenbacher, C.C. (2006). The Global Earth Observation System of Systems: Science Serving  
3417 Society. *Space Policy* 22, 8-11. <https://doi.org/10.1016/j.spacepol.2005.12.004>  
3418 LaViolette, P.E., & Chabot, P.L. (1968). Nimbus II satellite sea surface temperatures versus  
3419 historical data in a selected region: a comparative study. *Deep Sea Research and Oceanographic*  
3420 *Abstracts* 15, 617-622. [https://doi.org/10.1016/0011-7471\(68\)90068-5](https://doi.org/10.1016/0011-7471(68)90068-5)  
3421 Le Borgne, P., Legendre, G., & Péré, S. (2012a). Comparison of MSG/SEVIRI and drifting buoy  
3422 derived diurnal warming estimates. *Remote Sensing of Environment* 124, 622-626.  
3423 <http://dx.doi.org/10.1016/j.rse.2012.06.015>  
3424 Le Borgne, P., Marsouin, A., Orain, F., & Roquet, H. (2012b). Operational sea surface  
3425 temperature bias adjustment using AATSR data. *Remote Sensing of Environment* 116, 93-106.  
3426 10.1016/j.rse.2010.02.023



3427 Le Traon, P.Y., Antoine, D., Bentamy, A., Bonekamp, H., Breivik, L.A., Chapron, B., Corlett,  
3428 G., Dibarboure, G., DiGiacomo, P., Donlon, C., Faugère, Y., Font, J., Girard-Ardhuin, F., Gohin,  
3429 F., Johannessen, J.A., Kamachi, M., Lagerloef, G., Lambin, J., Larnicol, G., Le Borgne, P.,  
3430 Leuliette, E., Lindstrom, E., Martin, M.J., Maturi, E., Miller, L., Mingsen, L., Morrow, R., Reul,  
3431 N., Rio, M.H., Roquet, H., Santoleri, R., & Wilkin, J. (2015). Use of satellite observations for  
3432 operational oceanography: recent achievements and future prospects. *Journal of Operational*  
3433 *Oceanography* 8, s12-s27. 10.1080/1755876X.2015.1022050

3434 Le Traon, P.Y., Reppucci, A., Alvarez Fanjul, E., Aouf, L., Behrens, A., Belmonte, M.,  
3435 Bentamy, A., Bertino, L., Brando, V.E., Kreiner, M.B., Benkiran, M., Carval, T., Ciliberti, S.A.,  
3436 Claustre, H., Clementi, E., Coppini, G., Cossarini, G., De Alfonso Alonso-Muñoyerro, M.,  
3437 Delamarche, A., Dibarboure, G., Dinessen, F., Drevillon, M., Drillet, Y., Faugere, Y., Fernández,  
3438 V., Fleming, A., Garcia-Hermosa, M.I., Sotillo, M.G., Garric, G., Gasparin, F., Giordan, C.,  
3439 Gehlen, M., Gregoire, M.L., Guinehut, S., Hamon, M., Harris, C., Hernandez, F., Hinkler, J.B.,  
3440 Hoyer, J., Karvonen, J., Kay, S., King, R., Lavergne, T., Lemieux-Dudon, B., Lima, L., Mao, C.,  
3441 Martin, M.J., Masina, S., Melet, A., Buongiorno Nardelli, B., Nolan, G., Pascual, A., Pistoia, J.,  
3442 Palazov, A., Piolle, J.F., Pujol, M.I., Pequignet, A.C., Peneva, E., Pérez Gómez, B., Petit de la  
3443 Villeon, L., Pinardi, N., Pisano, A., Pouliquen, S., Reid, R., Remy, E., Santoleri, R., Siddorn, J.,  
3444 She, J., Staneva, J., Stoffelen, A., Tonani, M., Vandenbulcke, L., von Schuckmann, K., Volpe,  
3445 G., Wettre, C., & Zacharioudaki, A. (2019). From Observation to Information and Users: The  
3446 Copernicus Marine Service Perspective. *Frontiers in Marine Science* 6.  
3447 10.3389/fmars.2019.00234

3448 Lean, K., & Saunders, R.W. (2013). Validation of the ATSR Reprocessing for Climate (ARC)  
3449 Dataset Using Data from Drifting Buoys and a Three-Way Error Analysis. *Journal of Climate*  
3450 26, 4758-4772. 10.1175/JCLI-D-12-00206.1

3451 Legeckis, R. (1975). Application of synchronous meteorological satellite data to the study of  
3452 time dependent sea surface temperature changes along the boundary of the Gulf Stream.  
3453 *Geophysical Research Letters* 2, 435-438. 10.1029/GL002i010p00435

3454 Legeckis, R. (1977). Long Waves in the Eastern Equatorial Pacific Ocean: A View from a  
3455 Geostationary Satellite. *Science* 197, 1179-1181. 10.1126/science.197.4309.1179

3456 Legeckis, R. (1978). A survey of worldwide sea surface temperature fronts detected by  
3457 environmental satellites. *Journal of Geophysical Research: Oceans* 83, 4501-4522.  
3458 10.1029/JC083iC09p04501

3459 Legeckis, R., & Gordon, A.L. (1982). Satellite observations of the Brazil and Falkland  
3460 currents— 1975 1976 and 1978. *Deep Sea Research Part A. Oceanographic Research Papers*  
3461 29, 375-401. [https://doi.org/10.1016/0198-0149\(82\)90101-7](https://doi.org/10.1016/0198-0149(82)90101-7)

3462 Legeckis, R.V. (1979). Satellite Observations of the Influence of Bottom Topography on the  
3463 Seaward Deflection of the Gulf Stream off Charleston, South Carolina. *Journal of Physical*  
3464 *Oceanography* 9, 483-497. 10.1175/1520-0485(1979)009<0483:sootio>2.0.co;2

3465 Lei, G., & Cong, M. (2013). Sea Surface temperature from HY-1B COCTS. In Proceedings of  
3466 Geoscience and Remote Sensing Symposium (IGARSS), 2013 IEEE International, (652-655 pp).  
3467 doi: 10.1109/IGARSS.2013.6721241

3468 Lellouche, J.M., Greiner, E., Le Galloudec, O., Garric, G., Regnier, C., Drevillon, M., Benkiran,  
3469 M., Testut, C.E., Bourdalle-Badie, R., Gasparin, F., Hernandez, O., Levier, B., Drillet, Y., Remy,  
3470 E., & Le Traon, P.Y. (2018). Recent updates to the Copernicus Marine Service global ocean  
3471 monitoring and forecasting real-time 1/12° high-resolution system. *Ocean Sci.* 14, 1093-1126.  
3472 10.5194/os-14-1093-2018

3473 Li, X., J. Derber, S. Moorthi, & Collard, C.A. (2019). Sea surface temperature analysis within  
3474 the NCEP GFS, *National Centers for Environmental Prediction Office Notes*, 496, (xx pp.):  
3475 NCEP. Available at <https://www.lib.ncep.noaa.gov/ncepofficenotes/>  
3476 Li, Y., & He, R. (2014). Spatial and temporal variability of SST and ocean color in the Gulf of  
3477 Maine based on cloud-free SST and chlorophyll reconstructions in 2003–2012. *Remote Sensing*  
3478 *of Environment 144*, 98-108. <https://doi.org/10.1016/j.rse.2014.01.019>  
3479 Liu, Y., Chin, T.M., & Minnett, P.J. (2017). Sampling errors in satellite-derived infrared sea-  
3480 surface temperatures. Part II: Sensitivity and parameterization. *Remote Sensing of Environment*  
3481 *198*, 297-309. <http://dx.doi.org/10.1016/j.rse.2017.06.011>  
3482 Liu, Y., & Minnett, P.J. (2015). Evidence linking satellite-derived sea-surface temperature  
3483 signals to changes in the Atlantic meridional overturning circulation. *Remote Sensing of*  
3484 *Environment 169*, 150-162. <http://dx.doi.org/10.1016/j.rse.2015.08.014>  
3485 Liu, Y., & Minnett, P.J. (2016). Sampling errors in satellite-derived infrared sea-surface  
3486 temperatures. Part I: Global and regional MODIS fields. *Remote Sensing of Environment 177*,  
3487 48-64. <http://dx.doi.org/10.1016/j.rse.2016.02.026>  
3488 Llewellyn-Jones, D.T., Minnett, P.J., Saunders, R.W., & Zavody, A.M. (1984). Satellite  
3489 multichannel infrared measurements of sea surface temperature of the N.E. Atlantic Ocean using  
3490 AVHRR/2. *Quarterly Journal of the Royal Meteorological Society 110*, 613-631.  
3491 [10.1002/qj.49711046504](https://doi.org/10.1002/qj.49711046504)  
3492 Louet, J., & Bruzzi, S. (1999). ENVISAT mission and system. In Proceedings of IEEE 1999  
3493 International Geoscience and Remote Sensing Symposium. IGARSS'99 (Cat. No.99CH36293),  
3494 3, (1680-1682 vol.1683 pp). doi: 10.1109/IGARSS.1999.772059  
3495 Luo, B., Minnett, P.J., Gentemann, C., & Szczodrak, G. (2019). Improving satellite retrieved  
3496 night-time infrared sea surface temperatures in aerosol contaminated regions. *Remote Sensing of*  
3497 *Environment 223*, 8-20. <https://doi.org/10.1016/j.rse.2019.01.009>  
3498 Luo, J., Ault, J.S., Shay, L.K., Hoolihan, J.P., Prince, E.D., Brown, C.A., & Rooker, J.R. (2015).  
3499 Ocean Heat Content Reveals Secrets of Fish Migrations. *PLoS ONE 10*, e0141101.  
3500 [10.1371/journal.pone.0141101](https://doi.org/10.1371/journal.pone.0141101)  
3501 Malkus, J.S., & Riehl, H. (1960). On the Dynamics and Energy Transformations in Steady-State  
3502 Hurricanes. *Tellus 12*, 1-20. [10.3402/tellusa.v12i1.9351](https://doi.org/10.3402/tellusa.v12i1.9351)  
3503 Manley, J., & Willcox, S. (2010). The Wave Glider: A persistent platform for ocean science. In  
3504 Proceedings of OCEANS'10 IEEE SYDNEY, (5 pp). doi: 10.1109/OCEANSSYD.2010.5603614  
3505 Markham, B.L., Boncyk, W.C., Helder, D.L., & Barker, J.L. (1997). Landsat-7 Enhanced  
3506 Thematic Mapper Plus Radiometric Calibration. *Canadian Journal of Remote Sensing 23*, 318-  
3507 332. [10.1080/07038992.1997.10855218](https://doi.org/10.1080/07038992.1997.10855218)  
3508 Marsouin, A., Le Borgne, P., Legendre, G., Péré, S., & Roquet, H. (2015). Six years of OSI-SAF  
3509 METOP-A AVHRR sea surface temperature. *Remote Sensing of Environment 159*, 288-306.  
3510 <http://dx.doi.org/10.1016/j.rse.2014.12.018>  
3511 Martin, M., Dash, P., Ignatov, A., Banzon, V., Beggs, H., Brasnett, B., Cayula, J.-F., Cummings,  
3512 J., Donlon, C., Gentemann, C., Grumbine, R., Ishizaki, S., Maturi, E., Reynolds, R.W., &  
3513 Roberts-Jones, J. (2012). Group for High Resolution Sea Surface temperature (GHRSSST)  
3514 analysis fields inter-comparisons. Part 1: A GHRSSST multi-product ensemble (GMPE). *Deep*  
3515 *Sea Research Part II: Topical Studies in Oceanography 77–80*, 21-30.  
3516 [10.1016/j.dsr2.2012.04.013](https://doi.org/10.1016/j.dsr2.2012.04.013)  
3517 Martin, S. (2014). *An Introduction to Ocean Remote Sensing*. (2 ed.) Cambridge: Cambridge  
3518 University Press. 9781107019386. DOI: 10.1017/CBO9781139094368

3519 Martínez Avellaneda, N., Serra, N., Minnett, P., & Stammer, D. (2010). Response of the eastern  
3520 subtropical Atlantic SST to Saharan dust: A modeling and observational study. *Journal of*  
3521 *Geophysical Research: Oceans* (1978–2012) 115

3522 Marullo, S., Buongiorno Nardelli, B., Guarracino, M., & Santoleri, R. (2007). Observing the  
3523 Mediterranean Sea from space: 21 years of Pathfinder-AVHRR sea surface temperatures (1985  
3524 to 2005): re-analysis and validation. *Ocean Sci.* 3, 299-310. 10.5194/os-3-299-2007

3525 Marullo, S., Minnett, P., Santoleri, R., Tonani, M., & N. Pinardi (2014a). SST Diurnal Cycle and  
3526 Heat Budget Estimates over the Mediterranean Sea. In Proceedings of Earth Observation for  
3527 Ocean-Atmosphere Interactions Science 2014, Responding to the new scientific challenges of  
3528 SOLAS. 28<sup>th</sup>-31<sup>st</sup> October 2014, European Space Research Institute, Frascati, Italy. pp):  
3529 European Space Agency. doi:

3530 Marullo, S., Minnett, P.J., Santoleri, R., & Tonani, M. (2016). The diurnal cycle of sea-surface  
3531 temperature and estimation of the heat budget of the Mediterranean Sea. *Journal of Geophysical*  
3532 *Research: Oceans* 121. 10.1002/2016jc012192

3533 Marullo, S., Salusti, E., & Viola, A. (1985). Observations of a small-scale baroclinic eddy in the  
3534 Ligurian Sea. *Deep Sea Research Part A. Oceanographic Research Papers* 32, 215-222.  
3535 [https://doi.org/10.1016/0198-0149\(85\)90029-9](https://doi.org/10.1016/0198-0149(85)90029-9)

3536 Marullo, S., Santoleri, R., Banzon, V., Evans, R.H., & Guarracino, M. (2010). A diurnal-cycle  
3537 resolving sea surface temperature product for the tropical Atlantic. *Journal of Geophysical*  
3538 *Research: Oceans* 115, C05011. 10.1029/2009JC005466

3539 Marullo, S., Santoleri, R., Ciani, D., Le Borgne, P., Péré, S., Pinardi, N., Tonani, M., & Nardone,  
3540 G. (2014b). Combining model and geostationary satellite data to reconstruct hourly SST field  
3541 over the Mediterranean Sea. *Remote Sensing of Environment* 146, 11-23.  
3542 <http://dx.doi.org/10.1016/j.rse.2013.11.001>

3543 Marullo, S., Santoleri, R., Malanotte-Rizzoli, P., & Bergamasco, A. (1999a). The sea surface  
3544 temperature field in the Eastern Mediterranean from advanced very high resolution radiometer  
3545 (AVHRR) data: Part I. Seasonal variability. *Journal of Marine Systems* 20, 63-81.  
3546 [https://doi.org/10.1016/S0924-7963\(98\)00071-2](https://doi.org/10.1016/S0924-7963(98)00071-2)

3547 Marullo, S., Santoleri, R., Malanotte-Rizzoli, P., & Bergamasco, A. (1999b). The sea surface  
3548 temperature field in the Eastern Mediterranean from advanced very high resolution radiometer  
3549 (AVHRR) data: Part II. Interannual variability. *Journal of Marine Systems* 20, 83-112.  
3550 [https://doi.org/10.1016/S0924-7963\(98\)00072-4](https://doi.org/10.1016/S0924-7963(98)00072-4)

3551 Matsuoka, Y., Kawamura, H., Sakaida, F., & Hosoda, K. (2011). Retrieval of high-resolution sea  
3552 surface temperature data for Sendai Bay, Japan, using the Advanced Spaceborne Thermal  
3553 Emission and Reflection Radiometer (ASTER). *Remote Sensing of Environment* 115, 205-213.  
3554 <https://doi.org/10.1016/j.rse.2010.08.018>

3555 Maturi, E., Harris, A., Merchant, C., Mittaz, J., Potash, B., Meng, W., & Sapper, J. (2008).  
3556 NOAA's Sea Surface Temperature Products From Operational Geostationary Satellites. *Bulletin*  
3557 *of the American Meteorological Society* 89, 1877-1888.

3558 Maturi, E., Harris, A., Mittaz, J., Sapper, J., Wick, G., Zhu, X., Dash, P., & Koner, P. (2017). A  
3559 New High-Resolution Sea Surface Temperature Blended Analysis. *Bulletin of the American*  
3560 *Meteorological Society* 98, 1015-1026. 10.1175/bams-d-15-00002.1

3561 Mauri, E., & Poulain, P.-M. (2001). Northern Adriatic Sea surface circulation and  
3562 temperature/pigment fields in September and October 1997. *Journal of Marine Systems* 29, 51-  
3563 67. [https://doi.org/10.1016/S0924-7963\(01\)00009-4](https://doi.org/10.1016/S0924-7963(01)00009-4)

3564 McClain, E.P. (1980). Passive radiometry of the ocean from space—an overview. *Boundary-*  
3565 *Layer Meteorology* 18, 7-24. 10.1007/bf00117908

3566 McClain, E.P., Pichel, W.G., & Walton, C.C. (1985). Comparative performance of AVHRR-  
3567 based multichannel sea surface temperatures. *J. Geophys. Res.* 90, 11587-11601.

3568 McGranahan, G., Balk, D., & Anderson, B. (2007). The rising tide: assessing the risks of climate  
3569 change and human settlements in low elevation coastal zones. *Environment and Urbanization* 19,  
3570 17-37. 10.1177/0956247807076960

3571 McMillin, L. (1975). Estimation of sea-surface temperatures from two infrared window  
3572 measurements with different absorption. *Journal of Geophysical Research* 80, 5113-5117.

3573 McMillin, L., & Crosby, D.S. (1984). Theory and validation of the multiple window sea surface  
3574 temperature technique. *J. Geophys. Research* 89, 3655-3661.

3575 McMillin, L., & Crosby, D.S. (1985). Some physical interpretations of statistically derived  
3576 coefficients for split-window corrections to satellite derived sea surface temperatures. *Quart. J.*  
3577 *Royal Meteorological Soc.* 111, 867-871.

3578 McPhaden, M.J. (2012). A 21st century shift in the relationship between ENSO SST and warm  
3579 water volume anomalies. *Geophysical Research Letters* 39. doi:10.1029/2012GL051826

3580 McPhaden, M.J., Ando, K., Bourlès, B., Freitag, H.P., Lumpkin, R., Masumoto, Y., Murty,  
3581 V.S.N., Nobre, P., Ravichandran, M., Vialard, J., Vousden, D., & Yu, W. (2010). The Global  
3582 Tropical Moored Buoy Array. J. Hall, D.E. Harrison, & D. Stammer (Eds.), *Proceedings of*  
3583 *OceanObs'09: Sustained Ocean Observations and Information for Society (Vol 2), Venice, Italy,*  
3584 *21-25 September 2009,*, ESA Publication WPP-306, (16 pp.): European Space Agency.  
3585 Available at. doi:10.5270/OceanObs09.cwp.61

3586 McPhaden, M.J., Zhang, X., Hendon, H.H., & Wheeler, M.C. (2006). Large scale dynamics and  
3587 MJO forcing of ENSO variability. *Geophysical Research Letters* 33.  
3588 doi:10.1029/2006GL026786

3589 Meissner, T., & Wentz, F. (2007). High quality sea surface temperature from the windsat  
3590 radiometer: algorithm and validation. In Proceedings of 2007 IEEE International Geoscience and  
3591 Remote Sensing Symposium, Barcelona, Spain., (862-864 pp). Barcelona, Spain.: IEEE. doi:  
3592 10.1109/IGARSS.2007.4422933

3593 Meissner, T., & Wentz, F.J. (2012). The Emissivity of the Ocean Surface Between 6 and 90 GHz  
3594 Over a Large Range of Wind Speeds and Earth Incidence Angles. *IEEE Transactions on*  
3595 *Geoscience and Remote Sensing* 50, 3004-3026. 10.1109/TGRS.2011.2179662

3596 Menzel, W.P., & Purdom, J.F.W. (1994). Introducing GOES-I: The first of a new generation of  
3597 geostationary operational environmental satellites. *Bulletin of the American Meteorological*  
3598 *Society.* 75, 757-781. [https://doi.org/10.1175/1520-0477\(1994\)075<0757:IGITFO>2.0.CO;2](https://doi.org/10.1175/1520-0477(1994)075<0757:IGITFO>2.0.CO;2)

3599 Menzel, W.P., Smith, W.L., & Herman, L.D. (1981). Visible infrared spin-scan radiometer  
3600 atmospheric sounder radiometric calibration: an inflight evaluation from intercomparisons with  
3601 HIRS and radiosonde measurements. *Applied Optics* 20, 3641-3644. 10.1364/AO.20.003641

3602 Merchant, C.J., Embury, O., Bulgin, C.E., Block, T., Corlett, G., Fiedler, E., Good, S.A., Mittaz,  
3603 J., Rayner, N.A., Berry, D., Eastwood, S., Taylor, M., Tsushima, Y., Waterfall, A., Wilson, R., &  
3604 Donlon, C. (2019). Satellite-based time-series of sea-surface temperature since 1981 for climate  
3605 applications. *Scientific Data.* In review.

3606 Merchant, C.J., Embury, O., Rayner, N.A., Berry, D.I., Corlett, G.K., Lean, K., Veal, K.L., Kent,  
3607 E.C., Llewellyn-Jones, D.T., Remedios, J.J., & Saunders, R. (2012). A 20 year independent  
3608 record of sea surface temperature for climate from Along Track Scanning Radiometers. *Journal*  
3609 *of Geophysical Research* 117. 10.1029/2012JC008400

3610 Merchant, C.J., Filipiak, M.J., Le Borgne, P., Roquet, H., Autret, E., Piollé, J.F., & Lavender, S.  
3611 (2008a). Diurnal warm-layer events in the western Mediterranean and European shelf seas.  
3612 *Geophysical Research Letters* 35, L04601. doi:10.1029/2007GL033071

3613 Merchant, C.J., & Harris, A.R. (1999). Toward the elimination of bias in satellite retrievals of  
3614 skin sea surface temperature. 2: Comparison with in situ measurements. *J. Geophys. Res.* 104,  
3615 23579-23590.

3616 Merchant, C.J., Harris, A.R., Maturi, E., Embury, O., MacCallum, S.N., Mittaz, J., & Old, C.P.  
3617 (2009a). Sea Surface Temperature Estimation from the Geostationary Operational Environmental  
3618 Satellite-12 (GOES-12). *Journal of Atmospheric and Oceanic Technology* 26, 570-581.  
3619 10.1175/2008jtecho596.1

3620 Merchant, C.J., Harris, A.R., Maturi, E., & MacCallum, S. (2005). Probabilistic physically based  
3621 cloud screening of satellite infrared imagery for operational sea surface temperature retrieval.  
3622 *Quarterly Journal of the Royal Meteorological Society* 131, 2735–2755. doi: 10.1256/qj.05.15

3623 Merchant, C.J., Harris, A.R., Roquet, H., & Le Borgne, P. (2009b). Retrieval characteristics of  
3624 non-linear sea surface temperature from the Advanced Very High Resolution Radiometer.  
3625 *Geophysical Research Letters* 36. 10.1029/2009gl039843

3626 Merchant, C.J., Le Borgne, P., Roquet, H., & Legendre, G. (2013). Extended optimal estimation  
3627 techniques for sea surface temperature from the Spinning Enhanced Visible and Infra-Red  
3628 Imager (SEVIRI). *Remote Sensing of Environment* 131, 287-297.  
3629 <https://doi.org/10.1016/j.rse.2012.12.019>

3630 Merchant, C.J., Le Borgne, P., Roquet, H., & Marsouin, A. (2009c). Sea surface temperature  
3631 from a geostationary satellite by optimal estimation. *Remote Sensing of Environment* 113, 445-  
3632 457.

3633 Merchant, C.J., LeBorgne, P., Marsouin, A., & Roquet, H. (2008b). Optimal estimation of sea  
3634 surface temperature from split-window observations. *Remote Sensing of Environment* 112, 2469-  
3635 2484.

3636 Merchant, C.J., Mittaz, J., & Corlett, G.K. (2014). Climate Data Record Technical Advisory  
3637 Group: Climate Data Assessment Framework, *GHRSSST Document, CDR-TAG\_CDAF v 1.0.5*,  
3638 (24 pp.) Available at [https://www.ghrsst.org/wp-content/uploads/2018/01/CDR-TAG\\_CDAF-](https://www.ghrsst.org/wp-content/uploads/2018/01/CDR-TAG_CDAF-v1.0.5.pdf)  
3639 [v1.0.5.pdf](https://www.ghrsst.org/wp-content/uploads/2018/01/CDR-TAG_CDAF-v1.0.5.pdf).

3640 Merrill, R.T. (1988). Environmental Influences on Hurricane Intensification. *Journal of the*  
3641 *Atmospheric Sciences* 45, 1678-1687. 10.1175/1520-0469(1988)045<1678:Eiohi>2.0.Co;2

3642 Meyers, P.C., Shay, L.K., & Brewster, J.K. (2014). Development and Analysis of the  
3643 Systematically Merged Atlantic Regional Temperature and Salinity Climatology for Oceanic  
3644 Heat Content Estimates. *Journal of Atmospheric and Oceanic Technology* 31, 131-149.  
3645 10.1175/jtech-d-13-00100.1

3646 Michelson, A.A., & Morely, E.W. (1887). On the Relative Motion of the Earth and the  
3647 Luminiferous Ether. *American Journal of Science* 35, 333-345.

3648 Miller, A.J., Collins, M., Gualdi, S., Jensen, T.G., Misra, V., Pezzi, L.P., Pierce, D.W.,  
3649 Putrasahan, D., Seo, H., & Tseng, Y.-H. (2017). Coupled ocean-atmosphere modeling and  
3650 predictions. *Journal of Marine Research* 75, 361-402. 10.1357/002224017821836770

3651 Miller, B.I. (1958). On the Maximum Intensity of Hurricanes. *Journal of Meteorology* 15, 184-  
3652 195. 10.1175/1520-0469(1958)015<0184:Otmioh>2.0.Co;2

3653 Millot, C., & Taupier-Letage, I. (2005). Circulation in the Mediterranean Sea. In A. Saliot (Ed.),  
3654 *The Mediterranean Sea* (pp. 29-66). Berlin, Heidelberg: Springer Berlin Heidelberg. 978-3-540-  
3655 31492-9. 10.1007/b107143.

3656 Millot, C., & Wald, L. (1980). The effect of Mistral wind on the Ligurian current near Provence.  
3657 *Oceanologica Acta* 3, 399-402.

3658 Minnett, P.J. (1986). A numerical study of the effects of anomalous North Atlantic atmospheric  
3659 conditions on the infrared measurement of sea-surface temperature from space. *Journal of*  
3660 *Geophysical Research* 91, 8509-8521.

3661 Minnett, P.J. (1990). The regional optimization of infrared measurements of sea-surface  
3662 temperature from space. *Journal of Geophysical Research* 95, 13,497-413,510.

3663 Minnett, P.J. (1991). Consequences of sea surface temperature variability on the validation and  
3664 applications of satellite measurements. *Journal of Geophysical Research* 96, 18,475-418,489.

3665 Minnett, P.J. (1995). Measurements of the summer surface heat budget of the Northeast Water  
3666 Polynya in 1992. *Journal of Geophysical Research* 100, 4309-4322.

3667 Minnett, P.J. (1999). The influence of solar zenith angle and cloud type on cloud radiative  
3668 forcing at the surface in the Arctic. *Journal of Climate* 12, 147-158.

3669 Minnett, P.J. (2003). Radiometric measurements of the sea-surface skin temperature - the  
3670 competing roles of the diurnal thermocline and the cool skin. *International Journal of Remote*  
3671 *Sensing* 24, 5033-5047.

3672 Minnett, P.J. (2010). The Validation of Sea Surface Temperature Retrievals from Spaceborne  
3673 Infrared Radiometers. In V. Barale, J.F.R. Gower, & L. Alberotanza (Eds.), *Oceanography from*  
3674 *Space, revisited*. (pp. 273-295): Springer Science+Business Media B.V. ISBN 978-90-481-  
3675 8681-5 <https://doi.org/10.1007/978-90-481-8681-5>.

3676 Minnett, P.J., & Corlett, G.K. (2012). A pathway to generating Climate Data Records of sea-  
3677 surface temperature from satellite measurements. *Deep Sea Research Part II: Topical Studies in*  
3678 *Oceanography* 77–80, 44-51. 10.1016/j.dsr2.2012.04.003

3679 Minnett, P.J., Eyre, J.R., & Pescod, R.W. (1987). The variability of the North Atlantic marine  
3680 atmosphere and its relevance to remote sensing. *International Journal of Remote Sensing* 8, 871-  
3681 880. 10.1080/01431168708948695

3682 Minnett, P.J., & Kaiser-Weiss, A.K. (2012). Group for High Resolution Sea-Surface  
3683 Temperature Discussion Document: Near-Surface Oceanic Temperature Gradients, (7 pp.)  
3684 Available at <https://www.ghrsst.org/wp-content/uploads/2016/10/SSTDefinitionsDiscussion.pdf>.

3685 Minnett, P.J., Knuteson, R.O., Best, F.A., Osborne, B.J., Hanafin, J.A., & Brown, O.B. (2001).  
3686 The Marine-Atmospheric Emitted Radiance Interferometer (M-AERI), a high-accuracy, sea-  
3687 going infrared spectroradiometer. *Journal of Atmospheric and Oceanic Technology* 18, 994-  
3688 1013.

3689 Minnett, P.J., & Smith, D.L. (2014). Postlaunch Calibration and Stability: Thermal Infrared  
3690 Satellite Radiometers. In G. Zibordi, C.J. Donlon, & A.C. Parr (Eds.), *Experimental Methods in*  
3691 *the Physical Sciences, Vol 47, Optical Radiometry for Ocean Climate Measurements* (pp. 201-  
3692 243): Academic Press. 1079-4042. <http://dx.doi.org/10.1016/B978-0-12-417011-7.00008-8>.

3693 Minnett, P.J., Smith, M., & Ward, B. (2011). Measurements of the oceanic thermal skin effect.  
3694 *Deep Sea Research Part II: Topical Studies in Oceanography* 58, 861-868.  
3695 10.1016/j.dsr2.2010.10.024

3696 Minobe, S., Kuwano-Yoshida, A., Komori, N., Xie, S.-P., & Small, R.J. (2008). Influence of the  
3697 Gulf Stream on the troposphere. *Nature* 452, 206. 10.1038/nature06690.  
3698 <https://www.nature.com/articles/nature06690#supplementary-information>

3699 Mittaz, J., Merchant, C.J., & Woolliams, E.R. (2019). Applying principles of metrology to  
3700 historical Earth observations from satellites. *Metrologia* 56, 032002. 10.1088/1681-7575/ab1705

3701 Miyazawa, Y., Varlamov, S.M., Miyama, T., Guo, X., Hihara, T., Kiyomatsu, K., Kachi, M.,  
3702 Kurihara, Y., & Murakami, H. (2017). Assimilation of high-resolution sea surface temperature  
3703 data into an operational nowcast/forecast system around Japan using a multi-scale three-  
3704 dimensional variational scheme. *Ocean Dynamics* 67, 713-728. 10.1007/s10236-017-1056-1  
3705 Mollo-Christensen, E., Cornillon, P., & Mascarenhas, A.D.S. (1981). Method for Estimation of  
3706 Ocean Current Velocity from Satellite Images. *Science* 212, 661-662.  
3707 10.1126/science.212.4495.661  
3708 Montanaro, M., Lunsford, A., Tesfaye, Z., Wenny, B., & Reuter, D. (2014). Radiometric  
3709 Calibration Methodology of the Landsat 8 Thermal Infrared Sensor. *Remote Sensing* 6, 8803-  
3710 8821.  
3711 Montenbruck, O., & Gill, E. (2000). *Satellite Orbits - Models, Methods and Applications*:  
3712 Springer. ISBN 978-3-540-67280-7. DOI 10.1007/978-3-642-58351-3  
3713 Mumby, P.J., Skirving, W., Strong, A.E., Hardy, J.T., LeDrew, E.F., Hochberg, E.J., Stumpf,  
3714 R.P., & David, L.T. (2004). Remote sensing of coral reefs and their physical environment.  
3715 *Marine Pollution Bulletin* 48, 219-228. <http://dx.doi.org/10.1016/j.marpolbul.2003.10.031>  
3716 Muraleedharan, P.M., Pankajakshan, T., & Harikrishnan, M. (2004). Validation of multi-channel  
3717 scanning microwave radiometer on-board Oceansat-I. *Current Science* 87, 370-376.  
3718 Murtugudde, R., Wang, L., Hackert, E., Beauchamp, J., Christian, J., & Busalacchi, A.J. (2004).  
3719 Remote sensing of the Indo-Pacific region: ocean colour, sea level, winds and sea surface  
3720 temperatures. *International Journal of Remote Sensing* 25, 1423-1435.  
3721 10.1080/01431160310001592391  
3722 Nalli, N.R., Minnett, P.J., Maddy, E., McMillan, W.W., & Goldberg, M.D. (2008a). Emissivity  
3723 and reflection model for calculating unpolarized isotropic water surface-leaving radiance in the  
3724 infrared. 2: Validation using Fourier transform spectrometers. *Applied Optics* 47, 4649-4671.  
3725 doi:10.1364/AO.47.004649  
3726 Nalli, N.R., Minnett, P.J., & van Delst, P. (2008b). Emissivity and reflection model for  
3727 calculating unpolarized isotropic water surface-leaving radiance in the infrared. I: Theoretical  
3728 development and calculations. *Applied Optics* 47, 3701-3721. doi:10.1364/AO.47.003701  
3729 Nerem, R.S., Beckley, B.D., Fasullo, J.T., Hamlington, B.D., Masters, D., & Mitchum, G.T.  
3730 (2018). Climate-change-driven accelerated sea-level rise detected in the altimeter era.  
3731 *Proceedings of the National Academy of Sciences* 115, 2022-2025. 10.1073/pnas.1717312115  
3732 Neumann, B., Vafeidis, A.T., Zimmermann, J., & Nicholls, R.J. (2015). Future Coastal  
3733 Population Growth and Exposure to Sea-Level Rise and Coastal Flooding - A Global  
3734 Assessment. *PLoS ONE* 10, e0118571. 10.1371/journal.pone.0118571  
3735 Nicholls, R.J., & Cazenave, A. (2010). Sea-Level Rise and Its Impact on Coastal Zones. *Science*  
3736 328, 1517-1520. 10.1126/science.1185782  
3737 Nielsen-Englyst, P., L. Høyer, J., Toudal Pedersen, L., L. Gentemann, C., Alerskans, E., Block,  
3738 T., & Donlon, C. (2018). Optimal Estimation of Sea Surface Temperature from AMSR-E.  
3739 *Remote Sensing* 10, 229.  
3740 Njoku, E.G.A., M.J.; Asrar, G.; Marzano, F.S.; Minnett, P.; Salomonson, V.V.; Singhroy, V.;  
3741 Turk, J. (Eds) (2014). *Encyclopedia of Remote Sensing*. (1<sup>st</sup> ed.): Springer-Verlag New York.  
3742 ISBN 978-0-387-36698-2  
3743 NRC (2000). *Issues in the Integration of Research and Operational Satellite Systems for Climate*  
3744 *Research: II. Implementation*. (pp. 82) Washington, DC, USA.: National Academy of Sciences.  
3745 ISBN: 0-309-06994-7

3746 Nykjaer, L. (2009). Mediterranean Sea surface warming 1985-2006. *Climate research (Open*  
3747 *Access for articles 4 years old and older)* 39, 11.

3748 O'Carroll, A.G., August, T., Le Borgne, P., & Marsouin, A. (2012). The accuracy of SST  
3749 retrievals from Metop-A IASI and AVHRR using the EUMETSAT OSI-SAF matchup dataset.  
3750 *Remote Sensing of Environment* 126, 184-194. <http://dx.doi.org/10.1016/j.rse.2012.08.006>

3751 O'Carroll, A.G., Eyre, J.R., & Saunders, R.W. (2008). Three-Way Error Analysis between  
3752 AATSR, AMSR-E, and In Situ Sea Surface Temperature Observations. *Journal of Atmospheric*  
3753 *and Oceanic Technology* 25, 1197-1207.

3754 O'Carroll, A.G., Armstrong, E.M., Beggs, H.M., Bouali, M., Casey, K.S., Corlett, G.K., Dash,  
3755 P., Donlon, C.J., Gentemann, C.L., Hoeyer, J., Ignatov, A., Kabobah, K., Kachi, M., Kurihara,  
3756 Y., Karagali, I., Maturi, E., Merchant, C.J., Marullo, S., Minnett, P.J., Pennybacker, M.,  
3757 Ramakrishnan, B., Ramsankaran, R., Santoleri, R., Sunder, S., Picart, S.S., Vázquez-Cuervo, J.,  
3758 & Wimmer, W. (2019). Observational Needs of Sea Surface Temperature. *Frontiers in Marine*  
3759 *Science Accepted, July 5, 2019.*

3760 O'Neill, L.W., Esbensen, S.K., Thum, N., Samelson, R.M., & Chelton, D.B. (2010). Dynamical  
3761 analysis of the boundary layer and surface wind responses to mesoscale SST perturbations.  
3762 *Journal of Climate* 23, 559-581.

3763 Oddo, P., Adani, M., Pinardi, N., Fratianni, C., Tonani, M., & Pettenuzzo, D. (2009). A nested  
3764 Atlantic-Mediterranean Sea general circulation model for operational forecasting. *Ocean*  
3765 *Science*, 461-473.

3766 Ohring, G., Wielicki, B., Spencer, R., Emery, B., & Datla, R. (2005). Satellite Instrument  
3767 Calibration for Measuring Global Climate Change: Report of a Workshop. *Bulletin of the*  
3768 *American Meteorological Society* 86, 1303-1313.

3769 Olmedo, E., Taupier-Letage, I., Turiel, A., & Alvera-Azcárate, A. (2018). Improving SMOS Sea  
3770 Surface Salinity in the Western Mediterranean Sea through Multivariate and Multifractal  
3771 Analysis. *Remote Sensing* 10, 485.

3772 Olsen, A., Triñanes, J., & Wanninkhof, R. (2004). Sea-air flux of CO<sub>2</sub> in the Caribbean Sea  
3773 estimated using in situ and remote sensing data. *Remote Sensing of Environment* 89, 309-325.

3774 Ouaknine, J., Gode, S., Napierala, B., Viard, T., Foerster, U., Fray, S., Peacocke, P., Hartl, M.,  
3775 Hallibert, P., & Durand, Y. (2013). MTG Flexible Combined Imager optical design and  
3776 performances. In Proceedings of SPIE Optical Engineering + Applications, 8866, (14 pp): SPIE.  
3777 doi:

3778 Palmen, E. (1948). On the formation and structure of tropical hurricanes. *Geophysica* 3, 26-38.

3779 Parekh, A., Sharma, R., & Sarkar, A. (2007). A Comparative Assessment of Surface Wind Speed  
3780 and Sea Surface Temperature over the Indian Ocean by TMI, MSMR, and ERA-40. *Journal of*  
3781 *Atmospheric and Oceanic Technology* 24, 1131-1142. 10.1175/jtech2021.1

3782 Park, E.-B., Han, K.-S., Yeom, J.-M., Lee, C.-S., Ryu, J.-H., Kim, H., & Kim, D.-H. (2015).  
3783 Effects of GSICS correction on estimation of sea surface temperature using COMS data.  
3784 *International Journal of Remote Sensing* 36, 1026-1037. 10.1080/01431161.2015.1007249

3785 Parkinson, C., Ward, A., & King, M. (2006). Earth science reference handbook: a guide to  
3786 NASA's earth science program and earth observing satellite missions. *National Aeronautics and*  
3787 *Space Administration*, 277.

3788 Pascual, A., Ruiz, S., Olita, A., Troupin, C., Claret, M., Casas, B., Mourre, B., Poulain, P.-M.,  
3789 Tovar-Sanchez, A., Capet, A., Mason, E., Allen, J.T., Mahadevan, A., & Tintoré, J. (2017). A  
3790 Multiplatform Experiment to Unravel Meso- and Submesoscale Processes in an Intense Front  
3791 (AlborEx). *Frontiers in Marine Science* 4. 10.3389/fmars.2017.00039



3792 Pastor, F., Valiente, J.A., & Palau, J.L. (2018). Sea Surface Temperature in the Mediterranean:  
3793 Trends and Spatial Patterns (1982–2016). *Pure and Applied Geophysics* 175, 4017-4029.  
3794 10.1007/s00024-017-1739-z

3795 Pearson, K., Merchant, C., Embury, O., & Donlon, C. (2018). The Role of Advanced Microwave  
3796 Scanning Radiometer 2 Channels within an Optimal Estimation Scheme for Sea Surface  
3797 Temperature. *Remote Sensing* 10, 90.

3798 Peralta-Ferriz, C., & Woodgate, R.A. (2015). Seasonal and interannual variability of pan-Arctic  
3799 surface mixed layer properties from 1979 to 2012 from hydrographic data, and the dominance of  
3800 stratification for multiyear mixed layer depth shoaling. *Progress In Oceanography* 134, 19-53.  
3801 <https://doi.org/10.1016/j.pocean.2014.12.005>

3802 Perlin, N., de Szoeko, S.P., Chelton, D.B., Samelson, R.M., Skyllingstad, E.D., & O'Neill, L.W.  
3803 (2014). Modeling the Atmospheric Boundary Layer Wind Response to Mesoscale Sea Surface  
3804 Temperature Perturbations. *Monthly Weather Review* 142, 4284-4307. 10.1175/mwr-d-13-  
3805 00332.1

3806 Petrenko, B., Ignatov, A., Kihai, Y., Stroup, J., & Dash, P. (2014). Evaluation and selection of  
3807 SST regression algorithms for JPSS VIIRS. *Journal of Geophysical Research: Atmospheres* 119,  
3808 2013JD020637. 10.1002/2013JD020637

3809 Piepmeier, J.R., Focardi, P., Horgan, K.A., Knuble, J., Ehsan, N., Lucey, J., Brambora, C.,  
3810 Brown, P.R., Hoffman, P.J., French, R.T., Mikhaylov, R.L., Kwack, E., Slimko, E.M., Dawson,  
3811 D.E., Hudson, D., Peng, J., Mohammed, P.N., Amici, G.D., Freedman, A.P., Medeiros, J., Sacks,  
3812 F., Estep, R., Spencer, M.W., Chen, C.W., Wheeler, K.B., Edelstein, W.N., O'Neill, P.E., &  
3813 Njoku, E.G. (2017). SMAP L-Band Microwave Radiometer: Instrument Design and First Year  
3814 on Orbit. *IEEE Transactions on Geoscience and Remote Sensing* 55, 1954-1966.  
3815 10.1109/TGRS.2016.2631978

3816 Pinardi, N., Allen, I., Demirov, E., De Mey, P., Korres, G., Lascaratos, A., Le Traon, P.-Y.,  
3817 Maillard, C., Manzella, G., & Tziavos, C. (2003). The Mediterranean ocean forecasting system:  
3818 first phase of implementation (1998-2001). *Annales Geophysicae* 21, 3-20.

3819 Pinardi, N., & Coppini, G. (2010). Preface "Operational oceanography in the Mediterranean Sea:  
3820 the second stage of development". *Ocean Sci.* 6, 263-267. 10.5194/os-6-263-2010

3821 Pinardi, N., & Woods, J. (Eds.) (2002). *Ocean forecasting: conceptual basis and applications*.  
3822 Berlin, Germany: Springer Science & Business Media. ISBN: 3540679642. pp. 472,

3823 Pisano, A., Buongiorno Nardelli, B., Tronconi, C., & Santoleri, R. (2016). The new  
3824 Mediterranean optimally interpolated pathfinder AVHRR SST Dataset (1982–2012). *Remote  
3825 Sensing of Environment* 176, 107-116. <https://doi.org/10.1016/j.rse.2016.01.019>

3826 Poli, P., Lucas, M., O'Carroll, A., Le Menn, M., David, A., Corlett, G.K., Blouch, P., Meldrum,  
3827 D., Merchant, C.J., Belbeoch, M., & Herklotz, K. (2018). The Copernicus Surface Velocity  
3828 Platform drifter with Barometer and Reference Sensor for Temperature (SVP-BRST): Genesis,  
3829 design, and initial results. *Ocean Sci. Discuss.* 2018, 1-34. 10.5194/os-2018-109

3830 Prabhakara, C., Wang, I., Chang, A.T.C., & Gloersen, P. (1983). A Statistical Examination of  
3831 Nimbus-7 SMMR Data and Remote Sensing of Sea Surface Temperature, Liquid Water Content  
3832 in the Atmosphere and Surface Wind Speed. *Journal of Climate and Applied Meteorology* 22,  
3833 2023-2037. 10.1175/1520-0450(1983)022<2023:Aseons>2.0.Co;2

3834 Prata, A.J., Cechet, R.P., Barton, I.J., & Llewellyn-Jones, D.T. (1990). The Along-Track  
3835 Scanning Radiometer for ERS-1 - scan geometry and data simulation. *IEEE Transactions on  
3836 Geoscience and Remote Sensing* 28, 3-13.

3837 Price, J.F., Weller, R.A., & Pinkel, R. (1986). Diurnal cycling: observations and models of the  
3838 upper ocean response to diurnal heating, cooling and wind mixing. *Journal of Geophysical*  
3839 *Research* 91, 8411-8427.

3840 Prospero, J.M. (1999). Long-range transport of mineral dust in the global atmosphere: Impact of  
3841 African dust on the environment of the southeastern United States. *Proceedings of the National*  
3842 *Academy of Science USA* 96, 3396-3403.

3843 Prospero, J.M., & Carlson, T.N. (1972). Vertical and areal distribution of Saharan dust over the  
3844 western Equatorial North Atlantic Ocean. *Journal of Geophysical Research* 77, 5255-5265.

3845 Prospero, J.M., Ginoux, P., Torres, O., Nicholson, S.E., & Gill, T.E. (2002). Environmental  
3846 Characterization of Global Sources of Atmospheric Soil Dust Identified with the Nimbus 7 Total  
3847 Ozone Mapping Spectrometer (TOMS) Absorbing Aerosol Product. *Reviews of Geophysics* 40  
3848 Puschell, J.J., Lowe, H.A., Jeter, J.W., Kus, S.M., Hurt, W.T., Gilman, D., Rogers, D.L., Hoelzer,  
3849 R.L., & Ravella, R. (2002). Japanese Advanced Meteorological Imager: a next-generation GEO  
3850 imager for MTSAT-1R. In Proceedings of International Symposium on Optical Science and  
3851 Technology, Earth Observing Systems VII., Seattle, WA, USA, 4814, (152-161 pp): SPIE. doi:  
3852 10.1117/12.453755

3853 Rabe, B., Karcher, M., Schauer, U., Toole, J.M., Krishfield, R.A., Pisarev, S., Kauker, F.,  
3854 Gerdes, R., & Kikuchi, T. (2011). An assessment of Arctic Ocean freshwater content changes  
3855 from the 1990s to the 2006–2008 period. *Deep Sea Research Part I: Oceanographic Research*  
3856 *Papers* 58, 173-185. <https://doi.org/10.1016/j.dsr.2010.12.002>

3857 Rajeev, K., Parameswaran, K., Nair, S.K., & Meenu, S. (2008). Observational evidence for the  
3858 radiative impact of Indonesian smoke in modulating the sea surface temperature of the equatorial  
3859 Indian Ocean. *Journal of Geophysical Research* 113. 10.1029/2007jd009611

3860 Ramage, C.S. (1974). The Typhoons of October 1970 in the South China Sea: Intensification,  
3861 Decay and Ocean Interaction. *Journal of Applied Meteorology* 13, 739-751. 10.1175/1520-  
3862 0450(1974)013<0739:Ttooit>2.0.Co;2

3863 Randelhoff, A., Fer, I., & Sundfjord, A. (2017). Turbulent Upper-Ocean Mixing Affected by  
3864 Meltwater Layers during Arctic Summer. *Journal of Physical Oceanography* 47, 835-853.  
3865 10.1175/jpo-d-16-0200.1

3866 Rappaport, E.N., Franklin, J.L., Schumacher, A.B., DeMaria, M., Shay, L.K., & Gibney, E.J.  
3867 (2010). Tropical Cyclone Intensity Change before U.S. Gulf Coast Landfall. *Weather and*  
3868 *Forecasting* 25, 1380-1396. 10.1175/2010waf2222369.1

3869 Rayner, N.A., Brohan, P., Parker, D.E., Folland, C.K., Kennedy, J.J., Vanicek, M., Ansell, T.J.,  
3870 & Tett, S.F.B. (2006). Improved Analyses of Changes and Uncertainties in Sea Surface  
3871 Temperature Measured In Situ since the Mid-Nineteenth Century: The HadSST2 Dataset.  
3872 *Journal of Climate* 19, 446-469.

3873 Reul, N., Chapron, B., Lee, T., Donlon, C., Boutin, J., & Alory, G. (2014). Sea surface salinity  
3874 structure of the meandering Gulf Stream revealed by SMOS sensor. *Geophysical Research*  
3875 *Letters* 41, 3141-3148. doi:10.1002/2014GL059215

3876 Reynolds, R.W. (1988). A Real-Time Global Sea Surface Temperature Analysis. *Journal of*  
3877 *Climate* 1, 75-87. doi: 10.1175/1520-0442(1988)001<0075:Artgss>2.0.Co;2

3878 Reynolds, R.W., & Marsico, D.C. (1993). An Improved Real-Time Global Sea Surface  
3879 Temperature Analysis. *Journal of Climate* 6, 114-119. 10.1175/1520-  
3880 0442(1993)006<0114:Airtgs>2.0.Co;2

3881 Reynolds, R.W., & Smith, T.M. (1994). Improved global sea surface temperature analysis using  
3882 optimum interpolation. *J. Climate* 7, 929-948.

3883 Rice, J.P., Butler, J.J., Johnson, B.C., Minnett, P.J., Maillet, K.A., Nightingale, T.J., Hook, S.J.,  
3884 Abtahi, A., Donlon, C.J., & Barton, I.J. (2004). The Miami2001 Infrared Radiometer Calibration  
3885 and Intercomparison: 1. Laboratory Characterization of Blackbody Targets. *Journal of*  
3886 *Atmospheric and Oceanic Technology* 21, 258-267.

3887 Richter-Menge, J.A., Perovich, D.K., & Pegau, W.S. (2001). Summer ice dynamics during  
3888 SHEBA and its effect on the ocean heat content. *Annals of Glaciology* 33, 201-206.  
3889 10.3189/172756401781818176

3890 Rignot, E., Velicogna, I., van den Broeke, M.R., Monaghan, A., & Lenaerts, J.T.M. (2011).  
3891 Acceleration of the contribution of the Greenland and Antarctic ice sheets to sea level rise.  
3892 *Geophysical Research Letters* 38. doi:10.1029/2011GL046583

3893 Rio, M.-H., Santoleri, R., Bourdalle-Badie, R., Griffa, A., Piterbarg, L., & Taburet, G. (2016).  
3894 Improving the Altimeter-Derived Surface Currents Using High-Resolution Sea Surface  
3895 Temperature Data: A Feasibility Study Based on Model Outputs. *Journal of Atmospheric and*  
3896 *Oceanic Technology* 33, 2769-2784. 10.1175/jtech-d-16-0017.1

3897 Rio, M.H., & Santoleri, R. (2018). Improved global surface currents from the merging of  
3898 altimetry and Sea Surface Temperature data. *Remote Sensing of Environment* 216, 770-785.  
3899 <https://doi.org/10.1016/j.rse.2018.06.003>

3900 Robinson, A.R., & Golnaraghi, M. (1993). Circulation and dynamics of the Eastern  
3901 Mediterranean Sea; quasi-synoptic data-driven simulations. *Deep Sea Research Part II: Topical*  
3902 *Studies in Oceanography* 40, 1207-1246. [https://doi.org/10.1016/0967-0645\(93\)90068-X](https://doi.org/10.1016/0967-0645(93)90068-X)

3903 Robinson, I.S. (2004). *Measuring the oceans from space: the principles and methods of satellite*  
3904 *oceanography*: Springer Science & Business Media. ISBN 978-3-540-42647-9

3905 Robinson, I.S. (2010). *Discovering the Ocean from Space*: Springer-Verlag Berlin Heidelberg.  
3906 978-3-540-24430-1. 10.1007/978-3-540-68322-3

3907 Rodgers, C.D. (2000). *Inverse Methods for Atmospheric Sounding: Theory and Practice*: World  
3908 Scientific. 9789810227401

3909 Roemmich, D., Johnson, G., Riser, S., Davis, R., Gilson, J., Owens, W.B., Garzoli, S., Schmid,  
3910 C., & Ignaszewski, M. (2009). The Argo program: observing the global ocean with profiling  
3911 floats. *Oceanography* 22, 34-43.

3912 Santoleri, R., Marullo, S., & Böhm, E. (1991). An objective analysis scheme for AVHRR  
3913 imagery. *International Journal of Remote Sensing* 12, 681-693. 10.1080/01431169108929685

3914 Santoleri, R., Nardelli, B.B., & Banzon, V. (2002). Sea Surface Characterization by Combined  
3915 Data. In F.S. Marzano, & G. Visconti (Eds.), *Remote Sensing of Atmosphere and Ocean from*  
3916 *Space: Models, Instruments and Techniques* (pp. 201-214). Dordrecht: Springer Netherlands.  
3917 978-0-306-48150-5. 10.1007/0-306-48150-2\_13.

3918 Saunders, R.W., Blackmore, T.A., Candy, B., Francis, P.N., & Hewison, T.J. (2013). Monitoring  
3919 Satellite Radiance Biases Using NWP Models. *IEEE Transactions on Geoscience and Remote*  
3920 *Sensing* 51, 1124-1138. 10.1109/TGRS.2012.2229283

3921 Schiller, A., & Godfrey, J.S. (2005). A diagnostic model of the diurnal cycle of sea surface  
3922 temperature for use in coupled ocean-atmosphere models. *Journal of Geophysical Research* 110,  
3923 C11014.

3924 Schmid, J. (2012). The SEVIRI Instrument, (10 pp.). Noordwijk, The Netherlands: ESA ESTEC.  
3925 Available at  
3926 [https://www.eumetsat.int/website/wcm/idc/groups/ops/documents/document/mday/mde1/~edisp/](https://www.eumetsat.int/website/wcm/idc/groups/ops/documents/document/mday/mde1/~edisp/pdf_ten_msg_seviri_instrument.pdf)  
3927 [pdf\\_ten\\_msg\\_seviri\\_instrument.pdf](https://www.eumetsat.int/website/wcm/idc/groups/ops/documents/document/mday/mde1/~edisp/pdf_ten_msg_seviri_instrument.pdf).

3928 Schueler, C.F., Lee, T.F., & Miller, S.D. (2013). VIIRS constant spatial-resolution advantages.  
3929 *International Journal of Remote Sensing* 34, 5761-5777. 10.1080/01431161.2013.796102  
3930 Screen, J.A., Simmonds, I., Deser, C., & Tomas, R. (2013). The Atmospheric Response to Three  
3931 Decades of Observed Arctic Sea Ice Loss. *Journal of Climate* 26, 1230-1248. 10.1175/jcli-d-12-  
3932 00063.1  
3933 Shaltout, M., & Omstedt, A. (2014). Recent sea surface temperature trends and future scenarios  
3934 for the Mediterranean Sea. *Oceanologia* 56, 411-443. <https://doi.org/10.5697/oc.56-3.411>  
3935 Shay, L.K., Goni, G.J., & Black, P.G. (2000). Effects of a Warm Oceanic Feature on Hurricane  
3936 Opal. *Monthly Weather Review* 128, 1366-1383.  
3937 Shibata, A. (2006). Features of ocean microwave emission changed by wind at 6 GHz. *Journal*  
3938 *of Oceanography* 62, 321-330.  
3939 Shine, K.P., Ptashnik, I.V., & Rädcl, G. (2012). The Water Vapour Continuum: Brief History  
3940 and Recent Developments. *Surveys in Geophysics* 33, 535-555. 10.1007/s10712-011-9170-y  
3941 Ships4SST (2019). The Recommended ISFRN L2R Data Specification and User Manual, (52 pp.)  
3942 Available at [http://www.shipborne-radiometer.org/sites/shipborne-](http://www.shipborne-radiometer.org/sites/shipborne-radiometer/files/documents/Recommended%20ISFRN%20L2R%20Data%20Specification%20and%20User%20Manual%20v1.2%20rev0.pdf)  
3943 [radiometer/files/documents/Recommended%20ISFRN%20L2R%20Data%20Specification%20a](http://www.shipborne-radiometer.org/sites/shipborne-radiometer/files/documents/Recommended%20ISFRN%20L2R%20Data%20Specification%20and%20User%20Manual%20v1.2%20rev0.pdf)  
3944 [nd%20User%20Manual%20v1.2%20rev0.pdf](http://www.shipborne-radiometer.org/sites/shipborne-radiometer/files/documents/Recommended%20ISFRN%20L2R%20Data%20Specification%20and%20User%20Manual%20v1.2%20rev0.pdf).  
3945 Simeoni, D., Astruc, P., Miras, D., Alis, C., Andreis, O., Scheidel, D., Degrelle, C., Nicol, P.,  
3946 Bailly, B., Guiard, P., Clauss, A., Blumstein, D., Maciaszek, T., Chalou, G., Carlier, T., & Kayal,  
3947 G. (2004). Design and development of IASI instrument. In Proceedings of Optical Science and  
3948 Technology, the SPIE 49th Annual Meeting, 5543, (12 pp): SPIE. doi:  
3949 Simpson, J.J., & Yhann, S.R. (1994). Reduction of noise in AVHRR channel 3 data with  
3950 minimum distortion. *IEEE Transactions on Geoscience and Remote Sensing* 32, 315-328.  
3951 10.1109/36.295047  
3952 Skliris, N., Sofianos, S., Gkanasos, A., Mantziafou, A., Vervatis, V., Axaopoulos, P., &  
3953 Lascaratos, A. (2012). Decadal scale variability of sea surface temperature in the Mediterranean  
3954 Sea in relation to atmospheric variability. *Ocean Dynamics* 62, 13-30. 10.1007/s10236-011-  
3955 0493-5  
3956 Small, R.J., deSzoek, S.P., Xie, S.P., O'Neill, L., Seo, H., Song, Q., Cornillon, P., Spall, M., &  
3957 Minobe, S. (2008). Air-sea interaction over ocean fronts and eddies. *Dynamics of Atmospheres*  
3958 *and Oceans* 45, 274-319. <http://dx.doi.org/10.1016/j.dynatmoce.2008.01.001>  
3959 Smedsrud, L.H., Esau, I., Ingvaldsen, R.B., Eldevik, T., Haugan, P.M., Li, C., Lien, V.S., Olsen,  
3960 A., Omar, A.M., Otterå, O.H., Risebrobakken, B., Sandø, A.B., Semenov, V.A., & Sorokina,  
3961 S.A. (2013). The Role of the Barents Sea in the Arctic Climate System. *Reviews of Geophysics*  
3962 51, 415-449. 10.1002/rog.20017  
3963 Smith, D., Mutlow, C., Delderfield, J., Watkins, B., & Mason, G. (2012). ATSR infrared  
3964 radiometric calibration and in-orbit performance. *Remote Sensing of Environment* 116, 4-16.  
3965 10.1016/j.rse.2011.01.027  
3966 Smith, D.L., Nightingale, T.J., Mortimer, H., Middleton, K., Edeson, R., Cox, C.V., Mutlow,  
3967 C.T., Maddison, B.J., & Coppo, P. (2014). Calibration approach and plan for the sea and land  
3968 surface temperature radiometer. *Journal of Applied Remote Sensing* 8, 084980-084980.  
3969 10.1117/1.JRS.8.084980  
3970 Smith, E.A., Asrar, G., Furuhashi, Y., Ginati, A., Mugnai, A., Nakamura, K., Adler, R.F., Chou,  
3971 M.-D., Desbois, M., & Durning, J.F. (2007). International global precipitation measurement  
3972 (GPM) program and mission: An overview. *Measuring precipitation from space* (pp. 611-653):  
3973 Springer. 1402058349,

3974 Smith, M., Stammerjohn, S., Persson, O., Rainville, L., Liu, G., Perrie, W., Robertson, R.,  
3975 Jackson, J., & Thomson, J. (2018). Episodic Reversal of Autumn Ice Advance Caused by  
3976 Release of Ocean Heat in the Beaufort Sea. *Journal of Geophysical Research: Oceans* 123,  
3977 3164-3185. doi:10.1002/2018JC013764

3978 Smith, N., & Koblinsky, C. (2001). The ocean observing system for the 21st Century, a  
3979 consensus statement. *Observing the Oceans in the 21st Century* (pp. 1-25). ISBN-10:  
3980 0642706182,

3981 Smith, W.L., Knuteson, R.O., Revercomb, H.E., Feltz, W., Howell, H.B., Menzel, W.P., Nalli,  
3982 N., Brown, O., Brown, J., Minnett, P., & McKeown, W. (1996). Observations of the infrared  
3983 radiative properties of the ocean - implications for the measurement of sea surface temperature  
3984 via satellite remote sensing. *Bulletin of the American Meteorological Society* 77, 41-51.

3985 Smyth, T.J., Miller, P.I., Groom, S.B., & Lavender, S.J. (2001). Remote sensing of sea surface  
3986 temperature and chlorophyll during Lagrangian experiments at the Iberian margin. *Progress In*  
3987 *Oceanography* 51, 269-281. [https://doi.org/10.1016/S0079-6611\(01\)00070-2](https://doi.org/10.1016/S0079-6611(01)00070-2)

3988 Soloviev, A.V., & Lukas, R. (2014). *The Near-Surface Layer of the Ocean: Structure, Dynamics,*  
3989 *and Applications. Second edition.* New York: Springer. ISBN 978-94-007-7620-3.  
3990 10.1007/978-94-007-7621-0

3991 Song, Q., Cornillon, P., & Hara, T. (2006). Surface wind response to oceanic fronts. *Journal of*  
3992 *Geophysical Research: Oceans* 111. 10.1029/2006jc003680

3993 Steele, M., & Dickinson, S. (2016). The phenology of Arctic Ocean surface warming. *Journal of*  
3994 *Geophysical Research: Oceans* 121, 6847-6861. doi:10.1002/2016JC012089

3995 Steele, M., & Ermold, W. (2015). Loitering of the retreating sea ice edge in the Arctic Seas.  
3996 *Journal of Geophysical Research: Oceans* 120, 7699-7721. doi:10.1002/2015JC011182

3997 Steele, M., Ermold, W., & Zhang, J. (2008). Arctic Ocean surface warming trends over the past  
3998 100 years. *Geophysical Research Letters* 35. doi:10.1029/2007GL031651

3999 Steele, M., Zhang, J., & Ermold, W. (2010). Mechanisms of summertime upper Arctic Ocean  
4000 warming and the effect on sea ice melt. *Journal of Geophysical Research: Oceans* 115.  
4001 doi:10.1029/2009JC005849

4002 Stommel, H., Saunders, K., Simmons, W., & Cooper, J. (1969). Observations of the diurnal  
4003 thermocline. *Deep Sea Research Supplement Vol 16*, 269-284.

4004 Stramma, L., Cornillon, P., Weller, R.A., Price, J.F., & Briscoe, M.G. (1986). Large diurnal sea  
4005 surface temperature variability: satellite and in situ measurements. *Journal of Physical*  
4006 *Oceanography* 16, 827-837.

4007 Stroeve, J.C., Crawford, A.D., & Stammerjohn, S. (2016). Using timing of ice retreat to predict  
4008 timing of fall freeze-up in the Arctic. *Geophysical Research Letters* 43, 6332-6340.  
4009 doi:10.1002/2016GL069314

4010 Strong, A.E., & McClain, E.P. (1984). Improved ocean surface temperatures from space -  
4011 comparisons with drifting buoys. *Bulletin of the American Meteorological Society* 65, 138-142.

4012 Strong, C., & Rigor, I.G. (2013). Arctic marginal ice zone trending wider in summer and  
4013 narrower in winter. *Geophysical Research Letters* 40, 4864-4868. doi:10.1002/grl.50928

4014 Stuart-Menteth, A., Robinson, I.S., & Challenor, P.G. (2003). A global study of diurnal warming  
4015 using satellite-derived sea surface temperature. *J. Geophys. Res.* 108, 3155.

4016 Stuart-Menteth, A.C., Robinson, I.S., & Donlon, C.J. (2005a). Sensitivity of the diurnal warm  
4017 layer to meteorological fluctuations. Part 2: A new parameterisation for diurnal warming.  
4018 *Journal of Atmospheric and Ocean Science* 10, 209-234.

4019 Stuart-Menteth, A.C., Robinson, I.S., Wellner, R.A., & Donlon, C.J. (2005b). Sensitivity of the  
4020 diurnal warm layer to meteorological fluctuations part 1: observations. *Journal of Atmospheric*  
4021 *and Ocean Science* 10, 193-208.

4022 Stuart, V., Platt, T., & Sathyendranath, S. (2011). The future of fisheries science in management:  
4023 a remote-sensing perspective. *ICES Journal of Marine Science* 68, 644-650.  
4024 10.1093/icesjms/fsq200

4025 Sykes, P., While, J., A. Sellar, & Martin, M. (2011). Diurnal Variability in Sea Surface  
4026 Temperature: Observation and model assessment, *Forecasting Research Technical Report*, 556,  
4027 (42 pp.). Exeter, UK: UK Met Office. Available at  
4028 [https://www.google.com/url?sa=t&rct=j&q=&esrc=s&source=web&cd=3&ved=2ahUKEwiKguj99O\\_eAhVhTd8KHR3iBMMQFjACegQIAxAC&url=https%3A%2F%2Fdigital.nmla.metoffice.gov.uk%2Fdownload%2Ffile%2Fsdb%253AdigitalFile%257C6cae475e-1177-41fa-806c-937ebeeacda0%2F&usq=AOvVaw2lSPuCluoYFvxvjjOrWcAy](https://www.google.com/url?sa=t&rct=j&q=&esrc=s&source=web&cd=3&ved=2ahUKEwiKguj99O_eAhVhTd8KHR3iBMMQFjACegQIAxAC&url=https%3A%2F%2Fdigital.nmla.metoffice.gov.uk%2Fdownload%2Ffile%2Fsdb%253AdigitalFile%257C6cae475e-1177-41fa-806c-937ebeeacda0%2F&usq=AOvVaw2lSPuCluoYFvxvjjOrWcAy).

4032 Szciodrak, M., Minnett, P.J., & Evans, R.H. (2014). The effects of anomalous atmospheres on  
4033 the accuracy of infrared sea-surface temperature retrievals: Dry air layer intrusions over the  
4034 tropical ocean. *Remote Sensing of Environment* 140, 450-465.  
4035 <http://dx.doi.org/10.1016/j.rse.2013.09.010>

4036 Szekiolda, K.-H., Salomonson, V., & Allison, L.J. (1972). Rapid Variations of Sea Surface  
4037 Temperature in the Persian Gulf as Recorded by Nimbus 2 HRIR. *Limnology and Oceanography*  
4038 17, 307-309. doi:10.4319/lo.1972.17.2.0307

4039 Taberner, M., Shutler, J., Walker, P., Poulter, D., Piolle, J., Donlon, C., & Guidetti, V. (2013).  
4040 The ESA FELYX High Resolution Diagnostic Data Set System Design and Implementation.  
4041 *ISPRS-International Archives of the Photogrammetry, Remote Sensing and Spatial Information*  
4042 *Sciences*, 243-249. doi:10.5194/isprsarchives-XL-7-W2-243-2013

4043 Tanaka, K., Okamura, Y., Mokuno, M., Amano, T., & Yoshida, J. (2018). First year on-orbit  
4044 calibration activities of SGLI on GCOM-C satellite. In Proceedings of SPIE Asia-Pacific Remote  
4045 Sensing, Honolulu, Hawaii, USA, 10781, (10 pp): SPIE. doi: <https://doi.org/10.1117/12.2324703>

4046 Tandeo, P., Chapron, B., Ba, S.O., Autret, E., & Fablet, R. (2014). Segmentation of Mesoscale  
4047 Ocean Surface Dynamics Using Satellite SST and SSH Observations. *IEEE Trans. Geoscience*  
4048 *and Remote Sensing* 52, 4227-4235.

4049 Taylor, B.N., & Thompson, A. (2008). *The International System of Units (SI). 8<sup>th</sup> Edition*.  
4050 Washington DC, USA: National Institute of Standards and Technology.

4051 Theocharous, E., Fox, N.P., Barker-Snook, I., Niclòs, R., Santos, V.G., Minnett, P.J., Götsche,  
4052 F.M., Poutier, L., Morgan, N., Nightingale, T., Wimmer, W., Høyer, J., Zhang, K., Yang, M.,  
4053 Guan, L., Arbelo, M., & Donlon, C.J. (2019). The 2016 CEOS Infrared Radiometer Comparison:  
4054 Part II: Laboratory Comparison of Radiation Thermometers. *Journal of Atmospheric and*  
4055 *Oceanic Technology* 36, 1079-1092. 10.1175/jtech-d-18-0032.1

4056 Thiébaux, J., Rogers, E., Wang, W., & Katz, B. (2003). A New High-Resolution Blended Real-  
4057 Time Global Sea Surface Temperature Analysis. *Bulletin of the American Meteorological*  
4058 *Society* 84, 645-656. 10.1175/bams-84-5-645

4059 Thomas, A.C., Blanco, J.L., Carr, M.E., Strub, P.T., & Osses, J. (2001). Satellite-measured  
4060 chlorophyll and temperature variability off northern Chile during the 1996–1998 La Niña and El  
4061 Niño. *Journal of Geophysical Research: Oceans* 106, 899-915. doi:10.1029/1999JC000052

4062 Thomas, A.C., Ted Strub, P., Weatherbee, R.A., & James, C. (2012). Satellite views of Pacific  
4063 chlorophyll variability: Comparisons to physical variability, local versus nonlocal influences and

4064 links to climate indices. *Deep Sea Research Part II: Topical Studies in Oceanography* 77-80, 99-  
4065 116. <https://doi.org/10.1016/j.dsr2.2012.04.008>

4066 Tonooka, H., Palluconi, F.D., Hook, S.J., & Matsunaga, T. (2005). Vicarious calibration of  
4067 ASTER thermal infrared bands. *IEEE Transactions on Geoscience and Remote Sensing* 43,  
4068 2733-2746. 10.1109/TGRS.2005.857885

4069 Trinh, R.C., Fichot, C.G., Gierach, M.M., Holt, B., Malakar, N.K., Hulley, G., & Smith, J.  
4070 (2017). Application of Landsat 8 for Monitoring Impacts of Wastewater Discharge on Coastal  
4071 Water Quality. *Frontiers in Marine Science* 4. 10.3389/fmars.2017.00329

4072 Trishchenko, A.P., Fedosejevs, G., Li, Z., & Cihlar, J. (2002). Trends and uncertainties in  
4073 thermal calibration of AVHRR radiometers onboard NOAA-9 to NOAA-16. *Journal of*  
4074 *Geophysical Research: Atmospheres* 107, 4778. 10.1029/2002JD002353

4075 Tyagi, G., Babu, K.N., Mathur, A.K., & Solanki, H.A. (2018). INSAT-3D and MODIS retrieved  
4076 sea surface temperature validation and assessment over waters surrounding the Indian  
4077 subcontinent. *International Journal of Remote Sensing* 39, 1575-1592.  
4078 10.1080/01431161.2017.1407051

4079 Uma, S.B., Donald, A.W., Martha, K.R., Peter, A.B., Howard, E.E., Josefino, C.C., Jorge, E.P.,  
4080 Compton, J.T., Michael, S., Wendy, E., & Jinlun, Z. (2017). Changing seasonality of panarctic  
4081 tundra vegetation in relationship to climatic variables. *Environmental Research Letters* 12,  
4082 055003.

4083 Vazquez-Cuervo, J., Font, J., & Martinez-Benjamin, J.J. (1996). Observations on the Circulation  
4084 in the Alboran Sea Using ERSI Altimetry and Sea Surface Temperature Data. *Journal of*  
4085 *Physical Oceanography* 26, 1426-1439. 10.1175/1520-0485(1996)026<1426:Ootcit>2.0.Co;2

4086 Vazquez-Cuervo, J., Gomez-Valdes, J., Bouali, M., Miranda, L.E., Van der Stocken, T., Tang,  
4087 W., & Gentemann, C. (2019). Using Saildrones to Validate Satellite-Derived Sea Surface  
4088 Salinity and Sea Surface Temperature along the California/Baja Coast. *Remote Sensing In reveiw*

4089 Vincent, R.F., Marsden, R.F., Minnett, P.J., & Buckley, J.R. (2008a). Arctic Waters and  
4090 Marginal Ice Zones: Part 2 - An Investigation of Arctic Atmospheric Infrared Absorption for  
4091 AVHRR Sea Surface Temperature Estimates. *Journal of Geophysical Research* 113, C08044.  
4092 10.1029/2007JC004354

4093 Vincent, R.F., Marsden, R.F., Minnett, P.J., Creber, K.A.M., & Buckley, J.R. (2008b). Arctic  
4094 Waters and Marginal Ice Zones: A Composite Arctic Sea Surface Temperature Algorithm using  
4095 Satellite Thermal Data. *Journal of Geophysical Research* 113, C04021. 10.1029/2007JC004353

4096 von Schuckmann, K., Le Traon, P.-Y., Smith, N., Pascual, A., Brasseur, P., Fennel, K., &  
4097 Djavidnia, S. (2018). Copernicus Marine Service Ocean State Report. *Journal of Operational*  
4098 *Oceanography* 11, S1-S142. 10.1080/1755876X.2018.1489208

4099 Voosen, P. (2018). Saildrone fleet could help replace aging buoys. *Science* 359, 1082.  
4100 10.1126/science.359.6380.1082

4101 Wald, L., & Nihous, G. (1980). Ligurian Sea: Annual variation of the sea surface thermal  
4102 structure as detected by satellite NOAA-5. *Oceanol. Acta* 3, 465-469.

4103 Wallner, O., Reinert, T., & Straif, C. (2017). METIMAGE: a spectro-radiometer for the VII  
4104 mission onboard METOP-SG. In Proceedings of International Conference on Space Optics —  
4105 ICSO 2016, Biarritz, France, Bruno Cugny, Nikos Karafolas, & Z. Sodnik (Eds.), 10562, (8 pp):  
4106 SPIE. doi: 10.1117/12.2296103

4107 Walton, C.C. (2016). A review of differential absorption algorithms utilized at NOAA for  
4108 measuring sea surface temperature with satellite radiometers. *Remote Sensing of Environment*  
4109 187, 434-446. <http://dx.doi.org/10.1016/j.rse.2016.10.011>

4110 Walton, C.C., Pichel, W.G., Sapper, J.F., & May, D.A. (1998). The development and operational  
4111 application of nonlinear algorithms for the measurement of sea surface temperatures with the  
4112 NOAA polar-orbiting environmental satellites. *Journal of Geophysical Research* 103, 27,999-  
4113 928,012.

4114 Wang, D., Pan, D., Wei, J.-A., Gong, F., Zhu, Q., & Chen, P. (2016). Monitoring thermal  
4115 discharge from a nuclear plant through Landsat 8. In Proceedings of SPIE Remote Sensing of the  
4116 Ocean, Sea Ice, Coastal Waters, and Large Water Regions, 9999, (9 pp): SPIE. doi:  
4117 10.1117/12.2242253

4118 Wang, S., Cui, P., Zhang, P., Ran, M., Lu, F., & Wang, W. (2014). FY-3C/VIRR SST algorithm  
4119 and cal/val activities at NSMC/CMA. In Proceedings of SPIE Asia-Pacific Remote Sensing,  
4120 9261, (8 pp): SPIE. doi:  
4121 Wang, Y., & Ientilucci, E. (2018). A Practical Approach to Landsat 8 TIRS Stray Light  
4122 Correction Using Multi-Sensor Measurements. *Remote Sensing* 10, 589.

4123 Wang, Y., Ientilucci, E.J., Raqueno, N.G., & Schott, J.R. (2017). Landsat 8 TIRS calibration  
4124 with external sensors. In Proceedings of SPIE Earth Observing Systems XXII., San Diego, CA,  
4125 USA, 10402, (11 pp): SPIE. doi: 10.1117/12.2272766

4126 Wanninkhof, R., Asher, W.E., Ho, D.T., Sweeney, C., & McGillis, W.R. (2009). Advances in  
4127 Quantifying Air-Sea Gas Exchange and Environmental Forcing. *Annual Review of Marine*  
4128 *Science* 1, 213-244. doi:10.1146/annurev.marine.010908.163742

4129 Wanninkhof, R., Park, G.H., Takahashi, T., Sweeney, C., Feely, R., Nojiri, Y., Gruber, N.,  
4130 Doney, S.C., McKinley, G.A., Lenton, A., Le Quéré, C., Heinze, C., Schwinger, J., Graven, H.,  
4131 & Khatiwala, S. (2013). Global ocean carbon uptake: magnitude, variability and trends.  
4132 *Biogeosciences* 10, 1983-2000. 10.5194/bg-10-1983-2013

4133 Ward, B. (2006). Near-Surface Ocean Temperature. *Journal of Geophysical Research* 111,  
4134 C02005.

4135 Warnecke, G., Allison, L.J., McMillin, L.M., & Szekiolda, K.-H. (1971). Remote Sensing of  
4136 Ocean Currents and Sea Surface Temperature Changes Derived from the Nimbus II Satellite.  
4137 *Journal of Physical Oceanography* 1, 45-60. 10.1175/1520-  
4138 0485(1971)001<0045:Rsocca>2.0.Co;2

4139 Warren, D. (1989). AVHRR channel-3 noise and methods for its removal. *International Journal*  
4140 *of Remote Sensing* 10, 645-651. <https://doi.org/10.1080/01431168908903905>

4141 Webster, P.J., Clayson, C.A., & Curry, J.A. (1996). Clouds, radiation, and the diurnal cycle of  
4142 sea surface temperature in the tropical western Pacific. *Journal of Climate* 9, 1712-1730.

4143 While, J., Mao, C., Martin, M.J., Roberts-Jones, J., Sykes, P.A., Good, S.A., & McLaren, A.J.  
4144 (2017). An operational analysis system for the global diurnal cycle of sea surface temperature:  
4145 implementation and validation. *Quarterly Journal of the Royal Meteorological Society* 143,  
4146 1787-1803. doi:10.1002/qj.3036

4147 Wickramaratna, K., Kubat, M., & Minnett, P. (2008). Discovering numeric laws, a case study:  
4148 CO<sub>2</sub> fugacity in the ocean. *Intelligent Data Analysis* 12, 379-391.

4149 Wilheit, T.T. (1979). A Model for the Microwave Emissivity of the Ocean's Surface as a  
4150 Function of Wind Speed. *IEEE Transactions on Geoscience Electronics* 17, 244-249.  
4151 10.1109/TGE.1979.294653

4152 Wimmer, W., & Robinson, I.S. (2016). The ISAR Instrument Uncertainty Model. *Journal of*  
4153 *Atmospheric and Oceanic Technology* 33, 2415-2433. 10.1175/jtech-d-16-0096.1



4154 Wong, E.W., & Minnett, P.J. (2018). The Response of the Ocean Thermal Skin Layer to  
4155 Variations in Incident Infrared Radiation. *Journal of Geophysical Research: Oceans* 123, 19.  
4156 doi:10.1002/2017JC013351

4157 Woods, J.D., & Barkmann, W. (1986). The response of the upper ocean to solar heating. I: The  
4158 mixed layer. *Quarterly Journal of the Royal Meteorological Society* 112, 1-27.  
4159 <https://doi.org/10.1002/qj.49711247102>

4160 Woods, J.D., Barkmann, W., & A. Horch (1984). Solar heating of the oceans - diurnal, seasonal  
4161 and meridional variations. *Q. J. R. Meteorolog. Soc.*, 110, 633-686.  
4162 <https://doi.org/10.1002/qj.49711046505>

4163 Worley, S.J., Woodruff, S.D., Reynolds, R.W., Lubker, S.J., & Lott, N. (2005). ICOADS release  
4164 2.1 data and products. *International Journal of Climatology* 25, 823-842. doi:10.1002/joc.1166

4165 Wu, F., Cornillon, P., Boussidi, B., & Guan, L. (2017). Determining the Pixel-to-Pixel  
4166 Uncertainty in Satellite-Derived SST Fields. *Remote Sensing* 9. 10.3390/rs9090877

4167 Xiong, X., Butler, J., Wu, A., Chiang, K.V., Efremova, B., Madhavan, S., McIntire, J., &  
4168 Oudrari, H. (2012). Comparison of MODIS and VIIRS onboard blackbody performance. In  
4169 Proceedings of Proc. SPIE 8533, Sensors, Systems, and Next-Generation Satellites XVI, 853318,  
4170 R. Meynart, S.P. Neeck, & H. Shimoda (Eds.), 8533pp). doi: 10.1117/12.977560

4171 Xu, F., & Ignatov, A. (2010). Evaluation of in situ sea surface temperatures for use in the  
4172 calibration and validation of satellite retrievals. *Journal of Geophysical Research: Oceans* 115,  
4173 C09022. 10.1029/2010JC006129

4174 Xu, F., & Ignatov, A. (2014). In situ SST Quality Monitor (iQuam). *Journal of Atmospheric and*  
4175 *Oceanic Technology* 31, 164-180. 10.1175/JTECH-D-13-00121.1

4176 Yamaguchi, Y., Fujisada, H., Kudoh, M., Kawakami, T., Tsu, H., Kahle, A.B., & Pniel, M.  
4177 (1999). ASTER instrument characterization and operation scenario. *Advances in Space Research*  
4178 23, 1415-1424. [https://doi.org/10.1016/S0273-1177\(99\)00293-8](https://doi.org/10.1016/S0273-1177(99)00293-8)

4179 Yamaguchi, Y., Kahle, A.B., Tsu, H., Kawakami, T., & Pniel, M. (1998). Overview of Advanced  
4180 Spaceborne Thermal Emission and Reflection Radiometer (ASTER). *IEEE Transactions on*  
4181 *Geoscience and Remote Sensing* 36, 1062-1071. 10.1109/36.700991

4182 Yang, J., Zhang, Z., Wei, C., Lu, F., & Guo, Q. (2017). Introducing the New Generation of  
4183 Chinese Geostationary Weather Satellites, Fengyun-4. *Bulletin of the American Meteorological*  
4184 *Society* 98, 1637-1658. 10.1175/bams-d-16-0065.1

4185 Závody, A.M., Mutlow, C.T., & Llewellyn-Jones, D.T. (1995). A radiative transfer model for sea  
4186 surface temperature retrieval for the along-track scanning radiometer. *Journal of Geophysical*  
4187 *Research: Oceans* 100, 937-952. 10.1029/94JC02170

4188 Zeng, X., & Beljaars, A. (2005). A prognostic scheme of sea surface skin temperature for  
4189 modeling and data assimilation. *Geophysical Research Letters* 32, L14605.  
4190 doi:10.1029/2005GL023030

4191 Zhang, H., Beggs, H., Majewski, L., Wang, X.H., & Kiss, A. (2016a). Investigating sea surface  
4192 temperature diurnal variation over the Tropical Warm Pool using MTSAT-1R data. *Remote*  
4193 *Sensing of Environment* 183, 1-12.

4194 Zhang, H., Beggs, H., Merchant, C.J., Wang, X.H., Majewski, L., Kiss, A.E., Rodríguez, J.,  
4195 Thorpe, L., Gentemann, C., & Brunke, M. (2018). Comparison of SST Diurnal Variation Models  
4196 Over the Tropical Warm Pool Region. *Journal of Geophysical Research: Oceans* 123, 3467-  
4197 3488. 10.1029/2017jc013517

4198 Zhang, H., Beggs, H., Wang, X.H., Kiss, A.E., & Griffin, C. (2016b). Seasonal patterns of SST  
4199 diurnal variation over the Tropical Warm Pool region. *Journal of Geophysical Research: Oceans*  
4200 *121*, 8077-8094. 10.1002/2016JC012210  
4201 Zhang, L., Shi, H., Du, H., Zhu, E., Zhang, Z., & Fang, X. (2016c). Comparison of WindSat and  
4202 buoy-measured ocean products from 2004 to 2013. *Acta Oceanologica Sinica* *35*, 67-78.  
4203 10.1007/s13131-016-0798-9  
4204 Zhao, Y., Zhu, J., Lin, M., Chen, C., Huang, X., Wang, H., Zhang, Y., & Peng, H. (2014).  
4205 Assessment of the initial sea surface temperature product of the scanning microwave radiometer  
4206 aboard on HY-2 satellite. *Acta Oceanologica Sinica* *33*, 109-113. 10.1007/s13131-014-0402-0  
4207 Zou, X., Zhuge, X., & Weng, F. (2016). Characterization of Bias of Advanced Himawari Imager  
4208 Infrared Observations from NWP Background Simulations Using CRTM and RTTOV. *Journal*  
4209 *of Atmospheric and Oceanic Technology* *33*, 2553-2567. 10.1175/jtech-d-16-0105.1  
4210  
  
4211

4212

### List of Figure Captions.

4213 Figure 1. An extract of the Franklin-Folger Map of the currents of the North Atlantic showing  
4214 the position of the strong surface current named here as the Gulph Stream. From the Library  
4215 of Congress (<https://www.loc.gov/resource/g9112g.ct000753/>).

4216 Figure 2. Near-surface oceanic temperature gradients. From Minnett and Kaiser-Weiss (2012).

4217 Figure 3. Left: Spatial extent of hours of diurnal heating of SST  $\geq 1$  K (defined as the difference  
4218 between a given daytime hourly SST value and the corresponding foundation temperature of  
4219 the previous night) from SEVIRI hourly retrievals for 2006–2011. White areas indicate zero  
4220 occurrences. After Karagali and Høyer (2014). Right: Location of diurnal events over 5 K  
4221 (black '+' and 'o'). Events generally occur in the summer. The background color shows the  
4222 days in a year (on average) that wind speed was  $<1$  ms<sup>-1</sup> at 14:00 LMT. From Gentemann et  
4223 al. (2008) with permission.

4224 Figure 4. Spectral dependence of the atmospheric transmission for wavelengths of  
4225 electromagnetic radiation from about 1 to 14  $\mu$ m, for three characteristic atmospheres  
4226 (above), and (below) the black-body emission for temperatures of 0, 10, 20 and 30°C, and the  
4227 relative spectral response functions of the bands of MODIS on Aqua used to derive SST. The  
4228 upper panel is adapted from Llewellyn-Jones et al. (1984) and the lower panel is taken from  
4229 Kilpatrick et al. (2015).

4230 Figure 5. Simulated spectra of atmospheric transmission in the thermal IR transmission window  
4231 for dry winter conditions (left) and moister summer conditions (right) at the same location  
4232 (66°N, 2°E) in the Norwegian Sea. The atmospheric conditions were given by radiosondes.

4233 Note the units on the abscissa are in wavenumber units; 850 cm<sup>-1</sup> corresponds to  $\lambda = 12 \mu\text{m}$   
4234 and 1000 cm<sup>-1</sup> to  $\lambda = 10 \mu\text{m}$ .

4235 Figure 6. Schematic of relative sensitivity in BT (normalized by the maximum value) for some  
4236 geophysical parameters for measurements at an incidence angle of 55° as a function of  
4237 frequency. Typical primary and secondary frequency bands for retrieving each geophysical  
4238 parameter are shown by black and gray circles. Note that atmospheric contribution was  
4239 neglected for ocean surface parameters, and oxygen absorption was not included for  
4240 atmospheric parameters. From Imaoka et al. (2010), with permission.

4241 Figure 7. A schematic of a MODIS 1km pixel growth from nadir to the edge of swath. The total  
4242 swath width is 2330 km and comprises 1354 pixels. At the swath edges, the satellite zenith  
4243 angle is ~65°.

4244 Figure 8. VHRR IR image 4531 from NOAA 4 was obtained on November 12, 1975. The Gulf  
4245 Stream north of Cape Hatteras and south of Cape Cod appears as the warmest (darkest)  
4246 water. The large amplitude meanders as well as two warm core eddies are evident south of  
4247 Cape Cod and Long Island. (Legeckis, 1978).

4248 Figure 9. Scan geometry of the SLSTR. The dual-view measurements are made by an inclined  
4249 conical scan, which covers the same swath through two different atmospheric path lengths.  
4250 The oblique swath is limited to 740 km by geometrical constraints. Interleaved between  
4251 successive conical scans, a wider, single view swath is obtained. (Reprinted with permission  
4252 from Donlon et al., 2012a).

4253 Figure 10. SST in the vicinity of Japan derived from SGLI on 27 February 2018, showing  
4254 complex structure both inshore and offshore, and the sharp temperature contrast with the  
4255 waters of the Kuroshio to the south. From Tanaka et al., 2018, with permission

4256 Figure 11. ECOSTRESS composite of two Level-2 images of SST derived with the Land Surface  
4257 Temperature (LST) retrieval algorithm, acquired on September 16, 2018 at 13:04 and 13:05  
4258 UTC. Colder SSTs are associated with upwelling north of Santa Barbara. The enlargement  
4259 shows fine-scale SST gradients around the Channel Islands National Marine Sanctuary – note  
4260 the color scale has been stretched to cover 14°C to 22°C to show the fine-scale detail. The  
4261 western islands (San Miguel, Santa Rosa) experience much cooler ocean temperatures than  
4262 the eastern islands due to differences in upwelling, winds and currents. Image credit: Daniel  
4263 Otis, Institute for Marine Remote Sensing (IMaRS), College of Marine Science, University  
4264 of South Florida. Reproduced from <https://ecostress.jpl.nasa.gov/gallery/viewgalleryimage>  
4265 with permission.

4266 Figure 12. Global SST's from SMMR, June 1979. Plate 1 of Gloersen et al., 1984.

4267 Figure 13. Global SST distribution derived by compositing AMSR2 measurements over three  
4268 days ending 21 November 2018. Credit: Wentz, F.J., T. Meissner, C. Gentemann, K.A.  
4269 Hilburn, J. Scott, 2014: Remote Sensing Systems GCOM-W1 AMSR2 Environmental Suite  
4270 on 0.25° grid, Version V.8. Remote Sensing Systems, Santa Rosa, CA. Available online at  
4271 [www.remss.com/missions/amr](http://www.remss.com/missions/amr). Accessed 24 November 2018.

4272 Figure 14. Maps of the differences between Metop-B AVHRR and drifting buoys temperatures at  
4273 night for October 2018. Top left: Mean differences (mean = -0.16 K, standard deviation =  
4274 0.53 K); top right: Median differences (median = -0.05 K, robust standard deviation = 0.39  
4275 K); bottom: number of matchups in 5° latitude x longitude bins – bins with < 5 matchups are

4276 excluded from the analysis. There are 14560 cases. (Data produced by the OSI SAF; quality  
4277 index data from 3 to 5 have been used).

4278 Figure 15. Example of validation of an uncertainty model for ESA SST\_CCI V1.1 NOAA-18  
4279 AVHRR SST products for (left) day time and (right) nighttime. Match-ups to drifting buoys  
4280 are binned in terms of the product uncertainty; vertical blue lines indicate the measured  
4281 dispersion for each uncertainty level and red dots indicate the standard error for each  
4282 uncertainty level and also provide an indication of the number of match-ups. The dashed  
4283 green lines indicated the theoretical dispersion of uncertainties (assuming an average drifting  
4284 buoy measurement uncertainty of 0.2 K) if the product uncertainty estimates (and uncertainty  
4285 models) are accurate. The agreement at night time is very good but the day time results show  
4286 the product uncertainties were overestimated. (Corlett, G., 2018.  
4287 Uncertainty\_validation\_example.jpg. <https://doi.org/10.6084/m9.figshare.7286168.v2>.)

4288 Figure 16. An example of L3 to L4 SST interpolation using DINEOF (Data Interpolating  
4289 Empirical Orthogonal Functions); (left): original VIIRS SST<sub>skin</sub> data on 8 October 2018 and  
4290 (right): DINEOF L4 SST<sub>skin</sub> reconstruction.

4291 Figure 17. Demonstration of a “gridless” interpolation and importance of avoiding truncation of  
4292 geolocation data. Left: observations (open circles) are typically averaged at a nearest grid-  
4293 point (closed circles) effectively truncating the subgrid portion of the location parameters.  
4294 Center: such bin-averaging (colors inside big circles) can distort spatial information like the  
4295 orientation of the front (background), due to the nearest-neighbor approximation of  
4296 geolocation data. Right: a gridless interpolation method tends to ingest the observations at  
4297 their original locations, reducing the distortion in front orientation, even at a low resolution  
4298 shown.

4299 Figure 18. Error budget framework with sources of errors and uncertainties (left column) and  
4300 how they accumulate in the progression to L4 gap-filled SST fields (right column). From Wu  
4301 et al. (2017), reproduced through CC BY 4.0.

4302 Figure 19. Mean Sea Surface Temperature field in the Mediterranean Sea from 1982 to 2017  
4303 derived from CMEMS reprocessing.

4304 Figure 20. Comparison of selected L4 SST analyses in the Beaufort Sea on 13 August 2012  
4305 (DOY 226). The color scale has been fixed to facilitate comparisons between products, and  
4306 the trajectory of one of the drifting buoys (Louis 2012-03) has been plotted over the images  
4307 with the circle showing the position of the buoy for that particular day and the color  
4308 indicating the corresponding buoy temperature. The gray areas indicate that the respective ice  
4309 mask has been applied, if available. Note that no ice mask is shown in the OISST since the  
4310 ice and water masks were mistakenly inverted during this period and the buoy location was  
4311 inaccurately flagged as ice covered. The anomalously low OISST temperature at the buoy  
4312 location is a result of the improper masking. From Castro et al. (2016), with permission.

4313 Figure 21. An example of the improvement in the NWP forecasting skill when a more realistic  
4314 SST field is used as the bottom marine boundary. The mean error in temperature at 850 hPa  
4315 in the Northern Hemisphere when using old AVHRR and in situ low resolution SST data as a  
4316 bottom boundary condition (grey line) and high resolution SST data from the OSTIA system  
4317 (black line). The trial period was from 1st August 2007 until 31st August 2007. (From  
4318 Donlon et al. (2012b), with permission).

4319 Figure 22. 3-hourly verification against drifting buoys of four SST analyses. Global data for  
4320 March 2, 2019 to March 11, 2019. The solid curves are for  $O - A = T_{zob}^{ob} - [T_f^{an} +$

4321  $T_w'^{bg}(zob)]$ , black: NCEP NSST (NST); red: OSTIA (OST); blue: CMC; green: MUR. The  
4322 upper, middle and lower panel is for bias, root mean square and used counts respectively.  
4323 The black dashed curve is  $(O - B) = T_{zob}^{ob} - [T_f^{bg} + T_w'^{bg}(zob)]$  for NSST.

4324 Figure 23. As Figure 22 but excluding the diurnal warming at the observed depth in the analysis  
4325 and background fields.

4326 Figure 24. OHC estimate (relative to 26°C: color bar) and geostrophic velocity vectors from  
4327 space-based measurements of satellite altimetry and SST on 1 August 2015 in the Intra-  
4328 American Seas.

4329 Figure 25. Tracks and positions of maximum intensity for fourteen of the strongest hurricanes  
4330 1998-2011, plotted over OHC relative to the 26°C isotherm for September 2005.

4331 Figure 26. SST on 3 December, 2018 (top) and Chlorophyll-a concentration (units  $\log(\text{mg m}^{-3})$ )  
4332 on 4 December, 2018 (bottom), western Mediterranean Sea, derived from measurements of  
4333 MODIS on Aqua.

4334 Figure 27. The SST anomaly derived from the Multi-Scale Ultra-High Resolution (MUR) SST  
4335 overlaid on a true color image from MODIS on Aqua. Clearly visible (blue colors) is the  
4336 cooling of the Gulf of Mexico as Hurricane Michael made landfall on October 10th, 2018.  
4337 Image provided by JPL/Caltech/PO.DAAC.

4338 Figure 28: The track of the Saildrone deployment from April 11, 2018-June 11, 2018 (top left),  
4339 colored by the measured SST, as indicated by the temperature scale at right. Other panels  
4340 show the differences between three L4 satellite-derived SST fields and the Saildrone  
4341 measurements, colored according to the temperature difference scale at far right. After  
4342 Vazquez-Cuervo et al. (2019)).